UNIVERSITY OF OKLAHOMA

GRADUATE COLLEGE

# SELECTION OF METAL COMPLEX CATALYSTS BY TEMPLATING WITH TRANSITION STATE ANALOGS

A DISSERTATION

SUBMITTED TO THE GRADUATE FACULTY

in partial fulfillment of the requirements for the

Degree of

DOCTOR OF PHILOSOPHY

By

ANH TUAN TRAN
Norman, Oklahoma
2015

SELECTION OF METAL COMPLEX CATALYSTS BY TEMPLATING WITH TRANSITION STATE ANALOGS

A DISSERTATION APPROVED FOR THE
DEPARTMENT OF CHEMISTRY AND BIOCHEMISTRY

BY

_____
Dr. Kenneth M. Nicholas, Chair

_____
Dr. Mark A. Nanny

_____
Dr. George Richter-Addo

_____
Dr. Daniel T. Glatzhofer

_____
Dr. Robert Thomson

*To my parents, my wife & my children, thank you.*

## Acknowledgements

I would like to thank Professor Kenneth M. Nicholas for his mentorship and support over years in the chemistry world odyssey. I would like to thank past and present Nicholas research group members from whom I learned many things. I would like to thank, Jacob Rapp for his valuable contribution about kinetic experiments. I would like to thank Dr. Steven Foster for training and let me use his mass spectrometer. I would like to thank Dr. Peng Liu and Dr. Kendall Houk at UCLA for their collaboration in computational studies. I would like to thank Michael Woodman at Agilent Technologies for his generous donation of HPLC columns. I would like to thank my parents, De M. Tran and To M. Vu, for their encouragement and for all their help along the way. No words can adequately express my gratitude. I would like to thank my wife, Trang, for her sacrifice, support and unconditional love. Thanks Minh and Linh for making me understand what I am doing.

## Table of Contents

Acknowledgements ..... iv

List of Tables ..... x

List of Figures ..... xi

Abstract ..... xix

Chapter 1: Transition State Analogs and Catalyst Evolution ..... 1

1. Transition state theory and transition state analogs. ..... 1

1.2. Reaction Energy Diagram and Transition State Analog. ..... 1

1.2.1 One-product and Two-product Reaction Energy Diagram. ..... 1

1.2.2. Transition State Analog (TSA), early and late TSA. ..... 3

1.3. TSA-Hapten Induced Catalytic Antibody. ..... 5

1.3.1 Hydrolytic Catalytic Antibodies. ..... 5

1.3.2 Diels-Alder Catalytic Antibodies ..... 10

1.4 Molecular Imprinted Polymers ..... 13

1.4.1 Hydrolytic Catalytic MIPs ..... 14

1.4.1 Diels-Alder Catalyst MIP. ..... 17

1.5 Dynamic Combinatorial Chemistry. ..... 20

1.5.1 DCL templating by host-guest interactions ..... 20

1.5.2 DCL templating as a catalyst selection method. ..... 23

1.6 Affinity Chromatography ..... 29

1.6.1 Examples of using TSAs as affinity ligands for protein purification. ..... 30

1.7 Conclusions and Preview. ..... 33

Chapter 2. Selection of Regioselective Diels-Alder Catalysts by Dynamic Templating with Transition State Analogs ..... 36
2.1 Introduction ..... 36
2.1.1 Hetero Diels-Alder (HDA) reaction. ..... 36
2.1.1 Nitroso Diels-Alder reaction (NDA) ..... 37
2.1.2 Asymmetric catalysts NDA reaction. ..... 38
2.1.3. Regioselective NDA reactions. ..... 39
2.1.3.1 Catalytic regioselective HDA reactions ..... 39
2.2 Results and Discussion. ..... 41
2.2.1 Uncatalyzed (thermal) Reaction of PyrNO and Unsymmetrical Diene. ... 41
2.2.2. Cu(I) Catalyzed Reaction of Nitrosopyridine with Unsymmetrical Dienes ..... 44
2.2.2.1 Cu(I)-imine complex formation. ..... 44
2.2.2.2 $Cu(CH_3CN)_4PF_6$ as a catalyst for NDA reactions. ..... 45
2.2.2.3 Cu-imine complexes as catalysts for NDA reactions. ..... 47
2.2.3. Mass Spectral Binding Studies. ..... 51
2.2.4 Computational studies ..... 54
2.2.4.1 Uncatalyzed Nitrosopyridine - Diene Reactions ..... 54
2.2.4.2 $Cu^+$-Catalyzed the reactions of 2-nitrosopyridine and 1,3-pentadienes. 58
2.2.4.3. Cu(diimine)$^+$- Catalyzed Reaction of Nitrosopyridine and 1,3-pentadiene. ..... 59
2.3 Conclusions and future work. ..... 61
2.4 Experimental ..... 63

2.4.1 Materials Preparation..... 63

2.4.2 ESI-MS quantification of the $LCu(TSA)^+$ complex library ..... 76

2.4.3. Copper (I) catalyzed reactions..... 78

2.4.3.1 Diene-PyrNO reactions catalyzed by tetrakis(acetonitrile)copper(I) hexafluorophosphate..... 78

2.4.3.2 Diene-PyrNO reactions catalyzed by $(imine)_2$copper(I) hexafluorophosphate..... 78

2.4.4 Computational methods..... 79

Chapter 3. A Survey of other (non-Cu(I)) Transition Metal Complexes as HDA Catalysts by Templating with Transition States Analogs..... 81

3.1 Introduction. ..... 81

3.1.1 Zinc, Nickel, Palladium and Copper (II) as the catalysts for HDA reaction. ..... 81

3.1.2 Ligand design. ..... 82

3.2 Results and Discussion. ..... 82

3.2.1 Rates of the uncatalyzed and catalyzed reactions..... 83

3.2.2 Catalytic tests with (imine)M complexes. ..... 87

3.2.3. Templating with substrate and TSA. ..... 95

3.2.3.1 Ligand Exchange ability of metal-imine complexes. ..... 96

3.2.3.2 Templating with substrates as “early” TSAs..... 99

3.2.3.3 Templating with products as “late” TSAs ..... 101

3.2.4 Computational studies. ..... 105

3.3 Conclusions. ..... 108

3.4 Future directions. ..... 110
3.5 Experimental ..... 112
3.5.1 Reaction rate measurement. ..... 112
3.5.1.1 Rate constant of thermal background reaction. ..... 113
3.5.1.2 Rate constants of metal catalyzed HDA reactions. ..... 113
3.5.1.3 Rate constants for metal catalyzed decomposition of nitrosopyridine. 115
3.5.2 Catalytic test. ..... 118
3.5.2.1 Diene-PyrNO reactions catalyzed by $Ni^{2+}$, $Cu^{2+}$, $Zn^{2+}$ and $Pd^{2+}$. ..... 118
3.5.2.2 Diene-PyrNO reactions catalyzed by $(diimine)_2$-metal complexes. ..... 119
3.5.2.3 ESI-MS qualification of the $LCu(nitrosopyridine)^+$ complex library ..... 120
3.5.2.4 ESI-MS quantification of the $LCu(TSA)^+$ complex library ..... 120
3.5.3 Material Preparation. ..... 121
Chapter 4. Solid Supported Transition State Analogs for Catalyst Selection ..... 122
4.1 Introduction. ..... 122
4.3 Results and discussion ..... 126
4.3.1 Synthesis of the affinity silica gel. ..... 126
4.3.2 Affinity chromatography testing. ..... 133
4.3.3 Kinetics assay. ..... 137
4.3.4. Discussion. ..... 141
4.4 Conclusion. ..... 148
4.5 Future directions. ..... 149
4.6 Experimental ..... 151
4.6.1. Materials preparation. ..... 151

4.6.2 Silica Functionalization ..... 167

4.6.3 Kinetics measurements. ..... 172

References ..... 174

## List of Tables

**Table 1:** List of first examples of using phosphoramidate, sulfonamide and boronic acid hapten, substrate for the reaction, products and $k_{cat}/k_{uncat}$. ..... 7

**Table 2:** Common ligands and applications in affinity chromatography. Hage et al.[73] 30

**Table 3:** Regioselectivity of PyrNO/pentadiene reactions catalyzed by (Imine)$Cu^{+}$. ... 50

**Table 4:** Crystal data and structure refinement for (**85**) ..... 76

**Table 5:** Calculated activation barriers for the reaction of 2-nitrosopyridine and (*E*)-1,3-pentadiene ..... 80

**Table 6:** Adduct regioselectivity in 2-PyrNO/pentadiene reactions catalyzed by (Imine)$Ni^{2+}$ in MeOH with 10 mol % catalyst loading. [a]1 mol % catalyst loading ..... 88

**Table 7:** Solvent effect of the imine-$Cu^{2+}$ (10 mol% loading) catalyzed nitrosopyridine and pentadiene reactions. ..... 89

**Table 8:** Ligand/$Cu^{2+}$ ratio effects on the regioselectivity of the reaction between nitrosopyridine and 1,3 pentadiene. ..... 89

**Table 9:** Adduct regioselectivity in PyrNO/pentadiene reactions catalyzed by (imine)$Cu^{2+}$ in MeOH with 10% catalyst loading. ..... 91

**Table 10:** Regioselectivity of (aldehyde)$Cu^{2+}$ catalysts for the HDA reaction. ..... 92

**Table 11:** Regioselectivity in the PyrNO/pentadiene reaction catalyzed by (Imine)$Zn^{2+}$. [a] reaction at 1 mol % catalyst loading. ..... 94

**Table 12:** (Imine)$Pd^{2+}$ catalysts for the HDA reaction. ..... 95

**Table 13:** Retention times of (imine)$Zn(OTf)_2$ complexes with benzyl, substrate and TSA bound columns. ..... 136

**Table 14:** Kinetic data of 14 tested ligands. ..... 138

## List of Figures

**Figure 1:** One-product reaction energy diagram. ..... 2

**Figure 2:** Two –product reaction energy diagram. ..... 3

**Figure 3:** Hydrolysis of 4-nitrophenyl carbonate reaction and proposed TSA (**3**). Schultz et al.[6] ..... 6

**Figure 4:** Lerner hapten (**4**) and substrates (**5a** (top) and **5b** (bottom). Schultz et al.[6].... 6

**Figure 5:** E1cB (top) and $B_{AC}2$ (bottom) mechanisms for carbamate hydrolysis.[17] ..... 8

**Figure 6:** Phosphoamidate as TSA for E1cB mechanism (R= $NO_2$, Br, F, $OCH_3$).[16] ..... 8

**Figure 7:** N-methyl phosphoamidate **7** as TSA for $B_{Ac}2$ mechanism.[18] ..... 9

**Figure 8:** Hydrolytic kinetic resolution with antibody 2H6 ..... 10

**Figure 9:** First example of antibody-catalyzed Diels-Alder reaction. ..... 11

**Figure 10:** Product like derivative as late TSA for D-A catalytic antibody. ..... 11

**Figure 11:** Diagram of making of MIP. Mayer et al.[30] ..... 13

**Figure 12:** First example of catalytic MIP..... 14

**Figure 13:** Metal free catalyst MIP by Sagawa group. ..... 15

**Figure 14:** Substrate analog as early TSA for amide hydrolysis MIP catalyst (top). Schematic depiction of the imprinting process.[39] ..... 16

**Figure 15:** Stereoselective MIP catalyst. Top: substrate and TSA. Bottom: synthesis scheme. [41] ..... 17

**Figure 16:** Silica supported TSA for making catalytic MIP. Bruggemann et al.[43]..... 18

**Figure 17:** Schematic of heterogeneity of binding sites. Zimmerman et al.[53]..... 19

**Figure 18:** Sander's building blocks and oligomerization reaction. ..... 21

**Figure 19:** Tetramethyl ammonium ion **40** and disulfide library. Sanders et al. [63] ..... 22

**Figure 20:** DCL of Schiff base with crown ether macrocycles. ..... 23

**Figure 21:** First example of using DCC to make a DA catalyst. ..... 24

**Figure 22:** First example of using DCC to select an acetal hydrolysis catalyst. ..... 25

**Figure 23:** Reaction and proposed transition states for metal-catalyzed ester hydrolysis. ..... 26

**Figure 24:** Plot of multiple turnover rate constants vs. amplification factor for **63** with Zn-**128,** Zn-**129**, Zn-**130** and Zn-**131**. ..... 26

**Figure 25**: The most differentially amplified metal-ligand-TSA complex is predicted to be the most selective catalyst ..... 27

**Figure 26:** Reaction, chiral TSA and catalyst for kinetic resolution of picolinate ester. ..... 28

**Figure 27:** Example of amplified library by R and S isomers ESI-MS quantification. 28

**Figure 28:** Typical scheme of an affinity chromatography application. Hage et al.[73] .. 29

**Figure 29:** Transcarbamase reaction, TSA and solid-supported TSA. ..... 31

**Figure 30:** Trifloromethylketone as the TSA for insect juvenile hormone esterase separation. ..... 32

**Figure 31:** Building blocks and solid supported guest molecule in Otto experiments.. 32

**Figure 32:** First example of Diels-Alder reaction[81] ..... 36

**Figure 33:** NDA reaction and reduction of the 1,2 oxazine adduct. ..... 37

**Figure 34:** Up to 4 isomers can be formed from the nitroso-DA reaction with unsymmetrical dienes (2 enantiomers and 2 regioisomers)**.** ..... 38

**Figure 35:** Inomata's proposed transition state. Inomata et al.[115,133] ..... 40

**Figure 36:** Hapten and Lineweaver–Burk plot of **309-1G7** catalysis of the reaction between nitrosobenzene and 1,3 pentadiene. Pandit et al.[134,135] ..... 40

**Figure 37:** Reaction of 2-nitrosopyridine with 1,3-pentadiene. ..... 42

**Figure 38:** 2-Nitrosopyridine and E,E-2,4-hexadienol reaction with proposed transition state. ..... 43

**Figure 39:** 2-Nitrosopyridine reaction with 1-phenyl-E-1,3-pentadiene. ..... 43

**Figure 40**: Formation of complex **85** and X-ray crystal diffraction structure. ..... 45

**Figure 41:** Formation of $LCu(TSA)^+$ complexes from $(imine)_2Cu^+$ complexes. ..... 47

**Figure 42:** Amines and aldehydes for producing imine ligands. ..... 49

**Figure 43:** ESI-Mass spectra of (a) **107** + **89** + **90** + **91** + $Cu(CH_3CN)_4^+$; (b) $L_2Cu^+$ + **78**; (c) $L_2Cu^+$ + **77**. ..... 52

**Figure 44:** Correlation of ESI-MS (imine)Cu-$TSA^+$ binding selectivity and catalytic product selectivity. ..... 54

**Figure 45:** Calculated transition states for the reaction of 1,3-pentadiene with 2-nitrosopyridine. ..... 56

**Figure 46:** Most stable transition states for the reaction between 2-nitrosopyridine and 1-phenylbutadiene. ..... 57

**Figure 47:** Calculated transition states for the $(CH_3CN)_2Cu^+$ -catalyzed DA reaction between nitrosopyridine and 1,3-pentadiene. ..... 58

**Figure 48:** Calculated transition states for Cu(**87**-**98**)$_2^+$ catalyzed nitrosopyridine and 1,3-pentadiene. ..... 61

**Figure 49:** 1D-NOE of compound **77** (left) and compound **78 (**right**).** ..... 65

**Figure 50:** $^1$H NMR and $^{13}$C NMR of compound (**80**) ..... 67

**Figure 51:** HBMC and expansion of compound (**80**)..... 68

**Figure 52:** $^{1}$H NMR and $^{13}$C NMR of compound (**81**)..... 70

**Figure 53:** HBMC spectrum and expansion of spectrum for compound **81.** ..... 71

**Figure 54:** $^{1}$H NMR and $^{13}$C-NMR of compound **84.** ..... 73

**Figure 55** HMBC and 1D-NOE of compound **84**..... 74

**Figure 56** $^{1}$H NMR spectrum of compound **85**..... 75

**Figure 57:** Proposed substrate complexes with square planar geometries. ..... 82

**Figure 58:** Absorbance vs. time plot of the uncatalyzed reaction between 2-nitrosopyridine (**75**) and 1,3-pentadiene (**76**). ..... 84

**Figure 59:** Suggested formation of azoxypyridine.[173] ..... 85

**Figure 60:** Kinetics of Ni(OTf )$_2$ catalyzed decomposition of nitrosopyridine in MeOH ..... 86

**Figure 61:** New bulky aldehydes..... 91

**Figure 62:** New amines and (imine)$_2$Zn$^{2+}$ complexes. ..... 93

**Figure 63:** Library of (MeCN)$_2$Pd(O$_3$SC$_6$H$_4$CH$_3$)$_2$ + **104** + **87**. ..... 95

**Figure 64:** Exchange ability of (imine)Ni$^{2+}$ with aliphatic amine (**90**) ..... 97

**Figure 65:** Imine exchange ability of Cu$^{2+}$. Top: Cu$^{2+}$ + **94** + **104.** Bottom: added **90** to the mixture of Cu$^{2+}$ + **94** + **104** ..... 98

**Figure 66:** (**94**-**104**)Cu$^{2+}$ with "early" TSA library. ..... 99

**Figure 67:** ESI-MS of Ni(OTf)$_2$ with nitrosopyridine **75**. M/z from 260 to 450 (top) and 590 to 670 (bottom)..... 100

**Figure 68:** ESI-Mass spectra of (top) **77**+ **105** + **107** + **108** + **89** + **90** + Cu(OTf)$_2$ (bottom) **78** + **105** + **107** + **108** + **89** + **90** + Cu(OTf)$_2$ ..... 102

**Figure 69:** ESI-Mass spectra of (a) **77** + **107** + **108** + **89** + **90** + **91** + $Cu(OTf)_2$ (b) **78** + **107** + **108** + **89** + **90** + **91** + $Cu(OTf)_2$. ..... 104

**Figure 70**: Binding selectivity vs catalyst regioselectivity of (**107**-**89**)$Cu^{2+}$, (**107**-**90**) $Cu^{2+}$ and (**107**-**91**)$Cu^{2+}$..... 104

**Figure 71**: (**107**-**86**)$Ni^{2+}$ complex used in this study and previously calculated pyrrolide-imine-$Ni^{2+}$ complexes (Y = $CH_2C(CH_2)_3CH_2$ and $CH_2CH(OH)CH_2$). ..... 106

**Figure 72:** Three possible ground states of (**107**-**86**)(**75**)$Ni^{2+}$ ..... 107

**Figure 73**: Three possible ground states of (**107**-86)(**75**)$Cu^{2+}$ ..... 108

**Figure 74:** Computational studies with (**98**-**90**)Rh(nitrosopyridine)$^+$ (Top) and (**98**-**90**)Ir(nitrosopyridine)$^+$ (bottom). ..... 111

**Figure 75**: ESI-Mass spectra of (a) **98** + **94** + Ir and ESI-Mass spectra of (b) **98** + **94** + **90** + Ir. ..... 112

**Figure 76:** Kinetic data of $Ni(OTf)_2$ catalyzed HDA reaction ..... 114

**Figure 77:** Kinetic data of $Cu(OTf)_2$ catalyzed HDA reaction. ..... 114

**Figure 78:** Kinetic data of $Zn^{2+}$ catalyzed the HDA reaction. ..... 115

**Figure 79:** Kinetic data of $[(MeCN)_2Pd(O_3SC_6H_4CH_3)_2]$ catalyzed HDA reaction.... 115

**Figure 80:** Absorbance vs. time of $Ni^{2+}$ catalyzed decomposition of nitrosopyridine (**75**). ..... 116

**Figure 81:** Absorbance vs. time of $Cu^{2+}$ catalyzed the decomposition of nitrosopyridine (**75**). ..... 117

**Figure 82** Absorbance vs. time of $Zn^{2+}$ catalyzed the decomposition of nitrosopyridine (**75**). ..... 117

**Figure 83** Absorbance vs. time of $Pd^{2+}$-catalyzed decomposition of nitrosopyridine (**75**)**.** ..... 118

**Figure 84:** Schematic of the catalyst selection by affinity chromatography. (A) Injection, (B) Stationary phase Interaction, (C) No-binding interaction, (D) Non-specific interaction, (E) Weak binding interaction, (F) Strong binding interaction. ..... 123

**Figure 85:** Hydrolysis of 4-nitrophenyl picolinate **122**. ..... 123

**Figure 86:** Formation of imine ligands and the list of ligands used in this project. .... 124

**Figure 87:** Three affinity columns: TSA **(139),** substrate analog **(140)** and reference **(141)** ligands. ..... 126

**Figure 88:** Synthesis of substrate-like (ethyl picolinate) column. ..... 127

**Figure 89**: Synthesis of the reference (benzyl) column ..... 128

**Figure 90:** First idea for making **139.** ..... 129

**Figure 91:** Direct functionalized **140** from compound **139** plan**.** ..... 130

**Figure 92:** Third plan to synthesis **139.** ..... 131

**Figure 93:** Synthesis of TSA (trifluoromethyl diol) silica gel **139**..... 133

**Figure 94:** Imine equilibrium (top) and the solution (bottom) ..... 135

**Figure 95**: Plot of binding constant vs $k_{cat}$ with all of the tested ligands. ..... 139

**Figure 96**: Plot of binding constant vs $k_{cat}$ with 2-coordinate ligands. ..... 140

**Figure 97**: Plot of binding constant vs kcat with 2-coordinate –OH ligands. ..... 140

**Figure 98:** Plot of substrate column – benzyl column retention time vs $1/K_{M.}$ ..... 142

**Figure 99:** Plot of substrate column – benzyl column retention time vs $1/K_M$ for two-coordination hydroxyl catalysts. ..... 143

**Figure 100:** Plot of substrate column – benzyl column retention time vs $1/K_M$ for bidentate, non-hydroxyl ligand complexes..... 144

**Figure 101:** Catalyzed reaction energy diagram..... 145

**Figure 102:** Plot of $k_{TSA}/k_{sub}$ and $k_{cat}$ for two-coordinate catalysts. ..... 146

**Figure 103**: Plot of $k_{TSA}/k_{sub}$ and $k_{cat}$ for two-coordinate with - OH moiety catalysts. 147

**Figure 104:** Possible side reaction chain when attaching **162** onto the silica gel. ..... 148

**Figure 105:** Possible hydrated ketone - hemiacetal – acetal problem. ..... 148

**Figure 106:** Proposed phosphonate esters as the new TSA affinity ligands. ..... 150

**Figure 107:** $^{1}$H-NMR spectrum of **144.**..... 153

**Figure 108:** $^{13}$C-NMR spectrum of **144.**..... 153

**Figure 109:** $^{1}$H-NMR spectrum of **145**..... 155

**Figure 110:** $^{13}$C-NMR spectrum of **145**..... 155

**Figure 111:** FTIR spectrum of **145**..... 156

**Figure 112:** $^{1}$H-NMR spectrum of **160.**..... 157

**Figure 113:** $^{13}$C-NMR spectrum of compound **160.**..... 158

**Figure 114:** $^{19}$F-NMR spectrum of compound **160.** ..... 158

**Figure 115:** $^{1}$H-NMR spectrum of **157.**..... 160

**Figure 116:** $^{13}$C-NMR spectrum of **157.**..... 160

**Figure 117:** $^{19}$F-NMR spectrum of **157.** ..... 161

**Figure 118:** $^{1}$H-NMR spectrum of **161.** ..... 162

**Figure 119:** $^{13}$C-NMR spectrum of **161.**..... 163

**Figure 120:** $^{19}$F-NMR spectrum of **161.** ..... 163

**Figure 121:** $^{1}$H-NMR spectrum of **162** ..... 165

**Figure 122:** $^{13}$C-NMR spectrum of **162**..... 166

**Figure 123:** $^{19}$F-NMR spectrum of **162** ..... 166

**Figure 124:** IR spectrum of compound **162**..... 167

**Figure 125:** In column functionalization set up..... 169

**Figure 126:** IR spectrum of amino silica gel **146**. ..... 170

**Figure 127:** IR spectrum of substrate analog with linker on silica gel 140. ..... 170

**Figure 128:** IR spectrum of benzyl reference with linker **141**. ..... 171

**Figure 129:** IR spectrum of TSA with linker 139. ..... 171

## Abstract

Catalysts speed up reactions by providing an alternative, lower energy pathway for the reaction. However, the traditional method of catalyst discovery is time consuming and wastes chemicals. It is important to find a better way of discovering new catalysts preferably with minimal experiments from a collection of catalysts. In this study, transition state analogs (TSAs) were used as templates as a new methodology for catalyst discovery.

In the first chapter, products of hetero Diels-Alder (HDA) reaction between nitroso pyridine and 1,3-pentadiene were used as "late" TSAs for templating with a dynamic library of (imine)$Cu^{+}$ catalysts. MS quantification was employed as a powerful tool for analyzing the complex library, yielding both peak identification and relative concentration in one experiment. A marginal correlation has been found between library amplification and regioselectivity of the catalysts. Intensive computational studies were also conducted in order to draw a better understanding about the reaction mechanisms and additionally provide a guideline for further catalyst improvement.

The second chapter evaluated the potential of using other imine transition metal complexes: e.g. (imine)$Cu^{2+}$, (imine)$Zn^{2+}$, (imine)$Ni^{2+}$ and (imine)$Pd^{2+}$ as regioselective catalysts and attempted to use these complexes for templating with TSAs. The $Cu^{2+}$, $Zn^{2+}$ and $Ni^{2+}$ imine complexes catalyze the HDA reaction between 2-nitrosopyridine and 1,3-pentadiene with a small range of selectivity. The templating experiments with these transition metals, however, were not able to draw a better correlation between amplification versus regioselectivity of the catalysts. Computational studies have also been used as a supplemental tool in order to better understand the complex formation

and geometry as well as provide a guide to improve the experimental results. In both of the cases, templating with TSAs proved the concept that most regio-selective catalyst can be determined from a library of catalysts with only one set of experiments.

The final chapter investigated the correlation of binding affinity of catalysts to solid-supported substrate analog with catalyst-substrate binding constant and the correlation between binding affinity of catalysts to solid supported trifluoromethyl ketone hydrate as a TSA and rate of the ester hydrolysis reaction. A strong positive correlation with high statistical significance between catalyst-substrate analog binding affinities and catalyst-substrate binding constant was found, which indicates that the substrate analog perfectly mimics substrate-catalyst interaction. A positive correlation with less statistical significance was observed between catalysts-TSA binding and the rate of the catalyzed reactions. With a large set of tested catalysts, 13 (imine)$Zn^{2+}$ complexes, the experiments proved the concept that affinity chromatography with solid supported substrate analog and TSA can be an effective tool for catalyst discovery. Better TSAs, phosphate esters, and better linkages were also proposed to improve the experimental results.

# Chapter 1: Transition State Analogs and Catalyst Evolution

## 1. Transition state theory and transition state analogs.

The transition state theory was first proposed by Eyring, Evans and Polanyi, and it considers all aspects of the reaction such as thermodynamics, kinetic-theory treatment, potential energy surfaces.[1,2] In general, the theory assumes that the reaction goes through several equilibria between reactants and the activated transition state which is, usually, the highest energy point. A reaction can have several transition states, but usually the highest energy transition state (rate determining step) is the most important.

## 1.2. Reaction Energy Diagram and Transition State Analog.

### 1.2.1 One-product and Two-product Reaction Energy Diagram.

In a one-product reaction without a catalyst, compound A and compound B react and form product AB. According to the transition state theory, the rate of the reaction is determined by the activation energy ($\Delta G_{uncat}$). When a catalyst is used for the same reaction, compound *A* will react with the catalyst to form intermediate *Cat-A* then the Cat-A reacts with B to from B-Cat-A*, presumed to be the transition state of the reaction. The reaction then goes to the second intermediate Cat-AB before breaking down to the product AB and catalyst. The rate of the catalyzed reaction is determined by the activation energy $(\Delta G_{Cat})^{‡}$ and the difference in the rate of catalyzed and uncatalyzed reaction is determined by the Arrhenius equation $\Delta\Delta G^{‡} = RT \ln(k_{cat}/k_{uncat})$ (**Figure 1**). In a catalyzed one-product reaction, the fastest catalyst is the one that has

the lowest $\Delta G_{cat}^{\ddagger}$. Generally speaking, the main focus of catalyst design for a one-product reaction is to have the fastest reaction, in other words, the lowest $\Delta G_{cat}^{\ddagger}$.

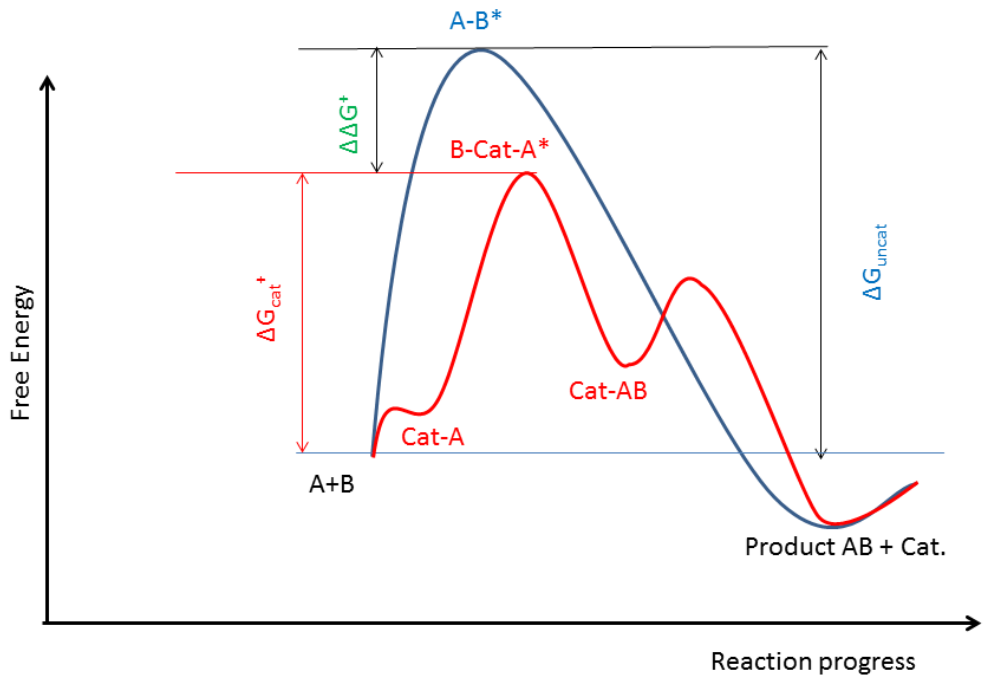


**Figure 1:** One-product reaction energy diagram.

A two-product (or multiple-product, generally speaking) reaction also follows the same main states. The kinetic selectivity of a reaction (difference in the distribution of final products) is determined by the difference in the activation energies of both pathways. With both the uncatalyzed and the catalyzed reactions, the distribution of the final products is also determined by the Arrhenius equation $\Delta G^{\ddagger} = RT \ln(P_1/P_2)$, in which $\Delta G^{\ddagger}$ is the difference in the activation energies of two transition states and $P_1/P_2$ is the ratio of product 1 to product 2. In **Figure 2**, the distribution of the two products depends on the difference in activation energies, $\Delta\Delta G^{\ddagger}$, for the uncatalyzed reaction,

and $\Delta\Delta G_{cat}^{\ddagger}$ for the catalyzed reaction. However, unlike the one-product reaction, having the fastest catalyst might not be the ultimate goal for catalyst design. The ultimate goal for a two-product reaction, usually, is to maximize the selectivity with which a catalyst is able to promote the desired product pathway while prohibiting the undesired pathway.

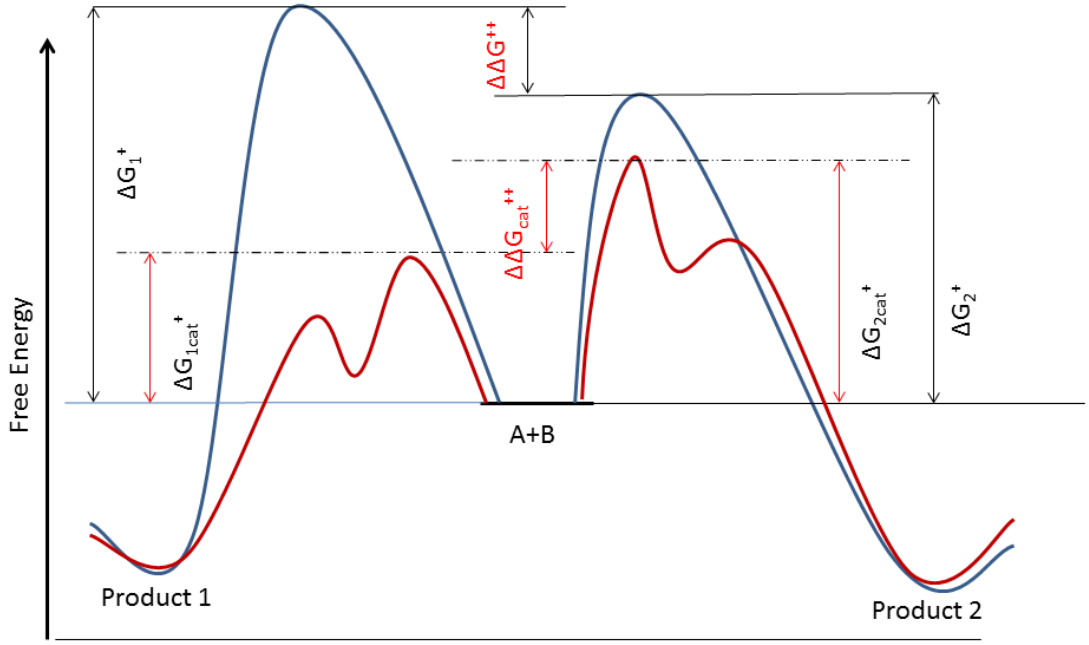


**Figure 2:** Two –product reaction energy diagram.

### 1.2.2. Transition State Analog (TSA), early and late TSA.

The transition state is the highest energy point on the potential energy diagram, but due to instability, it is impossible to detect. However, a TSA can be used as an alternative for investigating a reaction. The TSA resembles the transition state of a

reaction both electronically and sterically. Jencks proposed a the transition state analog could be used to generate enzymatic catalysts:[3]

> "If complementarity between the active site and the transition state contributes significantly to enzymatic catalysis, it should be possible to synthesize an enzyme by constructing such an active site. One way to do this is to prepare an antibody to a haptenic group which resembles the transition state of a given reaction. The combining site of such antibodies should be complementary to the transition state and should cause acceleration by forcing bound substrates to resemble the transition state"

Pauling first suggested the idea of enzyme active site:[4]

> "The only reasonable picture of the catalytic activity of enzymes is that which involves an active region of the surface of the enzyme which is closely complementary in structure not to the substrate molecule itself in its normal configuration, but rather to the substrate molecule in a strained conformation corresponding to the 'activated complex' for the reaction catalyzed by the enzyme."

The combination of Pauling and Jencks' hypothesis led to an expansion of the study and discovery of catalyst antibodies. Studies concerning catalyst antibodies have led to important insights about reaction mechanisms, enzyme structure and function, catalysis and the immune system.[5]

Although it is not a clear line, TSAs can be categorized into three different stages: *early* TSA, TSA and *late* TSA. They resemble three different stages of the transition state: *early* TSA is substrate like; TSA is transition state like; and *late* TSA is product like. The application of TSAs in chemistry is very broad, ranging from making catalytic antibodies, to enzyme inhibitors, to molecular imprinted polymer catalysts, to dynamic combinatorial homogeneous catalysts.

### 1.3. TSA-Hapten Induced Catalytic Antibody.

TSAs were first used to generate catalytic antibodies, a class of monoclonal antibodies with catalytic activity.[6-8] In this approach, a transition state analog tethered to a protein is used as a hapten to stimulate the immune system. The immune system responds by generating protein antibodies and the antibodies are harvested. All new antibodies can bind with the tethered transition state analog, but not all of them are catalytically active, and thus the next step is testing for catalytic activity. The first examples of using TSAs to generate catalytic antibodies were reported by Schultz[6] and Lerner[7,8] in 1986. Separately they came up with the same brilliant idea- to use protein-tethered phosphonate and phosphate esters to mimic the tetrahedral transition state in the hydrolysis of esters.

#### 1.3.1 Hydrolytic Catalytic Antibodies.

Hydrolytic catalytic antibodies were one of the earliest antibody catalysts to be discovered. Schultz reported using **3** as a transition state analog for the hydrolysis reaction of **1** which is believed to go through the tetrahedral transition state **2**. Hapten **3** triggered the mice in the study to generate active catalytic antibody MOPC167. The catalytic antibodies were isolated and showed substrate specificity with **1** with the $k_{cat}/k_{uncat}$ = 770 (**Figure 3**).[6] With the same methodology, Lerner found that the catalytic antibodies, generated from hapten **4**, catalyzed the hydrolysis of **5a** and **5b** (**Figure 4**).[6]

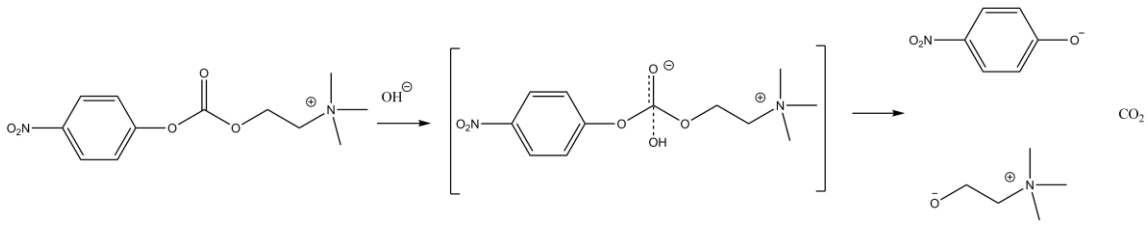

**1** **2**

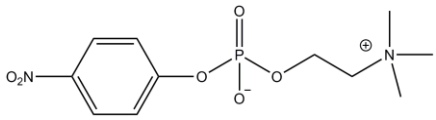

**3**

**Figure 3:** Hydrolysis of 4-nitrophenyl carbonate reaction and proposed TSA (**3**). Schultz et al.[6]

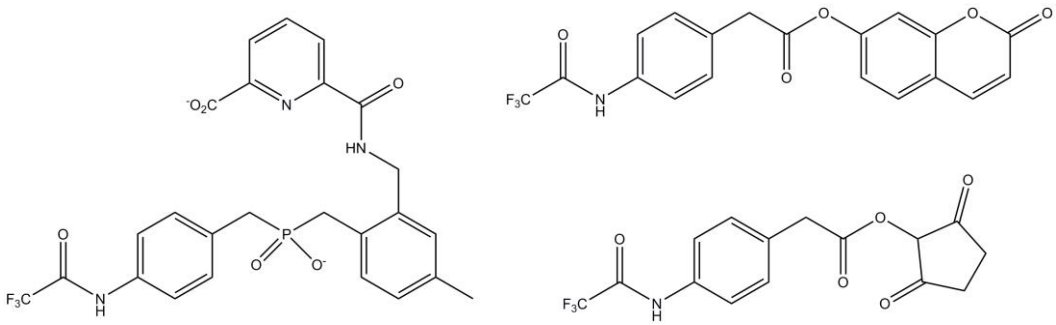

**4** **5a** (top) and **5b** (bottom)

**Figure 4:** Lerner hapten (**4**) and substrates (**5a** (top) and **5b** (bottom). Schultz et al.[6]

Following the first two successful examples, the use of hydrolytic catalytic antibodies bloomed in the 90s. Compared to esters, amides are harder to hydrolyze. Unsurprisingly, Lerner's group was the first group to report the use of a phosphoramidate to generate the catalytic antibody 43C9 for hydrolyzing amides.[9] Sulfonamides, like phosphoramidates, also have a tetrahedral structure and thus potentially can be used as haptens for amide hydrolysis. Tonizzo's group reported the use of a sulfonamide hapten to elicit a catalytic antibody, 312D6, to hydrolyze N-p-

toluoylindole and its derivatives.[10] It is known that at pH ~ 8, boronic acids adopt a tetrahedral structure by $OH^-$ addition, thus a boronic acid derivative can be used as a TSA for the amide hydrolysis reaction. Janda's group reported the use of boronic acid derivative as hapten to get catalytic antibody Fab BL 25 to carry out primary amide hydrolysis (**Table 1**).[11]

| Hapten | Substrate | Product | $k_{cat}/k_{uncat}$ |
|---|---|---|---|
| 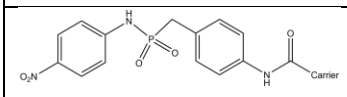 | 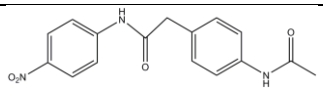 | 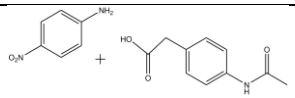 | 250,000 [9] |
| 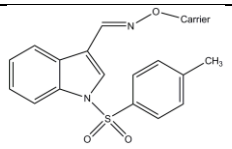 | 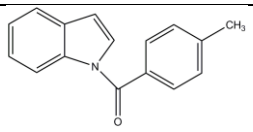 | 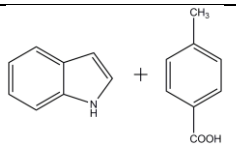 | 750 [10] |
| 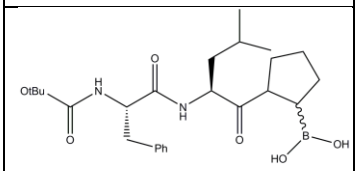 | 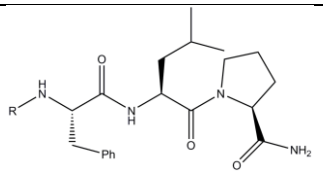 | 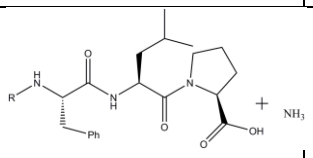 | 4000 [11] |

**Table 1:** List of first examples of using phosphoramidate, sulfonamide and boronic acid hapten, substrate for the reaction, products and $k_{cat}/k_{uncat}$.

There are two proposed mechanisms for carbamate ester hydrolysis: elimination-addition (E1cB) and addition-elimination ($B_{Ac}2$), depending on the conditions and substrate. Aryl carbamate hydrolysis is known to occur by the E1cB mechanism exclusively, while the $B_{Ac}2$ mechanism only occurs with carbamates that have a non-ionizable N-H group (**Figure 5**).[12-15] In both cases, phosphonate-based haptens are employed with small modifications for each mechanism. The Blackburn group reported the antibody DF8-D5 raised against the phosphoamidate hapten (**6**) as

the TSA. The ratio of $k_{cat}/k_{uncat}$ with various substrates ranged from 3.0 x $10^3$ to 1.2 x $10^6$ (**Figure 6**). Interestingly, the catalyzed reaction had a significantly smaller Hammett ρ value compared to that of the uncatalyzed reaction, which suggests that the catalyzed reaction proceeds by the $B_{Ac}2$ rather than the E1cB mechanism of the uncatalyzed reaction.[16]

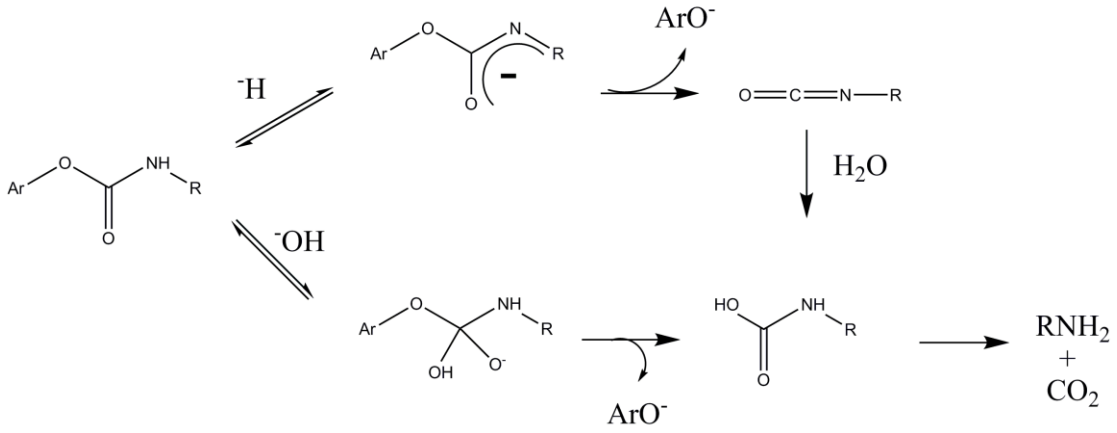


**Figure 5:** E1cB (top) and $B_{AC}2$ (bottom) mechanisms for carbamate hydrolysis.[17]

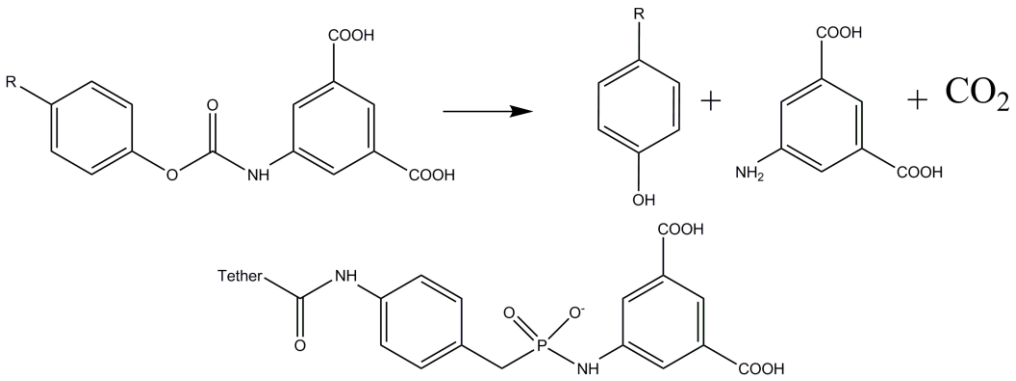


**6**

**Figure 6:** Phosphoamidate as TSA for E1cB mechanism (R= $NO_2$, Br, F, $OCH_3$).[16]

The antibody ST51 was raised against N-methyl phosphoamidate **7** as the TSA for the $B_{Ac}2$ mechanism. The rate of carbamate hydrolysis by a $B_{Ac}2$ mechanism is significantly slower than that by the E1cB mechanism by up to $10^8$ times (depending on the substrate).[16] Despite having p-nitrophenyl as a good leaving group, the uncatalyzed reaction is very slow with a half-life of ~ 5.7 years. The antibody ST51 catalyzes the reaction with $k_{cat}/k_{uncat}$ = 6,500.[18]

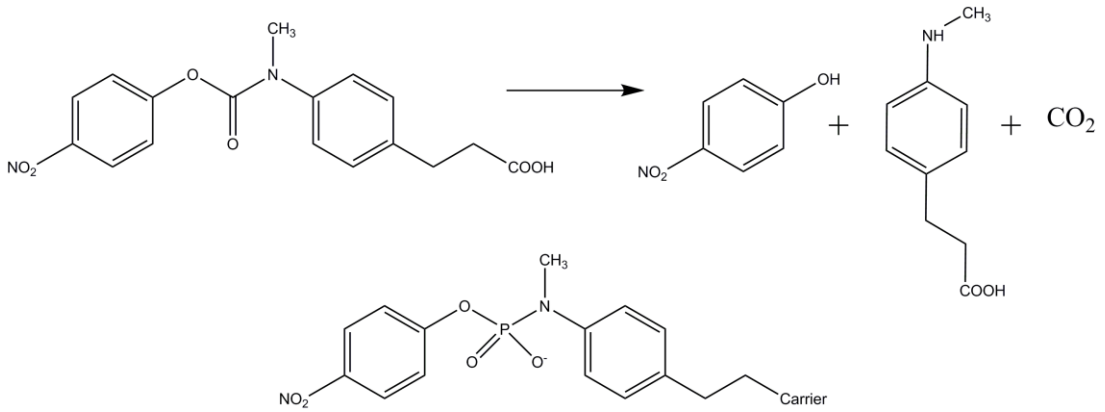


**7**

**Figure 7:** N-methyl phosphoamidate **7** as TSA for $B_{Ac}2$ mechanism.[18]

Amino acids used in living animals are uniformly chiral, thus it is not surprising that a racemic hapten mixture can trigger the immune system to generate different antibodies for each isomer. The Lerner group reported that when using a racemic mixture of TSA **9**, they were able to isolate a total of 11 active hydrolytic antibodies. From the 11 active antibodies, antibody 2H6 catalyzes the hydrolysis of (R)-**8** much faster than (S)-**8**, while antibody 21H3 catalyzed the hydrolysis of (S)-**8** much faster than (R)-**8**.[19] In both of the cases, the selectivity is more than 98% ee. It was suggested that (R) and (S)-**9** trigger the immune system separately, thus selective antibodies were

generated. The antibodies generated by this method can be used in kinetic resolution to hydrolyze one enantiomer selectively, leaving the other untouched (**Figure 8**).

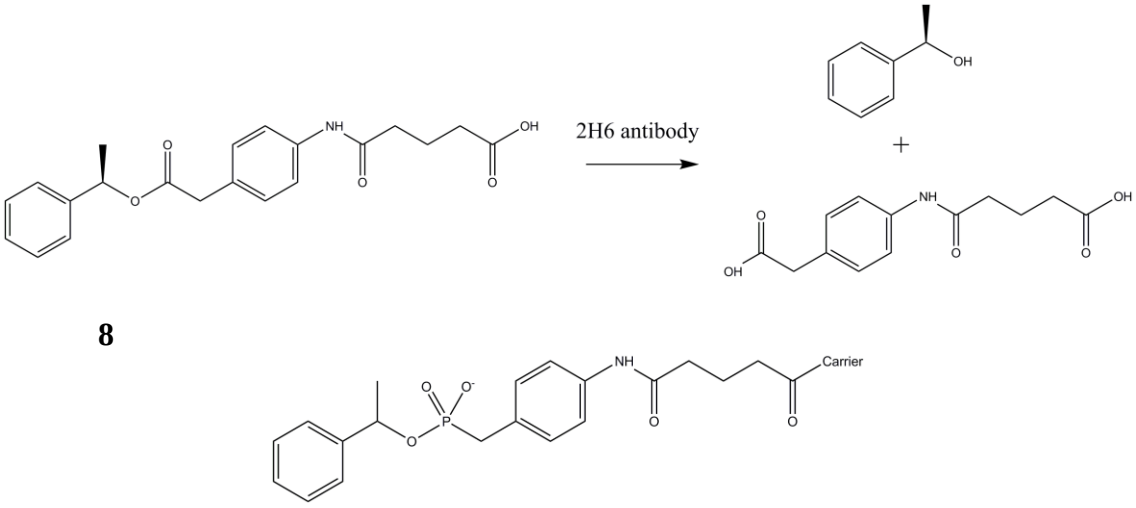


**8**

**9**

**Figure 8:** Hydrolytic kinetic resolution with antibody 2H6

### 1.3.2 Diels-Alder Catalytic Antibodies

Hydrolytic antibodies were popular and were among the very first examples of catalytic antibodies. However, the applications of catalytic antibodies are not limited to hydrolysis. Auditors' group, also at Scripps, was the first group to report the use of highly ordered TSA hapten for the Diels-Alder (DA) reaction.[20] Antibody 1E9 was isolated when using hapten **13** to trigger the immune system. Hapten **13** resembles the transition state of the DA reaction between tetrachlorothiophene dioxide (**10**) and N-ethylmaleimide (**11**). The bicyclic intermediate (not observed) is unstable and undergoes $SO_2$ extrusion to generate the final product (**12**). It is important to note that they were one of the first groups to employ a reaction product as a "late" TSA for the DA reaction: "The transition state of a Diels-Alder cycloaddition is highly ordered,

resembling product more closely than starting material."[20,21] They were not able to measure the $k_{cat}$ because of the low solubility of the catalyst.[19]

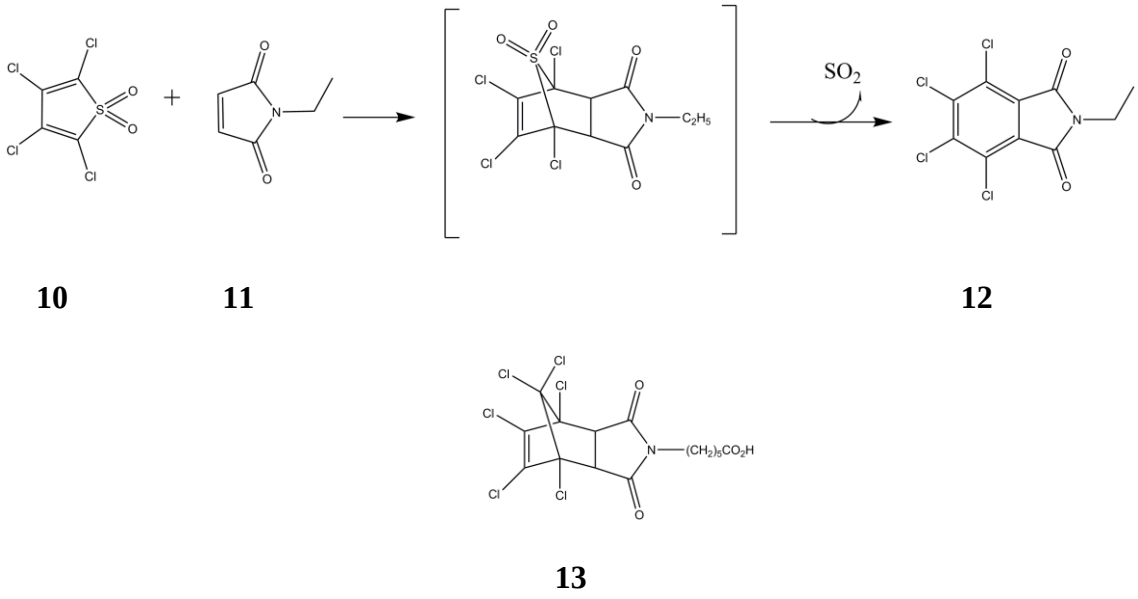


**10** **11** **12**

**13**

**Figure 9:** First example of antibody-catalyzed Diels-Alder reaction.

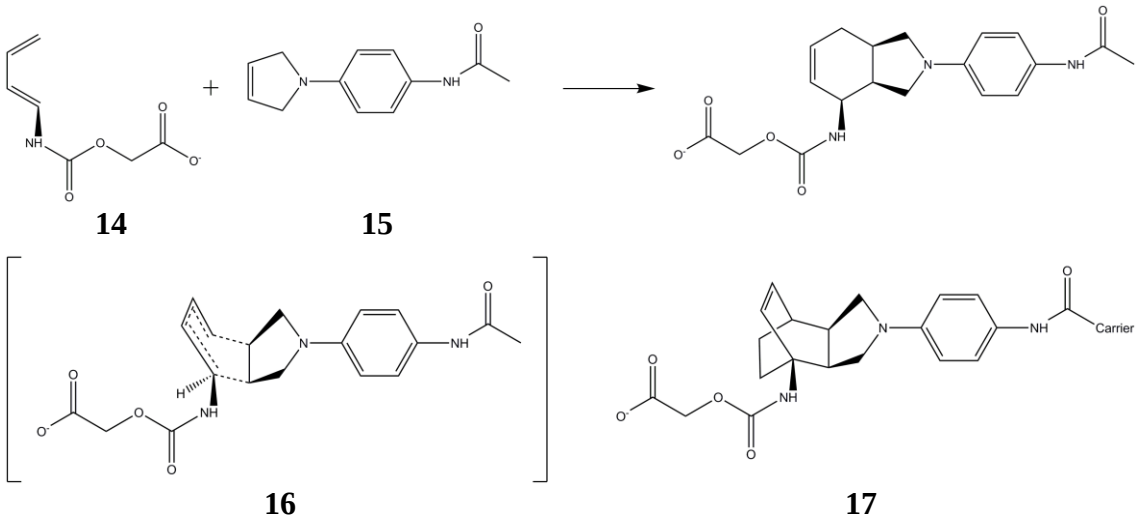

**14** **15**

**16** **17**

**Figure 10:** Product like derivative as late TSA for D-A catalytic antibody.

Another D-A catalytic antibody was reported by the Schultz group. The reaction between diene (**14**) and dienophile (**15**) is thought to have a highly ordered transition

state (**16**). Compound **17,** the product of the DA reaction between the cyclohexadiene derivative of (**14**) and (**15**), was used as the hapten. They realized that in order to mimic the highly ordered transition state, the TSA of the reaction must be a rigid analog to resemble the ring formation. Other than that, this "late" TSA **17** is identical to the product. This example showed that it is possible to use a product analog as "late" TSA for making catalytic antibodies.

Within about 10 years from mid-80's to the mid-90's, TSA-hapten induced catalytic antibodies were expanded to many reaction types including: aldol and retro-aldol reactions,[22] Michael additions,[23] Claisen rearrangements (stereo-specific),[24,25] Cope rearrangements,[26] decarboxylation,[27] etc. Despite excellent activity and selectivity as well as the number of publications, the practical applications of catalytic antibodies are still limited.[5] The main reason for this is that making the catalytic antibodies requires a lot of time, special equipment and laboratory animals, and a great number of steps including: the design and synthesis of the hapten, injection of the hapten into the mouse, waiting for the mouse immune system to generate B cells, collection of the B cells (killing the mouse), separation of the antibodies, and screening for catalytic activity.[6,7,17] The last step, separation and screening for catalytic activity, is the most time consuming and labor intensive.[5,28] The catalytic antibodies also generally showed lower performance in organic solvents and are less tolerant to high temperature. From the end of the 80's a new kind of catalyst, molecularly imprinted polymer catalysts,[29] was developed to take advantage of the specific binding idea, while requiring less time and labor.

## 1.4 Molecular Imprinted Polymers

A molecular imprinted polymer (MIP) is one that has been imprinted with a specific template. The molecule imprinted polymer technique employs a template molecule in the mixture, a functional monomer, a cross linker, porogens (solvent), and an initiator. Upon the polymerization, organic molecules are "co-polymerized" with the functional monomer to make organic imprinted polymer. After the polymerization, the template is washed out of the polymer leaving cavities. The procedure to make a MIP is illustrated in **Figure 11**.[30]

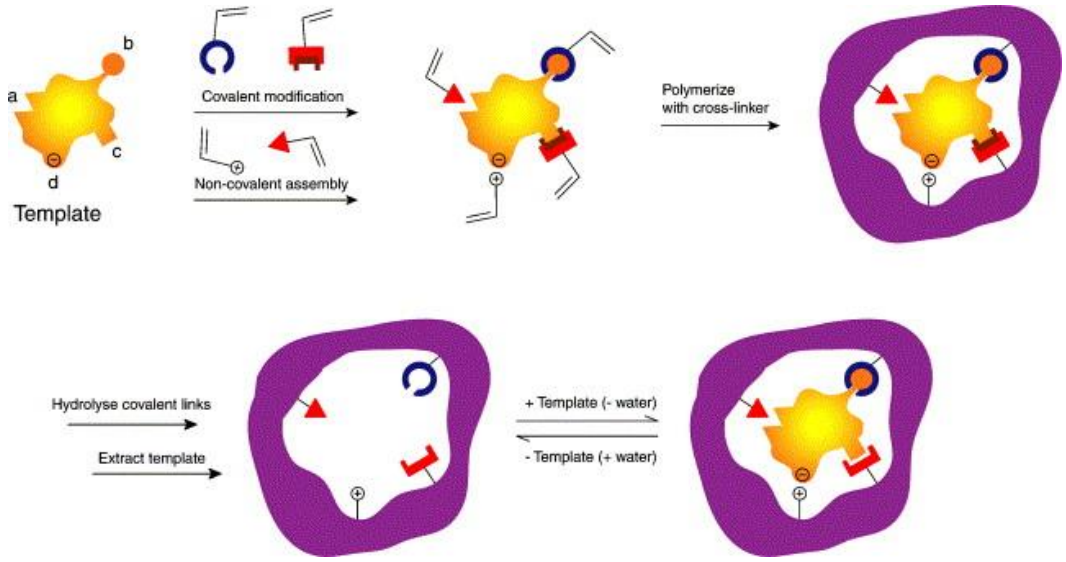


**Figure 11:** Diagram of making of MIP. Mayer et al.[30]

Similar to the active site of enzymes, the active sites of the MIPs selectively bind with the template or template-like molecules (shape and charge). The specific binding of MIPs can be used for many applications such as: chromatography,[31] pharmaceutical chemistry,[32] environmental molecular sensing,[33] catalysts,[34] drug delivery,[35] antibody and receptor mimics,[36] on both the laboratory and industrial scale.

The applications of MIPs are broad and very promising. However this chapter only focuses on catalytic MIP applications. In catalytic MIPs, a TSA is imprinted into the polymer creating specific size/shape cavities. The TSA is chosen so that it mimics the transition state of the desired reaction. After removing the template, the empty cavities can act as active sites for catalysis.

### 1.4.1 Hydrolytic Catalytic MIPs

Mosbach reported the first example of a TSA imprinted polymer as a catalyst. Employing the stable tetrahedral structure of *p*-nitrophenol methylphosphonate (**19**) as the TSA for the hydrolysis of *p*-nitrophenyl acetate (**18**), they were able to imprint **19** into the polymer with $Co^{2+}$, with 4(5)-vinylimidazole and 1,4-dibromobutane as cross linkers. After template removal, the polymer was tested for catalytic activity in methanol/phosphate buffer (pH 7). The imprinted polymer showed 60% higher activity than the reference polymer without the imprinted TSA. In the presence of **19**, the imprinted polymer was found to be completely inactive, presumably due to strong binding of **19** to the active sites.[37]

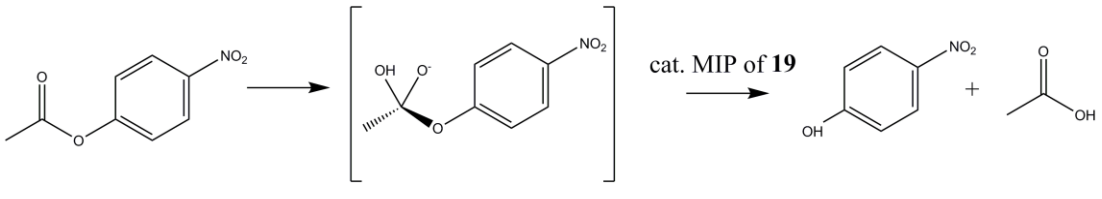


**18**

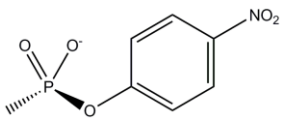


**19**

**Figure 12:** First example of catalytic MIP.

A metal free hydrolytic catalyst MIP was also made by the Sagawa group.[38] Compound **21** was used as the TSA for the ester hydrolysis of **20.** The novel idea of using N-methyl acryloyl L-histidine (**22**) as functional monomer and compounds **23**, **24**, and **25** as cross linkers gave the polymer a tremendous amount of hydrogen bonding capability with the TSA **21** in the templating step and substrate **20** in the reaction, thus no metal ion is needed in the polymer compared to the Mosbach method. The imprinted polymer showed a small $k_{cat}/k_{uncat} = 5.78$.

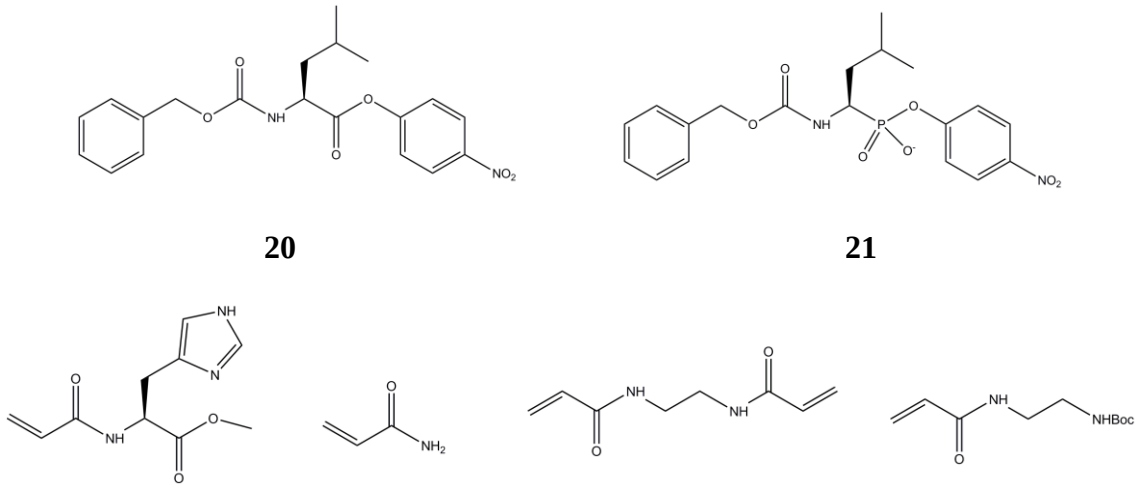


**20** **21**

**22** **23** **24** **25**

**Figure 13:** Metal free catalyst MIP by Sagawa group.

Substrate analogs, compounds similar to the substrate with additional moieties for binding with solid media, can also be used as "early" TSAs for imprinting. Mosbach reported using compounds **27** and **29** as the substrate TSA of compound **26** and **28** respectively (**Figure 14** - top).[39] In the first step, the TSA/4-(5)-vinylimidazole complex with $Co^{2+}$ was pre-formed before the polymerization (step 1 - **Figure 14** bottom). After the polymerization with *p*-divinylbenzene (DVB), the template with $Co^{2+}$

was then removed by extraction. In both of the cases, the imprinted catalysts showed hydrolysis rate increases with $k_{cat}/k_{uncat}$ = 3.6 and 7.1 with substrate **26** and **28**, respectively, compared to that of the control polymer.

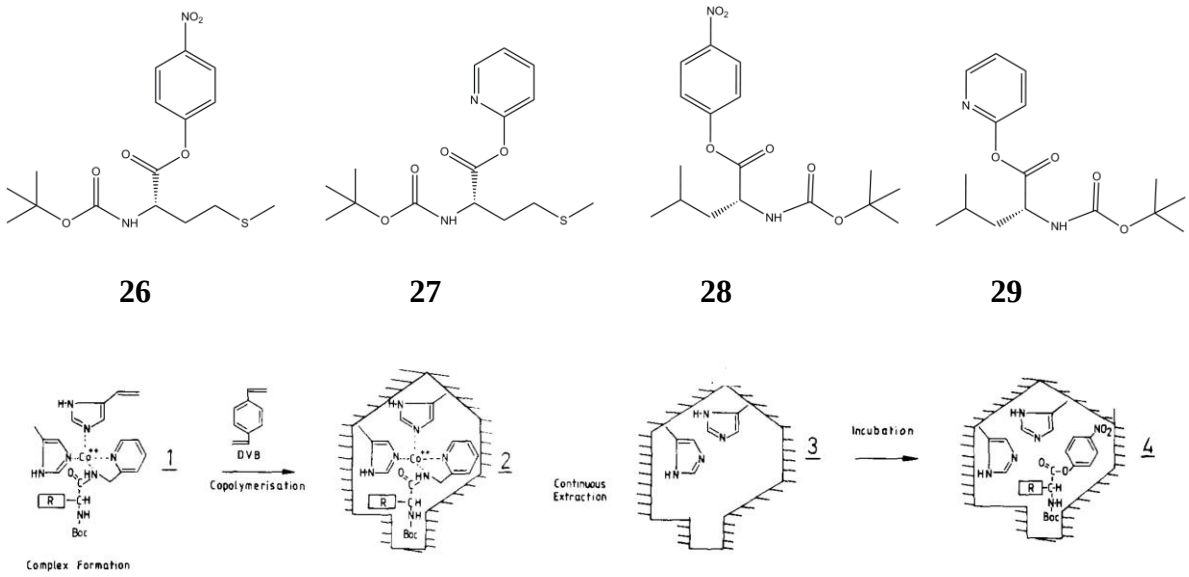


**Figure 14:** Substrate analog as early TSA for amide hydrolysis MIP catalyst (top). Schematic depiction of the imprinting process.[39]

Catalytic MIPs can still retain the chirality after the removal of the chiral template, thus the catalyst can differentiate enantiomers. The Shea group reported the first example of a stereoselective ester hydrolysis catalytic MIP.[40] Compound **31** was used as the TSA in the D-**30** hydrolysis reaction (**Figure 15** Top). The D-phenyl moiety in **31** is a chiral center and was later imprinted into the polymer. One interesting feature of the design of compound **31** was the phenyl imidazole moiety then later became part of the polymer. This phenyl imidazole selectively blocked L-substrate while allowing D-substrate to get into the pocket which created a stereoselective binding site.[40,41] The D-imprinted catalyst showed $k_D/k_L$ = 1.9.

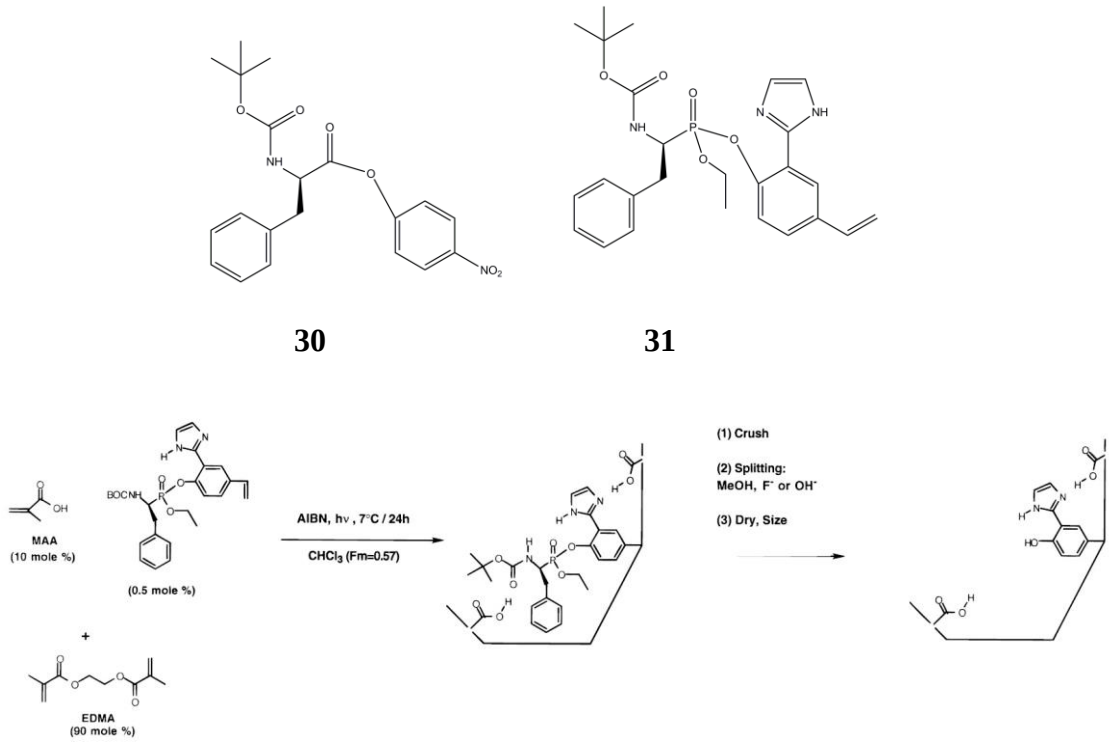


**Figure 15:** Stereoselective MIP catalyst. Top: substrate and TSA. Bottom: synthesis scheme. [41]

### 1.4.1 Diels-Alder Catalyst MIP.

Inspired by Auditor's work (**Figure 9**),[20] the Mosbach group used exactly the same TSA for the same DA reaction to create a catalytic MIP. They found that the imprinted polymer had a $k_{cat}/k_{uncat}$ = 270. Interestingly, the product bound to the cavity so strongly that there was no turnover for the catalyst (product inhibition).[42]This was the first example of using a TSA in making DA catalytic MIP.

Bruggemann's group reported using product as a "late" TSA for imprinting in the polymer.[43] Compound **34** is the product of the DA reaction between **33** and **32**. The same compound was bound into aminopropyl silica and used as template (**Figure 16** – top). After polymerization, the TSA-amino silica was removed and used as a catalyst (**Figure 16** – bottom). They reported that the catalyst MIP prepared by this method

increased the rate of reaction from ~2 to 4 times (depending on solvent) compared to that of the direct imprinted method which did not catalyze the reaction (approximately equal rate of thermal reaction). The main reason for this phenomenon is that if the substrate was imprinted directly into the polymer then it either cannot be removed from the matrix or the substrate inhibitor effect blocked all of the available binding sites.

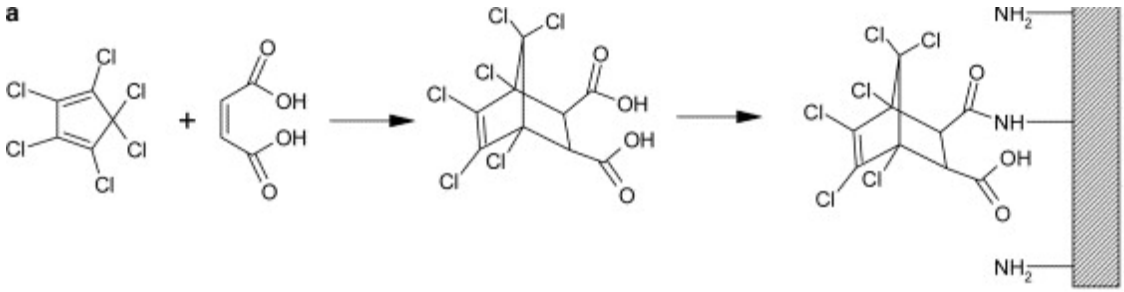


**32** **33** **34** **34** on amino silica

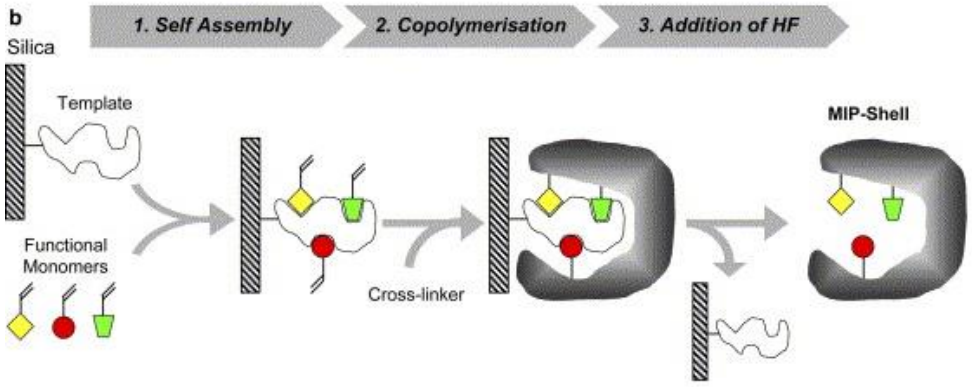


**Figure 16:** Silica supported TSA for making catalytic MIP. Bruggemann et al.[43]

Like the catalytic antibodies, MIP catalysts were popular in the literature during the 90's. Several important reactions promoted by MIPs were reported including: β-elimination,[44] decarboxylation,[45] the aldol reaction,[46] hydride transfer,[47,48] etc. Most of the MIP catalysts are tolerant of higher temperatures compared to that of catalytic

antibodies. Also, catalytic MIPs are compatible with many organic solvents and are relatively easier to make. Low reactivity and selectivity, however, are the main drawbacks of catalyst MIP's. Despite innovations in preparation methodologies to increase the accessibility to the active sites including: monolithic silica coating,[49] in column bulk synthesis,[50] suspension in solvent,[51] two stage swelling,[52] etc., the main limitation of catalytic MIP's is the low availability and activity of selective binding sites. Mainly the binding sites on the surface are active, but most of the active sites are inaccessible (**Figure 17**). It is estimated that no more than 20% of the active site is available to be a selective binding site.[53] Only embedded sites (D) and micropore sites (F) in **Figure 17** are selective binding sites while other types are either inactive (C and E) or unselective (A and B). The main problem with binding site accessibility and selectivity of catalyst MIP could potentially be overcome with a newer methodology of catalyst discovery and selection: dynamic combinatorial chemistry.

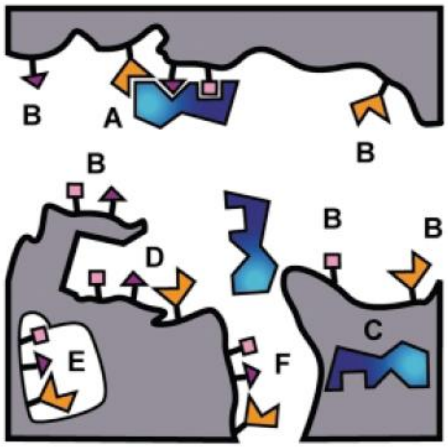


**Figure 17:** Schematic of heterogeneity of binding sites. Zimmerman et al.[53]
High affinity site in macropore (A), lower affinity sites (B), in macropore (C), trapped template (E), embedded site (D) and micropore (F).

## 1.5 Dynamic Combinatorial Chemistry.

Dynamic combinatorial chemistry (DCC) is defined as combinatorial chemistry under thermodynamic control.[54] Theoretically, formation of products in a library of reacting compounds follows statistical rules in which all potential products can be formed. However, the statistical rules cannot predict the relative amount of each possible product. The relative amount (concentration) each of product will be determined by the thermodynamic driving force in which the total free energy of the whole library is minimized. One interesting feature of a DCC system is its ability to adapt to an external stimulus. When a foreign stimulus, e.g. another reactive compound, is added to the library, the library can be disturbed and thus shift to a new equilibrium, as such each product changes concentration. The favored (increased amount) product is said to be *amplified*.

This concept has been utilized for molecular recognition as well as to make receptors, inhibitors, ligands for biomolecules, drugs, sensors and catalysts. Several important reviews on this subject have been published over the last few years.[54-59] This chapter highlights a few important examples of DCC with host-guest interactions and the discovery of catalysts by templating with TSAs.

### 1.5.1 DCL templating by host-guest interactions

Sander's group first demonstrated the amplification of hydrazone libraries with external simulants, alkyl ammonium salts, as templates. The set of four hydrazone derivatives, **35**, **36**, **37** and **38**, was mixed and allowed to equilibrate. The ESI-MS of the mixture showed a combination of hydrazones ranging from dimers to undecamers (

**Figure 18**).[60] If compound **36** were on the library alone, a similar phenomenon was observed in which cyclic dimers, trimers, tetramers up to undecamers coexist at about the same concentration. However, when $Li^+$ ion was added to the library, the composition of the library drastically changed. Cyclic trimer was found as the primary species while the other species either were not found or only found at very low concentration (by HPLC analysis).[61] In a similar way, a library of **37** was dominated with cyclic dimer at equilibrium while other cyclic oligomers were in the minority. When alkyl ammonium iodide salts such as trimethylethyl, *N*-methyl quinuclidinium or acetylcholine were added to the library, the cyclic trimer was amplified and became the primary constituent of the library.[62] These three publications by Sanders' group[60-62] are the foundation of host-guest dynamic combinatorial with hydrazone exchange.

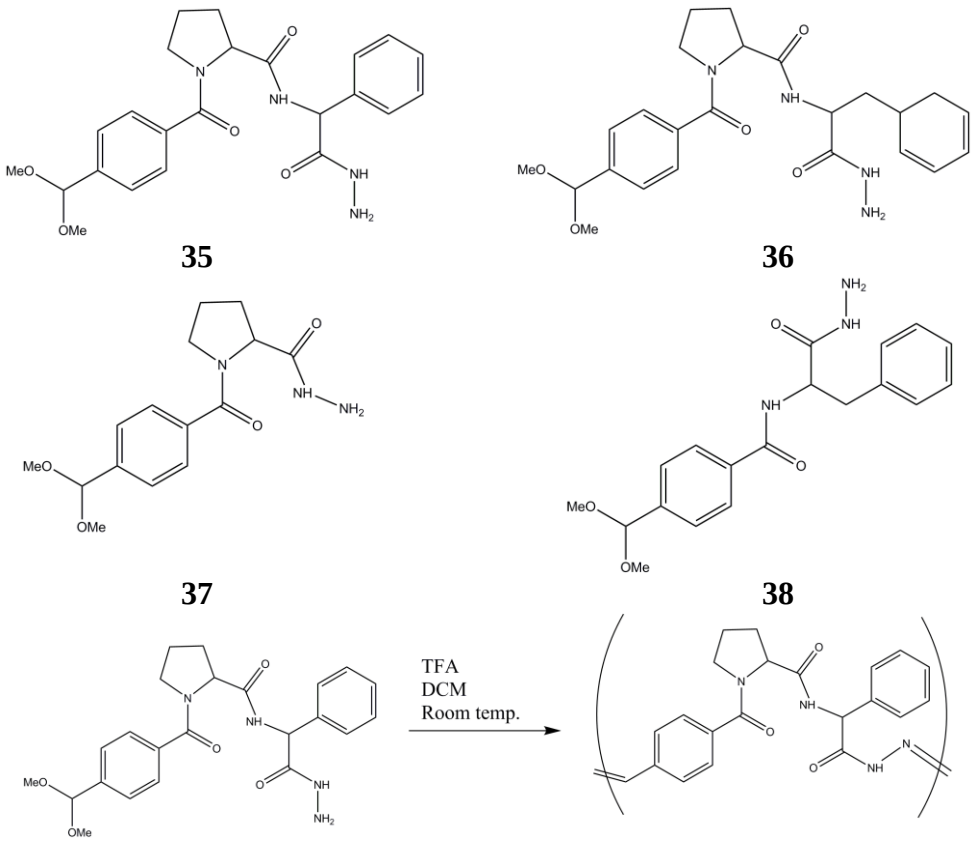


**Figure 18:** Sander's building blocks and oligomerization reaction.

Disulfide linkages, which are exchangeable, were also used to produce a library of macrocytic host-guest interactions. Sanders, et al. showed that the library of racemic **39** at equilibrium predominated with compound **42** and **41** (racemic)**.** However when tetramethylammonium iodide **40** was added to the library, racemic-**43** was found predominantly (**Figure 19**). Futher studies of the complex racemic-**43** with tetramethylammonium iodide **40** showed that the binding constant is 4 x $10^6$ $M^{-1}$ (by isothermal titration calorimetry).[63]

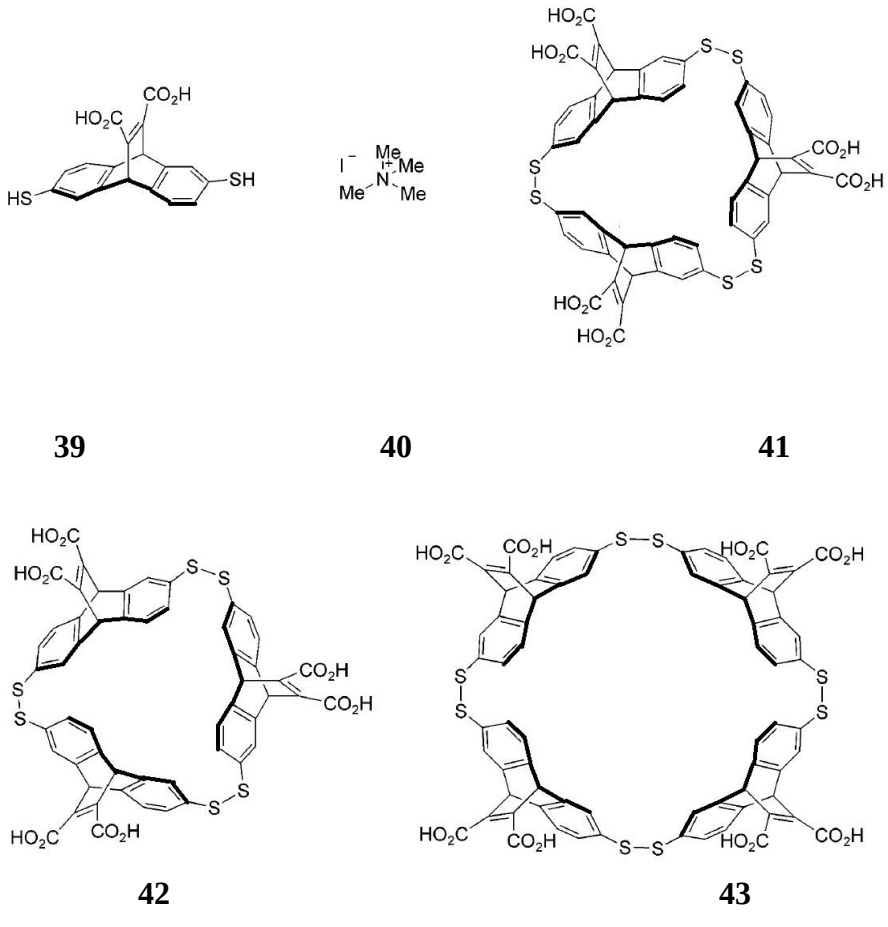


**Figure 19:** Tetramethyl ammonium ion **40** and disulfide library. Sanders et al. [63]

Compared to disulfides and hydrazones, Schiff base or imine complexes exchange at a much faster rate.[64] Also, imines can easily form metal complexes and thus can be used as coordinating ligands. The imine ligands are easy to build from simple aldehyde and amine building blocks. Metal ions and Lewis acids, promote the formation of imines and can also be guests of the macrocyclic Schiff base. Luning demonstrated that with the dialdehyde **44** and the mixture of amines **45** (top) and **46** (bottom) both macrocycles **47** or **48** can be formed (**Figure 20**:). However, depending on the alkaline earth metal ion $M^{2+}$ added to the library, each complex can be amplified differently.[65] In particular, when a smaller ion such as $Mg^{2+}$ was added to the library, **47** was amplified (81% more compared to the library at the equilibrium). However, when bigger ions such as $Ca^{2+}$ or $Sr^{2+}$ were added, then **48** was amplified by 71% and 74% respectively. The ring size of the macrocycle seems to be controlled by the size of the templating ion. The libraries were frozen by adding an excess of $NaBH_4$, to reduce the imine to a non-exchanging amine ligand, then analyzed by HPLC.

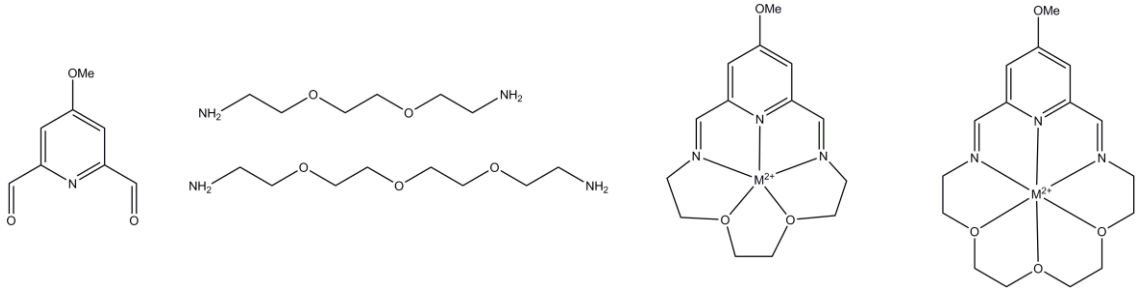


**44** **45** (top) and **46** (bottom) **47** **48**

**Figure 20:** DCL of Schiff base with crown ether macrocycles.

### 1.5.2 DCL templating as a catalyst selection method.

The first reported example of using DCC as a tool to find catalysts was reported by Sanders and Otto.[66] Compound **56** is the product of the DA reaction between **53** and

**54** and can be used as a late TSA for the reaction. Upon the addition of **56** to the library of dithiols **49**, **50**, **51** and **52**, it was found that compound **47** (**Figure 20**) was amplified. The test of **47** showed an active catalyst activity with $k_{cat} = 1.9 \times 10^{-3}\ s^{-1}$. It is thought that the catalytic effect of **47** comes from the fact that both reactants **53** and **54** can be traped inside the macrocyclic ring of **47**. Both **53** and **54** are nonpolar, thus they tend to stay close to the interior of **47**, which increases their effective concentration.

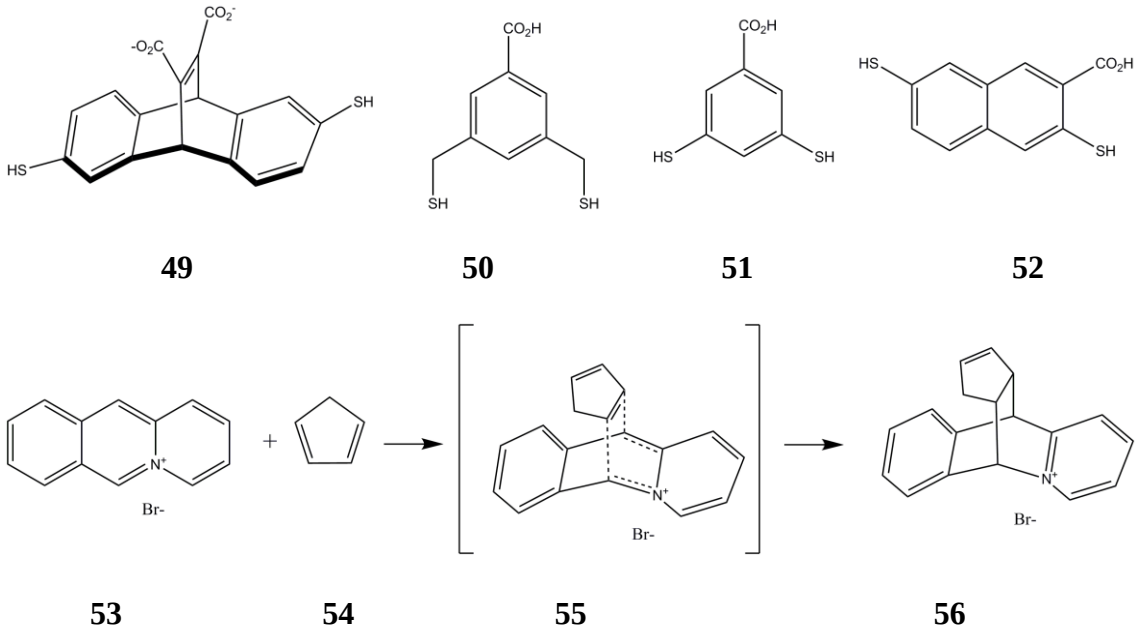


**Figure 21:** First example of using DCC to make a DA catalyst.

Sanders and Otto also demonstrated that the same technique can be used to select acetal hydrolysis catalysts.[67] The hydrolysis of acetal **57** can make alcohol **58** and **59**. Compound **60** was proposed as the transition state analog for this reaction (**Figure 22**). A library of **49**, **51** and **52** was pre-formed and when **60** was added to the library compound **47** was amplified. Compound **47** accelerated the DA reaction by a factor of 2. It is thought that the ability of compound **47** to stabilize the positive charge in the transition state accelerates the reaction.

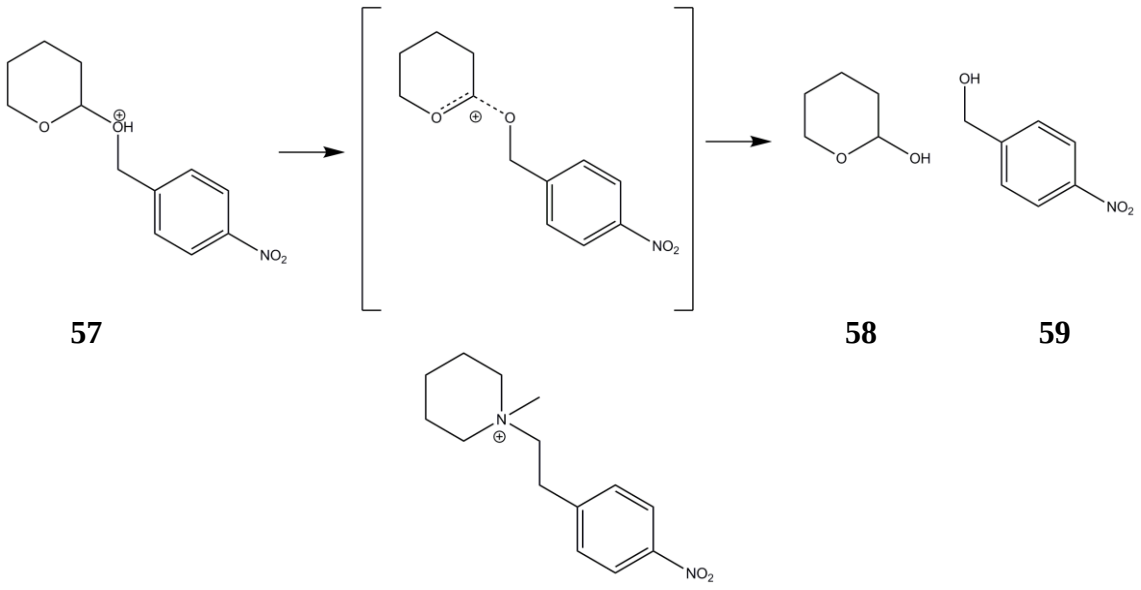


**Figure 22:** First example of using DCC to select an acetal hydrolysis catalyst.

Our group has demonstrated that zinc-imine complexes are excellent catalysts for the hydrolysis of coordinating esters. Two TSAs for the pyridine ester hydrolysis, phenyl-2-pyridylphosphonate[68] (**61**) and 2-pyridine trifluoromethyldiol[69] (**62**), were employed as transition state analogs for pyridine carboxyl ester hydrolysis (**Figure 23**).[70] In this work, 1-methyl-2-imidazolecarboxaldehyde and various amines were used as building blocks to form ligands with $Zn^{2+}$. The experiments showed that trifluoromethyl diol **62** is a good TSA for the hydrolysis reaction. There is a good correlation between the TSA binding affinity, measured by HPLC, and catalytic activity. Thus, the complexes that bind more strongly to the TSA are the faster catalysts (**Figure 24**). This was the first example of metal-based catalysts obtained from a dynamic combinatorial library (DCL). However, when the libraries got more complicated, analyzing by the HLPC method became very challenging because of overlapping peaks.

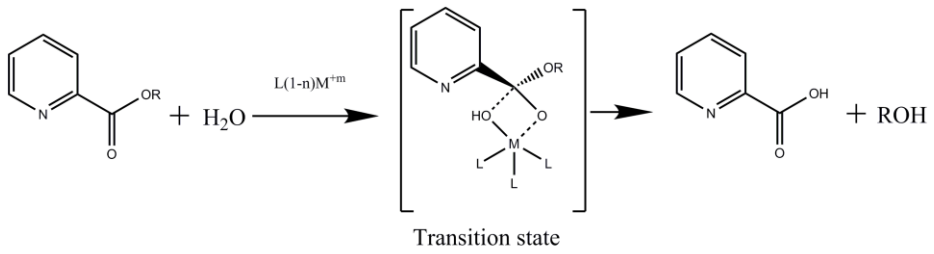


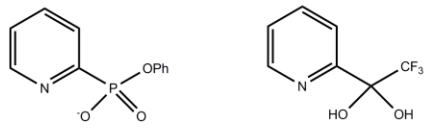


**61** **62**

**Figure 23:** Reaction and proposed transition states for metal-catalyzed ester hydrolysis.

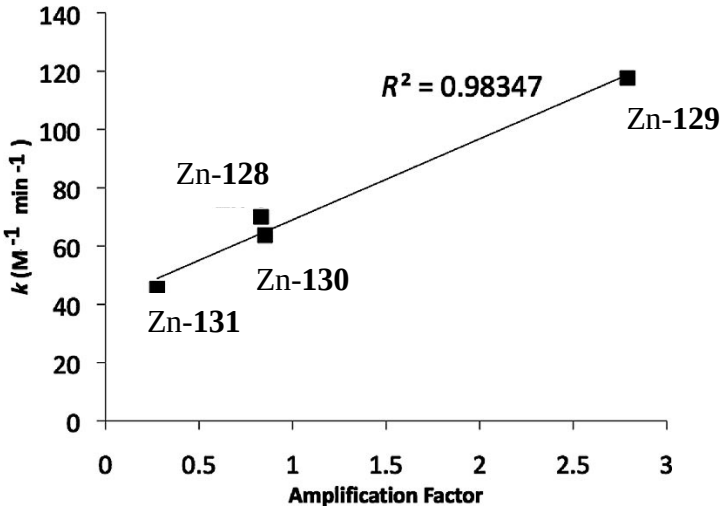


**Figure 24:** Plot of multiple turnover rate constants vs. amplification factor for **63** with Zn-**128,** Zn-**129**, Zn-**130** and Zn-**131**.

We envision that *selective* catalysts could be elicited by templating with suitable isomeric transition state analogs. Thus, instead of adding one TSA to a library of complexes, two isomeric TSAs would be added separately to the pool of catalysts, producing two libraries, of ligand-M-TSA1 and ligand-M-TSA2. When both new libraries reach equilibrium, a cross comparison of all ternary complexes between the

two libraries could reveal the most selectively amplified complexes. The most selective catalysts should be the complexes that have the largest relative binding affinity difference for the two TSAs (**Figure 25**).

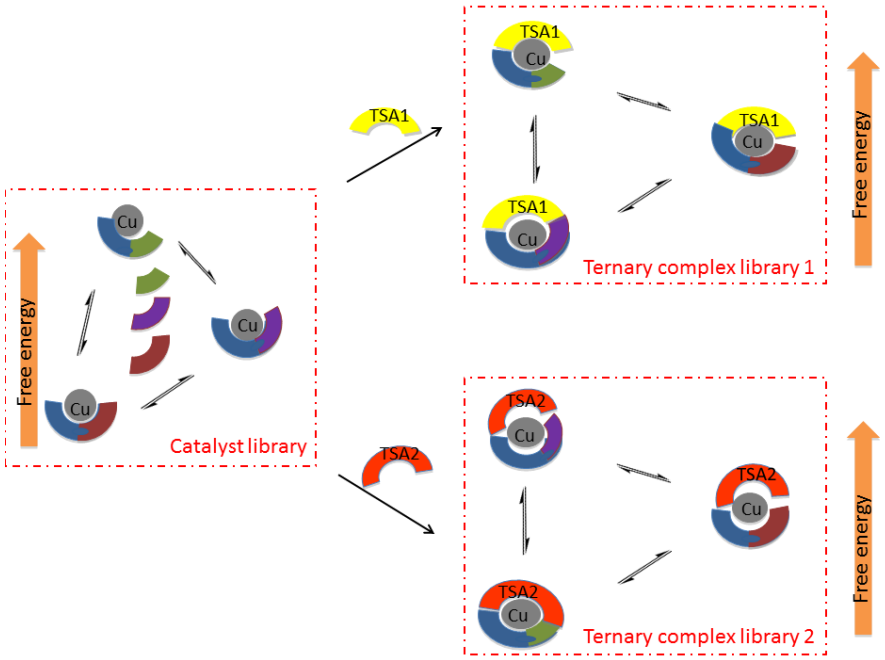


**Figure 25**: The most differentially amplified metal-ligand-TSA complex is predicted to be the most selective catalyst

To further develop the idea that the different binding affinity of isomeric TSAs result in reaction selectivity, Dr. Kannappan, a former post-doctoral fellow in our group, sought the kinetic resolution of chiral esters by dynamic templating with chiral TSAs. Enantiomeric chiral pyridine phosphonate esters were used to mimic the tetrahedral transition state of picolinate ester hydrolysis.[71,72] In this work chiral diamine ligands were used to give the metal complexes chirality. Various pyridine and imidazole based aldehydes were employed as imine building blocks (**Figure 26**). This work further extended the idea that the stronger the complex binding to the TSA, the more active the catalyst, and demonstrated that cross comparison between libraries is possible. Also in

this work, ESI-MS was used to identify and quantify the composition of the libraries. In particular, the libraries were analyzed by ESI-MS and the ion insensitive ratios were compared directly (**Figure 27**). This also shows enantio-differentiation of substrates by chiral Zn-complexes. This method is faster than HPLC and more accurately identifies the library components which can be quantified without requiring additional separation.

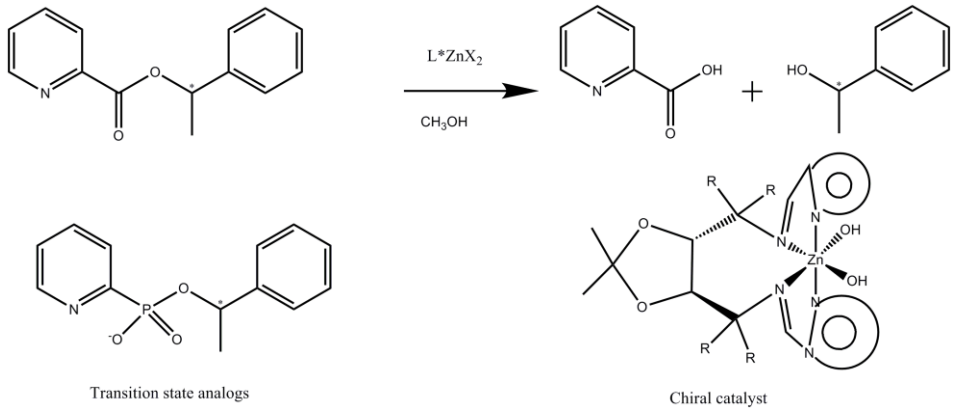


**Figure 26:** Reaction, chiral TSA and catalyst for kinetic resolution of picolinate ester.

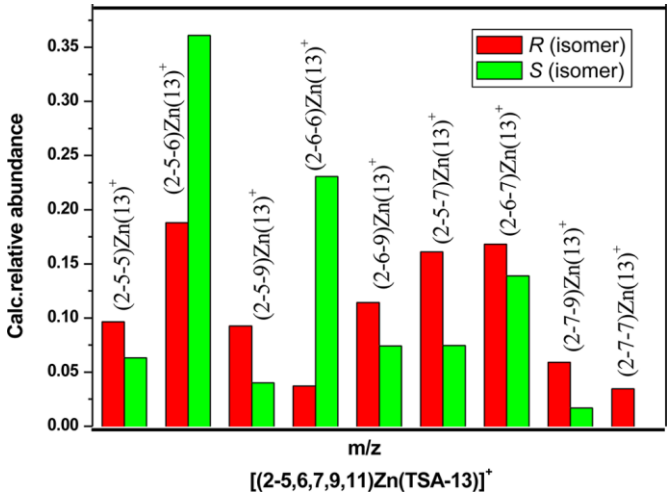


**Figure 27:** Example of amplified library by R and S isomers ESI-MS quantification.

## 1.6 Affinity Chromatography

Affinity chromatography is very popular in biology and biochemistry for purification. In this technique, an immobilized agent, an *affinity ligand*, is attached to a solid support material. The sample mixture, e.g. a crude protein-containing mixture, is run through the column. Only strongly binding macromolecules, e.g. proteins, are retained in the column while others are washed away. The retained compound is typically released from the column when a stronger eluent is used (**Figure 28**).[73] Due to the ability to bind with compounds selectively, the potential applications of this technique are also numerous in non-biological areas. **Table 2** shows common ligands used in affinity chromatography and applications. This chapter, however, highlights only some of the most important examples of using TSAs as affinity ligands to purify proteins and the use of a "guest" molecule on solid-supported material to purify "host" receptor in DCC.

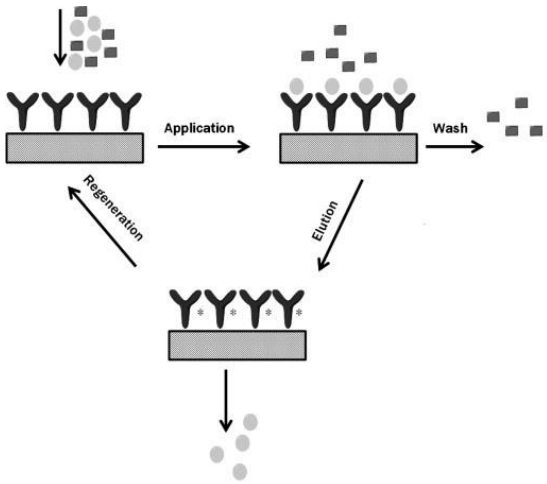


**Figure 28:** Typical scheme of an affinity chromatography application. Hage et al.[73]

| Type of ligand | Retained targets |
|---|---|
| BIOLOGICAL LIGANDS | |
| Antibodies | Antigens (drugs, hormones, peptides, proteins, viruses and cell components) |
| Inhibitors, substrates | Enzymes |
| COFACTORS AND COENZYMES | |
| Lectins | Sugars, glycoproteins and glycolipids |
| Nucleic acids | Complementary nucleic acids and DNA/RNA-binding proteins |
| Protein A/protein G | Antibodies |
| NONBIOLOGICAL LIGANDS | |
| Boronates | Sugars, glycoproteins and diol-containing compounds |
| Triazine dyes | Nucleotide-binding proteins and enzymes |
| Metal ion chelates | Metal-ion-binding amino acids, peptides and proteins |

**Table 2:** Common ligands and applications in affinity chromatography. Hage et al.[73]

### 1.6.1 Examples of using TSAs as affinity ligands for protein purification.

Ornithine transcarbamylase is an enzyme that catalyzes the reaction between ornithine (**64**) and carbamoyl phosphate (**63**) to form citrulline (**66**) and phosphate (**65**). The reaction is thought to have a tetrahedral transition state (**Figure 29**).[74] Hoogenraad's group reported that δ-N-(phosphonacetyl)-L-ornithine (**67**) can be used as the TSA of the reaction.[75] Compound **67** was coupled with Sepharose 6B to make a solid-supported TSA (**68**) (**Figure 29**). It was estimated that about 30% of **67** was coupled with the Sepharose 6B. Interestingly, **68** showed a good binding constant with the ornithine transcarbamylase enzyme. In particular they could load up to 8 mg of ornithine transcarbamylase into the affinity column (~ 10g) without overloading the column (87% yield). Besides high recovery yield, direct purification of the ornithine

transcarbamylase enzyme from liver extract could be done within one day instead of a few days like traditional methodology (reverse phase HPLC).[76]

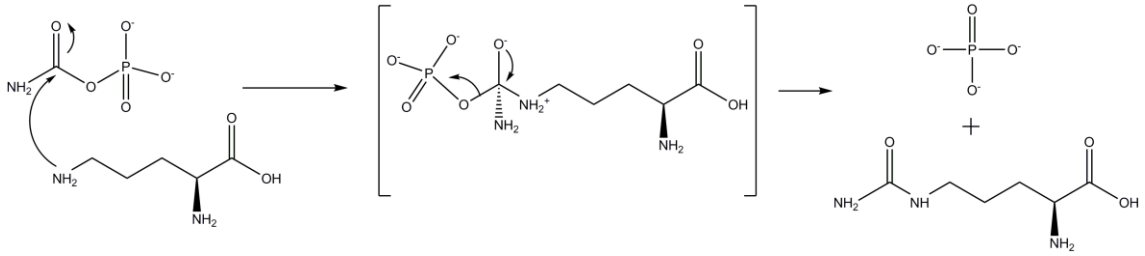

**63** **64** **65** (top) **66** (bottom)

**67** **68**

**Figure 29:** Transcarbamase reaction, TSA and solid-supported TSA.

Trifluoromethyl ketones are well known as enzyme inhibitors and TSAs for hydrolysis reactions.[77] Particularly trifluoromethylketone **69** was reported as the inhibitor and TSA of insect juvenile grown hormone **70**.[78] Hammock was the first to report the use of **69** as a TSA for purification of juvenile hormone esterase.[79] In particular, solid-supported **69**, compound **71**, was prepared as the affinity ligand for the chromatography. The column showed excellent capability of separating the insect juvenile hormone esterase with 98% isolated yield compared to 65% using the batch method (HPLC). The isolated enzyme showed excellent purity after it was radiolabeled and analyzed by electrophoresis. This example showed that trifloromethylketones can be used a TSA in affinity chromatography.

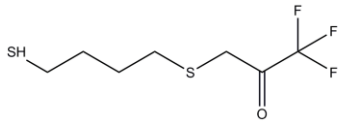


**69**

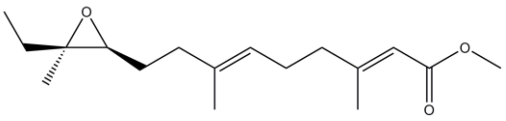


**70**

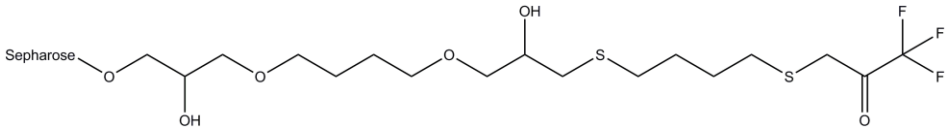


**71**

**Figure 30:** Triflоromethylketone as the TSA for insect juvenile hormone esterase separation.

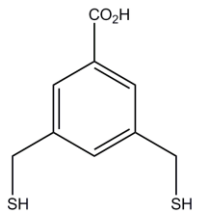


**50**

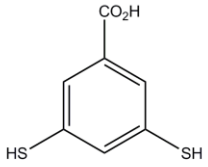


**51**

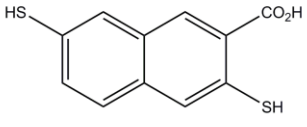


**52**

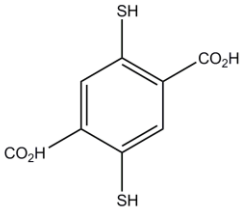


**72**

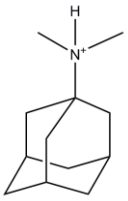


**73**

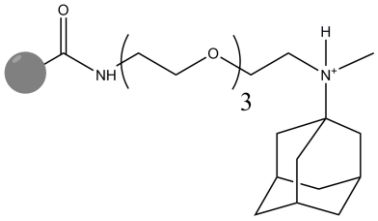


**74**

**Figure 31:** Building blocks and solid supported guest molecule in Otto experiments.

The Otto group showed that affinity chromatography can be used in DCC. Dimethyl adamantylamine (**73**) has been known to amplify the formation of macrocyclic **43**.[80] In this experiment, an analog of **73**, compound **74**, was bound to a gel-type polymer (DMAM GT1). A set of building blocks (**50, 51, 52** and **72**) were

equilibrated in the presence of **74** for 3 days (**Figure 31**). After the library reached equilibrium, the filtered solution after templating did not have any **43**. Interestingly, the eluent, washed with 100% EtOH, showed a significant amount of **43** compared to the other macrocyclics. This experiment demonstrated that a DCL can be formed and be separated by affinity chromatography.

### 1.7 Conclusions and Preview.

While traditional catalyst discovery is dominated by trial and error methodology, testing one potential catalyst at a time and then systematically modifying the successful catalysts until the best result is found, with little to guide the process in the early stages. It is better to find a more efficient way of selecting catalysts. Templating with TSA is one of the new directions. TSA have been used for templating in making catalytic antibodies, MIPs and DCLs. However each of the methodologies has several advantages as well as disadvantages.

Taking advantage of Nature, catalytic antibodies are one of the best catalysts that human can make. They are superior in reactivity along with selectivity. Research about catalytic antibodies has provided important understanding about reaction mechanisms, catalysis, and enzyme structure-function. However, catalytic antibodies also have disadvantages. The development is time consuming and expensive. On the other hand, after the discovery of a new catalyst, mass production is not practical. Because of these reasons, catalytic antibodies are considered as a topic of academic interest with little practical purpose in chemical synthesis.[5]

Employing the same idea about TSA, catalytic MIPs have several advantages compared to catalytic antibodies such as being readily available, being easier to make and easier to mass produce. However, the catalyst is heterogeneous which is harder to study. While multiple types of active sites can be created at the same time, not all of the active sites are available at the surface for reaction. At the same time, when active sites are available, not all of them are selective binders. The flexibility of the cavity at the surface is also limited, thus the rate of the reaction also depends on the diffusion of either the incoming substrates or outgoing products. The combination of these disadvantages make the catalytic MIP less reactive compared to that of catalytic antibodies.[53]

Even with only few examples of catalyst DCC, we envision that DCC-templating is likely to be an effective new approach to catalyst discovery and optimization. DCC generated catalysts can be made homogenous and are thus easier to study and, usually, more active. The catalyst can be formed from simple building blocks, thus making the catalyst design and preparation easier (time, equipment and labor). The ability to coordinate with metal ions is a big advantage of catalytic DCL compared to that of catalytic antibodies. As a frontier research group in catalytic DCL, we also foresee challenges in the design, and especially analysis of DCL catalysts. In chapter 2, we investigate the potential of using combinatorially generated ligand-$Cu^{+}$ complexes as regioselective homogeneous catalysts for hetero Diels-Alder (HDA) reaction between nitrosopyridine and dienes. In particular, we investigate the potential of using products as "late" TSAs. In chapter 3, we survey several imine ligand-metal ion complexes (of $Ni^{2+}$, $Zn^{2+}$, $Cu^{2+}$ and $Pd^{2+}$) as potential catalysts for the HDA reaction

by dynamic templating with “late” TSAs. In chapter 4, we switch to solid supported TSAs. The TSAs of hydrolysis reactions (“early”-substrate analog and TSA) are bound into the silica gel as affinity ligands for chromatography. The catalyst mixture was eluted though the solid-supported TSA column for testing the correlation between binding affinity and catalytic activity.

# Chapter 2. Selection of Regioselective Diels-Alder Catalysts by Dynamic Templating with Transition State Analogs

## 2.1 Introduction

### 2.1.1 Hetero Diels-Alder (HDA) reaction.

Since the first report in 1950 by Nobel laureates Otto Diels and Kurt Alder about [4+2] cycloadditions, the Diels-Alder (DA) reaction has been one of the most powerful tools in organic synthesis.[81] This [4+2] cycloaddition yields substituted cyclohexene derivatives and forms two new carbon-carbon sigma bonds to produce a new 6-membered ring. The applications of the DA reaction can be found from laboratory to industrial scale with remarkable control of regio and stereoselectivity (**Figure 32**). [82-84]

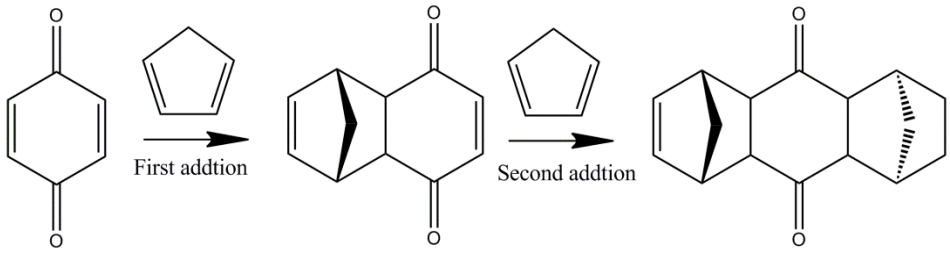


**Figure 32:** First example of Diels-Alder reaction[81]

However, the beauty of the DA reaction is not only limited to all-carbon dienes and dienophiles; it can also utilize heteroatom-containing reactants.[85-89] In fact, the first example of the hetero-DA (HDA) reaction was the reaction of acrolein with ethylene to form dihydropyran, reported by Alder.[85] Soon after the first report of Alder, Gresham and Steadman reported the first example of the oxo-Diels-Alder reaction.[88] In this

reaction, the diene reacts with a carbonyl moiety to form a 3,6-dihydropyran, a useful alcohol protecting agent and synthetic intermediate.[84,90]

### 2.1.1 Nitroso Diels-Alder reaction (NDA)

After Wichterle and Arbuzov reported making 1,2-oxazine derivatives using the NDA reaction between nitroso compounds and dienes[91,92], this methodology has been used in many organic reactions.[83,93-101] More significantly, the 1,2-oxazine products can be converted into 1,4-amino-oxo derivatives by reductive cleavage of the N-O bond in one step (**Figure 33**).

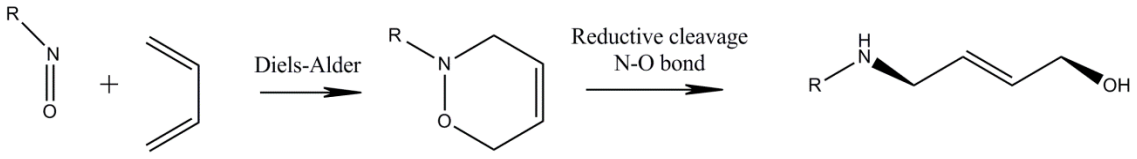


**Figure 33:** NDA reaction and reduction of the 1,2 oxazine adduct.

With broad substrate scope ranging from aliphatic-, aromatic-, acyl-, to imino-NO compounds (dienophile) and a diversity of cyclic, acyclic and intramolecular dienes, the NDA reaction has been utilized in the total synthesis of natural products and bioactive compounds.[102-106] Although HDA reactions are fast, atom efficient, easy to design and relatively easy to perform, HDA reactions in general, and NDA reactions in particular, suffer from stereo- and regio-selectivity problems with some unsymmetrical dienes especially with 1- and 2-alkyl dienes and 5-substituted cyclohexadienes (**Figure 34**).[107-111]

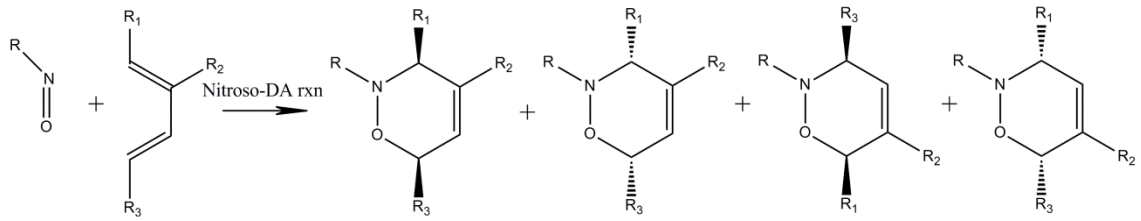


**Figure 34:** Up to 4 isomers can be formed from the nitroso-DA reaction with unsymmetrical dienes (2 enantiomers and 2 regioisomers)**.**

### 2.1.2 Asymmetric catalysts NDA reaction.

Recognizing the potential and limitations of the NDA reactions, Kresze, Kirby and Nazeer's groups have numerous publications on controlling the stereochemistry of the NDA reactions by taking advantage of substrate structures (substrate control method).[112-114] Due to the nature of the method, these approaches rely on the substrate structure and so are very limited for general applications.

To overcome the limitations of the substrate control method, a general method that can control the stereochemistry of the NDA reaction without relying on the starting materials would be preferable. The most common and reasonable approach employs metal complexes as Lewis acid catalysts. The catalysts, presumably, coordinate with the N-O moiety, thus lowering the LUMO of the dienophile, reducing the activation energy and increasing the rate of the reactions. Meanwhile the chiral auxiliaries block one site and open the other side of the N-O moiety thus the incoming diene can approach from only one direction and make a single enantiomer. This intriguing approach was reported by Inomata using $Zn^{2+}$ and tartaric acid ester as a chiral auxiliary.[115] This concept became popular after Shea and Yamamoto's group reported using transition metal: $Cu^{+}$,

$Ag^{+}$ and $Ru^{2+}$ as the catalytic metals, employing chiral phosphine and salen-type ligands.[108-111]

### 2.1.3. Regioselective NDA reactions.

The regioselectivities of the DA reactions, in general, are controlled by the nature of the dienophile and the diene. In particular, the substituted moieties on the diene and the dienophile hold the keys to the regioselectivity. The most abundant product is the one that is derived from the transition state that has maximum frontier orbital coefficient interactions. In the transition state, the reactants are aligned so that the amplified HOMO end of the diene interacts with the amplified LUMO end of the dienophile. This phenomenon has been observed and explained successfully both by frontier molecular orbital theory and computational modeling.[116-124] The regioselectivity of the NDA reaction also has been thoroughly investigated by Houk's group. The mechanism of the NDA reaction, in general, is found to be concerted, but highly asynchronous. A combination of frontier molecular orbital interaction, electrostatics and steric effects were found to contribute to the observed regioselectivity.[125-127]

#### 2.1.3.1 Catalytic regioselective HDA reactions

Compared to asymmetric HDA catalysts, there are fewer studies about controlling the regioselectivity of the HDA reactions.[98-106,128-132] One of the most successful examples of regioselective HDA reactions was reported by Inomata's group.[115,133] They employed an isopropyltartrate-zinc(II) complex as the catalyst. The idea was that the nitroso moiety of the dienophile and the hydroxyl moiety of the diene strongly coordinate with a dinuclear zinc catalyst to form a highly ordered transition

state which would lead to only one product (**Figure 35**). This approach, however, cannot be used with dienes lacking the hydroxyl moiety.

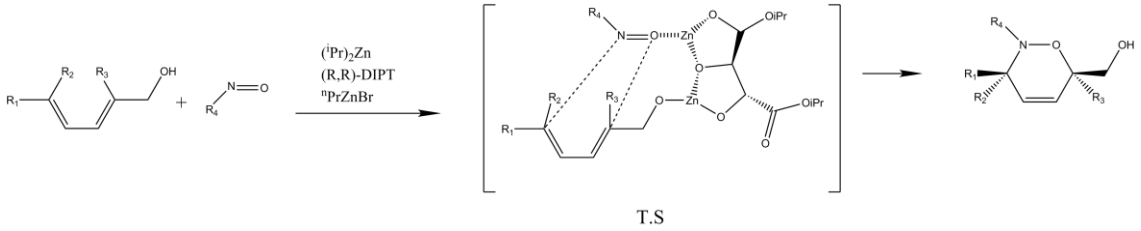


**Figure 35:** Inomata's proposed transition state. Inomata et al.[115,133]

A catalytic antibody method also has been employed to affect the regioselectivity of the NDA reaction between nitrosobenzene and *cis*- and *trans*-1,3 pentadiene. A derivative of 2-oxa-3-azabicyclo[2.2.2]oct-5-ene was employed as a hapten to generate antibodies. The 309-1G7 antibody was tested as a catalyst for the HDA reaction. This catalyst produced an increase in the targeted isomer (proximal/distal 68/32) over the thermal background reaction (proximal/distal 52/48) and a significant improvement of the reaction rate ($k_{cat}/k_{uncat}$ = 1205).[134,135] The catalytic antibody production methodology; however, is time-consuming and very expensive.

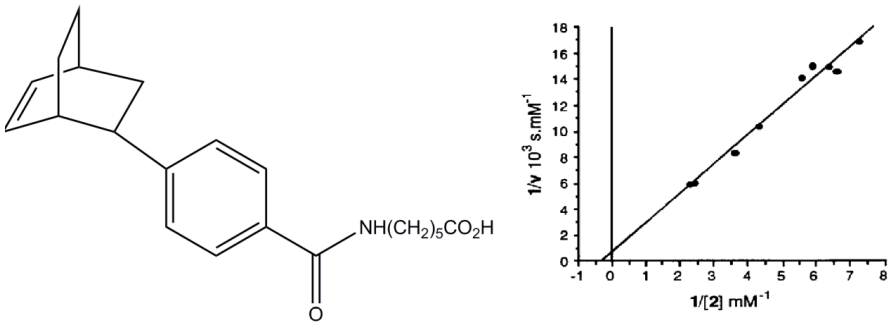


**Figure 36:** Hapten and Lineweaver–Burk plot of **309-1G7** catalysis of the reaction between nitrosobenzene and 1,3 pentadiene. Pandit et al.[134,135]

Inspired by all of the ideas cited above, we believed that control of the regioselectivity of the NDA reaction could be accomplished by employing suitable copper(I)-complexes as catalysts for NDA reaction.[108-111] Copper (I) was chosen because of its low cost, ready availability and proven reactivity. Imines were selected as the ligands because the resulting $d^{10}$ Cu(I)-imine complexes were expected to be exchange labile under mild conditions and reach equilibrium in a short period of time, practical for dynamic templating catalyst selection.[136-138] The other advantage of imine ligands is that complex imines can be formed from simple aldehyde and amine building blocks, which are usually commercially available. We wanted to test the idea of using product as late transition state analogs (TSAs). We were especially interested in the correlation of (imine)Cu-TSA binding ratio with catalyst selectivity.

## 2.2 Results and Discussion.

This work has been published in the Journal of Organic Chemistry.[139]

### 2.2.1 Uncatalyzed (thermal) Reaction of PyrNO and Unsymmetrical Diene.

The reaction between *N*-nitrosopyridine (**75**) and excess 1,3-pentadiene (**76**) in a 2:1 E/Z ratio in methanol gives a mixture of **77** and **78** (53:47 ratio) (**Figure 37**). They can be separated by careful HPLC and their structures are assigned by comparison with prior reported literature.[105] In order to further confirm the NMR assignments, the *meta* protons in the pyridine ring of each product is irradiated in NOE experiments, while the methyl group signals in the oxazine moiety are observed. The product **77** was assigned as *distal* due to the methyl group being further away from the oxygen atom (higher

atomic number), while the product **78** was assigned as *proximal* due to the methyl group being closer to the oxygen atom.

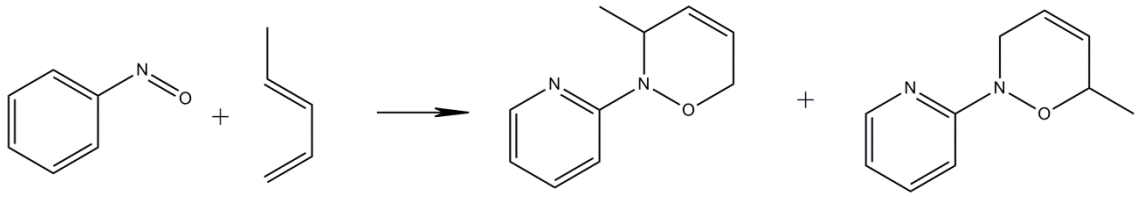

**75** **76** **77** (*dist*) **78** (*prox*)

**Figure 37:** Reaction of 2-nitrosopyridine with 1,3-pentadiene.

In the same manner, the reaction between **79** (E,E-2,4-hexadienol, sorbyl alcohol) and 2-nitrosopyridine (**75**) in methanol yields a mixture of **80** and **81** as products (35: 65 ratio). Surprisingly, the same reaction in $CH_2Cl_2$ gives a 10:90 mixture of **80** and **81**. We suggest that the difference in the selectivity when using methanol and $CH_2Cl_2$ is the result of intramolecular hydrogen bonding between the nitrogen of the pyridine moiety and the -OH moiety of the diene in the aprotic $CH_2Cl_2$, e.g. **82**. This pre-organized transition state accelerates the formation of **80**, therefore the reaction is highly selective. Meanwhile in methanol, MeOH-diene and the MeOH-pyridine hydrogen bonding would compete to limit the formation of **82**, which accounts for the low selectivity of the reaction (**Figure 38)**. See **2.4 Experimental** for more detail about the isolation and characterization of **80** and **81** (new compounds).

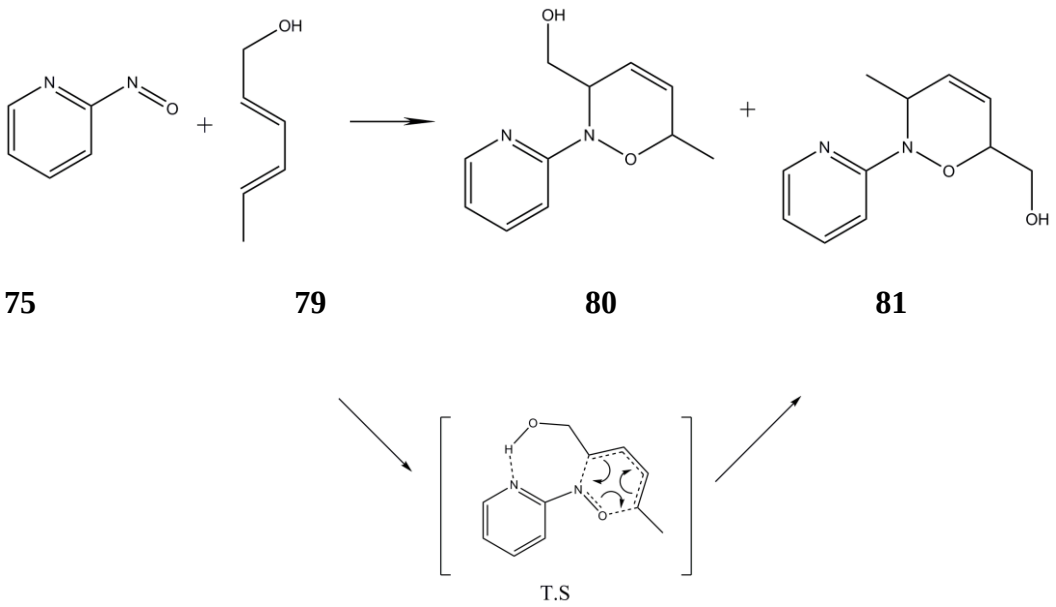


**75** **79** **80** **81**

**82**

**Figure 38:** 2-Nitrosopyridine and E,E-2,4-hexadienol reaction with proposed transition state.

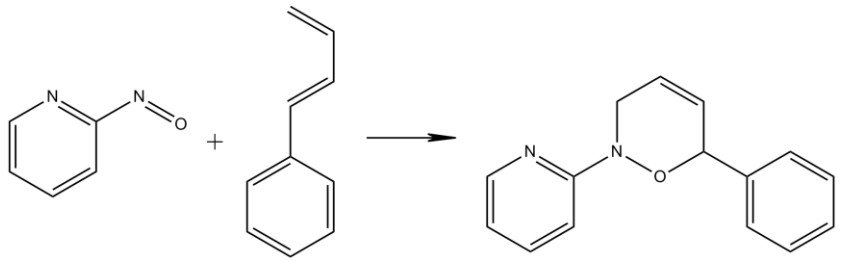

**75** **83** **84**

**Figure 39:** 2-Nitrosopyridine reaction with 1-phenyl-E-1,3-pentadiene.

The uncatalyzed reaction of 2-nitrosopyridine (**75)** with 1-phenyl-E-1,3-pentadiene (**83)** in methanol gives a single isomer **84** (**Figure 34).** Compound **84** is a new compound and the structure (*proximal*) was assigned by HMBC and 1D-NOE experiments. There is a small coupling constant (4Hz – 4 bonds) between the *ortho* carbon in the pyridine moiety and the benzylic proton of the benzyl moiety. If the

compound adopted the distal structure, the coupling constant should be at least 8 to 12Hz (3 bonds). See **2.4 experimental** for the isomer assignment and other characterization of this compound.

### 2.2.2. Cu(I) Catalyzed Reaction of Nitrosopyridine with Unsymmetrical Dienes

#### 2.2.2.1 Cu(I)-imine complex formation.

As we mentioned earlier (**2.1.3.1**), copper (I) complexes were chosen as the potential regioselective catalysts for NDA reactions.

In order to establish the catalyst structure, compound **85** was made by the condensation of 2-quinolinecarboxaldehyde (**107**), 1-adamantylmethylamine (**91**) and $Cu(CH_3CN)_4PF_6$ in MeOH at room temperature inside a glove-box. The X-ray diffraction crystal structure of **85** shows a slightly distorted tetrahedral geometry around the Cu which agrees with previous literature reports.[98,100,108,109,128,129,140-142] See **2.4 experimental** for more information about the preparation, NMR spectra and ESI-MS of **85**.

We anticipated that a pseudo-tetrahedral geometry would not be the best structure for regioselective catalysts. However, we hoped that sufficiently bulky and constrained ligands could compensate for the disadvantage of the geometry. Also note that the above crystal structure is for $L_2Cu^{2+}$; not the LCu(substrate)$^{2+}$ or the LCu(product)$^{2+}$ which might be closer to the square planar due to less steric hinderance compared to the (**107**-**91**)$_2Cu^{2+}$ complex.

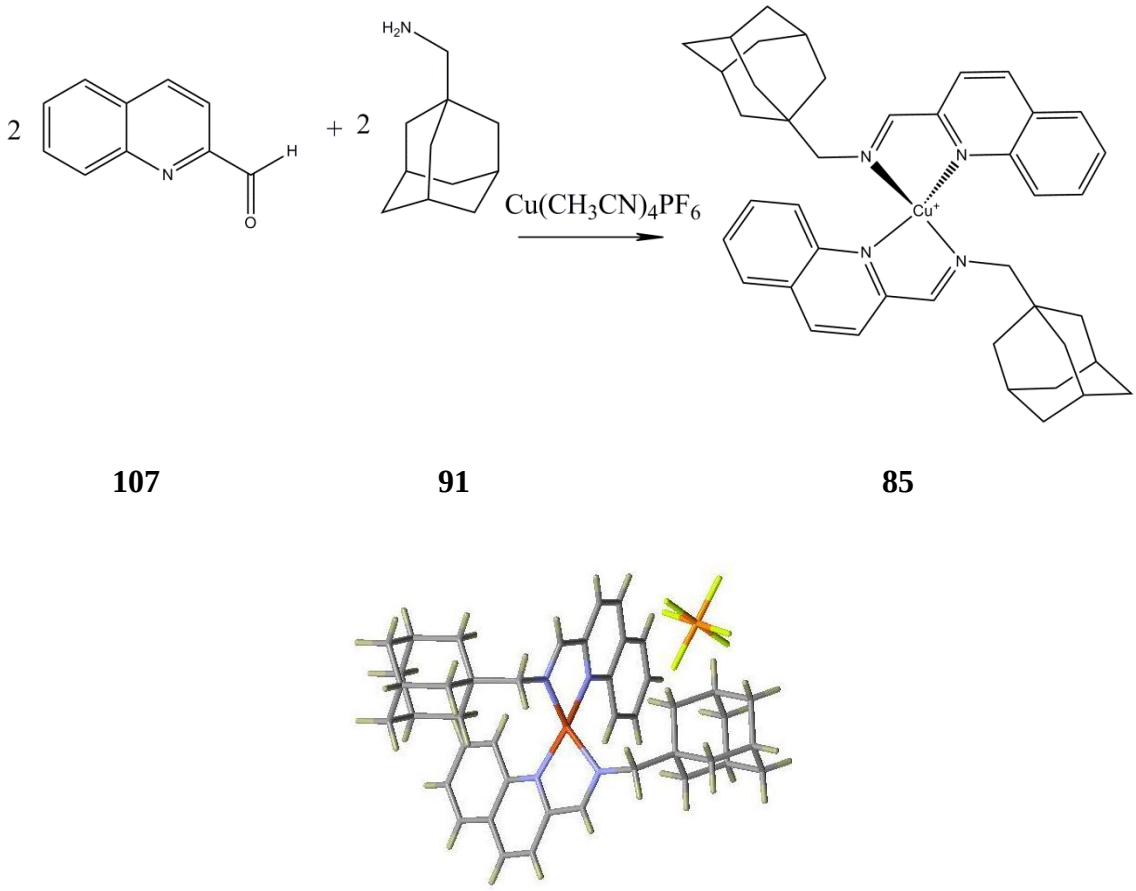


**107** **91** **85**

**Figure 40**: Formation of complex **85** and X-ray crystal diffraction structure. Atom key: Cu=red, C=grey, N=blue, P=orange, F=yellow).

### 2.2.2.2 $Cu(CH_3CN)_4PF_6$ as a catalyst for NDA reactions.

We wanted to test the catalytic activity of $Cu(CH_3CN)_4PF_6$ in the reaction between nitrosopyridine and 1,3-pentadiene in order to confirm that the complex is able to: **a**) effectively change the distribution of **77** and **78**, **b**) override the thermal background reaction, and **c**) not catalyze the reverse DA reaction.

The Cu-catalyzed reaction between 2-nitrosopyridine and 1,3-pentadiene with $Cu(CH_3CN)_4PF_6$ (10% catalyst loading) at room temperature shows a significant improvement in regioselectivity. The ratio of **77** and **78** is 90:10 compared to 53:47 of

the thermal background reaction. This experiment indicates that Cu(I) is a good regioselective catalyst for this NDA reaction. See **2.4 experimental** for more detail.

The same reaction above was tested at low temperature (-78 $^{o}$C), at which point the thermal background reaction is slow, then the reaction mixture was slowly warmed up to room temperature over 1 hour. The distribution of **77** and **78** was unchanged compared to the same reaction at room temperature. This experiment shows that thermal background reaction has minimal contribution to the final regioselectivity result. This conclusion is based on the fact that the thermal reaction has a different product distribution compared to that of the catalyzed reaction. If the contribution of the thermal reaction is significant then the product distribution should change depending on the temperature. However, that was not observed here.

To test the stability of the products under the catalyzed reaction conditions, in two separate vials 10% mol of $Cu(CH_3CN)_4PF_6$ was added to regioisomers **77** (> 98% pure, NMR) and **78** (> 95% pure, NMR) in MeOH. The two solutions were left at room temperature for 1 week and checked again by NMR to find that the individual regioisomers were unchanged. This result indicates that the two isomers (**77** and **78**) do not isomerize when the $Cu^{+}$ ion is present. The Cu-catalyzed HDA regioselectivity is thus purely kinetically controlled.

$Cu(CH_3CN)_4PF_6$ was also used as the catalyst for the reaction between 2-nitrosopyridine **75** and sorbyl alcohol **79** in methanol with 10% catalyst loading (room temp. for 15 min). The ratio of adducts **80**:**81** was 50:50 in the final mixture. The same reaction under thermal (uncatalyzed) conditions gave a ratio of 35:65. This result

indicates that $Cu(CH_3CN)_4PF_6$ catalyzed the reaction; however, the effect on the regioselectivity is modest.

The reaction of nitrosopyridine **75** and 1-phenyl-E-1,3-pentadiene **83** in methanol with $Cu(CH_3CN)_4PF_6$ (10 mol%) results in the formation of a single isomer **84**, the same as in the uncatalyzed reaction. Copper(I) does not change the regioselectivity of this reaction. Because another regioisomer was not found, this reaction was not useful for template experiments later.

### 2.2.2.3 Cu-imine complexes as catalysts for NDA reactions.

In previous studies by Dr. Matsumoto, a former group member, the equilibrated libraries were "frozen" by reduction with $NaBH_4$, then the mixtures were analyzed by HPLC.[70] This methodology is simple but time consuming. Direct ESI-MS quantification of the metal complex libraries has been proven as excellent tool due to the nature of soft ionization method.[143-147] In this study, ESI-MS was used exclusively for quantification of the copper-imine libraries with internal standard.

In general, $(imine)_2Cu^+$ complexes are generated from corresponding aldehydes and amines combined with $Cu(CH_3CN)_4PF_6$ (1:1:1 ratio) in methanol. The formation of the complexes can be detected by mass spectrometry (mass and isotope pattern). In general, however, the catalysts were generated *in situ* and used without isolation.

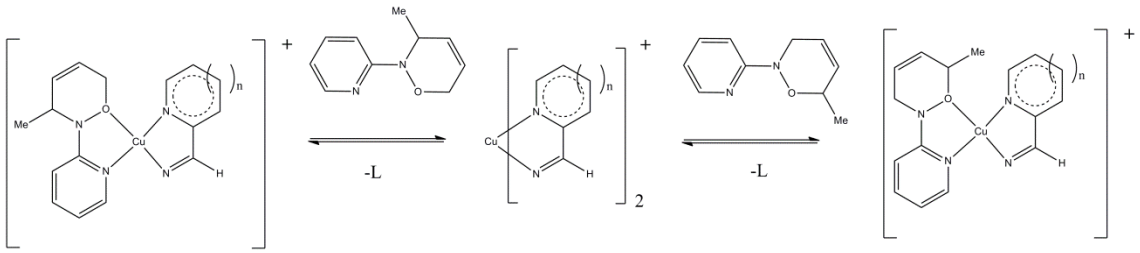


**Figure 41:** Formation of $LCu(TSA)^+$ complexes from $(imine)_2Cu^+$ complexes.

We have prepared and tested a total of 28 $(imine)_2Cu^+$ complexes, generated from condensation of corresponding amines (**86-97**), aldehydes (**98-109**) and $Cu(CH_3CN)_4PF_6$, as the catalysts for the reaction between 2-nitrosopyridine (**75**) and 1,3-pentadiene **76** (See **Table 3**). A variety of aldehydes- bulky (**99**, **101**, **108**), electron rich (**105**) and electron deficient (**106**)- and amines- bulky (**79, 91, 92, 93**), more basic aliphatic (**86**, **87**, **88**, **89**, **90**, **91**, **93**) and less basic aromatic (**92**, **94**, **95**, **96**, **97**)- have been used to generate mix and match combinations of bulky, electron rich, electron deficient imine ligands and $(imine)_2Cu^+$ catalysts.

Regardless of ligand electronic and steric variations (**Figure 42** and **Table 3**) it is surprising that we only observed a small variation in regioselectivity, slightly in favor of *distal* product **77** (55-65%) relative to *proximal* product **78** (35-45%). This interesting phenomenon was further studied by computational MO analysis, in collaboration with Prof. Kendall Houk's group at UCLA (see 2.2.4 for a summary of the computational studies).

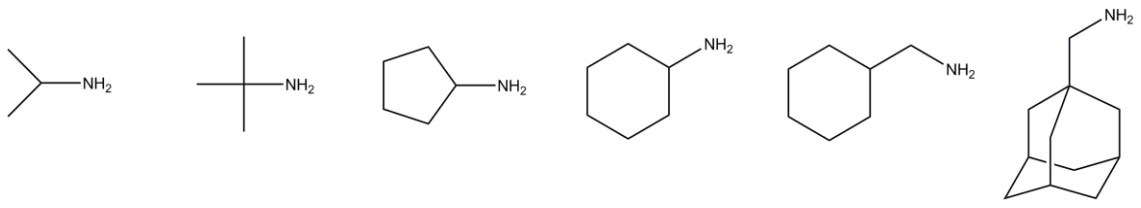


**86** **87** **88** **89** **90** **91**

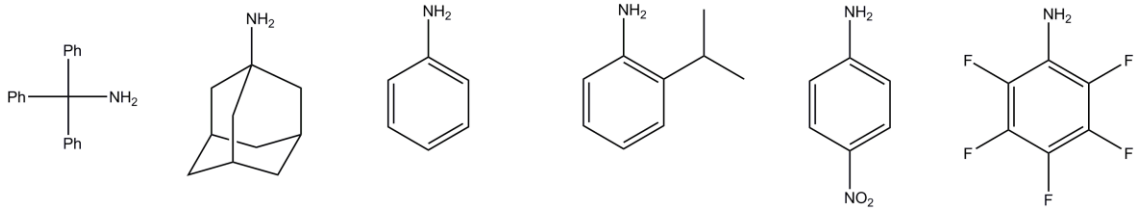


**92** **93** **94** **95** **96** **97**

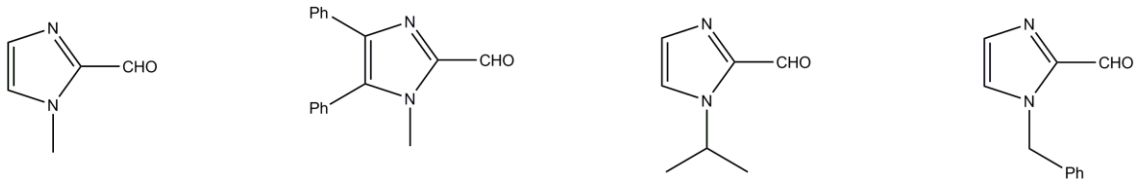


**98** **99** **100** **101**

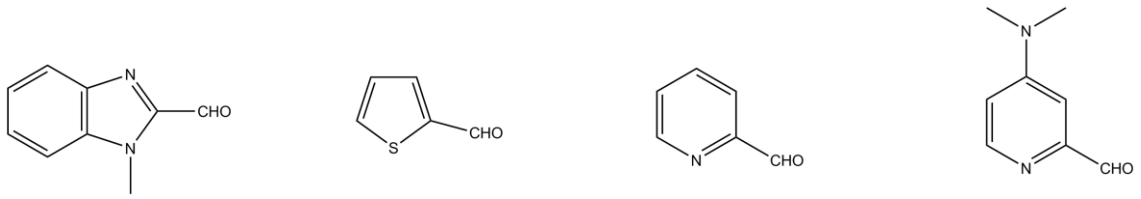


**102** **103** **104** **105**

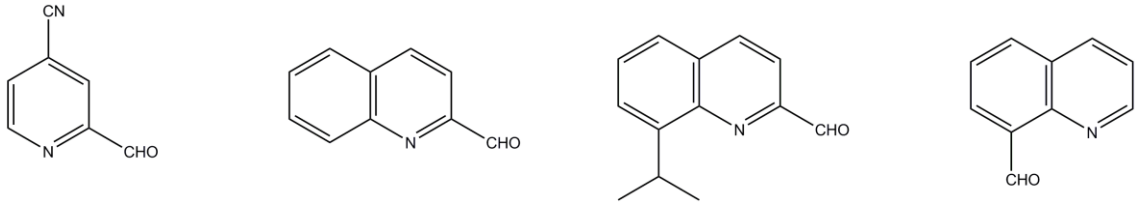


**106** **107** **108** **109**

**Figure 42:** Amines and aldehydes for producing imine ligands.

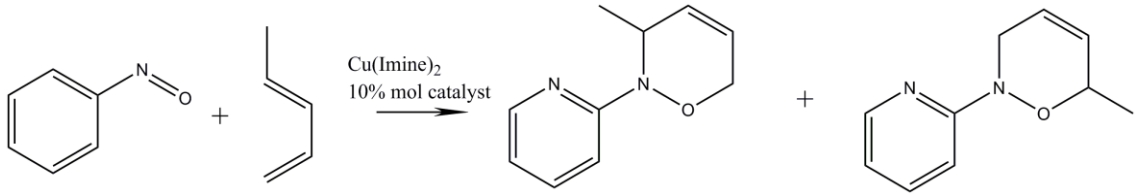


**75** **76** **77** (*dist*) **78** (*prox*)

| Entry | Aldehyde | Amine | Distal **77**: Proximal **78** ratio |
|---|---|---|---|
| **1** | **98** | **87** | 40:60 |
| **2** | **99** | **88** | 37:63 |
| **3** | **100** | **86** | 40:60 |
| **4** | | **87** | 38:62 |
| **5** | | **88** | 41:59 |
| **6** | | **89** | 40:60 |
| **7** | **101** | **88** | 38:62 |
| **8** | | **89** | 37:63 |
| **9** | **102** | **86** | 40:60 |
| **10** | **103** | **89** | 42:58 |
| **11** | | **90** | 40:60 |
| **12** | **104** | **87** | 45:55 |
| **13** | | **89** | 39:61 |
| **14** | | **93** | 42:58 |
| **15** | | **94** | 40:60 |
| **16** | **105** | **87** | 37:63 |
| **17** | | **88** | 38:62 |
| **18** | | **89** | 37:63 |
| **19** | | **95** | 38:62 |
| **20** | **106** | **89** | 35:65 |
| **21** | | **97** | 42:58 |
| **22** | | **98** | 42:58 |
| **23** | **107** | **91** | 37:63 |
| **24** | **108** | **89** | 45:55 |
| **25** | | **90** | 39:61 |
| **26** | **109** | **89** | 36:64 |
| **27** | | **90** | 37:63 |
| **28** | | **92** | 37:63 |

**Table 3:** Regioselectivity of PyrNO/pentadiene reactions catalyzed by (Imine)$Cu^{+}$.

We also wanted to test the $(diimine)_2Cu^+$ catalysts in the reaction between nitrosopyridine **75** and sorbyl alcohol **79**. The catalyst $(\mathbf{104}\text{-}\mathbf{89})_2Cu^+$ was chosen for this reaction because of its availability. The ratio of products **80**:**81** was 33:67, in the same range as the uncatalyzed reaction. With this result, we concluded that in general, $CuL_2^+$ complexes might have small effects on regioselectivity for this reaction.

### 2.2.3. Mass Spectral Binding Studies.

In order to probe the potential of using products as "late" transition state analogs (TSAs) for the HDA reactions, we monitored the formation of $LCu(\mathbf{77})^+$ and $LCu(\mathbf{4})^+$ complexes after the addition of the two isomeric products to the libraries of $(diimine)_2Cu^+$. Then, we wanted to examine the correlation between the regioselectivity of the HDA reaction using $L_2Cu^+$ as the catalyst to the ratio of $LCu(\mathbf{77})^+/LCu(\mathbf{4})^+$ (binding selectivity) at equilibrium. The reaction between nitrosopyridine (**75**) and 1,3-pentadiene (**76**) was chosen since $(imine)_2Cu^+$ catalysts showed the greatest range of regioselectivity (**Figure 37**).

Mixing 2-quinolinecarboxaldehyde (**107**) with a set of three primary amines-cyclohexylamine (**89**), 1-cyclohexylmethylamine (**90**), and 1-adamantylmethylamine (**91**)- together with $Cu(CH_3CN)_4^+$ in MeOH produced a library of all six possible $(diimine)_2Cu^+$ complexes. Tetrabutylammonium hexafluorophosphate (m/z = 242) was added to the library as an internal standard. The formation of all six possible $(imine)_2Cu^+$ complexes can be detected by ESI-MS (**Figure 43-a**). After 24 hours at room temperature, this library reaches equilibrium since no change in the ion count ratio of the $(diimine)_2Cu^+$ complexes to the internal standard was observed.

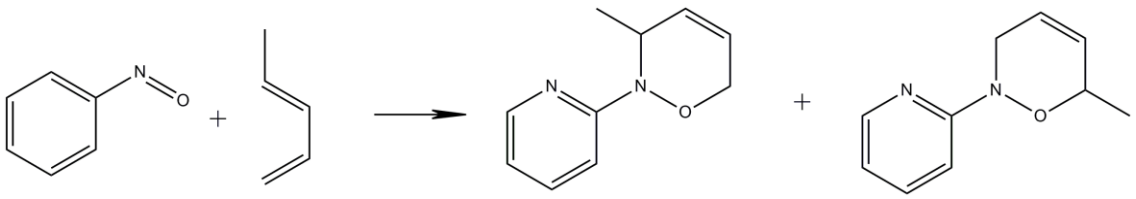

**75** **76** **77 (*dist*)** **78 (*prox*)**

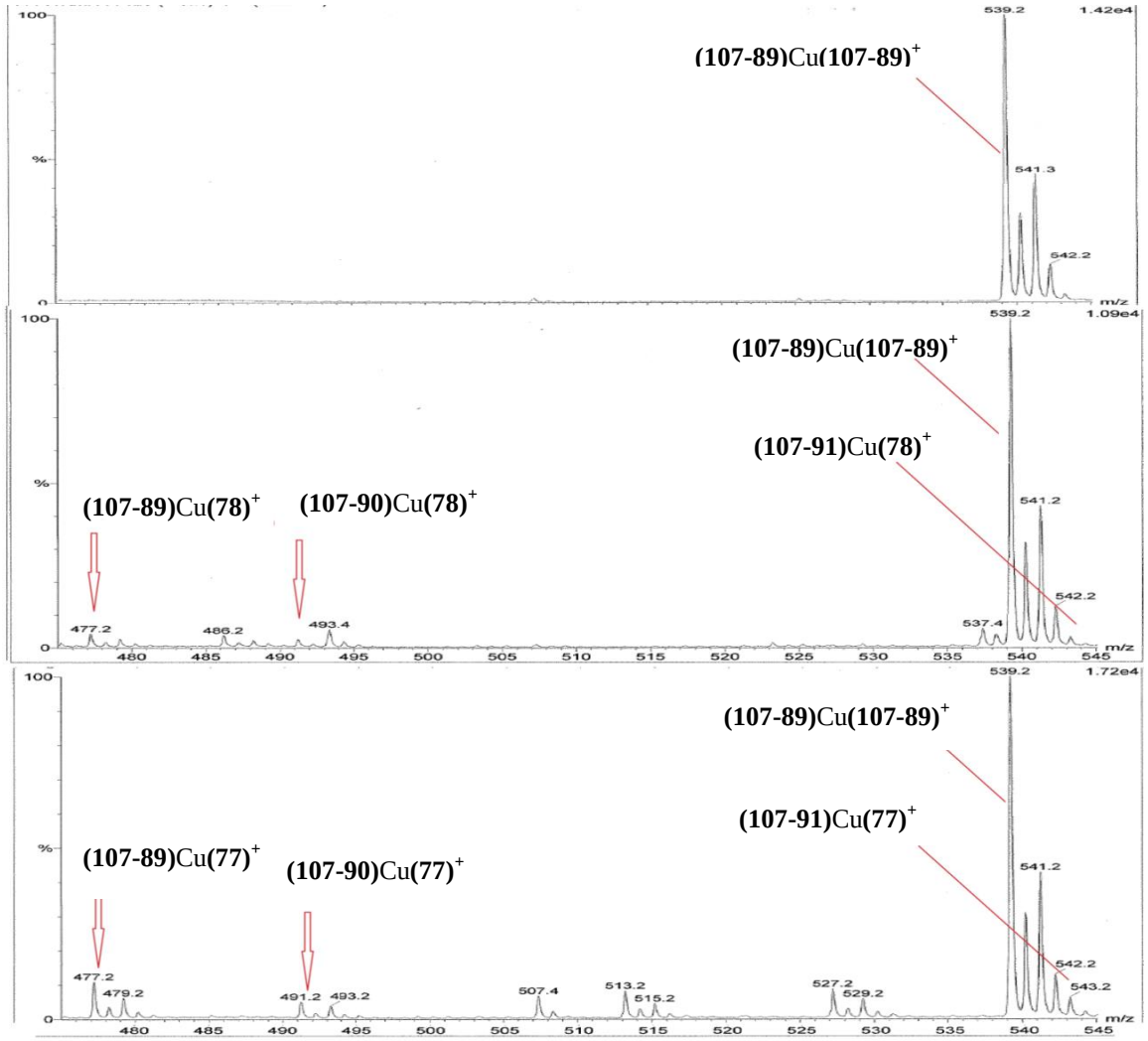


**Figure 43:** ESI-Mass spectra of (a) **107** + **89** + **90** + **91** + $Cu(CH_3CN)_4^+$; (b) $L_2Cu^+$ + **78**; (c) $L_2Cu^+$ + **77**.

To explore the $Cu^+$ complexes that mimic the regioisomeric transition states for the reaction between nitrosopyridine **75** and 1,3-pentadiene **76**, we chose **77** and **78** as "late" pro-TSAs (transition state analogs). To the $(diimine)_2Cu^+$ complex library (above) 100 equivalents of either **77** or **78** was added (**Figure 41**). The formation of new (imine)Cu(**77**)$^+$ and (imine)Cu(**78**)$^+$ complexes can be identified by their MS-isotope patterns ($^{63}$Cu:$^{65}$Cu 2:1) and molecular weight (M/z) (**Figure 43b,c**). Because the (imine)Cu(**77**)$^+$ and the (imine)Cu(**78**)$^+$ complexes are geometrically and electronically similar, their ionizabilities and detectabilities are presumed to be comparable, so the concentration of the two isomeric (imine)Cu(**77**)$^+$ and (imine)Cu(**78**)$^+$ complexes can be quantified using the built-in ion count program of the spectrometer[143-147]. A substantial difference in the relative ion count of (imine)Cu(**77**)$^+$ and (imine)Cu(**78**)$^+$ in the two libraries can be observed. This result shows that (imine)$Cu^+$ complexes are able to discriminate between regioisomers **77** and **78**, which indicates that **77** and **78** can be used as the TSAs for the binding investigation.

Interestingly, the internal standard ion count (m/z = 242) in the two libraries was identical. This result further supports our hypothesis that there is a correlation between the concentration of a LCu(TSA)+ complex and the ion count intensity in the ESI-MS of each library. Each (imine)Cu(**77**)$^+$/(imine)Cu(**78**)$^+$ ion count ratio was quantified and the average of the ion counts for each pair are compared directly. The TSA binding selectivity and the catalytic reaction's product ratios (selectivity) are plotted (**Figure 44**). Qualitatively, all tested (imine)Cu complexes have a stronger binding affinity with **78** than with **77** and also favor **78** to **77** when used as the catalysts. However, due to

ESI-MS experimental errors, the low spread of **78**/**77** regioselectivity and the relatively small data set, the correlation is judged to be marginal.

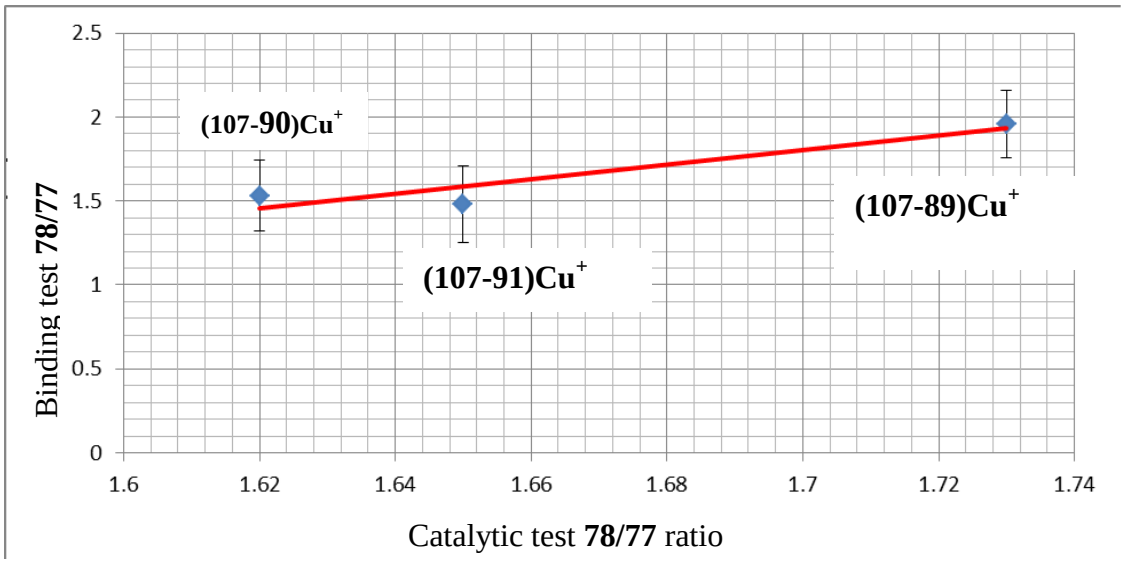


**Figure 44:** Correlation of ESI-MS (imine)Cu-TSA$^+$ binding selectivity and catalytic product selectivity.

### 2.2.4 Computational studies

This work was done at the University of California – Los Angeles by Dr. Peng Liu of Prof. Kendall Houk's group. The results and analysis are summarized below.

#### 2.2.4.1 Uncatalyzed Nitrosopyridine - Diene Reactions

Statistically, eight possible transition states can be formed in the reaction between nitrosopyridine (**75**) and 1,3-pentadiene (**76**). The NO bond of nitrosopyridine can be *syn* or *anti* to the pyridine ring; the methyl moiety of 1,3-pentadiene can be *distal* (closer to the N atom of the NO bond) or *proximal* (closer to the O atom of the NO bond); the orientation of 1,3-pentadiene to the pyridine ring can be *endo* or *exo.* The

calculations employed the Gaussian 09 program with the M06 functional and the 6-31G(d) basis set for light elements and LANL2DZ for $Cu^{2+}$ in MeOH using the PCM solvation model. A final single-point energy calculation employed M06/6-311+G(d,p) in MeOH with PCM solvation model.[148-151]

Due to the *exo* lone pair effect, all of the *exo* transition states have much higher energies than the *endo* transition states. The *exo* transition states are destabilized by four electron repulsions between the HOMO of the diene and the HOMO of the nitrosopyridine. Also, due to electron-electron repulsion, the *anti* transition states are more stable than *syn* transition states (**Figure 45**). The regioselectivity of this reaction is determined by the free activation energy difference of the most stable transition states, which are *endo-prox-anti*-**TS1** and *endo-dis-anti*-**TS1** in this case. They have the same Gibbs free energies ($\Delta G^{\ddagger}$ = 17.6 kcal/mol), which agrees remarkably well with the low selectivity of **77**/**78** (53/47) in the product mixture.

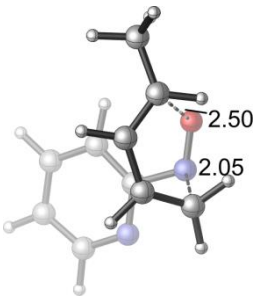


*endo-prox-anti*-**TS1**
$\Delta H^{\ddagger}$ = 3.5 kcal/mol
$\Delta G^{\ddagger}$ = 17.6 kcal/mol

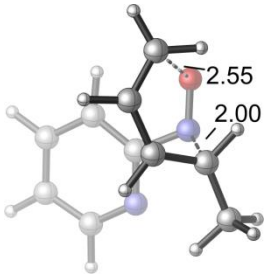


*endo-dist-anti*-**TS1**
$\Delta H^{\ddagger}$ = 3.6 kcal/mol
$\Delta G^{\ddagger}$ = 17.6 kcal/mol

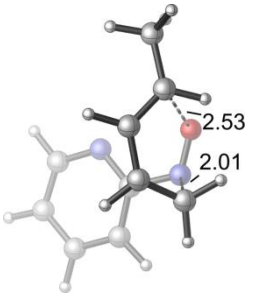


*endo-prox-syn*-**TS1**
$\Delta H^{\ddagger}$ = 5.5 kcal/mol
$\Delta G^{\ddagger}$ = 19.5 kcal/mol

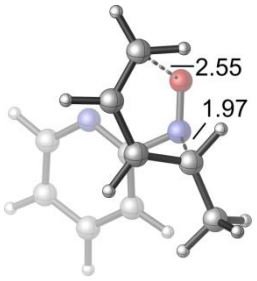


*endo-dist-syn*-**TS1**
$\Delta H^{\ddagger}$ = 5.7 kcal/mol
$\Delta G^{\ddagger}$ = 20.1 kcal/mol

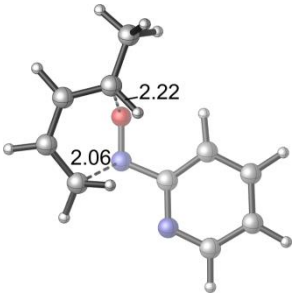


*exo-prox-anti*-**TS1**
$\Delta H^{\ddagger}$ = 9.2 kcal/mol
$\Delta G^{\ddagger}$ = 23.4 kcal/mol

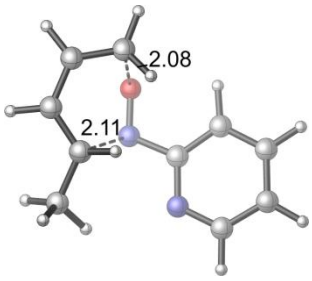


*exo-dist-anti*-**TS1**
$\Delta H^{\ddagger}$ = 11.3 kcal/mol
$\Delta G^{\ddagger}$ = 25.7 kcal/mol

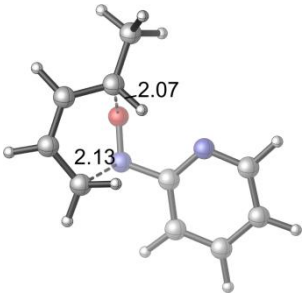


*exo-prox-syn*-**TS1**
$\Delta H^{\ddagger}$ = 10.7 kcal/mol
$\Delta G^{\ddagger}$ = 25.1 kcal/mol

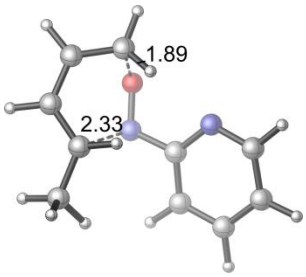


*exo-dist-syn*-**TS1**
$\Delta H^{\ddagger}$ = 12.5 kcal/mol
$\Delta G^{\ddagger}$ = 26.8 kcal/mol

**Figure 45:** Calculated transition states for the reaction of 1,3-pentadiene with 2-nitrosopyridine.

With the same methodology, eight concerted transition states of the reaction between nitrosopyridine (**75**) and 1-phenylbutadiene (**83**) were also calculated. Similar to the reaction with 1,3-pentadiene (**76**), the most stable transition states are *endo-dist-anti*-**TS1-Ph** and *endo-prox-anti*-**TS1-Ph (Figure 46**). Unlike the reaction with 1,3-pentadiene (**76**), where the methyl moiety has a small effect, the phenyl moiety of 1-phenylbutadiene (**83**) significantly changes the steric and electronic character of the diene. The stronger electron donating ability from the phenyl group polarizes the HOMO of the diene which favors the *proximal* transition state. The phenyl moiety is also bulkier than the methyl moiety which increases the steric repulsion when forming the C-N bond in distal transition state compared to forming the C-N bond *proximal* transition state **(Figure 46)**. In summary, both steric and electronic factors favor the *proximal* transition state to the distal *transition* state (3.7 kcal/mol more stable). This calculation also agrees with the experiment result because we only find compound **84** (*proximal* product) in the final product mixture.

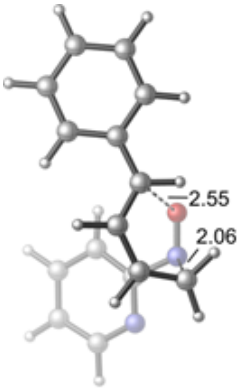


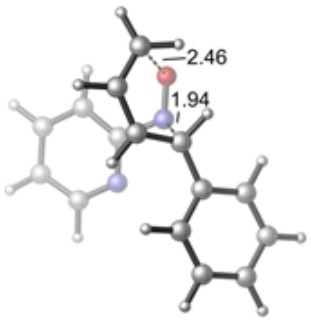


*endo-prox-anti*-**TS1-Ph**
$\Delta H^{\ddagger}$ = 2.8 kcal/mol
$\Delta G^{\ddagger}$ = 17.1 kcal/mol

*endo-dist-anti*-**TS1-Ph**
$\Delta H^{\ddagger}$ = 6.2 kcal/mol
$\Delta G^{\ddagger}$ = 20.8 kcal/mol

**Figure 46:** Most stable transition states for the reaction between 2-nitrosopyridine and 1-phenylbutadiene.

### 2.2.4.2 $Cu^{+}$-Catalyzed the reactions of 2-nitrosopyridine and 1,3-pentadienes.

In order to better understand the regio-selectivity of the reaction between nitrosopyridine and 1,3-pentadiene with $Cu(CH_3CN)_4^{+}$ as the catalyst, we performed a computational study; geometry optimization used the M06 functional, the 6-31G(d) basis set, and the PCM solvation model in methanol. Single-point calculations were performed with M06/6-311+G(d,p) and PCM solvation model. The SDD effective core potential basis set was used for Cu geometry optimizations and single-point energy calculations. The most stable transition states leading to the formation of distal (**77**) and proximal (**78**) products are *endo-prox-syn*-**TS2** and *endo-dist-syn*-**TS2** (**Figure 47**)**.**

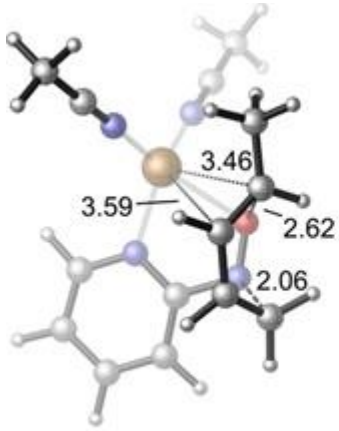


*endo-prox-syn*-**TS2**
$\Delta H^{\ddagger}$ = 1.4 kcal/mol
$\Delta G^{\ddagger}$ = 17.0 kcal/mol

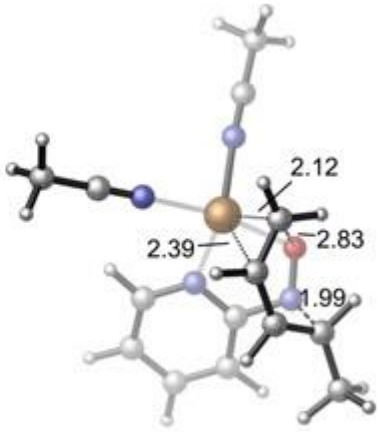


*endo-dist-syn*-**TS2**
$\Delta H^{\ddagger}$ = 0.3 kcal/mol
$\Delta G^{\ddagger}$ = 15.4 kcal/mol

**Figure 47:** Calculated transition states for the $(CH_3CN)_2Cu^{+}$ -catalyzed DA reaction between nitrosopyridine and 1,3-pentadiene.

Similar to the uncatalyzed reaction and many other DA reactions, the *endo* transition states are more stable than the *exo* transition states. Due to the binding with $Cu^{+}$, nitrosopyridine can only have a *syn* conformation, which is different from the

uncatalyzed reaction. The activation energy barriers of both *distal* and *proximal* transition states are lower than those of uncatalyzed reactions. The *distal* transition state (*endo-dist-syn*-**TS2**) is 1.6 kcal/mol more stable than the *proximal* transition state (*endo-prox-syn*-**TS2**), which is in agreement with the experimental result of more *distal* isomer **77** produced in the catalyzed the reaction. The coordination of $(CH_3CN)_2Cu^+$ with the nitrosopyridine further polarizes the NO bond, at the same time lowering the LUMO of dienophile. However, the high selectivity of this reaction is not only due to the Lewis acid effect. In the transition state, $(CH_3CN)_2Cu^+$ can weakly coordinate with one of the C=C double bonds of 1,3-pentadiene. The nitrosopyridine-$Cu(CH_3CN)_2^+$ is an 18-electron complex so the coordination is expected to be weak. Nonetheless, the Cu-C1 and Cu-C2 bonds in *endo-dist-syn*-**TS2** transition state are 2.12 and 2.39Å respectively, compared to Cu-C3 and Cu-C4 bonds of *endo-prox-syn*-**TS2** transition state which are 3.59 and 3.46Å (non-bonding) due to the methyl moiety repulsion and less nucleophilicity of the C4 carbon on 1,3-pentadiene. This additional stabilization of $(CH_3CN)_2Cu^+$ to *endo-dist-syn*-**TS2** transition state promotes the formation of *distal* product **77** over proximal product **78**.

### 2.2.4.3. Cu(diimine)$^+$- Catalyzed Reaction of Nitrosopyridine and 1,3-pentadiene.

The reaction between nitrosopyridine (**75**) and 1,3-pentadiene (**76)** with $Cu(diimine)^+$ as the catalyst was calculated with the same methodology as in **2.2.4.2**. The $Cu(\mathbf{87}\text{-}\mathbf{98})_2^+$ complex was chosen as the model ligand for this type of reaction due to its simplicity, thus reducing the calculational cost.

The most stable transition states leading to the *distal* product **77** and *proximal* product **78** are *endo-dist-syn*-**TS3** and *endo-prox-syn*-**TS3** respectively (**Figure 48**). In general, the geometry of (**87**-**98**)Cu(PyrNO)$^+$ complexes in the transition states is very similar to that of $(CH_3CN)_2Cu(PyrNO)^+$. As expected, the *endo* transition states are more favorable than the *exo*. Cu binds to the N of the pyridine moiety and the O of the nitroso moiety. The *tert*-butyl group of the aldehyde points away from the pyridine moiety. Interestingly, we observe the same situation as the $(CH_3CN)_2Cu^+$ case in which Cu binds with C1 and C2 of the diene in the distal transition state, but Cu does not bind with C3 and C4 of the diene in the proximal transition state. However, the *endo-dist-syn*-**TS3** transition state is only 0.9 kcal/mol more stable than *endo-prox-syn*-**TS3** transition state, compared to 1.6 kcal/mol as in the $(CH_3CN)_2Cu^+$ case. The greater steric effect and the more electron-rich ligand are two main factors that decrease the selectivity for the *distal* product (**77**). This is in agreement with the decrease of the selectivity observed experimentally.

Experimentally, the ligands have small effects on the regioselectivity of the reaction between nitrosopyridine (**75**) and 1,3-pentadiene (**76**). The computational results also suggest that electronic and steric effects on regioselectivity are small. The pseudo-tetrahedral geometry of $Cu^+$ center orients the imine ligand plane perpendicular to the nitrosopyridine plane. With this geometry, both of the substituents in the amine and aldehyde building blocks are pointed away from the methyl moiety of the 1,3-pentadiene, minimizing all steric interactions from the ligands to the substrate. The electronic effect from the ligands is also minimized due to the ligands not being able to change the polarity of the nitrosopyridine LUMO. The extra bonding between Cu and

*proximal* transition state is expected to be small due to the fact that the (nitrosopyridine)Cu(imine)$^+$ complexes have a closed valence shell 18-electron-count.

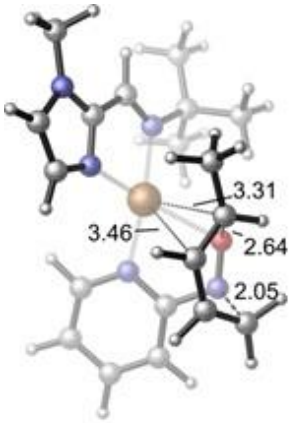


*endo-prox-syn*-**TS3**
$\Delta H^{\ddagger}$ = 0.3 kcal/mol
$\Delta G^{\ddagger}$ = 16.3 kcal/mol

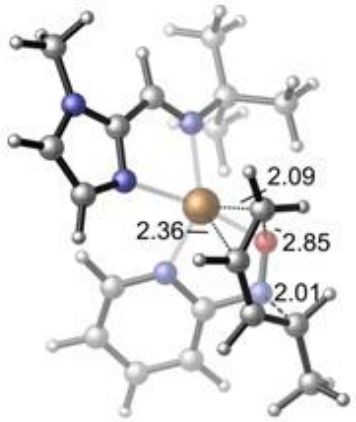


*endo-dist-syn*-**TS3**
$\Delta H^{\ddagger}$ = –1.8 kcal/mol
$\Delta G^{\ddagger}$ = 15.4 kcal/mol

**Figure 48:** Calculated transition states for Cu(**87**-**98**)$_2^+$ catalyzed nitrosopyridine and 1,3-pentadiene.

**2.3 Conclusions and future work.**

In this study, we found that the regioselectivity of the reaction between nitrosopyridine (**75**) and 1,3-pentadiene (**76**) can be significantly changed from 47:50 (*dist:prox*) to 90:10 with the use of $(CH_3CN)_4Cu^+$ as pre-catalyst. The regioselectivity of the reaction, however, deceases when using imine ligands coordinated to copper(I).

The regioselectivity of the reaction between nitrosopyridine (**75**) and sorbyl alcohol (**79**) is solvent dependent. The regioselectivity of the reaction (proximal **80**: distal **81**) changes from 35:65 in methanol to 10:90 in dichloromethane, presumably due to hydrogen bonding between the aromatic nitrogen moiety of nitrosopyridine (**75**) and the hydroxyl moiety of sorbyl alcohol.

The regioselectivity of the reaction between nitrosopyridine (**75**) and 1-phenyl-E-1.3-pentadiene (**83**) neither depends on solvent nor $Cu^+$ catalysts. Only proximal (**84**) product is formed. The regioselectivity of this reaction results from both electronic and steric effects.

Both *distal* (**77**) and *proximal* (**78**) isomers could be used as "late" transition states analogs for dynamic templating with $(imine)_2Cu^+$. However, the correlation between TSA-binding and catalytic rate is marginal due to the small regioselectivity range of the tested catalysts.

Computational studies were also employed to understand the thermal and $Cu^+$ catalyzed reactions between 1,3-pentadiene (**76**); 1-phenyl-E-1,3-pentadiene (**83**) and nitrosopyridine (**75**). The calculations suggest that both $(CH_3CN)_2Cu^+$ and $(imine)_2Cu^+$ can speed up the reaction. However, the pseudotetrahedral structure of the $Cu^+$ center in the transition states minimizes the steric and electronic interactions between diene and ligands leading to low regioselectivity of the $Cu^+$ catalysts. Meanwhile, the electronic effects from the $Cu^+$ catalysts are not strong enough to change the LUMO polarity of the dienophile significantly, thus electronic contributions to the regioselectivity are small.

From the experimental results and computational studies, the low regioselectivity of the reaction between nitrosopyridine and dienes can be explained by the pseudotetrahedral structure of copper(I) center which limits the steric effects from the ligand to the diene at the transition state. We suggest that the regioselectivity could be improved by using metal complexes that have square-planar structures to maximize the steric interactions between the ligands, dienes and the coordinated nitrosoarene.

From the literature precedent, $Cu^{2+}$; $Zn^{2+}$; $Ni^{2+}$ and $Pd^{2+}$ are the Lewis acid metal complexes that tend to form square-planar structures, which could be used to improve the regioselectivity of the same reactions.[152-156] These Lewis acids will be further investigated in the next chapter.

## 2.4 Experimental

### 2.4.1 Materials Preparation

**General.** Unless otherwise noted all solvents were pre-dried in a solvent still (MeOH dried over Mg, $CH_2Cl_2$ and acetonitrile dried over $CaH_2$), distilled and then freeze-pump-thawed for at least five cycles. The following compounds were prepared according to the cited procedures and identified by comparison of their $^1$H NMR spectra to those reported:

2-nitrosopyridine (**75**)[157] $^1$H NMR (300 MHz, $CDCl_3$) δ: 8.81 (1H, d), 7.88 (1H, d), 7.55-7.50 (2H, m).

N-Isopropylimidazole-2-carboxaldehyde (**100**)[71]: $^1$ H-NMR (300 MHz, CDCl3) δ 9.76 (1H, s), 7.34 (1H, d, J= 6.5 Hz), 7.22 (1H, d, 6.5 Hz),1.64 (9H, s).

4-(dimethylamino)-2-Pyridinecarboxaldehyde (**105**)[158] $^1$H NMR (300 MHz, $CDCl_3$): δ 9.97 (s, 1H), 8.37 (d, 1H, J = 6.0 Hz), 7.17 (d, 1H, J = 2.5 Hz), 6.64 (dd, 1H, J = 6.0, 3.0 Hz), 3.06 (s, 6H).

1-phenyl-1,3-butadiene (**83**) [159] $^1$H NMR (300 MHz, CDCl3): δ 7.37(d, J = 8.0 Hz, 2H), 7.30-7.27(m, 2H), 7.26-7.17(m, 1H), 6.70(dd, J = 15, 10.4 Hz, 1H), 6.56-6.44(m, 1H), 5.32(d, J = 17.2 Hz, 1H), 5.14(d, J = 10.0 Hz, 1H)

8-Isopropyl-2-quinolinecarboxaldehyde (**108**) [160]: $^1$H NMR (CDCl3, 300 MHz): δ 10.25 (s, 1 H), 8.27 (d, 1 H, J = 8.4 Hz), 8.01 (d, 1 H, J = 8.4 Hz), 7.62–7.75 (m, 3 H), 4.49 (sept, 1 H, J = 7.0 Hz), 1.44 (d, 6 H, J = 7.0 Hz).

3-methyl-2-(pyridin-2-yl)-3,6-dihydro-2H-1,2-oxazine **(77)** and 6-methyl-2-(pyridin-2-yl)-3,6-dihydro-2H-1,2-oxazine (**78**). 2-Nitrosopyridine **75** (0.216 g, 2.0 mmol) was dissolved in 100 mL of methanol followed by the addition of 1 mL of 1,3-pentadiene **76** (ca. 6 mmol, 75% pure, 2:1 E/Z). The solution was left for 1 hr then the solvent removed in vacuo to leave a brown liquid mixture. Column chromatography of the liquid over silica gel with 7:3 hexane:diethyl ether gave 0.295 g (84 %) of a light yellow liquid. The ratio of proximal/distal isomers was 46:54 (NMR integration).

A few reaction mixtures were combined to give 1.4 g of the regioisomeric mixture (8.0 mmol). Twenty-five µL of the reaction product mixture were separated on a C18 Bakerbond column (22.5 x 250 mm) using 4:6 MeOH:$H_2O$ at 16 mL/min (UV detection at 267 nm). Fraction 1 was collected from 19.5 m to 21.4 m and fraction 2 from 23.9 m to 25.4 m. After multiple injection/collection cycles each combined fraction was concentrated to 40 % of the original volume and then saturated with NaCl. Each fraction was extracted three times with 200 mL of $Et_2O$, then the combined organic layers were dried over $MgSO_4$ and concentrated in vacuo to yield 0.341 g of *dist*-adduct (**77**) in fraction 1 (1.94 mmol; from 4.32 mmol calculated in the original mixture by H-NMR analysis, 45% yield) and 0.261 g of the *prox* isomer (**78**) in fraction 2 (1.48 mmol; from 3.68 mmol calculated in the original mixture by H-NMR analysis, 40% yield) from 1.4 g (8.0 mmol) of thermal product mixture.

3-methyl-2-(pyridin-2-yl)-3,6-dihydro-2H-1,2-oxazine (*Distal* **77**)

$^1$H NMR (300 MHz, $CDCl_3$) δ 8.22 (dd, J= 5.1, 1.2 Hz, 1H), 7.58 (dt, J= 7.8, 1.8 Hz, 1H), 7.1 (d, J= 7.8 Hz, 1H), 6.75 (t, J= 6 Hz, 1H) 5.98 (ddd, J= 9.0, 4.2, 1.8 Hz, 1H), 5.83 (ddd, J= 11.7, 3.6, 1.8Hz, 1H), 4.83 (m, 1H), 4.64 (ddd, J= 17.7, 6.6, 2.4 Hz, 1H), 4.3 (ddd, J= 15.3, 6.6, 1.8 Hz, 1H), 1.21 (d, J= 6.6 Hz).

6-methyl-2-(pyridin-2-yl)-3,6-dihydro-2H-1,2-oxazine (*Proximal* **78**)

$^1$H NMR (300 MHz, $CDCl_3$) δ 8.23 (dd, J= 4.8, 1.8 Hz, 1H), 7.59 (dt, J= 7.2, 2.4 Hz, 1H), 7.20 (d, J= 8.4 Hz, 1H), 6.80 (t, J= 6Hz, 1H) 5.96 (ddd, J= 7.5, 5.7, 1.8 Hz, 1H), 5.83 (m, 1H), 4.73 (m, 1H), 4.36 (dquin, J= 17.1, 2.4 Hz, 1H), 3.95 (ddd, J= 17.1, 4.8, 2.4 Hz, 1H), 1.34 (d, J= 6.9 Hz).

Distal **77** and **78** isomers were identified by 1D-NOE $^1$H-NMR. The proton attached to C6 on the pyridine moiety is irradiated and the methyl moiety of each isomer is observed (**Figure 49)**.

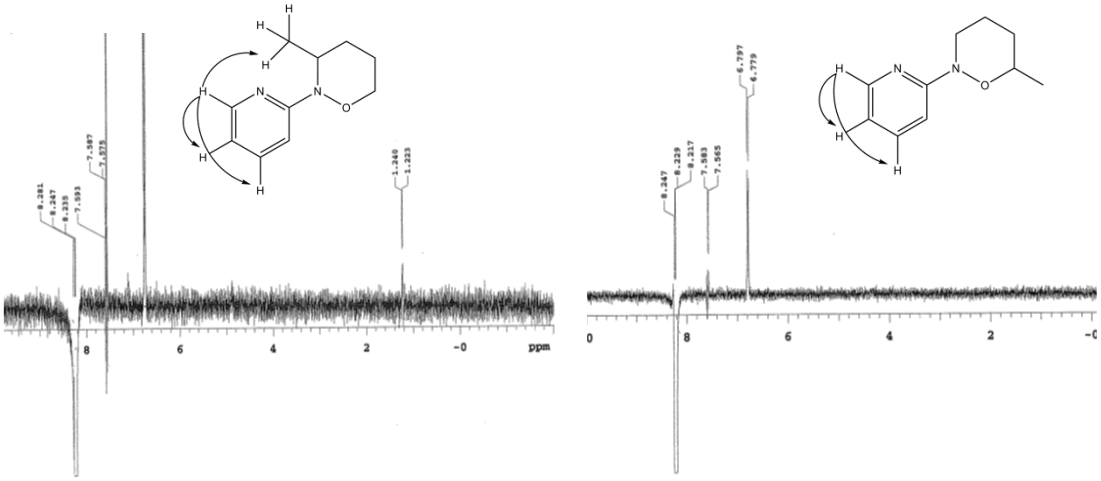


**Figure 49:** 1D-NOE of compound **77** (left) and compound **78 (**right**).**

Preparation of (6-methyl-2-(pyridin-2-yl)-3,6-dihydro-2H-1,2-oxazin-3-yl)methanol (**80**) and (3-methyl-2-(pyridin-2-yl)-3,6-dihydro-2H-1,2-oxazin-6-yl)methanol **(81).**

2-Nitrosopyridine (216 mg, 2.00 mmol) was dissolved in 100 mL of methanol followed by the addition of 196 mg (2.00 mmol) of sorbyl alcohol. The solution was left for 1 hour then the solvent removed in vacuo to leave a brown liquid mixture. Column chromatography of the liquid over silica gel 1:1 hexane: ethyl acetate gave 383 mg (93 %) of a light yellow liquid. The proximal/distal ratio of adducts was 66:34 (NMR). Column chromatography of the liquid above with 98/2 $CH_2Cl_2$/MeOH separated the two products.

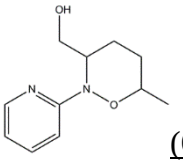


(6-methyl-2-(pyridin-2-yl)-3,6-dihydro-2H-1,2-oxazin-3-yl)methanol (**80**) (New compound) $^1$H NMR (500 MHz, $CDCl_3$): δ 8.15 (dd, J= 5.0, 1.7Hz, 1H), 7.59 (dt, J= 7.8, 7.8, 1.7 Hz, 1H), 7.12 (dd, J= 7.9, 1.0 Hz, 1H), 6.76 (ddd, J= 7.9, 5.0, 1.0 Hz, 1H), 5.92 (ddd, J= 10.5, 4.5, 2.0 Hz 1H), 5.83 (dt, J= 10.5, 1.6 Hz, 1H), 5.04 (m, 1H), 4.61 (m, 1H), 3.89 (dd, J= 11.6, 7.1 Hz, 1H), 3.81 (dd, J= 11.6, 3.3 Hz, 1H), 1.31 (d, 6.7 Hz, 3H). $^{13}$C NMR (125 MHz, $CDCl_3$): 159.9, 147.5, 138.2, 131.2, 124.0, 116.1, 110.2, 71.2, 64.0, 56.5, 19.1. HRMS (ESI) calculated for $C_{11}H_{15}N_2O_2$ ($M + H^+$) 207.1133 found 207.1130; calculated for $C_{11}H_{14}N_2O_2Na$ ($M + Na^+$) 229.0953 found 229.0947.

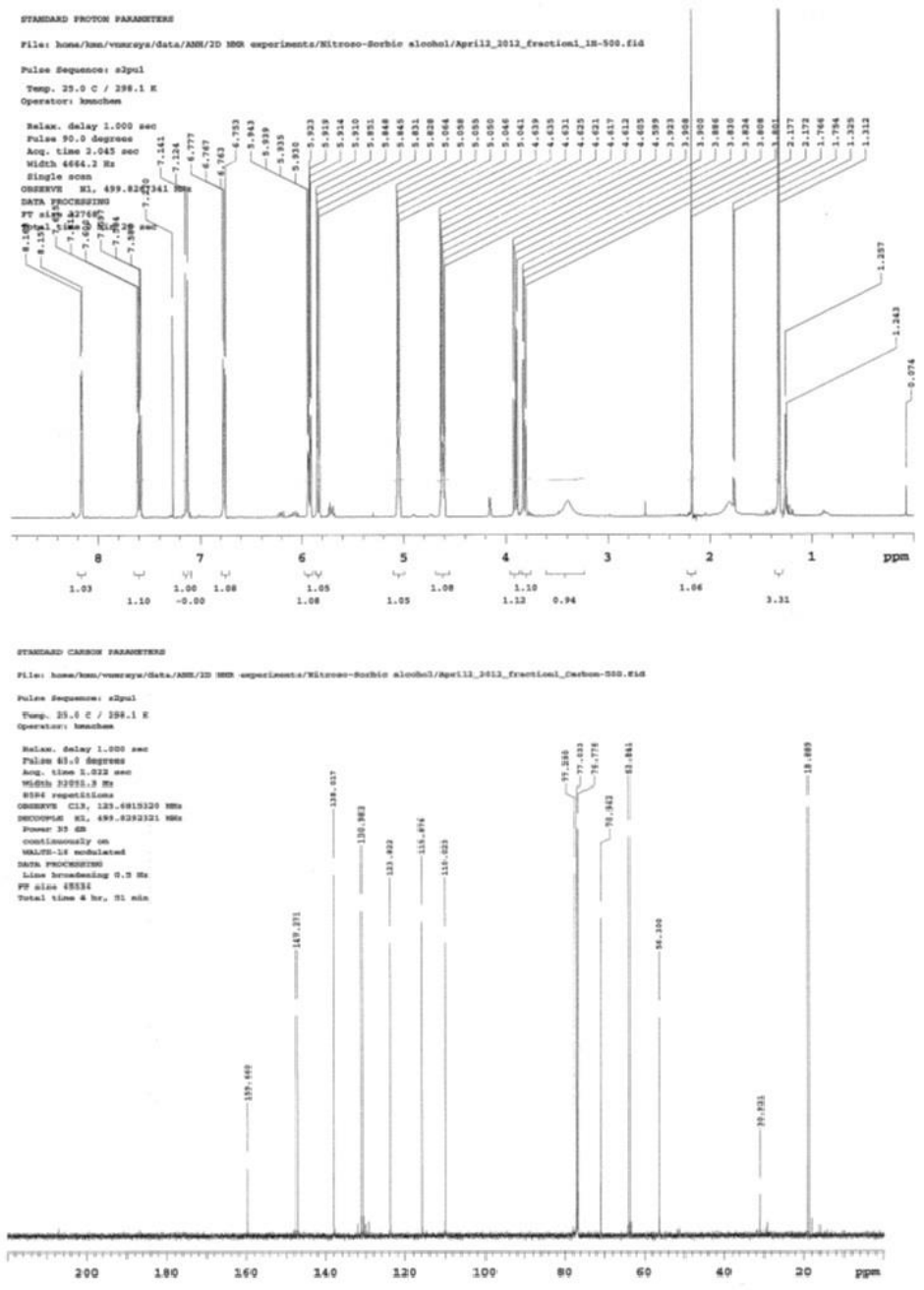

**Figure 50:** $^{1}$H NMR and $^{13}$C NMR of compound (**80**)

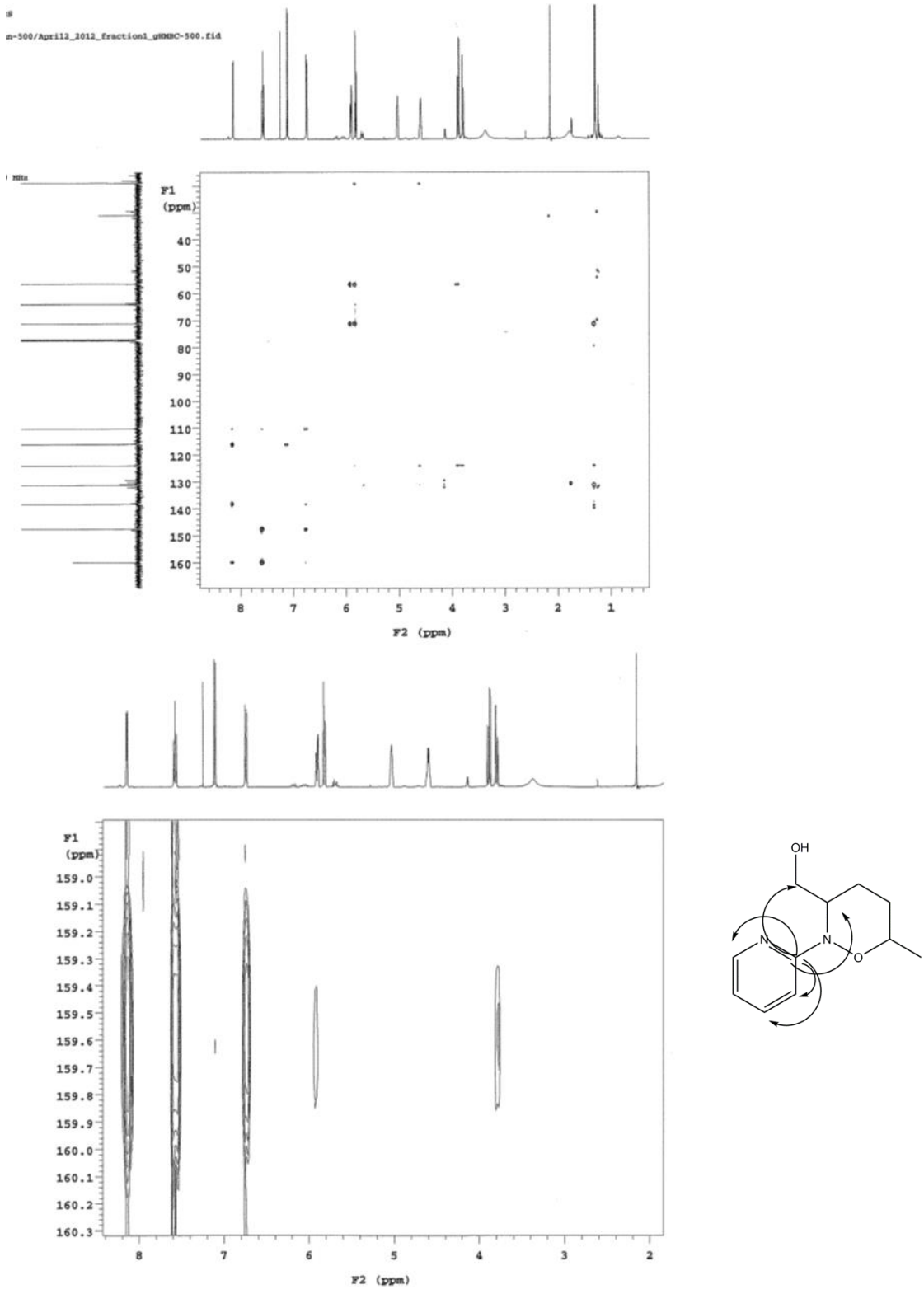


**Figure 51:** HBMC and expansion of compound (**80**)

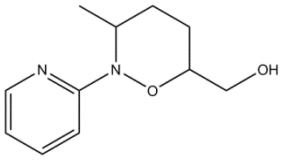


(3-methyl-2-(pyridin-2-yl)-3,6-dihydro-2H-1,2-oxazin-6-yl)methanol **(81).** (New compound) $^{1}$H NMR (500 MHz, $CDCl_3$): δ 8.24 (dd, J= 5.06, 1.8 Hz, 1H), 7.58 (dt, J= 7.8, 7.8, 1.8 Hz, 1H), 7.10 (d, J= 7.8 Hz, 1H), 6.77 (dd, J= 7.8, 5.06 Hz, 1H), 6.10 (ddd, J= 10.2, 4.8, 2.1 Hz, 1H), 5.70 (dt, J= 10.2, 1.3, 1H), 4.88 (m, 1H), 4.73 (m, 1H), 3.85 (dd, J= 12.2, 6.5 Hz, 1H), 3.76 (dd, J= 12.2, 6.5 Hz, 1H), 1.24 (d, J= 6.7 Hz, 3H). $^{13}$C NMR (125 MHz, $CDCl_3$): 159.8, 147.9, 137.93, 132.1, 124.0, 116.1, 110.0, 78.0, 64.3, 51.5, 16.2. HRMS (ESI) calculated for $C_{11}H_{15}N_2O_2$ ($M + H^+$) 207.1133 found 207.1130; calculated for $C_{11}H_{14}N_2O_2Na$ ($M + Na^+$) 229.0953 found 229.0947 (**Figure 52**)

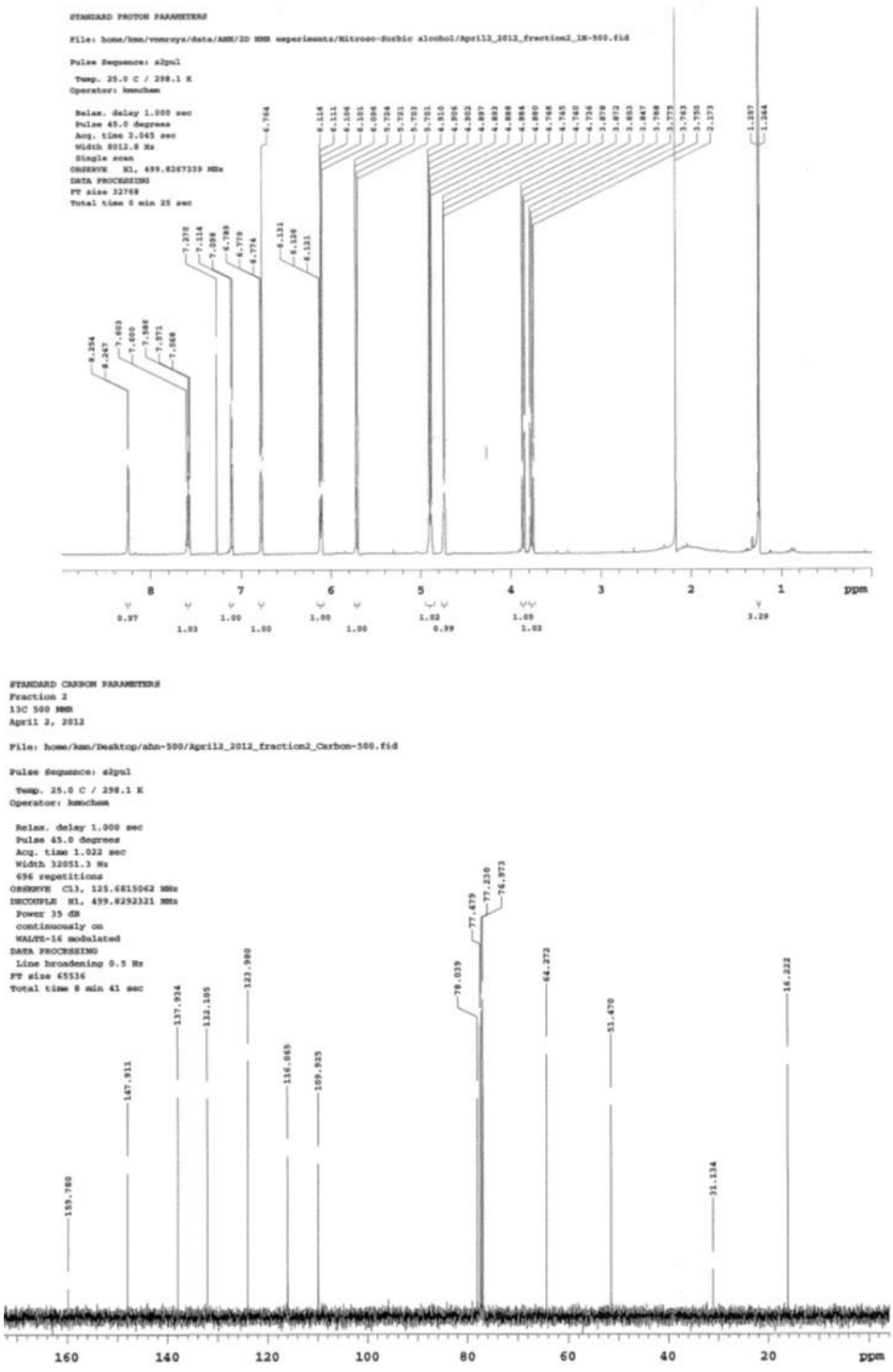


**Figure 52:** $^{1}$H NMR and $^{13}$C NMR of compound (**81**)

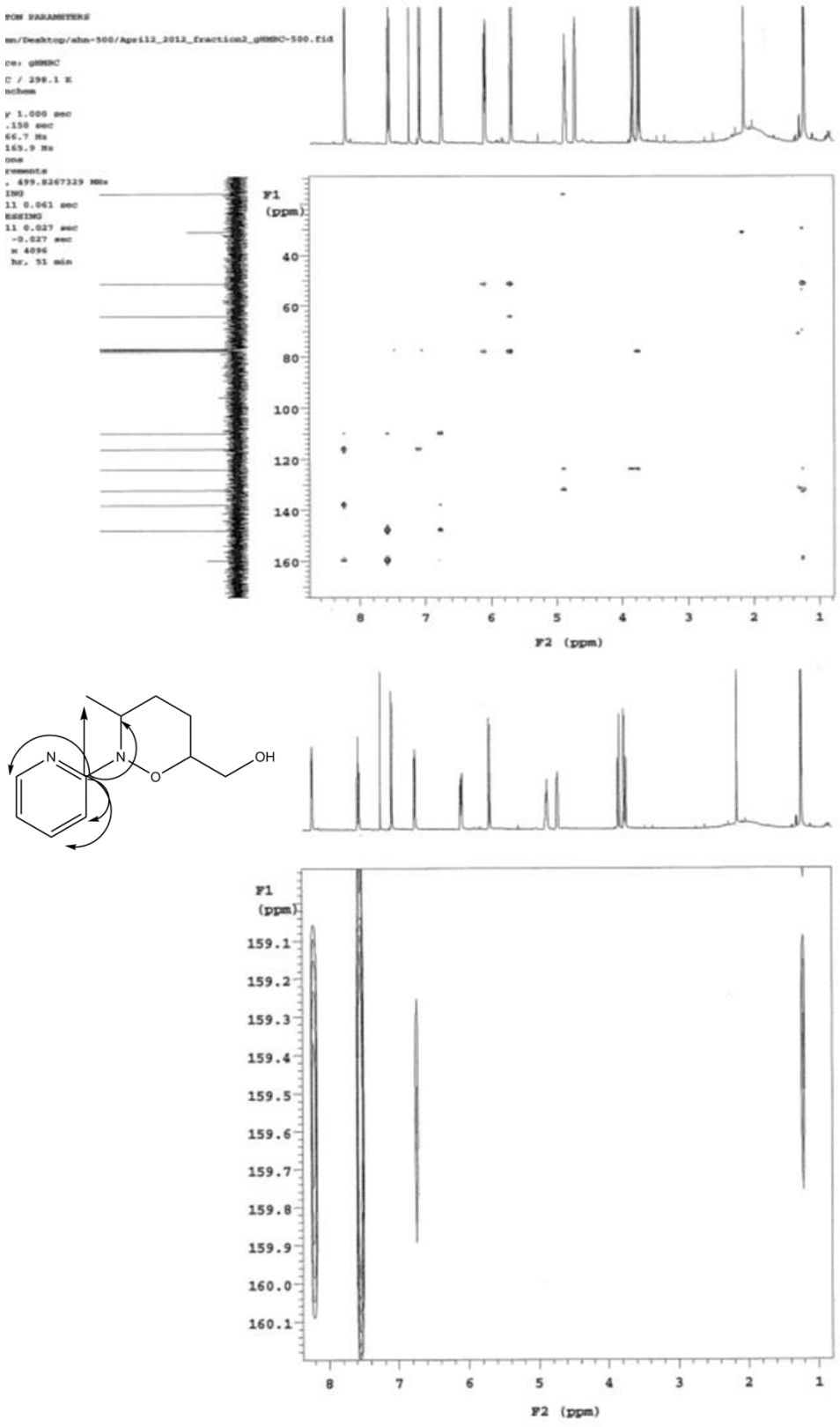


**Figure 53:** HBMC spectrum and expansion of spectrum for compound **81.**

Preparation of 6-phenyl-2-(pyridin-2-yl)-3,6-dihydro-2H-1,2-oxazine (**84**)

2-Nitrosopyridine (216 mg, 2.0 mmol) was dissolved in 100 mL of methanol followed by the addition of 260 mg (2.0 mmol) of 1-phenyl-butadiene. The solution was left for one hour, then the solvent removed in vacuo to leave a brown liquid mixture. Column chromatography of the liquid over silica gel with 6:4 hexane:diethyl ether gave 214 mg (45%) of light yellow liquid.

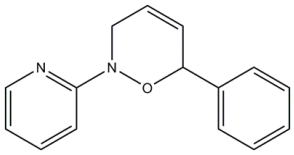


$^{1}$H NMR (500 MHz, $CDCl_3$): δ 8.23 (dd, J= 4.6, 1.8 Hz, 1H), 7.54 (dt, J= 7.9, 1.8 Hz, 1H), 7.50 (m, 2H), 7.39 (m, 2H), 7.14 (d, J= 7.9, 1H), 6.80 (dd, J= 7.9, 4.6 Hz), 6.21 (m, J= 10.4 Hz, 1H), 6.05 (m, J= 10.4Hz, 1H), 5.62 (m, 1H), 4.48 (m, J= 17.2Hz, 1H), 4.15 (m, J= 17.2Hz, 1H). $^{13}$C-NMR (125 MHz, $CDCl_3$): δ 160.9, 147.3, 138.6, 137.5, 128.5, 128.3, 128.1, 124.4, 116.6, 110.4, 79.8, 47.7. HRMS (ESI) calculated for $C_{15}H_{15}N_2O$ ($M + H^+$) 239.1185 found 239.1185 (**Figure 54**)

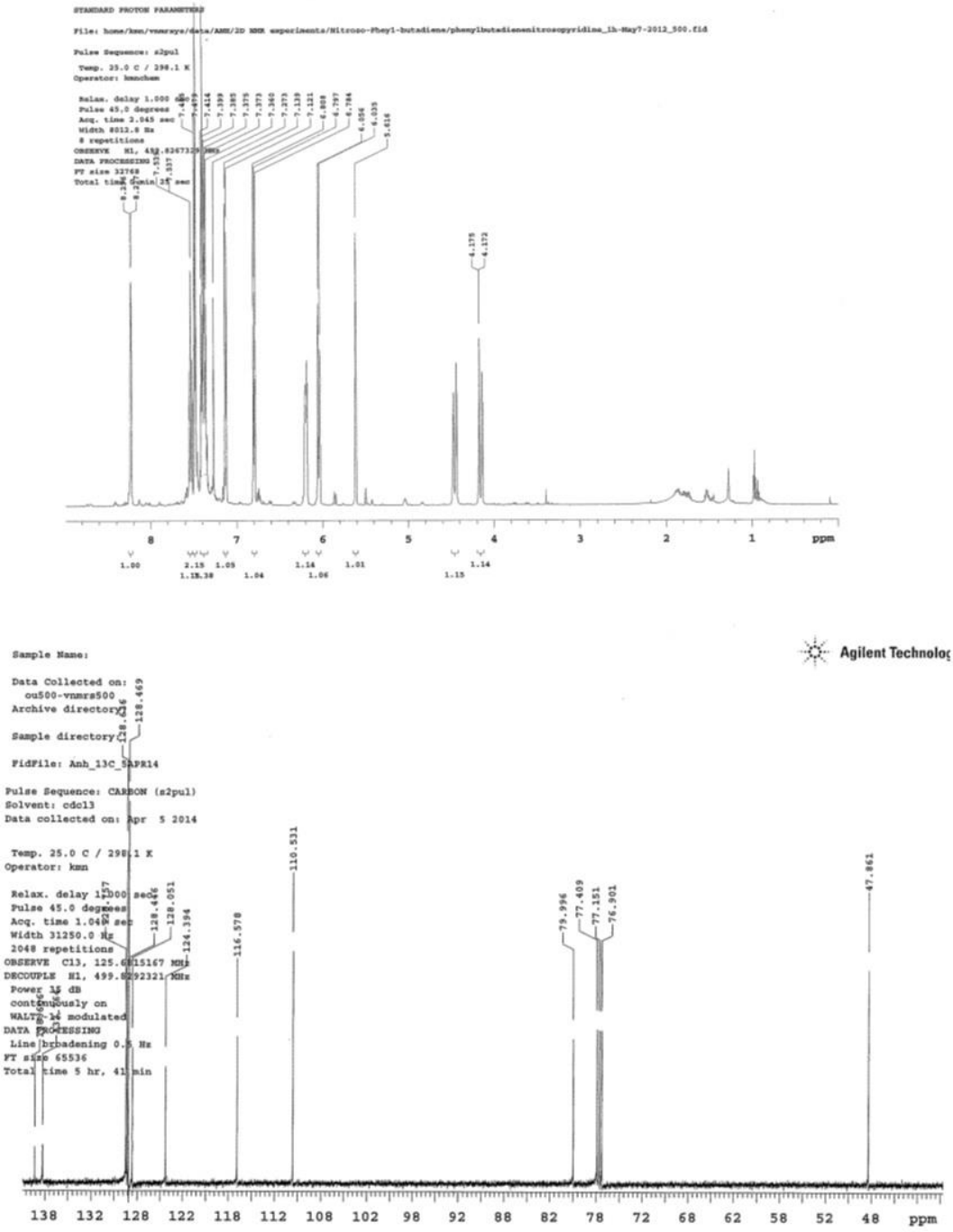


**Figure 54:** $^{1}$H NMR and $^{13}$C-NMR of compound **84.**

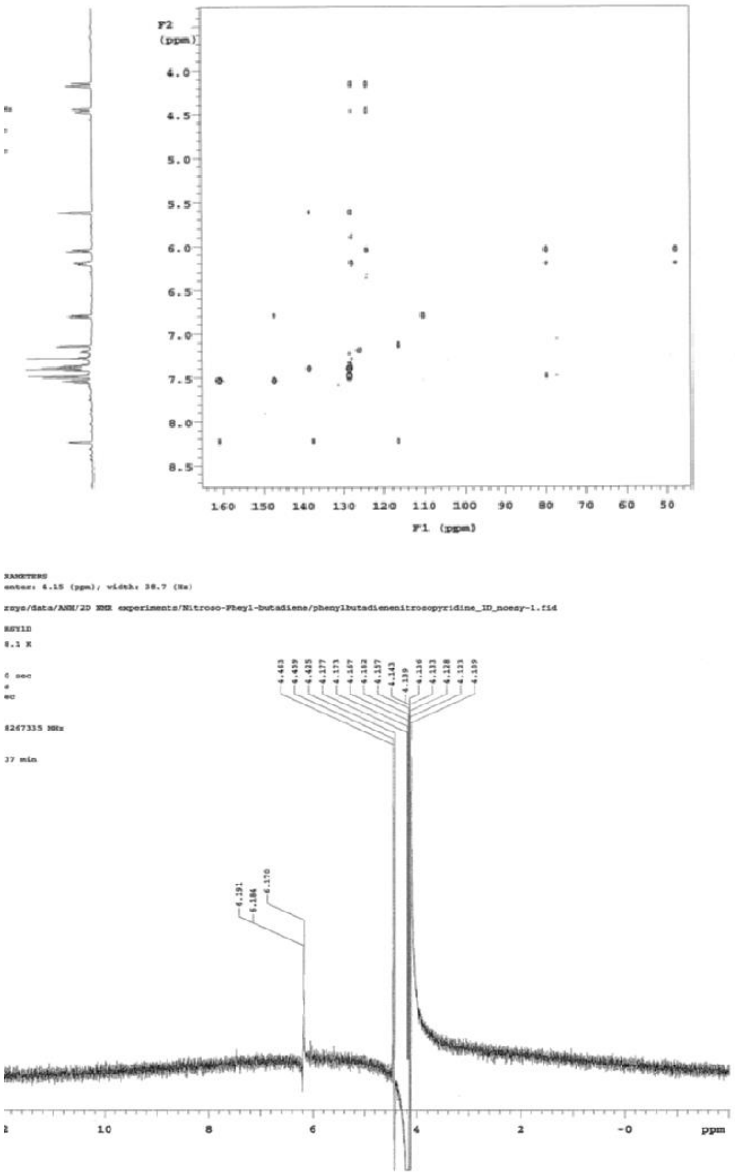


**Figure 55** HMBC and 1D-NOE of compound **84**

Copper(2-quinoline-1-methyl-adamantyl-imine)$_2$ hexafluorophosphate (**85**)

In a dry box 37 mg (0.10 mmol) of tetrakis(acetonitrile)copper(I) hexafluorophosphate was dissolved in 1.0 mL of methanol. In a different vial 31 mg (0.20 mmol) of 2-quinolinecarboxaldehyde and 32 µL (0.20 mmol) of 1-

adamantylmethylamine was added to 1 mL of methanol. The vial was shaken vigorously to partially dissolve the reactants and the solutions from the two vials were mixed to form a purple red solution. After 24 hours, the solvent was removed by pipet and dark purple crystals at the bottom of the vial were taken out of the dry box. The biggest crystal was chosen and carefully washed with cold acetone. The crystal appears to be air stable. $^1$H NMR (300 MHz, $CDCl_3$) δ 9.00 (s, 1H), 8.61 (d, J= 8.1 Hz, 1H), 8.13 (d, J= 8.1 Hz, 1H), 7.95 (dd, J= 5.4, 2.4 Hz, 1H), 7.59 (m, 3H), 2.62 (b, 3H), 1.85 (b, 6H), 1.57 (m, b, 8H).

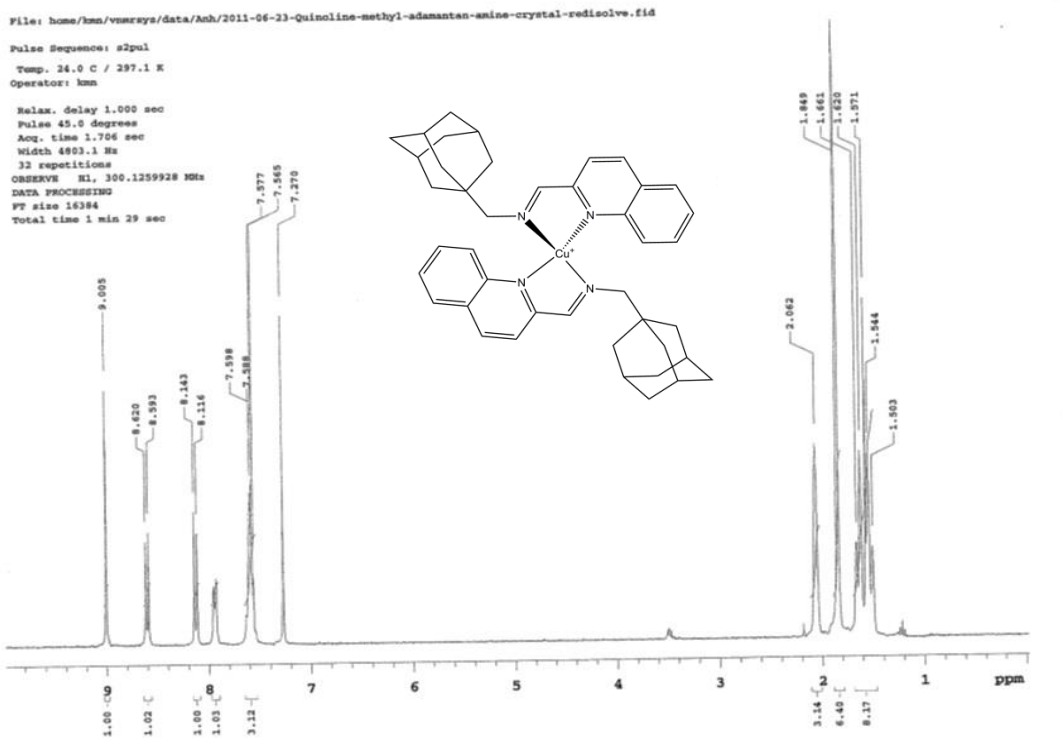


**Figure 56** $^1$H NMR spectrum of compound **85**

| | | |
|---|---|---|
| Empirical formula | $C_{42}$ $H_{48}$ Cu $F_6$ $N_4$ P | |
| Formula weight | 817.35 | |
| Crystal system | monoclinic | |
| Space group | *C*2/*c* | |
| Unit cell dimensions | *a* = 32.815(8) Å | α= 90° |
| | *b* = 11.058(3) Å | α= 124.773(4)° |
| | *c* = 25.545(6) Å | α= 90° |
| Volume | 7614(3) Å$^3$ | |
| Z, Z' | 8, 1 | |
| Density (calculated) | 1.426 Mg/m$^3$ | |
| Wavelength | 0.71073 Å | |
| Temperature | 100(2) K | |
| *F*(000) | 3408 | |
| Absorption coefficient | 0.682 mm$^{-1}$ | |
| Absorption correction | Semi-empirical from equivalents | |
| Max. and min. transmission | 0.8320 and 0.7181 | |
| Theta range for data collection | 1.64 to 26.00° | |
| Reflections collected | 29951 | |
| Independent reflections | 7489 [R(int) = 0.0410] | |
| Data / restraints / parameters | 7489 / 0 / 487 | |
| *wR*(*F*$^2$ all data) | *wR*2 = 0.1249 | |
| *R*(*F* obsd data) | *R*1 = 0.0524 | |
| Goodness-of-fit on *F*$^2$ | 1.007 | |
| Observed data [I > 2□(I)] | 5916 | |
| Largest and mean shift / s.u. | 0.001and 0.000 | |
| Largest diff. peak and hole | 0.729 and -0.752 e/Å$^3$ | |

**Table 4:** Crystal data and structure refinement for (**85**)

### 2.4.2 ESI-MS quantification of the LCu(TSA)$^+$ complex library

In a dry box, 37 mg (0.10 mmol) of tetrakis(acetonitrile)copper(I) hexafluorophosphate was dissolved in 1.0 mL of methanol. In a different vial the imine ligands were formed by adding one equivalent of 2-quinolinecarboxaldehyde (16 mg)

(1mmol), cyclohexylamine 12 µL (0.1 mmol), cyclohexylmethyl amine 13 µL (0.1mmol), and 1-adamantylmethyl amine 18 µL (0.1 mmol), and diluting with methanol to make 1.0 mL total volume. A red brown solution was formed upon mixing the imine- and copper-containing solutions; the resulting solution was left overnight to reach equilibrium. On the next day, 80 µL of the above solution and 10 µL of tetrabutylammonium hexafluorophosphate (0.0010 mmol/L) were combined and diluted with $CH_3OH$ to make a 4 mL stock solution. In two different septa-capped vials, 1 mL of the stock solution was added to each vial followed by 16 µL (0.10 mmol) of the distal or the proximal adduct TSA. The mixtures were left in the dry box for 72 hr to reach equilibrium. Without further dilution, the mixtures were injected to overfill a 20 µL sample loop under flow of methanol (1 mL/min). A Micromass Q-TOF mass spectrometer was used for analysis with a capillary voltage set at 3000V. The ion integration was measured with the most abundant isotopomer of each complex using the built in program. Each sample was injected into the mass spectrometer five times and the resulting mass spectra acquired and the ion integrations determined. The binding ratio of the isomers was determined by averaging the integrated ion count of each regioisomeric ternary complex. The tetrabutylammonium ion (m/z = 242) was monitored as the internal standard.

### 2.4.3. Copper (I) catalyzed reactions

#### 2.4.3.1 Diene-PyrNO reactions catalyzed by tetrakis(acetonitrile)copper(I) hexafluorophosphate

In a dry box 37 mg (0.10 mmol) of tetrakis(acetonitrile)copper(I) hexafluorophosphate were dissolved in 1.0 mL of methanol. In a Schlenk tube, 21.6 mg (0.20 mmol) of 2-nitrosopyridine was dissolved in 10 mL of methanol. The catalyst solution was injected into the nitrosopyridine solution 200 µL (10% loaded) followed by addition of 100 µL of 1,3-pentadiene (3 times excess, 75% pure, 2:1 *E/Z*) immediately to prevent any side reactions. The solution was left 15 min then the solvent was evaporated to form a brown sticky mixture. One or two drops of acetone were added to the mixture to dissolve the solid, followed by the addition of 1.5 mL of 7:3 hexane:diethyl ether to precipitate side products. The isomeric product mixture was isolated after passing the supernatant solution through a silica plug and rotary evaporating the solvent. The ratio of the two products was determined by NMR integration.

#### 2.4.3.2 Diene-PyrNO reactions catalyzed by $(imine)_2$copper(I) hexafluorophosphate

In a dry box 37 mg (0.10 mmol) of tetrakis(acetonitrile)copper(I) hexafluorophosphate was dissolved in 1.0 mL of methanol. In a different vial imines were formed by adding two equivalents (0.20 mmol) of the selected aldehyde (0.20 mmol), the selected amines (0.20 mmol) and methanol to make 1.0 mL total solution volume. A red brown solution was formed upon mixing the imine and the copper

solutions. The catalyst solution was left overnight to reach equilibrium. If dark brown crystals formed, more $CH_3OH$ was added to dissolve the crystals then the solution was left overnight again. In a Schlenk tube, 22 mg (0.20 mmol) of 2-nitrosopyridine was dissolved in 10 mL of methanol. The catalyst solution is injected into the nitrosopyridine solution (1% loaded) followed by addition of 100 µL of 1,3-pentadiene (three fold excess, 75% pure, 2:1 *E/Z*) immediately to prevent any side reaction. The solution was left 15 min then the solvent was evaporated to form a brown sticky mixture. One or two drops of acetone were added to the mixture to dissolve the solid, followed by the addition 1.5 mL of 7:3 hexane:diethyl ether to precipitate side products. The isomeric product mixture was isolated after passing the supernatant solution through a silica plug and rotary evaporating the solvent. The ratio of the two products was determined by NMR integration. A list of *prox/dist* regioselectivities from the 1,3-pentadiene/PyrNO reactions catalyzed by various $L_2Cu^+$ complexes is provided in the supporting information.

### 2.4.4 Computational methods

All geometry optimizations and frequency calculations were performed with the M06 functional and a mixed basis set of SDD for Cu and 6-31G(d) for other atoms. The PCM solvation model was used in the geometry optimizations and methanol was used as solvent. Single point energies were calculated with M06 and a mixed basis set of SDD for Cu and 6-311+G(d,p) for other atoms. PCM solvation model (methanol solvent) was also used in single point energy calculations. All calculations were performed with Gaussian 09. All reported Gibbs free energies include zero-point

vibrational energies and thermal corrections at 298K. Energies in solution were converted to the standard state (1 mol/L). We also tested the B3LYP functional, calculations in gas phase, and single point energies with different basis sets. The M06/6-311+G(d,p)–SDD(PCM)//M06/6-31G(d)–SDD(PCM) gives excellent agreement with the experimental regioselectivity for the benchmark calculations.

| Entry | Method | $\Delta G^{\ddagger}$ ($\Delta H^{\ddagger}$) -proximal | $\Delta G^{\ddagger}$ ($\Delta H^{\ddagger}$) -distal | $\Delta\Delta G^{\ddagger}$ ($\Delta\Delta H^{\ddagger}$) -dist–prox |
|---|---|---|---|---|
| 1 | B3LYP/6-31G(d) gas | 21.4 (7.9) | 22.7 (8.7) | 1.3 (0.8) |
| 2 | B3LYP/6-31G(d)-PCM | 21.3 (7.8) | 23.0 (9.0) | 1.7 (1.1) |
| 3 | M06/6-31G(d) gas | 15.1 (1.3) | 15.3 (0.8) | 0.2 (–0.5) |
| 4 | M06/6-31G(d)-PCM(MeOH) | 15.3 (1.2) | 15.1 (1.1) | –0.2 (–0.1) |
| 5 | M06/6-311+G(d,p)-PCM// M06/6-31G(d)-PCM(MeOH) | 17.6 (3.5) | 17.6 (3.6) | 0.0 (0.1) |
| 6 | M06/6-311++G(2d,p)-PCM// M06/6-31G(d)-PCM(MeOH) | 18.2 (4.1) | 18.3 (4.3) | 0.1 (0.2) |

**Table 5:** Calculated activation barriers for the reaction of 2-nitrosopyridine and (*E*)-1,3-pentadiene

# Chapter 3. A Survey of other (non-Cu(I)) Transition Metal Complexes as HDA Catalysts by Templating with Transition States Analogs.

## 3.1 Introduction.

### 3.1.1 Zinc, Nickel, Palladium and Copper (II) as the catalysts for HDA reaction.

From the previous study it was determined that $(imine)_2Cu^+$ complexes do not provide highly regioselective catalysts for the nitrosopyridine HDA reaction. The low regio- selectivity is presumably due to the pseudo-tetrahedral structure of $(imine)Cu(L)^+$ complexes. According to the computational work, the ligand plane is perpendicular to the nitrosopyridine plane, which minimizes the steric and electronic interactions from the ligands to the nitrosopyridine. It was thought that pseudo-square planar ligand-metal complexes could give better control of regioselectivity due to larger steric and electronic interactions between the auxiliary imine ligand and the coordinated diene/dienophile in the transition state (**Figure 57**). Imine complexes of the metal ions $Cu^{2+}$, $Zn^{2+}$, $Ni^{2+}$ and $Pd^{2+}$ were chosen as new catalysts for the HDA reaction for several reasons. First of all, the above metal complexes are stronger Lewis acids compared to $Cu^+$ and some of them are known to catalyze HDA reactions.[161-166] Secondly, depending on the ligands, they have been well documented to have pseudo-square planar structures.[152-156] Last but not least, they are known to catalyze the formation of metal-imine complexes.[71,156,167-169] This characteristic is very important for the dynamic combinatorial assembly of the L-M complexes from amine and aldehyde building blocks.

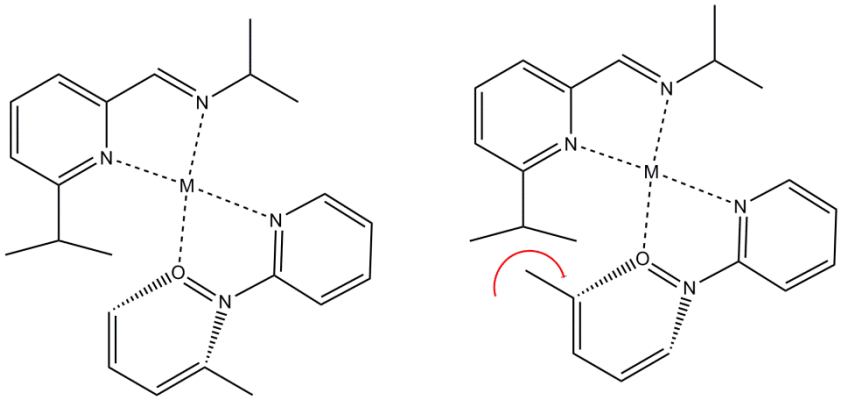

**Figure 57:** Proposed substrate complexes with square planar geometries. The distal configuration (left) is predicted to be more favorable than the proximal configuration (right) when a bulky aldehyde is used.

### 3.1.2 Ligand design.

The imine ligands were selected for several reasons. Our group has a long experience working with imine ligands and their metal complexes.[70-72,139] Compared to other ligand types, imine ligands are readily available and relatively easy to make from the corresponding amine or aldehyde building blocks. The imine linkage remains labile under the reaction and templating conditions,[170] providing the dynamic (equilibrating) feature for response to the transition state (or substrate) analog. The steric and/or electronic effects of the ligands can be controlled easily by modification of the aldehyde or the amine (**Figure 57**). With all of the advantages above, the combination of several 2-pyridinecarboxaldehyde derivatives and aliphatic as well as aromatic amines were used to test the catalytic activities of $Cu^{2+}$, $Zn^{2+}$, $Ni^{2+}$ and $Pd^{2+}$ for the HDA reactions.

## 3.2 Results and Discussion.

The literature precedent for the use of $Cu^{2+}$; $Zn^{2+}$; $Ni^{2+}$ and $Pd^{2+}$ with imine ligands as regioselective catalysts for the HDA reaction is very limited. In order to

investigate the regioselectivity of the potential catalysts, several tests were performed with complexes of each metal. First of all, each complex is tested to determine if it actually catalyzes the HDA reaction. Moreover, the catalytic rate must be more than 100 times faster than the uncatalyzed background reaction in order to override the selectivity of the background reaction. Since Lewis acids are known to catalyze the decomposition of nitroso compounds,[171] the catalyst must not only catalyze the HDA reaction, but not promote the nitroso compound's decomposition, to give a good isolated yields. Third, the metal catalyst must show exchange ability with the ligand building blocks and the products (**77** and **78**) in order to qualify for DCL experiments. This is an important point for the templating study. Last but not least, a wide range of ligand-based selectivity is desired to expand the correlation between the TSA binding and reaction selectivity.

### 3.2.1 Rates of the uncatalyzed and catalyzed reactions.

A UV-visible spectrum of nitrosopyridine (**75**) and 1,3-pentadiene (**76**) mixture shows that the 778 nm peak of nitrosopyridine is the best wavelength for monitoring the reaction in MeOH. The uncatalyzed (background) reaction was performed at very low concentration ($1 \times 10^{-4}$ M) at which point the reaction is slow enough for monitoring and the nitroso monomer – dimer equilibrium problem is minimized.[172] For the purpose of comparing the relative rates of the catalyzed, uncatalyzed and decomposition reactions, a simple rate measurement method was used in which the reactions are run under pseudo first order conditions with nitrosopyridine in the presence of a threefold excess of 1,3-pentadiene (76). The rate constant is calculated from the half life time, k =

$\frac{\ln(2)}{t_{1/2}}$ in which k is the rate constant of the reaction and $t_{1/2}$ is the half life (sec). With that method of rate measurement, the uncatalyzed reaction was determined to have a rate constant of 9.6 x $10^{-4}$ $s^{-1}$ (**Figure 58** and **3.3 experiments**), which is close to that of the similar substrate 4-nitroso-N-propyl-benzamine and 1,3 pentadiene, reported to be 7 x $10^{-5}$ $s^{-1}$.[134]

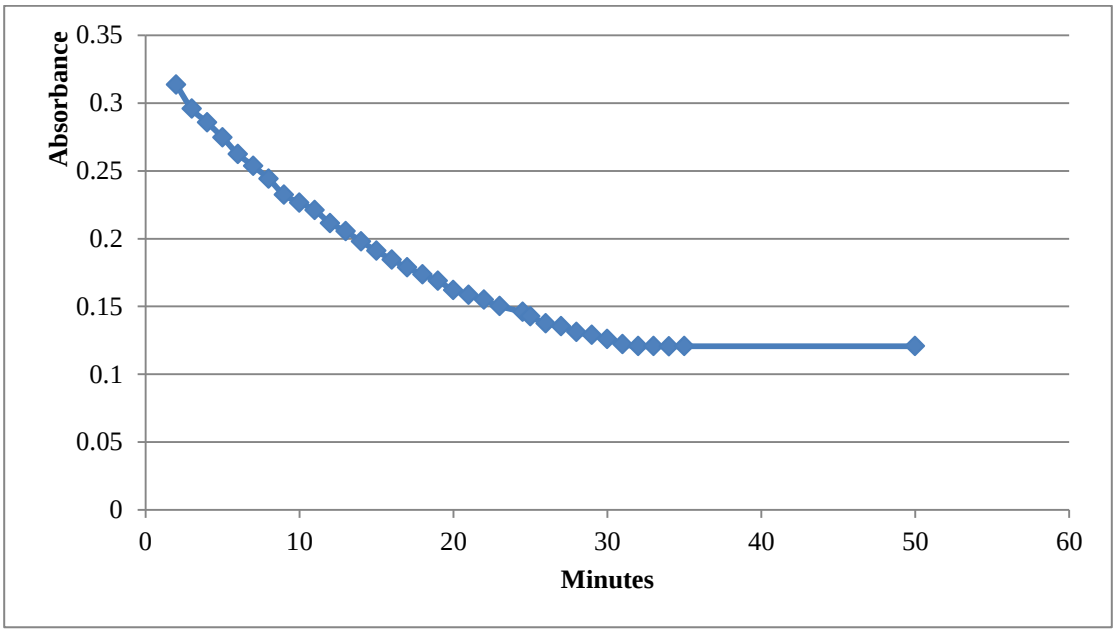


**Figure 58:** Absorbance vs. time plot of the uncatalyzed reaction between 2-nitrosopyridine (**75**) and 1,3-pentadiene (**76**).

With the same methodology, the rates of the HDA reaction between nitrosopyridine (**75**) and 1,3-pentadiene (**76**) in MeOH with $Cu^{2+}$ (copper(II) trifluoromethanesulfonate); $Zn^{2+}$ (zinc (II) trifluoromethanesulfonate); $Ni^{2+}$ (nickel (II) trifluoromethanesulfonate ) and $Pd^{2+}$ ( palladium (II) acetate) as the new catalysts (1 mol % catalyst loading) were also measured (see **3.4.1.2 Figure 76**, **Figure 77**, **Figure 78** and **Figure 79**). The rate constant of the reactions at 1 mol % catalyst loading for $Cu^{2+}$, $Zn^{2+}$, $Ni^{2+}$ and $Pd^{2+}$ are 23.1 x $10^{-4}$ $s^{-1}$; 16.5 x $10^{-4}$ $s^{-1}$; 28.9 x $10^{-4}$ $s^{-1}$ and 7.7 x $10^{-}$

$^{4}s^{-1}$ respectively. Comparing the rate of the thermal background reaction and the rate of the metal catalyzed reactions, the decreasing order of catalytic activities are $Ni^{2+}$ > $Cu^{2+}$ > $Zn^{2+}$ > $Pd^{2+}$. At this point, it was estimated that with 10 mol % catalyst loading the reactions catalyzed by $Ni^{2+}$, $Cu^{2+}$ and $Zn^{2+}$ will override the thermal reaction, while the reaction promoted by $Pd^{2+}$ would require 20 mol % loading.

One of the reasons that the catalyzed HDA reaction between nitrosopyridine (**75**) and 1,3-pentadiene (**76**) can give low isolated yields is that the Lewis acid catalysts not only catalyze the HDA reaction but also catalyze the decomposition of nitroso compounds into azoxypyridine (**110**).[94] An azoxy compound (**110**) was isolated when nitrosopyridine (**75**) was left in MeOH with $(MeCN)_4Cu^+$ for a few hours (see **3.4.3** and **Figure 59**).[173] The rates of the decomposition reaction with different catalysts were also measured to confirm that they are relatively slow compared to the HDA reaction and able to give good isolated yield of the adducts. The same method was used for the decomposition rate measurement (see **3.4.1.3** for more detail).

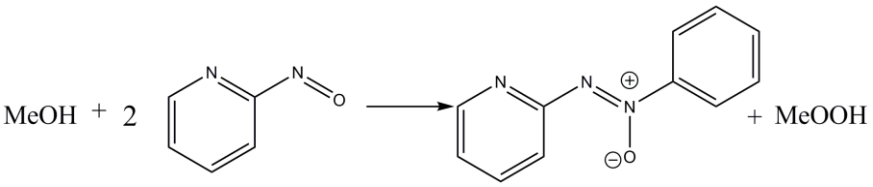


**75** **110**

**Figure 59:** Suggested formation of azoxypyridine.[173]

The decomposition rates (10 mol % catalyst) for $Cu^{2+}$, $Zn^{2+}$ and $Ni^{2+}$ are 3.85 x $10^{-5}$ $s^{-1}$, 5.8 x$10^{-5}$ $s^{-1}$, 2.6 x $10^{-4}$ $s^{-1}$ respectively. There is no significant change in the absorbance of the nitroso solution after $Pd^{2+}$ was added (see **3.4.1.3, Figure 80**, **Figure 81**, **Figure 82** and **Figure 83** for more detail). When comparing the decomposition rates

to the rate of the metal catalyzed HDA reactions, the decomposition rates are relatively small with $Cu^{2+}$and $Zn^{2+}$. A high isolated yield of the DA adduct is expected when $Cu^{2+}$ and $Zn^{2+}$ are used as the catalysts. The rates of both the HDA and decomposition reactions catalyzed by $Ni^{2+}$ are the fastest. However when comparing the relative rates, the HDA rate is still more than 10 times faster than the decomposition rate. If $Ni^{2+}$ is used as the catalyst for the HDA reaction, a lower isolated yield is expected compared to $Cu^{2+}$and $Zn^{2+}$. In all of the above experiments, the catalysts were metal salts instead of metal-imine complexes for the following reasons: First of all, we know with $Cu^{+}$ case, the $Cu^{+}$ catalyst is slower than any of the (imine)$Cu^{+}$ complexes; so we wanted to verify that the slowest catalyst was still be able to override the thermal reaction. Secondly, at this stage, no particular imine has been chosen because the formation of the metal-imine complex is undetermined. Last, but not least, is the availability of the catalysts.

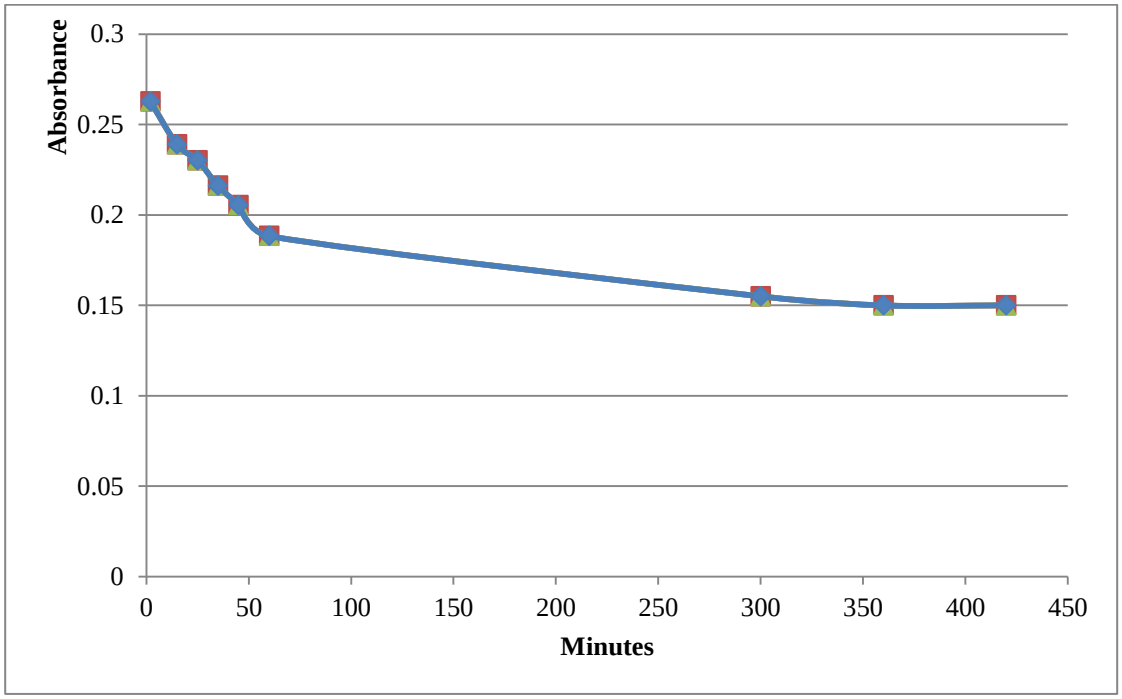


**Figure 60:** Kinetics of Ni(OTf )$_2$ catalyzed decomposition of nitrosopyridine in MeOH

### 3.2.2 Catalytic tests with (imine)M complexes.

Several metal-imine complexes were tested as catalysts for the HDA reaction between nitrosopyridine **75** and 1,3-pentadiene **76** in MeOH. A wide range of ligand based regioselectivity was sought in order to get a wider correlation between catalyst selectivity and TSA-binding selectivity.

According to the results from rate measurements (**3.2.1**), (imine)$Ni^{2+}$ was selected as the first candidate for regioselectivity testing (**Table 6**). The regioselectivity of the (imine)$Ni^{2+}$ catalyzed reaction was determined to be the same with either 1% or 10% catalyst loading (**Table 6** entry 1 and 2). The selectivity of the $Ni^{2+}$ catalyzed reactions was also different from that of the background reaction (53:47; distal 77/proximal 78). It is concluded that the $Ni^{2+}$ catalyzed reaction completely overrides the background reaction. This observation is strongly in agreement with the rate measurement experiment (**3.2.1**). However despite the electronic variations (amine **89**; **94**; **97** and aldehyde **104**; **105**; **106**) as well as the steric variations (amine **87**; **89**; **91**; **94** and aldehyde **104**; **108**), the regioselectivity range is very limited (distal 77/proximal 78 ranging from 37/63 to 40/60). We also observed no change in the regioselectivity when running the reaction in $CH_3CN$ or MeOH. A computational study was conducted to investigate the geometry of (imine)(**75**)$Ni^{2+}$ to account for the limited range of regioselectivity observed (see **3.2.4** experimental for more detail).

| Entry | Aldehyde | Amine | Distal 77: Proximal 78 ratio |
|---|---|---|---|
| 1 | - | - | 37:63 (37:63)[a] |
| 2 | **104** | **94** | 36:64 (36:64)[a] |
| 3 | | **89** | 40:60 |
| 4 | | **97** | 37:63 |
| 5 | **108** | **91** | 39:61 |
| 6 | | **87** | 37:63 |
| 7 | **105** | **94** | 37:63 |
| 8 | **106** | **94** | 37:63 |

**Table 6:** Adduct regioselectivity in 2-PyrNO/pentadiene reactions catalyzed by (Imine)$Ni^{2+}$ in MeOH with 10 mol % catalyst loading. [a]1 mol % catalyst loading

The next candidate, $Cu^{2+}$, was the second fastest catalyst on the list. Several interesting phenomena were observed when using $Cu^{2+}$ complexes as the catalysts for HDA reaction. First of all, the regioselectivity of the reaction is solvent dependent (**Table 7**). There is no selectivity when $Cu(OTf)_2$ were used as the catalyst in $CH_3CN$ as well as in MeOH (entry 1 and 4). However, the same set of ligand-Cu complexes in MeOH showed some regioselectivity (entry 2 and 3 versus entry 5 and 6). It is thought that $CH_3CN$ weakly coordinates with $Cu^{2+}$, but the concentration of ligands is very small ($10^{-3}$ M) compared to the solvent; the main catalyst in the reaction could be $(CH_3CN)_2Cu^{2+}$ instead of the (imine)$Cu^{2+}$ complexes. This complex, $(CH_3CN)_2Cu^{2+}$, may account for the low regioselectivity of the reactions. The linear $CH_3CN$-Cu is oriented away from the $Cu^{2+}$ and thus has minimal steric interactions with the nitroso moiety. Because of this phenomenon, all reactions with L-$Cu^{2+}$ catalysts were run in MeOH.

| Entry | Aldehyde | Amine | Solvent | Distal 77: Proximal 78 |
|---|---|---|---|---|
| 1 | - | - | MeOH | 50:50 |
| 2 | **107** | **90** | | 60:40 |
| 3 | **105** | **89** | | 50:50 |
| 4 | - | - | $CH_3CN$ | 50:50 |
| 5 | **107** | **90** | | 50:50 |
| 6 | **105** | **89** | | 50:50 |

**Table 7:** Solvent effect of the imine-$Cu^{2+}$ (10 mol% loading) catalyzed nitrosopyridine and pentadiene reactions.

| Entry | Aldehyde | Amine | Ligand/$Cu^{2+}$ ratio | Distal 77: Proximal 78 ratio |
|---|---|---|---|---|
| 1 | **108** | **90** | 0.5 | 70:30 |
| 2 | **108** | **90** | 1 | 74:26 |
| 3 | **108** | **90** | 1.5 | 70:30 |
| 4 | **108** | **90** | 2 | 67:33 |
| 5 | **108** | **90** | 4 | 50:50 |

**Table 8:** Ligand/$Cu^{2+}$ ratio effects on the regioselectivity of the reaction between nitrosopyridine and 1,3 pentadiene.

Unlike the other metals, the ratio of ligand to $Cu^{2+}$ also affects the regioselectivity of the HDA reaction (**Table 8**) It is suggested that the higher the ligand to $Cu^{2+}$ ratio, the more inactive $(diimine)_2Cu^{2+}$ is present in the reaction. Subsequently, the regioselectivity of the reaction with a less active $(imine)_2Cu^{2+}$ could be dominated by the uncatalyzed reaction. On the other hand, the absence of imine ligand (entry 1) could lead to more free $Cu^{2+}$, which is also is a non-selective catalyst. The best regioselectivity was achieved when a 1:1 ligand to $Cu^{2+}$ ratio is used.

Of all the catalyst candidates for the HDA reaction that we have tested, (imine)$Cu^{2+}$ complexes show the largest range of regioselectivity (**Table 9)**. Generally speaking, electronic variations of the aldehyde and amine ligand building blocks have a small effect on the regioselectivity of the catalysts (entries 1 to 10). Interestingly, ligands derived from sterically hindered aldehydes have a strong effect on the regioselectivity of the catalyst (**Table 9** entry 4 and 11-13). Two new aldehydes, **111** and **112** (**Figure 61**), were also used to test the regioselectivity of the new Cu(II) catalysts. The selectivity of the complex derived from aldehyde **112** was as good as that from aldehyde **108**, while the complex from aldehyde **111** showed average regioselectivity. The lower selectivity can be explained by the fact that the p-fluorobenzene moiety in aldehyde **111** is presumably rotatable which makes the imine complex derived from aldehyde **108** less hindered than expected. Nevertheless, the most regioselective catalysts are the ones with electron rich bulky aldehydes. From this set of experiments, it is concluded that the bulkier the aldehyde building block is, the more the distal product **77** is favored. This phenomenon agrees well with our original hypothesis (**Figure 57**). Computational modeling was employed to investigate the geometry of the (imine)Cu(PyrNO)$^{2+}$ complexes (See **3.2.4** for more detail).

| Entry | Aldehyde | Amine | Distal 77: Proximal 78 ratio |
|---|---|---|---|
| 1 | - | - | 50:50 |
| 2 | **98** | **87** | 50:50 |
| 3 | **104** | **89** | 47:53 |
| 4 | | **97** | 43:57 |
| 5 | **105** | **89** | 50:50 |
| 6 | **106** | **94** | 55:45 |
| 7 | | **97** | 52:48 |
| 8 | **107** | **89** | 58:42 |
| 9 | | **90** | 57:43 |
| 10 | | **91** | 60:40 |
| 11 | **108** | **89** | 74:26 |
| 12 | | **90** | 76:24 |
| 13 | | **91** | 76:24 |
| 14 | **111** | **91** | 56:44 |
| 15 | | **92** | 54:46 |
| 16 | **112** | **91** | 72:28 |
| 17 | | **92** | 63:37 |

**Table 9:** Adduct regioselectivity in PyrNO/pentadiene reactions catalyzed by (imine)$Cu^{2+}$ in MeOH with 10% catalyst loading.

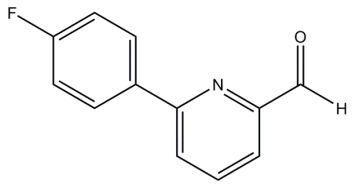


**111**

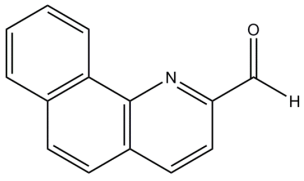


**112**

**Figure 61:** New bulky aldehydes

From the **Table 9** experiments, it was observed that amine variation (steric and electronic) had rather little effect on the regioselectivity of the catalysts. A set of experiments was designed to test whether (aldehyde)$Cu^{2+}$ or (imine) $Cu^{2+}$ are the active catalysts in the above reactions (**Table 10**). A mixture of 1:1 ratio of selected aldehyde and $Cu^{2+}$ was left overnight and used in situ as (aldehyde)$Cu^{2+}$ catalyst (10 mol %). Interestingly, the (aldehyde)$Cu^{2+}$ complexes are active catalysts. Despite the electronic variation (Entry 1 to 3), however, there was no change in the regioselectivity using these catalysts. When the bulkier aldehydes were used (entries 4 and 5), more of product **77** was produced. It was also observed that the (aldehyde)$Cu^{2+}$ complexes are less selective than the corresponding (imine)$Cu^{2+}$ complexes. At this point it is safe to conclude that the (imine)$Cu^{2+}$ complexes are the actual catalysts for these HDA reactions. See experimental section for more detail.

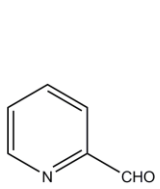


**104**

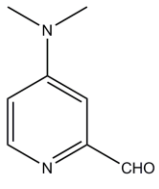


**105**

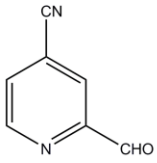


**106**

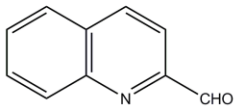


**107**

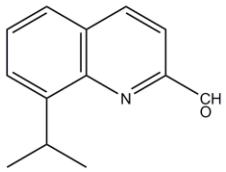


**108**

| **Entry** | **Aldehyde** | *Distal* **77** : *Proximal* **78** ratio |
|---|---|---|
| 1 | **104** | 50:50 |
| 2 | **105** | 50:50 |
| 3 | **106** | 48:52 |
| 4 | **107** | 54:46 |
| 5 | **108** | 66:44 |

**Table 10:** Regioselectivity of (aldehyde)$Cu^{2+}$ catalysts for the HDA reaction.

Of the four tested metal catalysts, $Zn^{2+}$-complexes were slower catalysts when compared to $Ni^{2+}$ and $Cu^{2+}$, but are still able to override the background reaction at 10 mol% loading, according to the estimation. Several experiments were run to test the catalytic activity of (imine)$Zn^{2+}$ complexes (**Table 11**). In terms of the selectivity, there was no significant change when using 1 or 10 mol % catalyst (entry 1 and 2). The product selectivity is also different than that of the thermal reaction (45:55). With this result, it is safe to assume the thermal background reaction has minimal contribution to the $Zn^{2+}$ catalyzed reaction. Despite electronic and steric variation, the regioselectivity of the all the catalysts tested was about the same (entries 2 to 6). On the other hand, $Zn^{2+}$ can adopt an octahedral geometry with 4 and 5 coordination.[70-72] Thus, a new amine **113** was synthesized in order to make new (diimine)$Zn^{2+}$ catalysts **114** (**Figure 62**). Interestingly, the new catalyst **114** did not show any difference compared to the other tested catalysts (entry 7). In all of the cases, (diimine)$Zn^{2+}$ catalysts were prepared by mixing the corresponding amines and aldehydes with $Zn^{2+}$ in a 1:1:1 ratio and left overnight. The catalysts were used in situ without further isolation or purification. One of the possibilities is that the actual catalyst in all of tested cases is the same $Zn^{2+}$ which is either (solvent)$Zn^{2+}$ or $(OTf)_2Zn$.

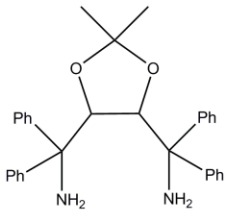


**113**

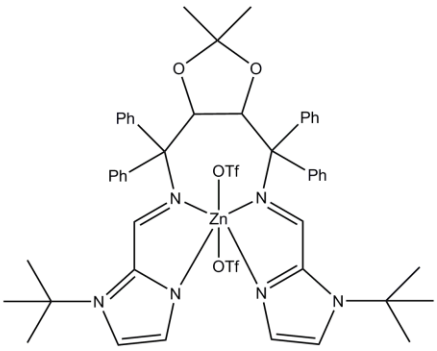


**114**

**Figure 62:** New amines and (imine)$_2Zn^{2+}$ complexes.

| Entry | Aldehyde | Amine | Distal 77: Proximal 78 ratio |
|---|---|---|---|
| 1 | - | - | 36:64 (37:63)[a] |
| 2 | **104** | **94** | 35:65 (38:62)[a] |
| 3 | **105** | **89** | 36:64 |
| 4 | **106** | **89** | 35:65 |
| 5 | **108** | **89** | 34:66 |
| 6 | **108** | **91** | 33:67 |
| 7 | **100** | **113** | 35:65 |

**Table 11:** Regioselectivity in the PyrNO/pentadiene reaction catalyzed by (Imine)$Zn^{2+}$. [a] reaction at 1 mol % catalyst loading.

Of all of the metal ion salts that were tested in **3.2.1**, palladium(II) was the slowest catalyst. However, due to the slow rate of the decomposition, and potentially higher product yields, it was worthwhile to run several experiments with (imine)$Pd^{2+}$ to test the catalytic activity and regioselectivity. If $Pd^{2+}$ complexes would show a good range of regioselectivity, then the slowness disadvantage could be overcome by using higher catalyst loading (e.g. 20 mol %) (**Table 12**). An interesting feature of the $Pd^{2+}$ catalyzed reactions is that the regioselectivity is $Pd^{2+}$ salt dependent. With $Pd(OAc)_2$, the distal 77: proximal 78 product ratio was 37:63 (**Table 12** entries 1 to 3). With ($(MeCN)_2Pd(O_3SC_6H_4CH_3)_2$), no regioselectivity was observed (**Table 12** entries 4 to 7). Despite the imine ligand variations, there was no selectivity variation with either $Pd^{2+}$ salt precursor. One interpretation is that the acetate counter ions strongly coordinate with $Pd^{2+}$, preventing imine coordination. The same argument was made about how the *p*-toluenesulfonate still coordinates stronger than imine ligands. At this point no further catalytic tests for (imine)$Pd^{2+}$ were made. To test the formation of

Imine-$Pd^{2+}$ complexes, a mixture of $(MeCN)_2Pd(O_3SC_6H_4CH_3)_2$, aldehyde **104** and amine **87** were mixed and left for 24 hours before being analyzed by ESI-MS. The peak at 423, which was assignable to the complex (**104**-**87**)$Pd(O_3SC_6H_4CH_3)$, was found at low insensitive. See experimental section for more detail.

| Entry | Palladium salt | Aldehyde | Amine | *Distal* **77**: *Proximal* **78** ratio |
|---|---|---|---|---|
| 1 | $Pd(OAc)_2$ | **104** | **87** | 37:63 |
| 2 | | | **97** | 37:63 |
| 3 | | **108** | **87** | 36:64 |
| 4 | $(MeCN)_2Pd(O_3SC_6$ $H_4CH_3)_2$ | **104** | **87** | 50:50 |
| 5 | | | **89** | 50:50 |
| 6 | | 108 | **87** | 50:50 |
| 7 | | | **89** | 50:50 |

**Table 12:** (Imine)$Pd^{2+}$ catalysts for the HDA reaction.

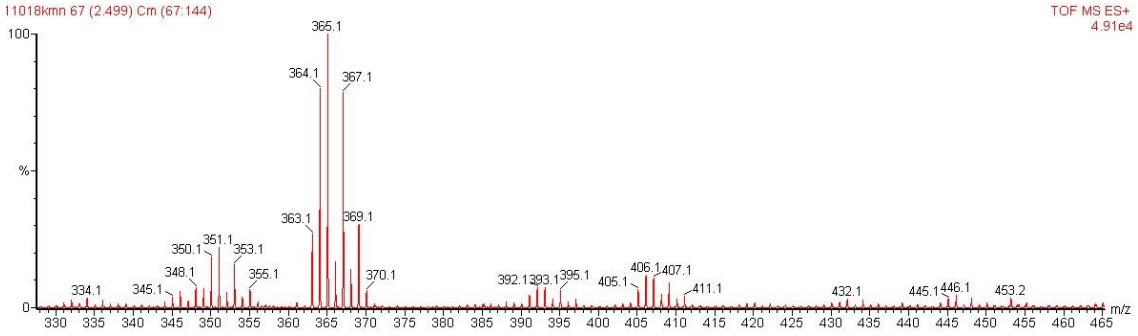


**Figure 63:** Library of $(MeCN)_2Pd(O_3SC_6H_4CH_3)_2$ + **104** + **87**.

### 3.2.3. Templating with substrate and TSA.

In order to probe the potential of using imine-metal complexes in substrate and TSA- templating experiments, we assessed: 1) the formation of metal-imine complexes

for each metal; 2) the lability of the newly formed imine-metal complexes; and 3) the formation of the binary complex with early TSA (substrate) and late TSAs (products). The ligand exchange ability is essential for the templating experiments. It is proposed that the instability of the imine-M-**75** (catalyst substrate complex) could indicate the rate of the catalyzed reaction. Meanwhile, the ratio of imine-M-(**77**)$^{2+}$/imine-M-(**78**)$^{2+}$ at equilibrium could have correlation with the regioselectivity of the catalysts.

### 3.2.3.1 Ligand Exchange ability of metal-imine complexes.

From the **3.2.2** results, only $Ni^{2+}$ and $Cu^{2+}$ were studied in the binding experiments because $Ni^{2+}$ is the fastest catalyst while imine-$Cu^{2+}$ complexes have the widest selectivity range.

The exchange ability between imine ligands is the most important criterion for building dynamic combinatorial libraries for the templating, thus it was tested first. From previous experience with imine ligands, the aliphatic amines are more favorable to form imine-metal complexes than the aromatic amines. Presumably the aliphatic amines are more electron rich, i.e. basic, relative to aromatic amines, thus they binding stronger with electron deficient $Zn^{2+}$. Aniline (**94**) and 2-pyridinecarboxaldehyde (**104**) were chosen to make [(**94**-**104**)$_2$Ni(OTf)]$^+$ complex. The complex can be detected by ESI-MS (m/z = 571). After adding one equivalent of methylcyclohexylamine (**90**) to the mixture and waiting for 24 hours, the new [(**90**-**104**)$_2$Ni(OTf)]$^+$ complex (m/z = 611) was observed, while the peak at 571 completely disappeared (**Figure 64**). The appearance of the new peak at 661 indicates that $Ni^{2+}$ promotes the imine exchange.

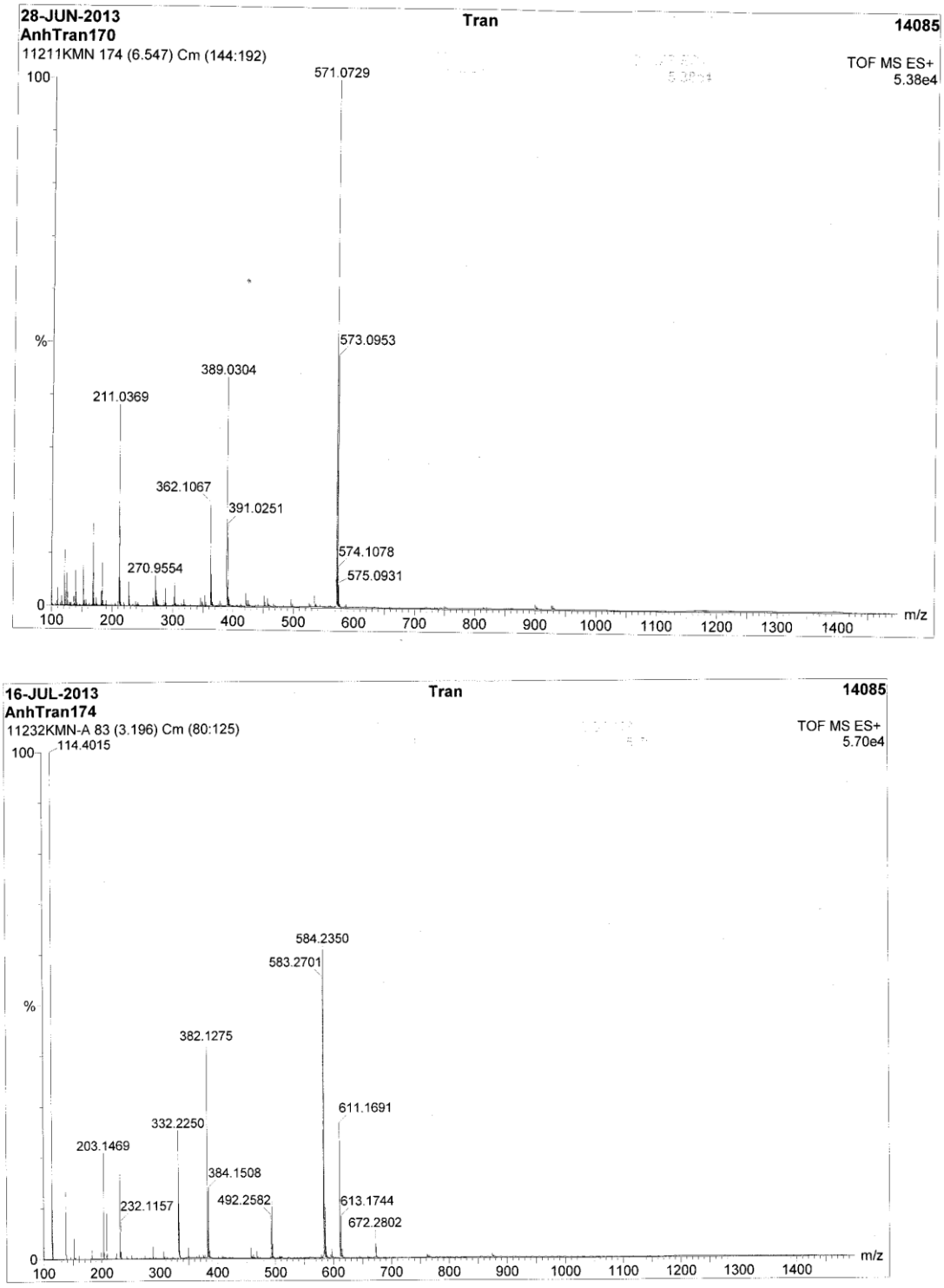


**Figure 64:** Exchange ability of (imine)$Ni^{2+}$ with aliphatic amine (**90**)

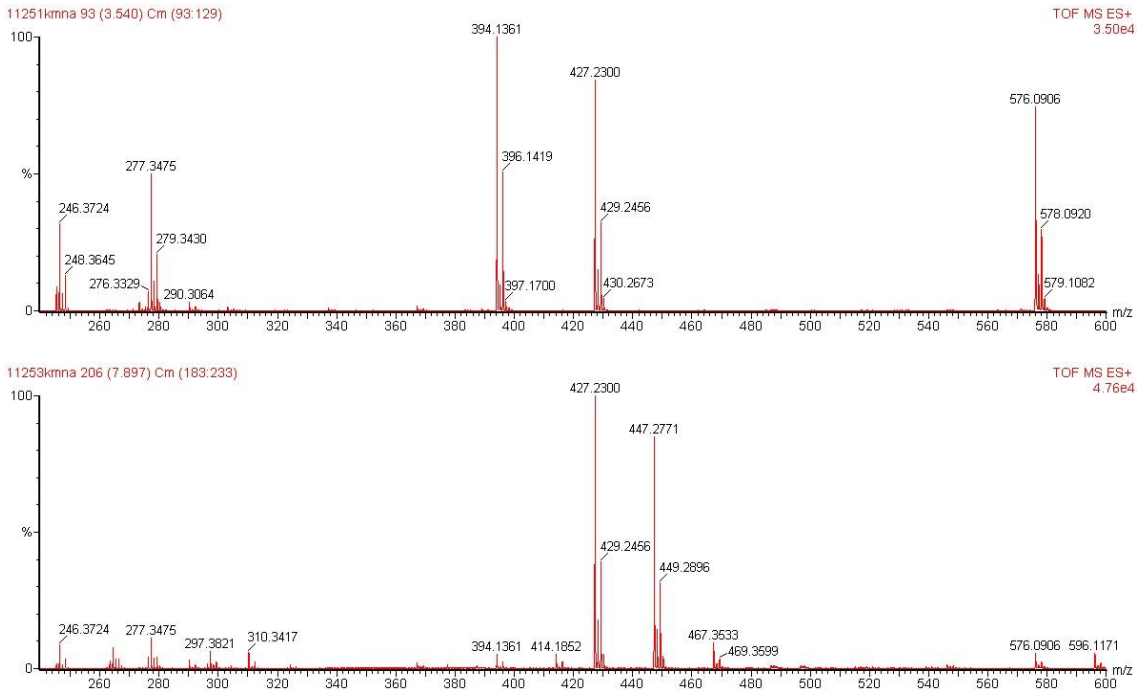


**Figure 65:** Imine exchange ability of $Cu^{2+}$. Top: $Cu^{2+}$ + **94** + **104.** Bottom: added **90** to the mixture of $Cu^{2+}$ + **94** + **104**

The same experiment was performed with $Cu^{2+}$. At first, several imine-$Cu^{2+}$ complexes were prepared by adding $Cu(OTf)_2$ with amine **94** and aldehyde **104** in a 1:1:1 ratio. Several important (imine)$Cu^{2+}$ were detected using ESI-MS such as (**94**-**104**)$Cu^{+}$, (**94**-**104**)(MeOH)$Cu^{+}$, (**94**-**104**)$_2Cu^{+}$, (**94**-**104**)$_2$(OTf)$Cu^{+}$ with m/z = 246, 277, 427 and 576 respectively. After adding amine **90** and the mixture stood at room temperature for 36 hours, the library was checked again and new peaks assignable to (**90**-**104**)$Cu^{+}$, (**90**-**104**)(MeOH)$Cu^{+}$, (**90**-**104**)(**94**-**104**)$Cu^{+}$, (**90**-**104**)$_2Cu^{+}$ and (**90**-**104**)$_2$(OTf)$Cu^{+}$ were detected with m/z = 264, 297, 447 and 467 respectively. However, unlike the imine-$Ni^{2+}$ complexes, the new aliphatic amine (**90**) does not completely displace the aromatic amine (**94**). Both aliphatic, aromatic imines and even a hybrid (**90**-**104**)(**94**-**104**)$Cu^{+}$ complex (m/z= 447) were observed**.** This test showed that $Cu^{2+}$ is

able to promote the imine exchange. At the same time, both aliphatic and aromatic amines can competitively form (imine)$Cu^{2+}$ complexes (**Figure 65).**

### 3.2.3.2 Templating with substrates as "early" TSAs

It is thought that the activation energy and the rate of a reaction can depend on the instability of the catalyst-substrate complexes. This hypothesis has been demonstrated with Pd-allyl complexes in which the more unstable the catalyst-substrate, the lower the activation energy, the faster the reaction.[174] To test this idea with the HDA reaction, nitrosopyridine (**75**) was added to a binary imine-metal complex while monitoring the formation of imine-metal-substrate complex by ESI-MS. Aniline (**94**) and 2-pyridinecarboxaldehyde (**104**) were chosen as imine building blocks with $Cu^{2+}$ as the metal ion. The mixture was analyzed by ESI-MS (**Figure 66**). Several important peaks that contain 2-nitrosopyridine (**75**) were detected, including **(94-104)Cu**(**75**)$(MeOH)^{2+}$ (m/z = 385) and $(\mathbf{75})_2Cu^{2+}$ (m/z =278). However, peaks containing side products were also detected such as $(\mathbf{110})_2Cu^{2+}$ (M+1 = 466) and (**110**)$Cu^{2+}$ (M+1 = 264). This result once again confirmed that (imine)$Cu^{2+}$ coordinates with nitrosopyridine (**75**).

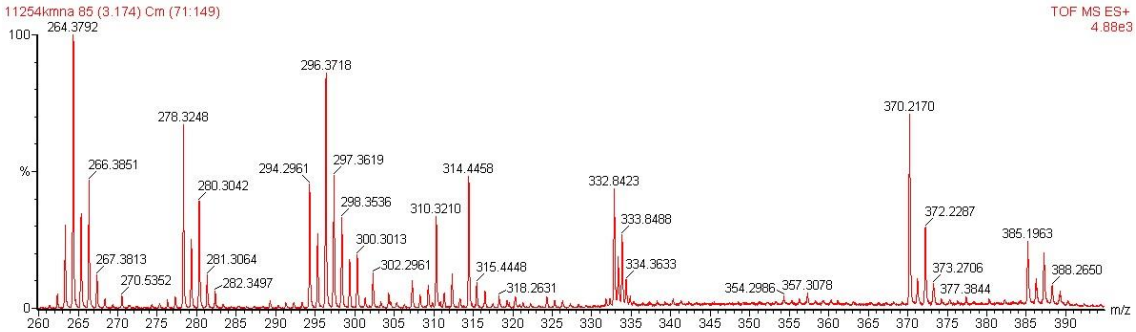


**Figure 66:** (**94-104**)$Cu^{2+}$ with "early" TSA library.

With the same methodology, a mixture of $Ni(OTf)_2$ with nitrosopyridine **75** was made. Due to the potential of decomposition of nitrosopyridine **75** with $Ni^{2+}$, the mixture was analyzed immediately after mixing. There were some peaks that contain nitrosopyridine (**75**) with $Ni^{2+}$ such as $(OTf)(\mathbf{75})_3(MeOH)_2Ni^{2+}$, $(OTf)(\mathbf{75})_3(MeOH)_4Ni^{2+}$ and $(OTf)(\mathbf{75})_3(MeOH)_5Ni^{2+}$ with m/z = 595, 627, 659 and 691 respectively. However, the strong $Ni^{2+}$-containing peaks detected were combinations with side product **110** with methanol units and triflate $(OTf)^-$ such as $(OTf)(MeOH)Ni^+$, $(\mathbf{110})(OTf)Ni^+$ and $(\mathbf{110})(OTf)(MeOH)Ni^+$ with m/z = 271, 407 and 439 respectively (**Figure 67**). The results of templating with the substrate agree with the section **3.2.1** experiments that the metals ions also decompose nitrosopyridine (**75**) to side product (**110**).

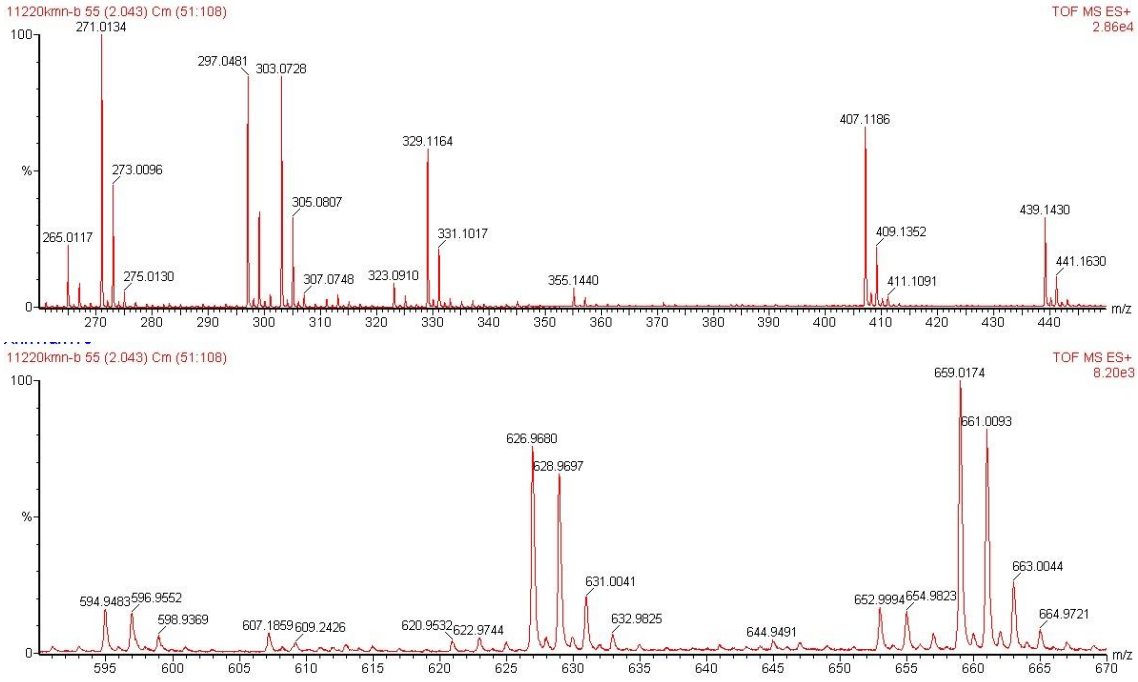


**Figure 67:** ESI-MS of $Ni(OTf)_2$ with nitrosopyridine 75. M/z from 260 to 450 (top) and 590 to 670 (bottom)

In both of the cases, attempts to quantify nitrosopyridine-metal complexes were not viable. The ion intensity of the nitrosopyridine containing peaks decreased significantly between two consecutive injections (about 10 minutes). At the same time, the ion intensity of the azoxypyridine-metal complexes increased. After 2 to 4 hours, the mixtures reached equilibrium. However, at this point no significant nitrosopyridine-metal peaks were detected.

### 3.2.3.3 Templating with products as "late" TSAs

Since the (imine)$Cu^{2+}$ complexes tested had the widest range of regioselectivity, $Cu^{2+}$ was chosen for templating with "late" TSAs of the tested catalysts (**Table 6** to **Table 12**). The same methodology was used as in **2.2.2** to generate the libraries of $Cu^{2+}$ with imines, $Cu^{2+}$ and 77 or 78 as "late" TSAs. The selectivity of the (imine)$Cu^{2+}$ catalysts mainly depended on the aldehyde component of the ligand (**Table 9**) and the most selective catalysts were the ones derived from aldehydes **108** and **112**. Therefore, aldehydes **108** and/or **112** were included in the library with imines derived from other less selective aldehydes such as **105**, **106** and **107**. Although not as important as the aldehyde ligand component in affecting the regioselectivity of the catalysts, aliphatic amines **87**, **89**, **90** and **91** were used due to their tendency to form more stable imine-$Cu^{2+}$-TSA complexes than the aromatic amines. Two identical solutions of $Cu^{2+}$, aldehydes (**105**, **107** and **108**) and amines (**89** and **90**) were mixed. Either compound **77** or **78** as the "late" TSA was added to each solution to generate two different sets of complexes, including (imine)(**77**)$Cu^{2+}$ and (imine)(**78**)$Cu^{2+}$. A total of 6 (imine)(TSA)$Cu^{2+}$ complexes were expected in each library. However, only (**107**-

**89**)(TSA)$Cu^{2+}$ and (**107**-**90**)(TSA)$Cu^{2+}$ complexes were detected with m/z = 477 and 491 respectively. There are differences in the binding selectivity between **77** or **78**. In particular the ion count ratio of (**107**-**89**)(**77**)$Cu^{2+}$/(**107**-**89**)(**78**)$Cu^{2+}$ and (**107**-**90**)(**77**)$Cu^{2+}$/(**107**-**90**)(**78**)$Cu^{2+}$ were 0.60. This result means that there is a difference in the binding affinity of (**107**-**89**) and (**107**-**90**) with either "late" TSA **77** or **78**. Meanwhile the internal standard ion count (tetrabutyl ammonium; m/z = 242) ratio between the same library is 0.9578. Interestingly, there is no significant peak of (imine)(TSA)$Cu^{2+}$ complexes which have aldehydes **105** or **108**. It is thought that the bulky isopropyl moiety in the aldehyde **108** prevents the formation of (**108**-imine)(TSA)$Cu^{2+}$. However it is unclear why the (imine)$Cu^{2+}$ complexes derived from more basic heterocyclic aldehyde **105** were not detected (**Figure 68**).

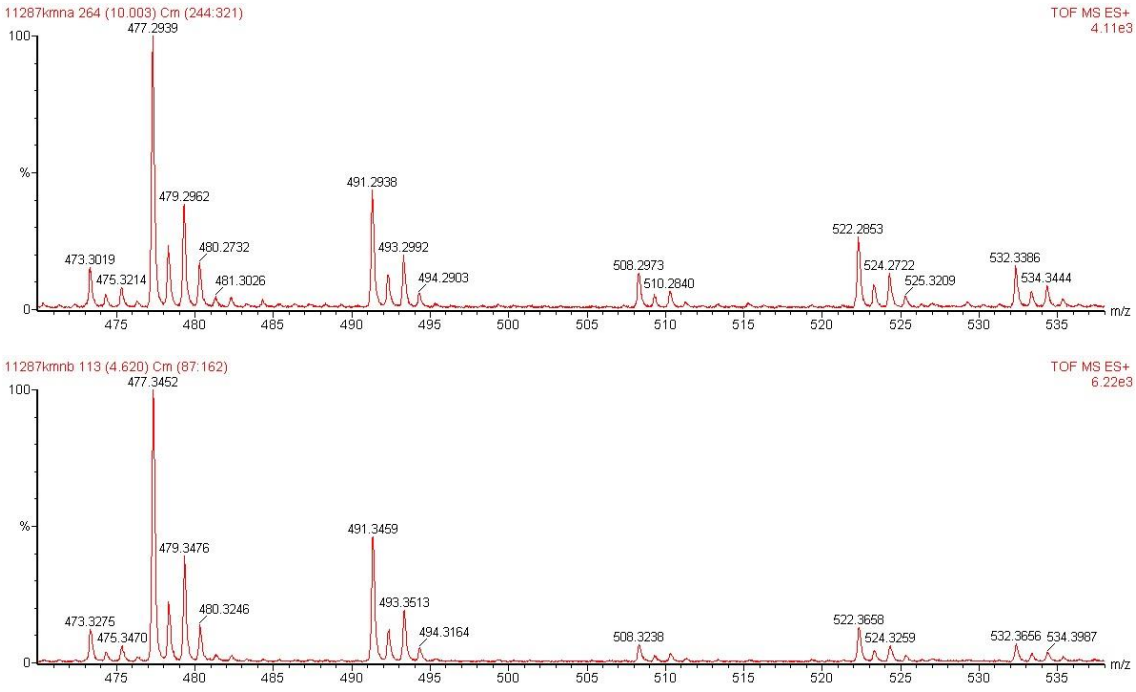


**Figure 68:** ESI-Mass spectra of (top) **77**+ **105** + **107** + **108** + **89** + **90** + $Cu(OTf)_2$ (bottom) **78** + **105** + **107** + **108** + **89** + **90** + $Cu(OTf)_2$

Another version of above the libraries was constructed with the elimination of aldehyde **105** while amine **91** was also added. This change makes the library less complicated while still maintaining a good number of potential complexes. Inclusion of amine **91** would theoretically produce up to 6 (imine)(TSA)$Cu^{2+}$ complexes in the library. However, similar to the previous libraries set, only 3 out of 6 (imine)(TSA)$Cu^{2+}$ complexes were observed and all of them were from the aldehyde 107: (**107**-89)(TSA)$Cu^{2+}$, (**107**-**90**)(TSA)$Cu^{2+}$ and (**107**-**91**)(TSA)$Cu^{2+}$ with m/z = 477, 491 and 543. There are also differences in the binding selectivity between **77** and **78**. In particular the ion count ratio of (**107**-**89**)(**77**)$Cu^{2+}$/(**107**-**89**)(**78**)$Cu^{2+}$, (**107**-**90**)(**77**)$Cu^{2+}$/(**107**-**90**)(**78**)$Cu^{2+}$, (**107**-**91**)(**77**)$Cu^{2+}$/(**107**-**91**)(**78**)$Cu^{2+}$ was 1.25, 1.06 and 1.03 respectively (**Figure 69**). However, the plot of binding selectivity vs catalyst regioselectivity with (**107**-**89**)$Cu^{2+}$, (**107**-**90**) $Cu^{2+}$ and (**107**-**91**)$Cu^{2+}$ showed little information about the correlation (**Figure 70)**. The main reason is that the regioselectivity range of these catalysts is small (58:42 to 60:40).

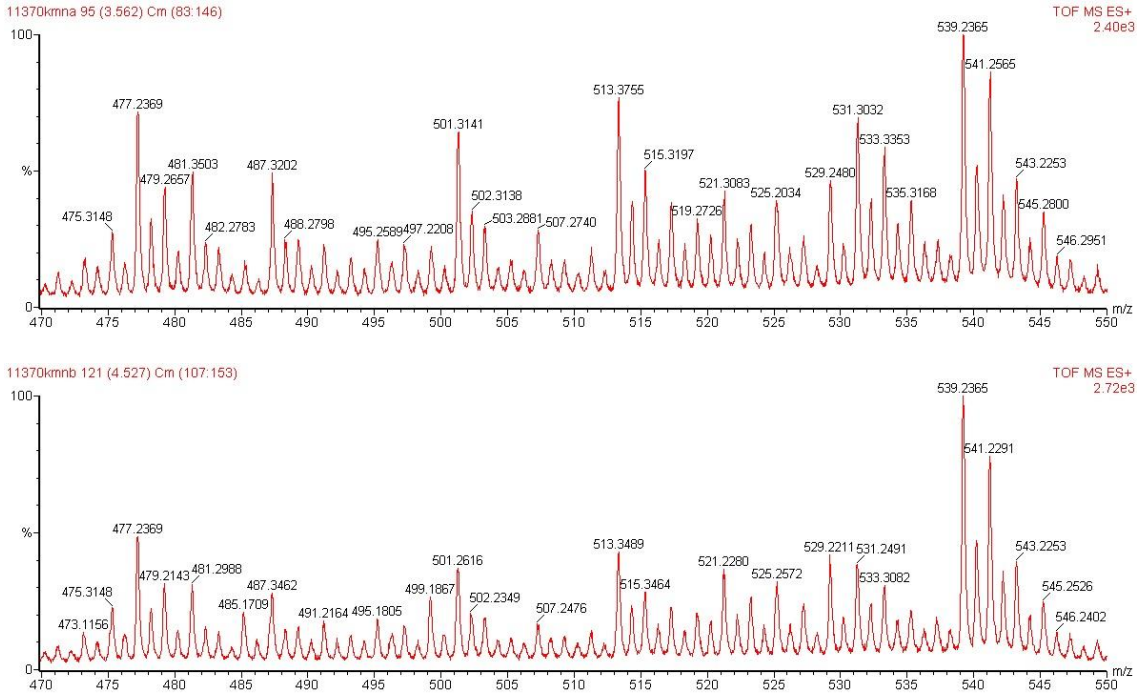


**Figure 69:** ESI-Mass spectra of (a) **77** + **107** + **108** + **89** + **90** + **91** + $Cu(OTf)_2$ (b) **78** + **107** + **108** + **89** + **90** + **91** + $Cu(OTf)_2$.

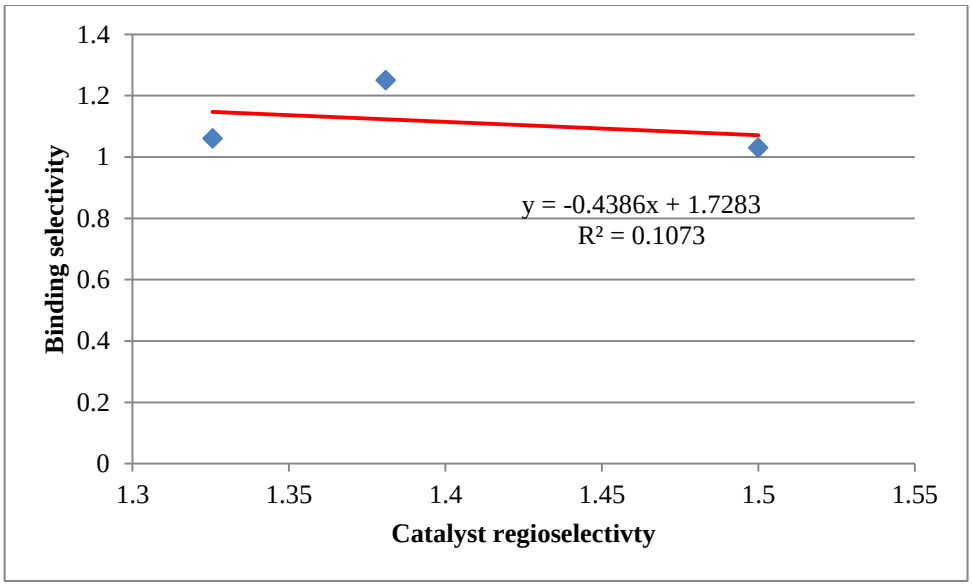


**Figure 70:** Binding selectivity vs catalyst regioselectivity of **(107-89)**$Cu^{2+}$**, (107-90)** $Cu^{2+}$ **and (107-91)**$Cu^{2+}$.

In both tested library series, the most dominant $Cu^{2+}$ complex peaks are the $(imine)_2Cu^{2+}$ complexes. It is thought that the electron deficient imines would disfavor the $(imine)_2Cu^{2+}$ complexes and thus increase formation of $(imine)(TSA)Cu^{2+}$ complexes. A large library of electron deficient imines was constructed to test this idea. Aldehydes **106**, **107** and **108** were used in combination with amines **96**, **97** and a new amine, 4-bromoaniline (**115**), to form up to 9 possible $(imine)(TSA)Cu^{2+}$ complexes. For the initial binding test, a mixture of **77** and **78** was used as a late-TSA. Overall, the ion counts for copper containing peaks are much less compared to those of the electron rich libraries. There were no $(imine)(TSA)Cu^{2+}$ and only a few $(imine)_2Cu^{2+}$ complexes detected, but the ion intensities were also small. The electron deficient imines disfavor the $(imine)_2Cu^{2+}$ complexes but also disfavor the $(imine)(TSA)Cu^{2+}$ complexes. The library needs a high concentration of $(imine)_2Cu^{2+}$ complexes in order to form the $(imine)(TSA)Cu^{2+}$ complexes.

In conclusion, the $(imine)(TSA)Cu^{2+}$ complexes form more readily when electron rich imines or less sterically bulky aldehydes are used in the library, while the more selective catalysts are ones that derive from sterically bulky aldehydes (**Table 9**). Because of these opposing trends, there was no amine-aldehyde combination found that readily formed $(imine)(TSA)Cu^{2+}$ and was highly selective.

### 3.2.4 Computational studies.

Because a single-crystal of catalyst could not be obtained, it was worthwhile to obtain structural information through modeling to better understand the origin of the catalyst selectivity. Imine complex **107**-**86** was chosen as a representative for the

calculation to save computational time. Following calculations on the similar system of pyrrolide-imine-$Ni^{2+}$, the computational modeling was set up using Gaussian 09 at the PBE/6-311G(d,p) level of theory.[175] In this particular calculation, all three possible geometries: tetrahedral (**116**), *trans*-square planar (**117**) and *cis*-square planar (**118**) of (**107**-**86**)(**75**)$Ni^{2+}$ were calculated. The *cis* and *trans* refer to the relative orientation of the pyridine moiety of the nitroso to the pyridine moiety of the aldehydes (**Figure 72**).

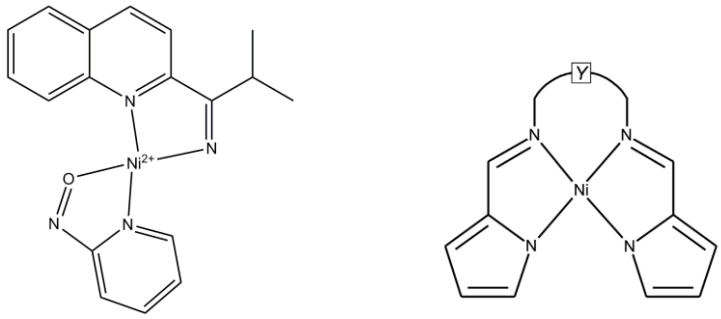


**Figure 71:** (**107**-**86**)$Ni^{2+}$ complex used in this study and previously calculated pyrrolide-imine-$Ni^{2+}$ complexes (Y = $CH_2C(CH_2)_3CH_2$ and $CH_2CH(OH)CH_2$).

Of all calculated ground states, it is no surprise that the tetrahedral (**116**) is the most stable geometry compared to *trans*-square planar (**117**) (3.6 Kcal) or *cis*-square planar (**118**) (11.0 Kcal). The dihedral angle between the aldehyde plane moiety and the nitrosopyridine moiety are 11.5º and 24.9º for the *trans*-square planar and *cis*-square planar respectively. Meanwhile the same angle in the tetrahedral structure is 90.74º. Presumably, the main difference in the free energies between all three possible structures comes from the distortion of the complex because they are all regioisomers. This modeling also agrees with the experimental results that the (imine)$Ni^{2+}$ complexes show low regioselectivity for the HDA reaction, in general, because the $Ni^{2+}$complexes have similar structures to the $Cu^{+}$ complexes in **Chapter 2.** Thus all of the ligand variations have small effects on the regioselectivity of the catalysts.

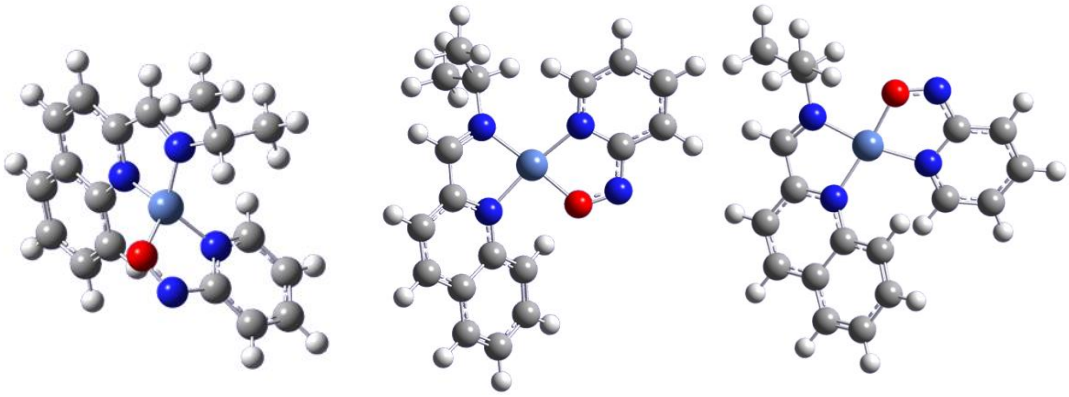

| tetrahedral **116** | *trans*-square planar **117** | *cis*-square planar **118** |
|---|---|---|
| ΔΔG = 0 kcal | ΔΔG = 3.6 kcal | ΔΔG = 11.0 kcal |

**Figure 72:** Three possible ground states of (**107**-**86**)(**75**)$Ni^{2+}$

The same set of building blocks with aldehyde **107** and amine **86** was also used in computational study with $Cu^{2+}$. The same setup using Gaussian 09 at the PBE/6-311G(d,p) level of theory was used for computational studies. Three possible geometries: tetrahedral **119**, *trans-square* planar **120** and *cis-square* planar **121** were setup for the study (**Figure 73**). It is thought that similar to the $Ni^{2+}$ case, the tetrahedral structure would be the most stable structure due to steric effects. However, the most stable calculated structure is the *trans-square* planar **120**. The angle between the pyridine moiety of substrate **75** and the quinoline moiety of the ligand **107** are: 21.11º; 30.65º and 15.67º with tetrahedral **119**; *trans-square* planar **120** and *cis-square* planar **121**, respectively. Interestingly, tetrahedral **119** looks more like a pseudo-square planar. At this point, it is clear that the most stable structure for the (**107**-**86**)(**75**)**$Cu^{2+}$** complex is the pseudo-square planar devivative. However, it is not clear whether the *cis* or *trans*-square planar is more favorable. According to the experimental results **Table 9**, the more sterically hindered aldehydes produce the more regioselective catalysts while the

amine variations (steric and electronic) effects are minimal, thus it is thought that the nitroso moiety of **75** must be *cis* to the aldehyde moiety, in other words, the (imine)(substrate)$Cu^{2+}$ complexes likely adopt the *trans*-square planar structure.

In an attempt to further understand the system a bulkier aldehyde **108** and amine **86** were used make (**107**-**86**)(**75**)$\mathbf{Cu^{2+}}$ complexes (tetrahedral, *trans* and *cis*-square planar) for computational study. Unfortunately, the calculation method, PBE/6-311G(d,p), was not able to find the minimized ground states. One possibility is that the isopropyl moiety of the aldehyde is too bulky, thus the super computer was not able to succeed with the given resources limit (24 hour of continuous running).

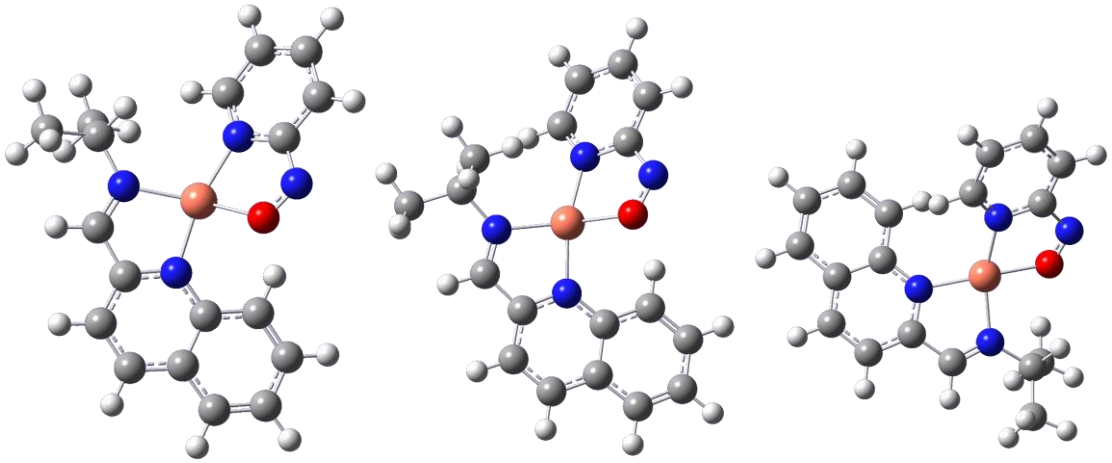

| tetrahedral **119** | *trans*-square planar **120** | *cis*-square planar **121** |
|---|---|---|
| ΔΔG = 0.64 kcal | ΔΔG = 0.0 kcal | ΔΔG = 0.14 kcal |

**Figure 73**: Three possible ground states of (107-86)(75)$Cu^{2+}$

### 3.3 Conclusions.

Four metal ion salts, $Pd^{2+}$, $Zn^{2+}$, $Ni^{2+}$ and $Cu^{2+}$, were tested as potential catalysts for the HDA reaction. All of them appear to catalyze the HDA reaction with different rates. In all tested cases, the decomposition reaction of the nitrosopyridine in the

presence of metal ion is relatively slow compared to the HDA reaction, thus the yields of HDA adducts are good.

Of the four metal ion candidates for the HDA reaction, palladium (II) is the slowest catalyst and the selectivity of the $Pd^{2+}$ catalysts depend on the Pd salts that were used. Both of the palladium (II) salts showed no change in the range of regioselectivity despite variation in the imine ligands.

While $Zn^{2+}$ catalyzes the HDA reaction with good rate, it is estimated that at the 10% catalytic loading, $Zn^{2+}$ overrides the background reaction. However, with all of the (imine)$Zn^{2+}$ that have been tested, the regioselectivity and the range of regioselectivity of the reactions is poor.

According to the rate measurement of all candidate catalysts, $Ni^{2+}$ salt appears to be the fastest catalyst. However, similar to $Zn^{2+}$, all of (imine)$Ni^{2+}$ catalysts have marginal regioselective range. Computational modeling reveals that the most stable and prevalent geometry of **(107-86)**(**75**)$Ni^{2+}$ is tetrahedral, as is the case for $Cu^{+}$; thus the range in regioselectivity is small.

Copper (II) complexes have the largest regioselectivity range. Some of the (imine)(TSA)$Cu^{2+}$ complexes have been detected. However, all of the (imine)$Cu^{2+}$ which were detected are low regioselectivity catalysts. With three cumulated data points, no confident correlation between selective binding and regioselectivity of the catalysts could be determined.

The binding of $Ni^{2+}$ and $Cu^{2+}$ with "early" TSA, nitrosopyridine (**75**), were investigated to evaluate the possibility of using the substrate as an early TSA, but the decomposition reaction prevented further study.

The computational modeling with (**107**-**86**)(**75**)$Ni^{2+}$ shows that $Ni^{2+}$ adopts tetrahedral structural. This could be the main reason why (imine)$Ni^{2+}$ complexes give low regioselectivity.

### 3.4 Future directions.

The computational studies and bench work results confirmed the idea that the square planar catalysts will improve the selectivity of the reaction. It is critical that the metal complexes keeping its square planar regardless of the change in the coordinated ligands. However, neither $Cu^{2+}$ nor $Ni^{2+}$ has this property. It has been known from the precedent literature that rhodium (I) and iridium (I) complexes were having square planar structures and also promote Diels-Alder reaction.[176,177] A quick computational study using hybrid basis set of LANL2DZ for transition metal and 6-31G for lighter elements showed that (**104**-**86**)Ir(nitrosopyridine)$^{+}$ adopted square planar with the dihedral angle between pyridine moiety plane and aldehyde moiety plane = 0.0º, a perfect square planar (**Figure 74**). Interestingly the startup tetrahedral structure of (**104**-**86**)Ir(nitrosopyridine)$^{+}$ also adopted pseudo-trans square planar with the dihedral angle between pyridine moiety plane and aldehyde moiety plane = 0.0º. The same calculation method was used for rhodium (I) with the same set of ligands also conducted. The result showed that the dihedral angle between pyridine moiety plane and aldehyde moiety plane are 0.0º and 38.7 º with square planar and tetrahedral, respectively. The energy, however, has a big difference between calculated structures. While the square planar (**104**-**86**)Ir(nitrosopyridine)$^{+}$ complex is more favorable than the tetrahedral by 9.0 kcal, the tetrahedral (**104**-**86**)Rh(nitrosopyridine)$^{+}$ complex is more stable than the square

planar by 16.1 kcal. From the computational studies, (**104**-**86**)Ir(nitrosopyridine)$^+$ is more likely adopted square planar structure than (**104**-**86**)Rh(nitrosopyridine)$^+$ thus a test of promoting imine exchange was performed with $Ir^+$. Aldehyde **98** and aniline **94** were added to Ir($SbF_6$) salt, which was prepared by a literature method, and left at room temperature for 24h.[176] The ESI-MS of the solution showed a peak at 477 which is assignable to (**98**-**94**)$_2$Ir$^+$. Upon adding aliphatic amine **90** to the solution and waiting for 3 hours, new peaks at 497 and 517 corresponding to (**98**-**94**)Ir((**98**-**90**)$^+$ and (**98**-**90**)Ir(**98**-**90**)$^+$ were detected. This experiment show that $Ir^+$ is able to promote the imine exchange and thus (imine)$Ir^+$ could be a good candidate for future study.

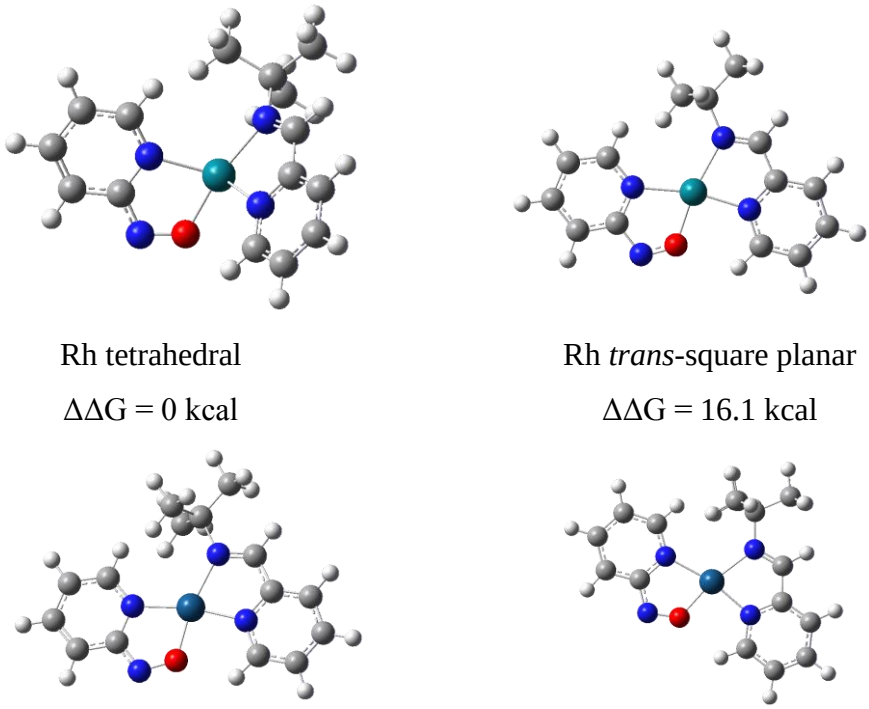

Rh tetrahedral
ΔΔG = 0 kcal

Rh *trans*-square planar
ΔΔG = 16.1 kcal

Ir tetrahedral
ΔΔG = 8.98 kcal

Ir *trans*-square planar
ΔΔG = 0.00 kcal

**Figure 74:** Computational studies with (**98**-**90**)Rh(nitrosopyridine)$^+$ (Top) and (**98**-**90**)Ir(nitrosopyridine)$^+$ (bottom).

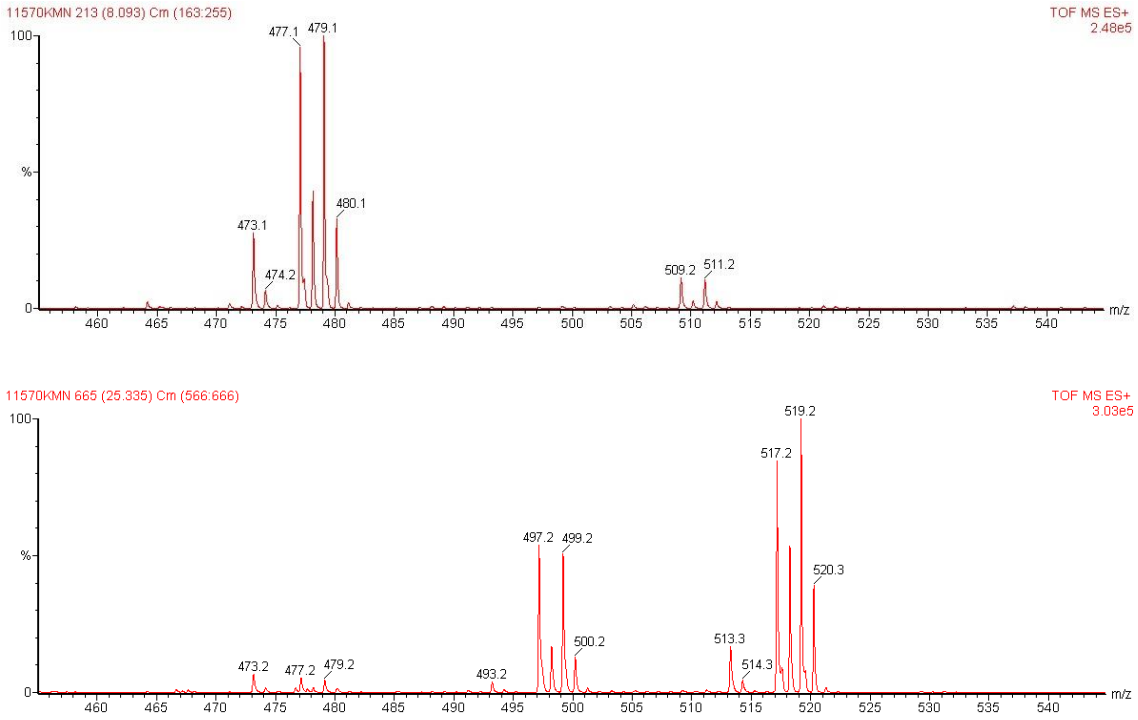


**Figure 75**: ESI-Mass spectra of (a) **98** + **94** + Ir and ESI-Mass spectra of (b) **98** + **94** + **90** + Ir.

### 3.5 Experimental

#### 3.5.1 Reaction rate measurement.

The rates of the HDA reactions were measured using a HP 8452A diode array spectrophotometer and 1 cm quartz cuvette. Solutions of nitrosopyridine (**75**), 1,3 pentadiene (**76**), copper(II) trifluoromethanesulfonate, nickel(II) trifluoromethanesulfonate, palladium (II) acetate, bis(acetonitrile)palladium(II) p-toluenesulfonate and zinc (II) trifluoromethanesulfonate in MeOH at 2 x $10^{-1}$ M were prepared by dissolution of 2 x $10^{-4}$ mol (21.6 mg; 10.6 mg; 72.2 mg; 71.2 mg; 44.9 mg; 160.2 mg and 72.6 mg respectively) of each compound with 10 mL of MeOH. Each of

the above solutions was diluted 100 times by adding 99 mL of MeOH to 1 mL of each solution to make 100 mL stock solutions at $2x10^{-4}$ M.

### 3.5.1.1 Rate constant of thermal background reaction.

For the purpose of comparing relative rates, all of the reactions were treated as first order with substrate. A solution of **75** (1 mL at $2x10^{-4}$M) was added into the cuvette followed by the addition of **76** (1 mL at $6x10^{-4}$M) to make 2 mL of solution. The reactions were monitored by recording the disappearance of the peak at 778 nm over time. The rate constant of the reaction was calculated by the half-life equation: $k = \frac{ln2}{t1/2} = = \frac{0.693}{t1/2}$ in which k is the rate constant and $t_{1/2}$ is the half-life time (sec.) (**Figure 58**).

### 3.5.1.2 Rate constants of metal catalyzed HDA reactions.

With a similar methodology, the rate constants of the metal catalyzed HDA reactions were determined. A solution of **75** (1mL at $2x10^{-4}$ M) was added into the cuvette followed by the addition of respectively catalyst (10µL at $2x10^{-4}$M) and **76** (1mL at $6x10^{-4}$M) to make 2ml with 1% catalyst loading reactions. The kinetics of $Ni^{2+}$, $Cu^{2+}$, $Zn^{2+}$ and $Pd^{2+}$ catalyzed the HDA reactions between nitrosopyridine and 1,3 pentadiene are plotted in the **Figure 76**, **Figure 77**, **Figure 78** and **Figure 79** respectively.

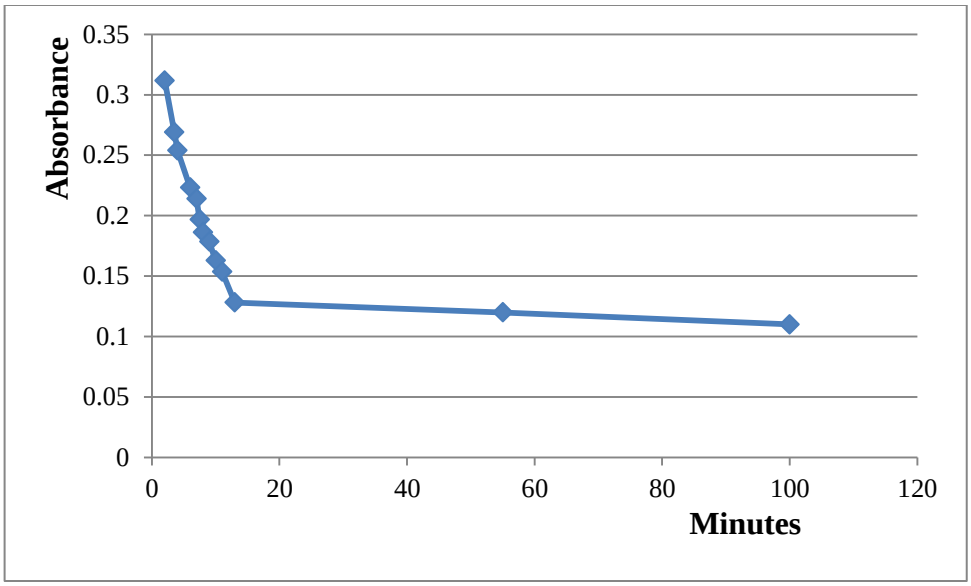


**Figure 76:** Kinetic data of $Ni(OTf)_2$ catalyzed HDA reaction

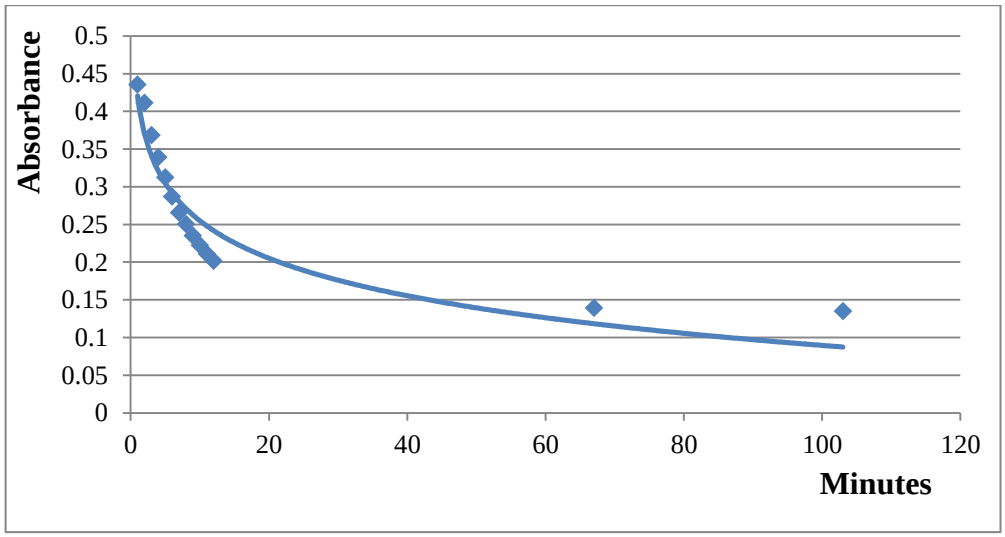


**Figure 77:** Kinetic data of $Cu(OTf)_2$ catalyzed HDA reaction.

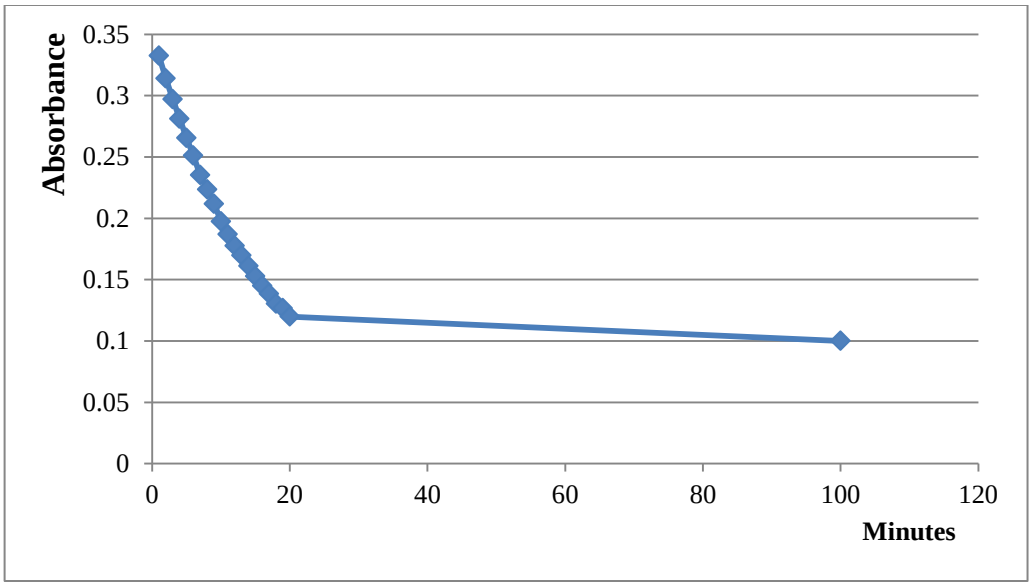


**Figure 78:** Kinetic data of $Zn^{2+}$ catalyzed the HDA reaction.

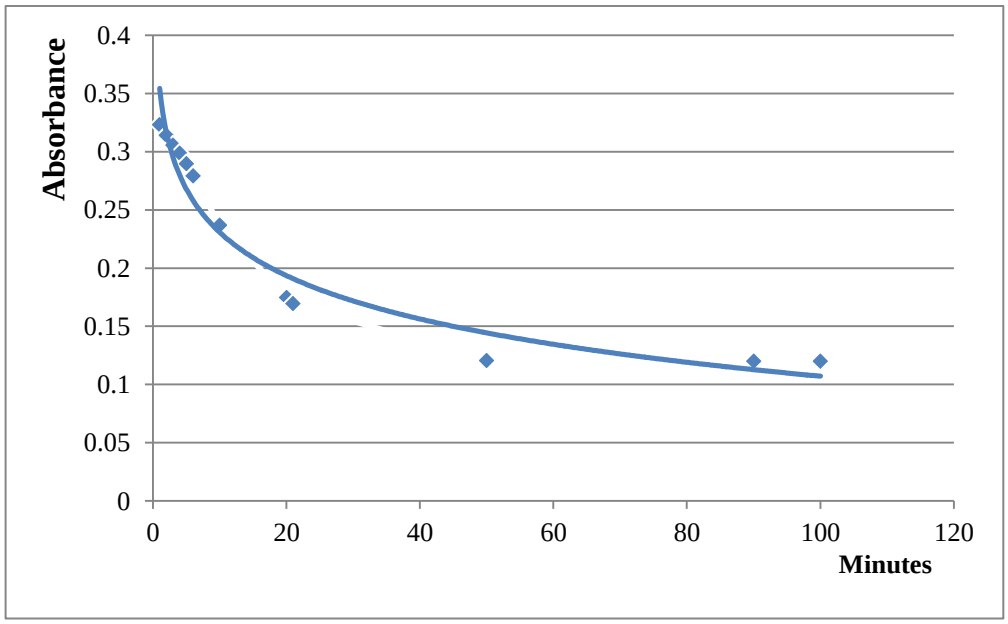


**Figure 79:** Kinetic data of $[(MeCN)_2Pd(O_3SC_6H_4CH_3)_2]$ catalyzed HDA reaction.

### 3.5.1.3 Rate constants for metal catalyzed decomposition of nitrosopyridine.

Because the rates of metal catalyzed decomposition of nitrosopyridine are "slow" compared to the HDA reaction, the catalysts were used at 10% catalyst loading

in MeOH. A solution of **75** (1mL at $2x10^{-4}$ M) was added into the cuvette followed by the addition of catalyst (100µL at $2x10^{-4}$M) and 1mL of pure methanol. Similar to the above reactions, the metals catalyzed decomposition of nitrosopyridine are treated as first order reaction. The rate of $Ni^{2+}$, $Cu^{2+}$, $Zn^{2+}$ and $Pd^{2+}$ catalyzed decomposition of nitrosopyridine (75) are plotted in the **Figure 80**, **Figure 81**, **Figure 82** and **Figure 83** respectively. In **Figure 83**, the absorbance difference between the starting (0.27498) and the end (0.26713 after 600 minutes) is very small (0.00785) compared to other cases (about 0.14 on average). This could due to the slow formation of (75)$Pd^{2+}$ complexes. This hypothesis is also supported by the fact that there is no detection of compound 110 (azoxypyridine, **Figure 59**) after mixing $Pd^{2+}$ with nitrosopyridine (75).

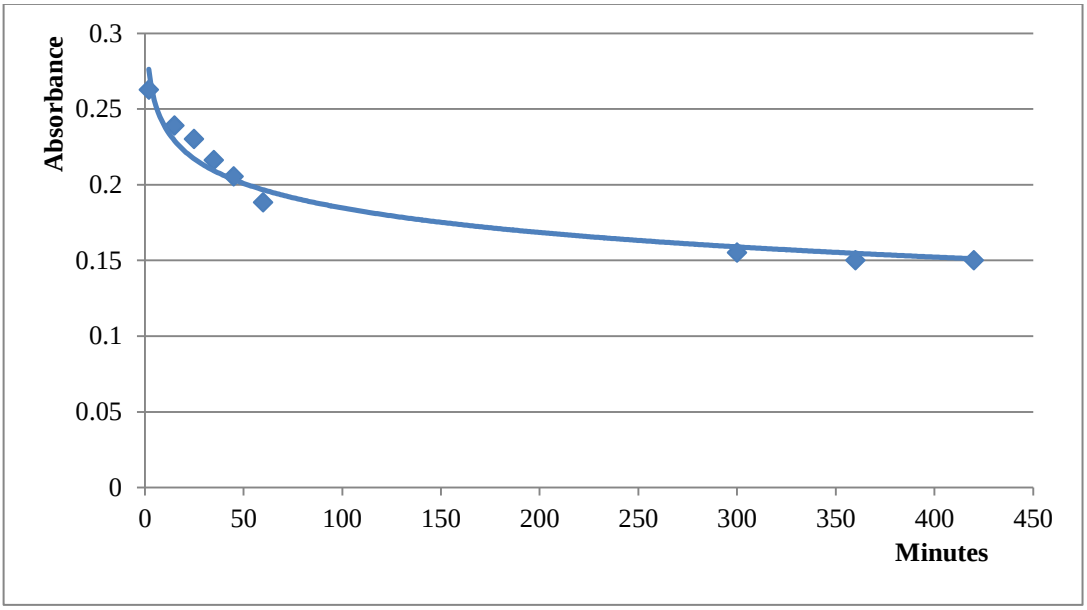


**Figure 80:** Absorbance vs. time of $Ni^{2+}$ catalyzed decomposition of nitrosopyridine (**75**).

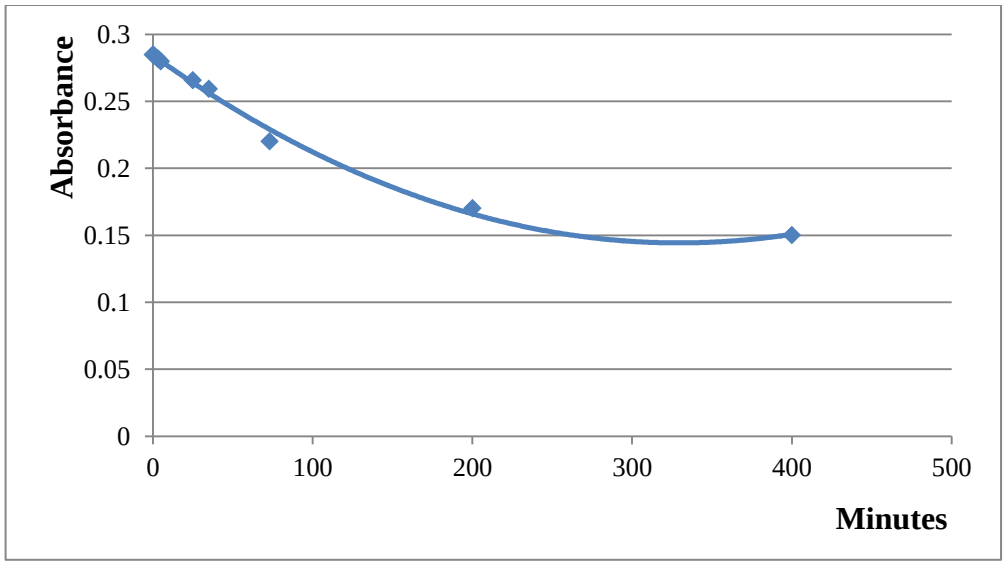


**Figure 81:** Absorbance vs. time of $Cu^{2+}$ catalyzed the decomposition of nitrosopyridine (**75**).

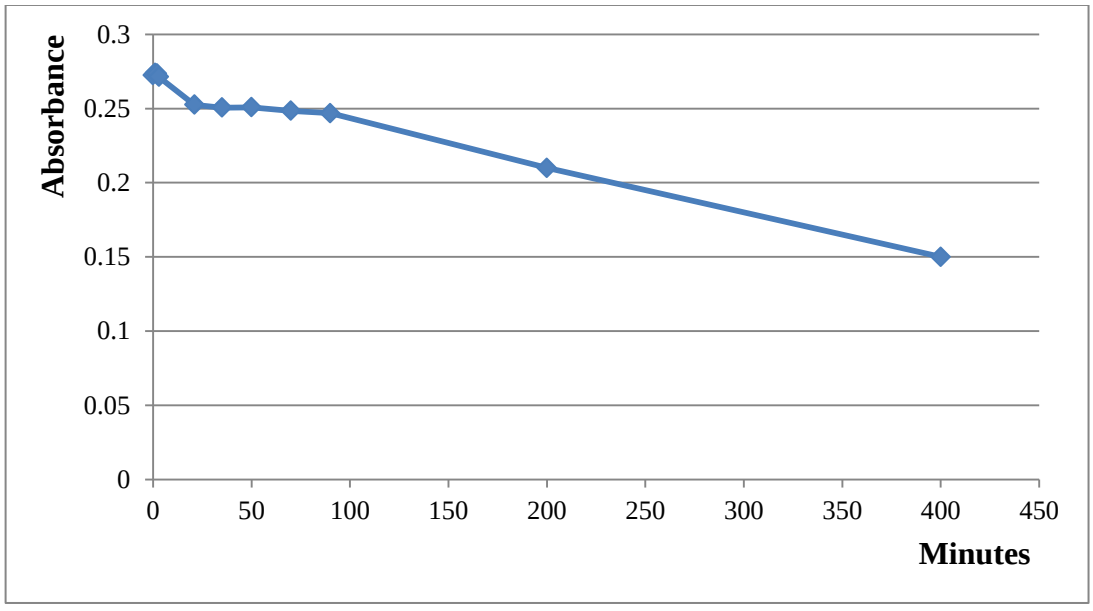


**Figure 82** Absorbance vs. time of $Zn^{2+}$ catalyzed the decomposition of nitrosopyridine (**75**).

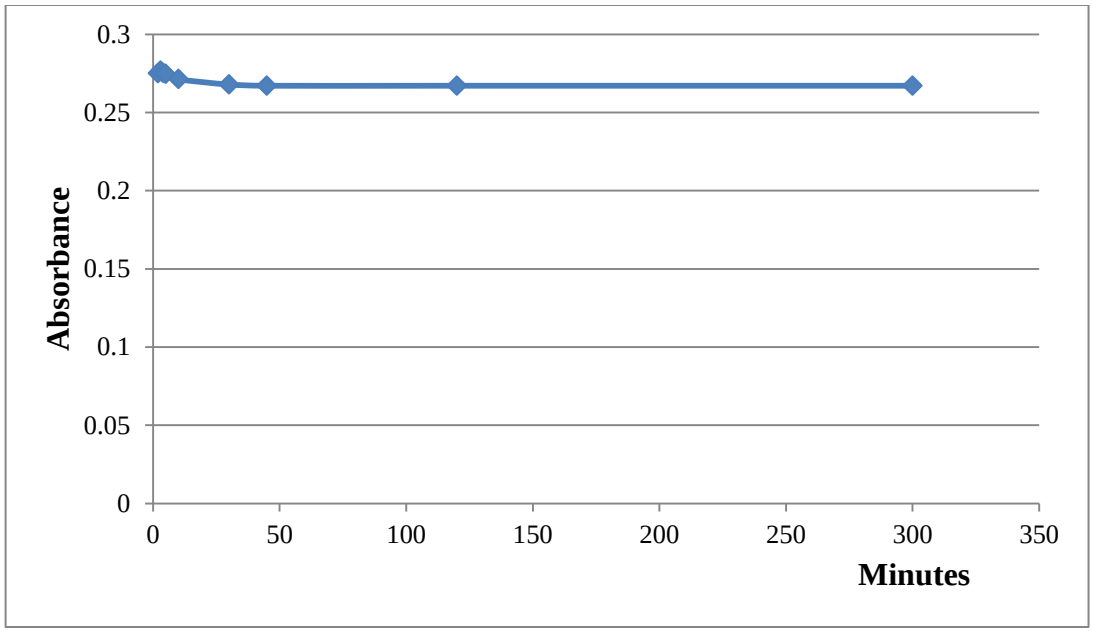


**Figure 83** Absorbance vs. time of $Pd^{2+}$-catalyzed decomposition of nitrosopyridine **(75).**

### 3.5.2 Catalytic test.

#### 3.5.2.1 Diene-PyrNO reactions catalyzed by $Ni^{2+}$, $Cu^{2+}$, $Zn^{2+}$ and $Pd^{2+}$.

Catalyst solutions of copper (II) trifluoromethanesulfonate; nickel(II) trifluoromethanesulfonate; palladium (II) acetate, bis(acetonitrile)palladium(II) p-toluenesulfonate and zinc (II) trifluoromethanesulfonate in MeOH at 1 x $10^{-1}$M were prepared by dissolution of 1 x $10^{-4}$ mol (36.1mg; 70.6mg; 22.5mg; 80.1mg and 36.6mg respectively) into 1.0 ml of MeOH. In a 4 dram vial, 21.6 mg (0.20 mmol) of 2-nitrosopyridine was dissolved in 10 mL of methanol. The catalyst solution (200 µL; 10% loading) is injected into the reaction mixture, followed rapidly by addition of 100 µL of 1,3-pentadiene (3 times excess, 75% pure, 2:1 *E/Z*) to prevent any side reaction. The solution was left 15 min then the solvent was evaporated to form a sticky mixture. One or two drops of acetone were added to the mixture to dissolve the solid, followed by the addition of 1.5 mL of 7:3 hexane:diethyl ether to precipitate side products. The

isomeric product mixture was isolated after passing the supernatant solution through a silica plug and rotary evaporating the solvent. The ratio of the two products was determined by NMR integration.

### 3.5.2.2 Diene-PyrNO reactions catalyzed by (diimine)$_2$-metal complexes.

Solutions of copper (II) trifluoromethanesulfonate; cickel(II) trifluoromethanesulfonate; palladium (II) acetate, bis(acetonitrile)palladium(II) p-toluenesulfonate and zinc (II) trifluoromethanesulfonate in MeOH at 1 x $10^{-1}$M were prepared by dissolution of 1 x $10^{-4}$ mol (36.1mg; 70.6mg; 22.5mg; 80.1mg and 36.6mg respectively) into 1.0 mL of MeOH. In a different vial, imines were formed by adding two equivalents (0.20 mmol) of the selected aldehyde (0.20 mmol), the selected amines (0.20 mmol) and methanol to make 1.0 mL total solution volume. The imine catalyst solutions were formed by mixing the corresponding metal salt solution with the imine solution, then left overnight to reach equilibrium. If crystals formed, more $CH_3OH$ was added to dissolve the crystals then the solution was left overnight again. In a 4 dram vial, 22 mg (0.20 mmol) of 2-nitrosopyridine was dissolved in 10 mL of methanol. The catalyst solution was injected into the nitrosopyridine solution (1% loaded) followed by addition of 100 µL of 1,3-pentadiene (three fold excess, 75% pure, 2:1 *E/Z*) immediately to prevent any side reaction. The solution was left 15 min then the solvent was evaporated to form a brown sticky mixture. One or two drops of acetone were added to the mixture to dissolve the solid, followed by the addition 1.5 mL of 7:3 hexane:diethyl ether to precipitate side products. The isomeric product mixture was isolated after passing the supernatant solution through a silica plug and rotary

evaporating the solvent. The ratio of the two products was determined by NMR integration.

### 3.5.2.3 ESI-MS qualification of the LCu(nitrosopyridine)$^+$ complex library

Solutions of copper (II) trifluoromethanesulfonate or nickel(II) trifluoromethanesulfonate in methanol at 1 x $10^{-1}$M were prepared by dissolution of 1 x $10^{-4}$ mol (36.1 mg and 70.6 mg respectively) to 1.0 mL of methanol. A solution of nitrosopyridine (**75**) at 1 x $10^{-1}$ M was prepared by dissolution of 10.8mg (1 x $10^{-4}$ mol) of nitrosopyridine (**75**) in 1mL of $CH_3OH$. In a new vial, 100 µL of the nitrosopyridine (**75**) solution and 10 µL of the metal salt solution were added to 890uL of methanol. Without further dilution and waiting, the mixtures were injected to overfill a 20 µL sample loop under flow of methanol (20 µL/min). A Micromass Q-TOF mass spectrometer was used for analysis with a capillary voltage set at 3000V.

### 3.5.2.4 ESI-MS quantification of the LCu(TSA)$^+$ complex library

Solutions of copper (II) trifluoromethanesulfonate and nickel(II) trifluoromethanesulfonate in MeOH at 1 x $10^{-1}$M were prepared by dissolution of 1 x $10^{-4}$ mol (36.1 mg and 70.6 mg respectively) to 1.0 ml of MeOH. In a different vial, the imine ligands were formed by adding one equivalent of selected aldehydes (1mmol each) and selected amines (1 mmol each). Methanol was added to the solution to make 1.0 mL total volume. The metal salt solutions were mixed with the imines solution and left overnight to reach equilibrium. On the next day, 80 µL of the above solution and 10 µL of tetrabutylammonium hexafluorophosphate (0.0010 mmol/L) were combined and

diluted with $CH_3OH$ to make a 4 mL stock solution. In two different vials, 1 mL of the stock solution was added to each vial followed by 16 µL (0.10 mmol) of the distal (**77**) or the proximal (**78**) adduct TSA. The mixtures were left 24 hr to reach new equilibria. Without further dilution, the mixtures were injected to overfill a 20 µL sample loop under flow of methanol (20 µL/min). A Micromass Q-TOF mass spectrometer was used for analysis with a capillary voltage set at 3000V. The ion integration was measured with the most abundant isotopomer of each complex using the built in program. Each sample was injected into the mass spectrometer five times and the resulting mass spectra acquired and the ion integrations determined. The binding ratio of the isomers was determined by averaging the integrated ion count of each regioisomeric ternary complex. The tetrabutylammonium ion (m/z = 242) was monitored as the internal standard.

### 3.5.3 Material Preparation.

The following compounds were prepared according to the cited procedures and identified by comparison of their $^1$H NMR spectra with those reported:

Benzo[h]quinoline-2-carboxaldehyde **112**.[160] $^1$H-NMR (300 MHz, $CDCl_3$) δ 7.79-7.85 (m, 3 H), 7.95 (d, 1 H, J = 8.56 Hz, CH), 7.96 (d, 1 H, J = 4.5 Hz), 8.17 (d, 1 H, J = 4.5 Hz), 8.33 (d, 1 H, J = 4.5 Hz), 9.43 (d, 1 H, J = 4.5 Hz), 10.38 (s, 1 H).

(Diimine)Zn(triflate)$_2$ **114**.[71] $^1$H-NMR ($CD_3CN$, δ): 8.23 (s, 2H), 7.68−7.0 (m, 14H), 4.19 (s, 2H), 1.56 (d, J = 6.6 Hz, 12H), 1.10 (s, 6H).

Bis(acetonitrile)palladium(II) bis(p-toluenesulfonate).[178] ESI-MS 529.9785. (No NMR provided in the literature)

# Chapter 4. Solid Supported Transition State Analogs for Catalyst Selection

## 4.1 Introduction.

Inspired by the idea of affinity chromatography for protein purification with a supported TSA, we envisioned that a solid supported transition state analog (SS-TSA) could be used for catalyst selection. To accomplish this, a TSA would be attached to a solid material to make SS-TSA to be used as the affinity ligand. When a mixture of potential catalysts is eluted though the SS-TSA column, the catalysts form temporary TSA-catalyst complexes. Since the TSA is immobilized on the solid support, the retention time of each catalyst depends on the binding affinity between the TSA and the catalyst. The greater the TSA-catalyst binding constant the longer the catalyst retains in the column, yielding a longer retention time (**Figure 84**). We are especially interested in the correlation between the catalyst activity and the retention time of each ligand-metal complex.

## 4.2 Reaction, Catalysts and Column Design.

Our group has a long experience with ester hydrolysis catalysts. In particular, we have developed several (imine)$Zn^{2+}$ complexes as the catalysts for the hydrolysis of various picolinate esters including catalytic kinetic resolution which selectively hydrolyzed only one enantiomer in the mixture.[70-72] Two main types of TSAs have been developed for the picolinate ester hydrolysis reactions: phosphonate ester and trifluoromethyl ketone hydrate. This project takes advantage of our prior work about

picolinate ester hydrolysis reaction that has been well developed in which 4-nitrophenyl picolinate **122** undergoes hydrolysis into picolinic acid (**123**) and 4-nitrophenol (**124)** (**Figure 85**).[70]

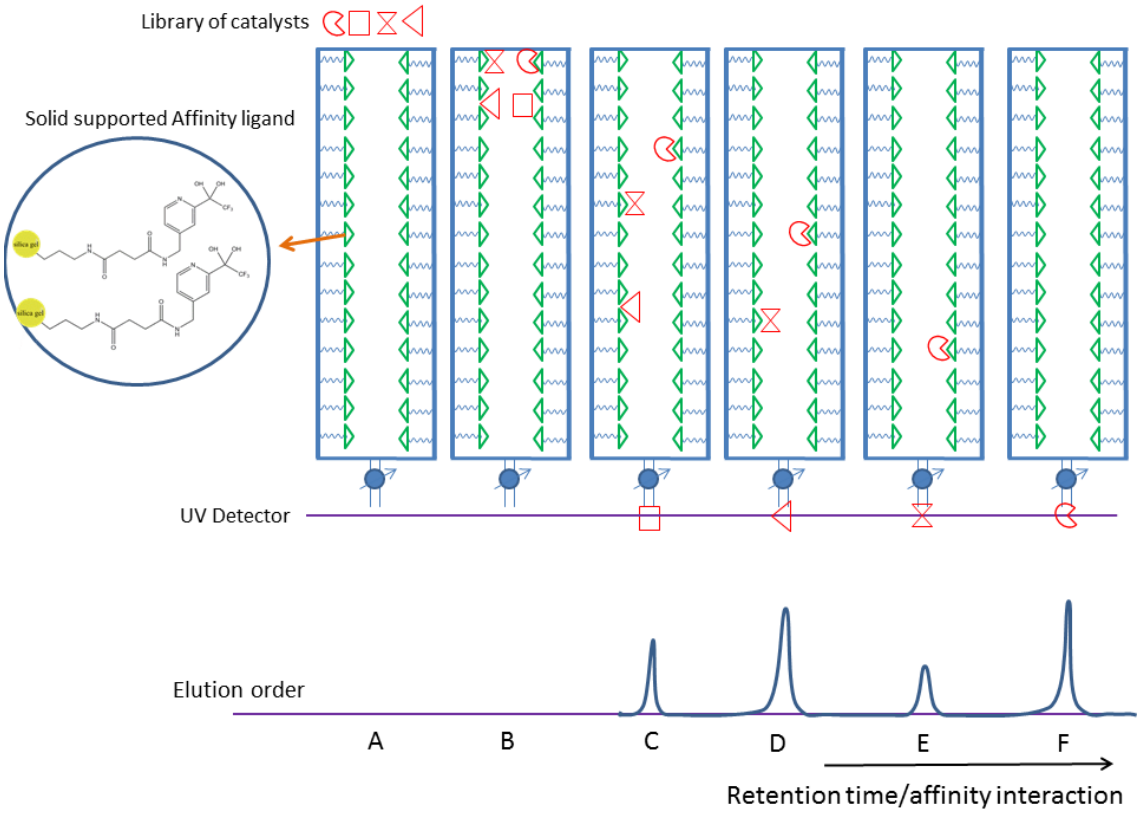


**Figure 84:** Schematic of the catalyst selection by affinity chromatography. (A) Injection, (B) Stationary phase Interaction, (C) No-binding interaction, (D) Non-specific interaction, (E) Weak binding interaction, (F) Strong binding interaction.

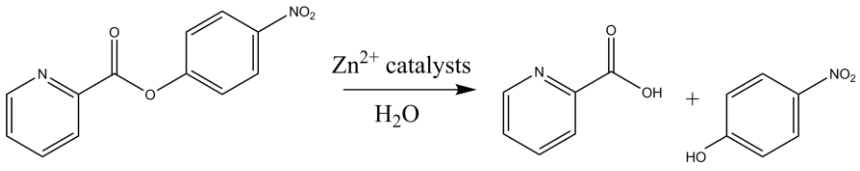


**122** **123** **124**

**Figure 85:** Hydrolysis of 4-nitrophenyl picolinate **122**.

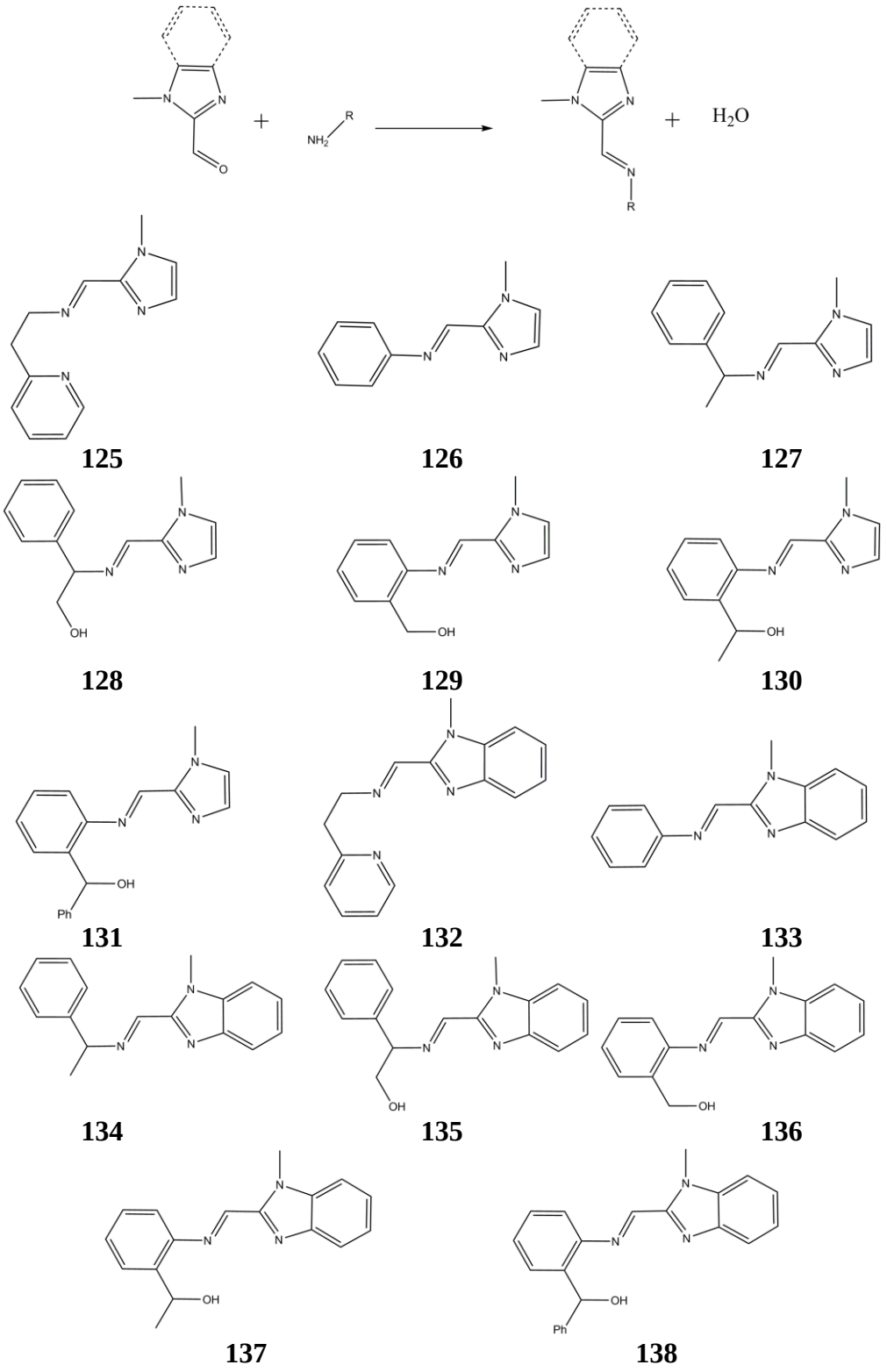


**Figure 86:** Formation of imine ligands and the list of ligands used in this project.

In the original publication various imine ligands, generated from the condensation reaction of aromatic amines and 1-methyl-2-imidazolecarboxaldehyde, were used with $Zn^{2+}$ to form (imine)$Zn^{2+}$ catalysts.[70] In order to increase the diversity of the library, 1-methyl-2-benzimidazolecarboxaldehyde was also introduced. A total of fourteen ligands were generated from the combination of seven amines and two heterocyclic aldehydes (

**Figure 86**).

Of the two TSAs that have been developed for ester hydrolysis, the trifluoromethyl ketone hydrate showed a better correlation between TSA binding and catalyst activity in Matsumoto's study. Thus a solid supported version of compound **62** was chosen as the target SS-TSA. The ability of pyridyl ketones to add water when coordinating with metal complexes to form hydrated ketone-metal complexes has been well studied.[179,180] These hydrated ketone-metal complexes adopt tetrahedral structures, thus they can be used as transition state analogs in combinatorial binding studies. At the same time, a substrate analog column with bound picolinate ester was also made in order to study the interactions between substrate and catalyst. A reference column was also made to test the non-specific binding between the solid support, the linker and the catalyst complexes. In terms of column design, each column has an active affinity ligand (red) connected with a linker (blue) attached to the aminopropyl functionalized silica gel in order to increase the availability of binding site. The linkers are put at the para position of the aromatic rings to minimize possible steric effects. One carbon spacer is also added between the linker and the aromatic moiety in order to minimize the electronic effects from the linker. Two amide bonds, presumably not easily

hydrolyzed, were used to connect the active affinity ligand to the linker and from the linker to the amino moiety of the silica gel (**Figure 87**).

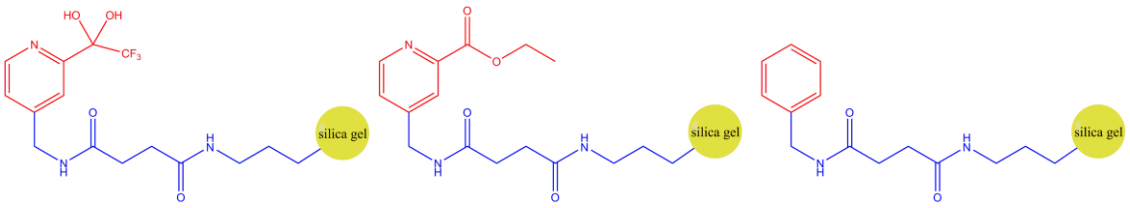


**139** **140** **141**

**Figure 87:** Three affinity columns: TSA **(139),** substrate analog **(140)** and reference **(141)** ligands.

### 4.3 Results and discussion

#### 4.3.1 Synthesis of the affinity silica gel.

The total synthesis schemes for compound **140** (substrate analog bound) and **141** (reference ligand) are shown in **Figure 88** and **Figure 89** respectively. The general pathway is as follows: 1) the affinity ligands were functionalized with methyl amino at the para position of the pyridine ring; 2) the linker is added by reacting the methyl amino moieties with succinic anhydride; and 3) the affinity ligands with linker are coupled with the amino silica gel using N,N'-diisopropylcarbodiimide (DIC) as coupling reagent. In both of the cases, the reaction mixture was pumped cycling thought the amino silica gel by an HPLC pump rather than a traditional batch reaction. Compound **143** was prepared using a previously reported method.[181] Hydrogenation of **143** gave compound **144** in high isolated yield (> 95%). Compound **144** was reacted with succinic anhydride immediately after isolation in order to prevent intermolecular reaction. DIC was chosen as the reagent for the coupling of **145** and **146** because the

byproduct N,N'-diisopropylurea is soluble in DMF. The IR spectra of **140** showed the disappearance of the peak at 1750 $cm^{-1}$ (assignable to carboxylic moiety) of **145** and the appearance of a new strong peak at 1654 $cm^{-1}$ (assignable to 2 amide moieties). See experimental section for more detail and spectra of the prepared compounds.

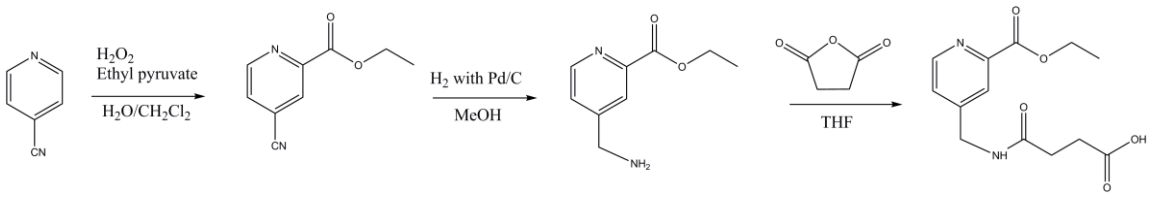


**142** **143** **144** **145**

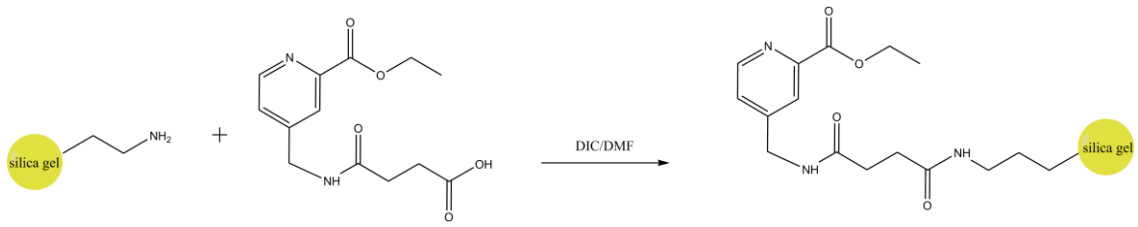


**146** **145** **140**

**Figure 88:** Synthesis of substrate-like (ethyl picolinate) column.

Similar to the synthesis of the substrate-like column, the benzyl reference column was prepared by reacting benzylamine **147** with succinic anhydride in THF according to the precedent literature.[182] Compound **141,** benzyl reference column, were synthesized by coupling **146** with **148** using DIC, a similar reaction was used in the synthesis of the substrate-like column. The IR spectra of **141** showed a clear disappearance of the peak 1720 $cm^{-1}$, assignable to carboxylic acid moiety, and the new peak at 1658 $cm^{-1}$, assignable to amide moieties.

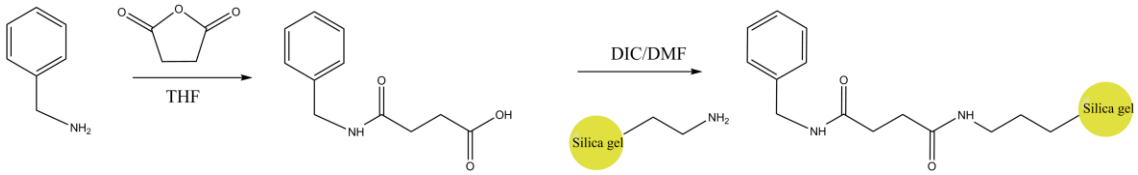


**147** **148** **146** **141**

**Figure 89**: Synthesis of the reference (benzyl) column

Compound **139**, the supported TSA, however, was much harder to synthesize. The first problem in making **139** compared to **140** and **141** is that under normal (non-anhydrous) conditions the trifluoromethyl ketone moiety of the **149** exists mostly in the hydrated form **150** which is unreactive to nucleophilic attack. A small amount of the keto form **149** has the potential for intermolecular nucleophilic attack by another methyl amino moiety. The product of this reaction would be the trifluoromethyl imine, which is very stable. Because of this problem, it was first thought that the trifluoromethyl ketone must be protected during the reaction and deprotected later (**Figure 90**). However, attempts to deprotect either compound **151** or **152** as described by several literature reports were not successful including $BBr_3$ in hexane, p-toluenesulfonic acid in acetone and formic acid in acetic anhydrite mix.[183-185] An explanation for this unreactivity is that the combination of electron-withdrawing pyridine moiety and trifluoromethyl ketone makes the either moieties less nucleophilic and thus is harder to hydrolyze. See the experimental section for procedures and spectra.

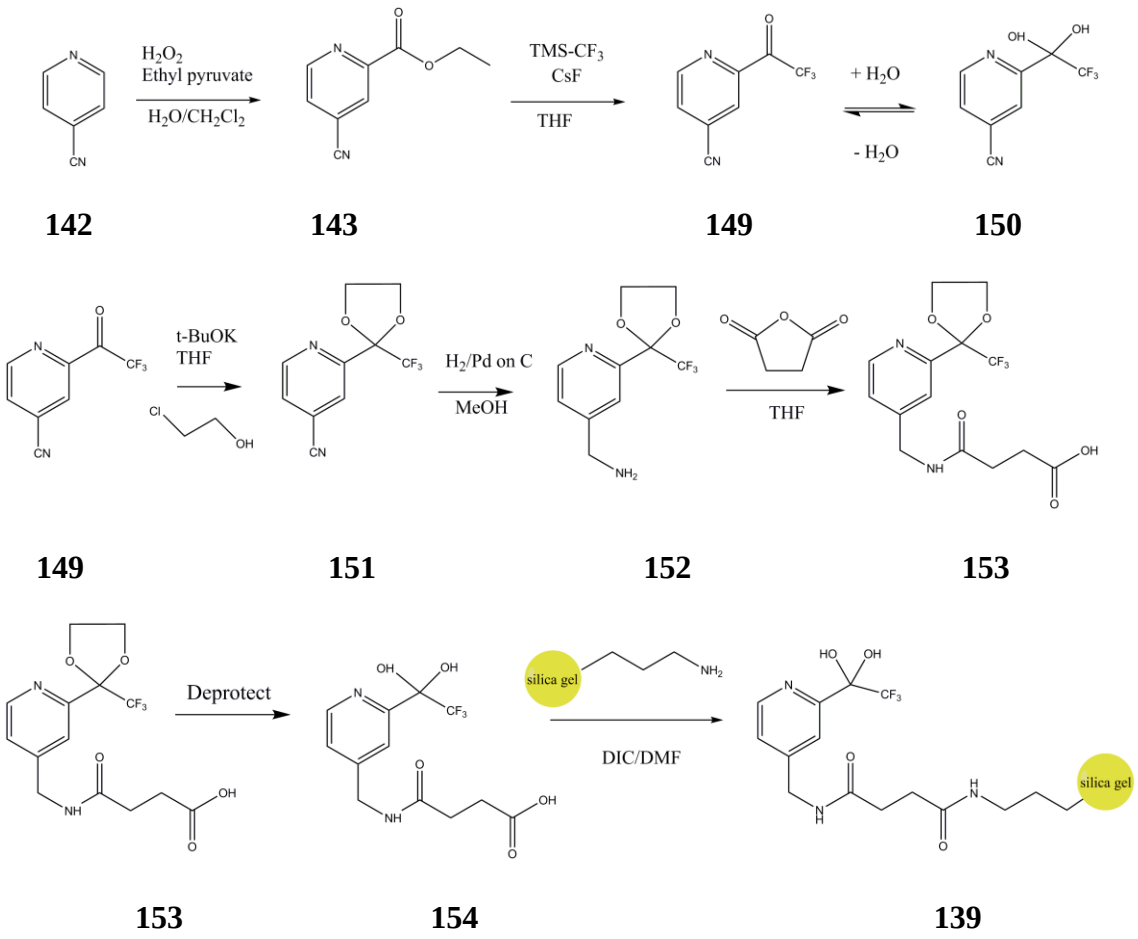


**Figure 90:** First idea for making **139.**

The other attempt to make **139** was direct functionalization of compound **140** with TMS-$CF_3$ (**Figure 91**). This method, if successful, would be the quickest and most convenient way of making **139**. In order for the reaction to work, CsF must be used as the catalyst.[186] Some problem was anticipated because the only analytical tool available for the solid-supported product is IR. However, the reaction can be followed by monitoring the disappearance of the peak at 1750 $cm^{-1}$, which is assigned to the ester carbonyl stretching vibration. Unfortunately, the reaction was not successful with the detection of the peak at 1736 $cm^{-1}$, assignable to the ethyl ester moiety. One of the possible reasons is that trace amounts of water in the silica gel may have decomposed

the TMS-$CF_3$ reagent. Also the reaction is thought to occur at the surface of the CsF catalyst, thus the solid-solid reaction in this case may not be effective. Other catalysts which contain soluble $F^-$ ion such as t-BuF indeed catalyze double addition to the ester carbonyl when excess TMS-$CF_3$ is used.[187]

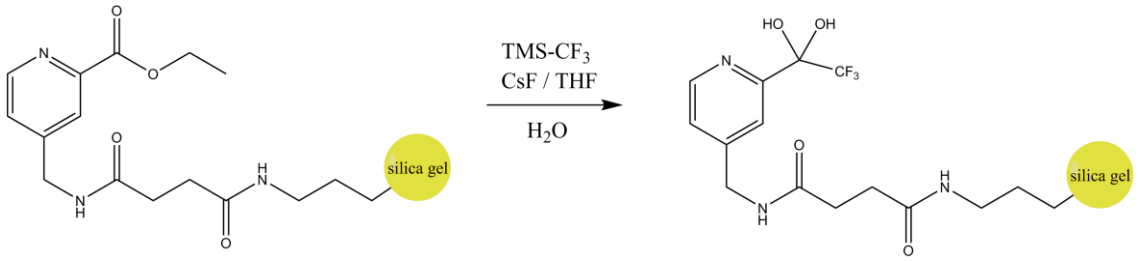


**140** **139**

**Figure 91:** Direct functionalized **140** from compound **139** plan**.**

After the successful conversion of compound **144** to compound **145** (**Figure 88**), it was hoped that the intermolecular condensation of amine moiety and trifluoromethyl ketone moiety might not be too fast thus another plan was proposed (**Figure 92**). At room temperature, most of the **149** absorbs water from the air thus hydrated diol **150** was found predominately. If hydrogenation of the nitrile moiety is faster than that of the trifluoromethyl ketone (due to lower concentration and/or being less selective), then compound **155** will be stable long enough to be converted into compound **156**, which can be coupled with the amino silica gel **146** to give **139**. However the hydrogenation reaction was not successful. Instead of **155**, compound **157** was found in ~ 20% yield. The side product was an amorphous material that was not soluble in MeOH, presumably oligomer or polymer. An explanation is that the hydrogenation of the nitrile moieties of compound **149** and **150** is faster than the trifluoromethyl ketone moiety of **149** (as

expected). Subsequently, the nucleophilic amino groups from the hydrogenation attack the trifluoromethyl ketone unit of **149** to form a polymer or oligomer. Compound **157** is produced when the hydrogenation occurs at the trifluoromethyl ketone moiety of **149** first, then followed by the hydrogenation at the nitrile moiety. In either case, the amorphous oligomer/polymer or compound **157** is not the desired product, compound **155**. However, this reaction brought up one important idea, which led to the synthesis of **139** successfully.

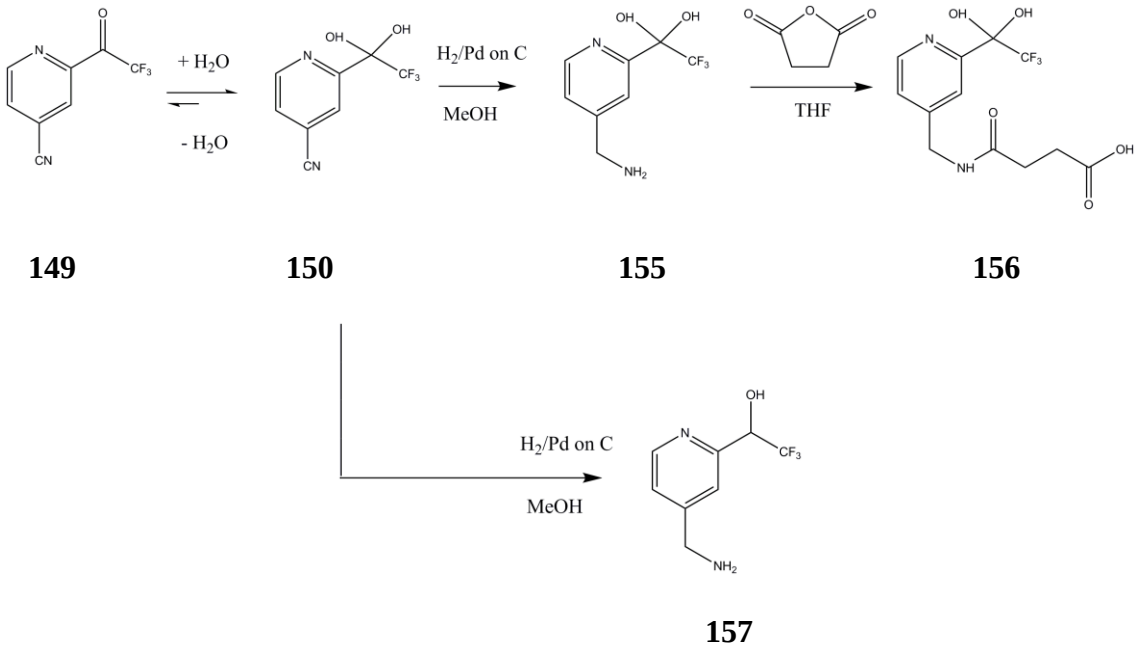


**149** **150** **155** **156**

**157**

**Figure 92:** Third plan to synthesis **139.**

If making a compound like **157**, which has the trifluoromethyl alcohol and methyl amino moieties, is unavoidable, then the keys to the success lie in the ability to make **157** effectively - and the ability to later convert the trifluoromethyl alcohol into the trifluoromethyl ketone in high yield. For the first problem, the ester carboxyl functionality is less reactive to nucleophiles than the aldehyde carbonyl. Thus, the addition of the trifluoromethyl anion to the aldehyde is faster, cleaner and higher

yielding, generally speaking. Also, only one trifluoromethyl anion can be added to the aldehyde instead of the possible double addition to the ester when TMS-$CF_3$ is used in excess. Compound **158** can be made from **142** in moderate yield (~ 40%) by precedent reported literature.[188] After that all subsequent reactions gave good isolated yields (> 88%). Compound **158** reacted with $SeO_2$ giving **159** (> 90%).[189] After this step all intermediates are new. The detail procedures and characterizations are reported in the experimental section. Compound **159** reacted with TMS-$CF_3$ with 1% of tetra-*n*-butylammonium fluoride (TBFA) in THF yielding **160** (96%). Hydrogenation of **160** with Pd/C in MeOH gave key intermediate **157** (92%). The compound **157** reacted selectively with succinic anhydride to produce amide **161**, because the amine moiety of **157** is more nucleophilic than deactivated trifluoromethyl alcohol moiety. The specific oxidation reaction, which transforms trifluoromethyl alcohol **161** to trifluoromethyl ketone which subsequently turned into hydrated form **162**, is not reported in the literature. Nevertheless, oxidizing pyridine trifluoromethyl alcohol derivatives to trifluoromethyl ketone and subsequently turned into hydrated form, have been reported by several methods including: oxoammonium salt,[190] iodoxybenzoic acid (IBX),[191] Martin reagent,[192] etc. However, $SeO_2$ in dioxane was chosen even though it has not been reported in oxidation of trifluoromethyl alcohol because we had success oxidizing hydroxyl 2-methyl pyridine using $SeO_2$ in dioxane. The reaction was clean, high yielding and has an easy workup (88%).

The in-column functionalization method was used for coupling **146** and **162** to make TSA bound silica gel **139** (**Figure 93**). The reaction was followed by the

disappearance of the IR peak at 1734 $cm^{-1}$, assignable to the C=O bond of the carboxylic moiety. See experimental section for more detail and spectra.

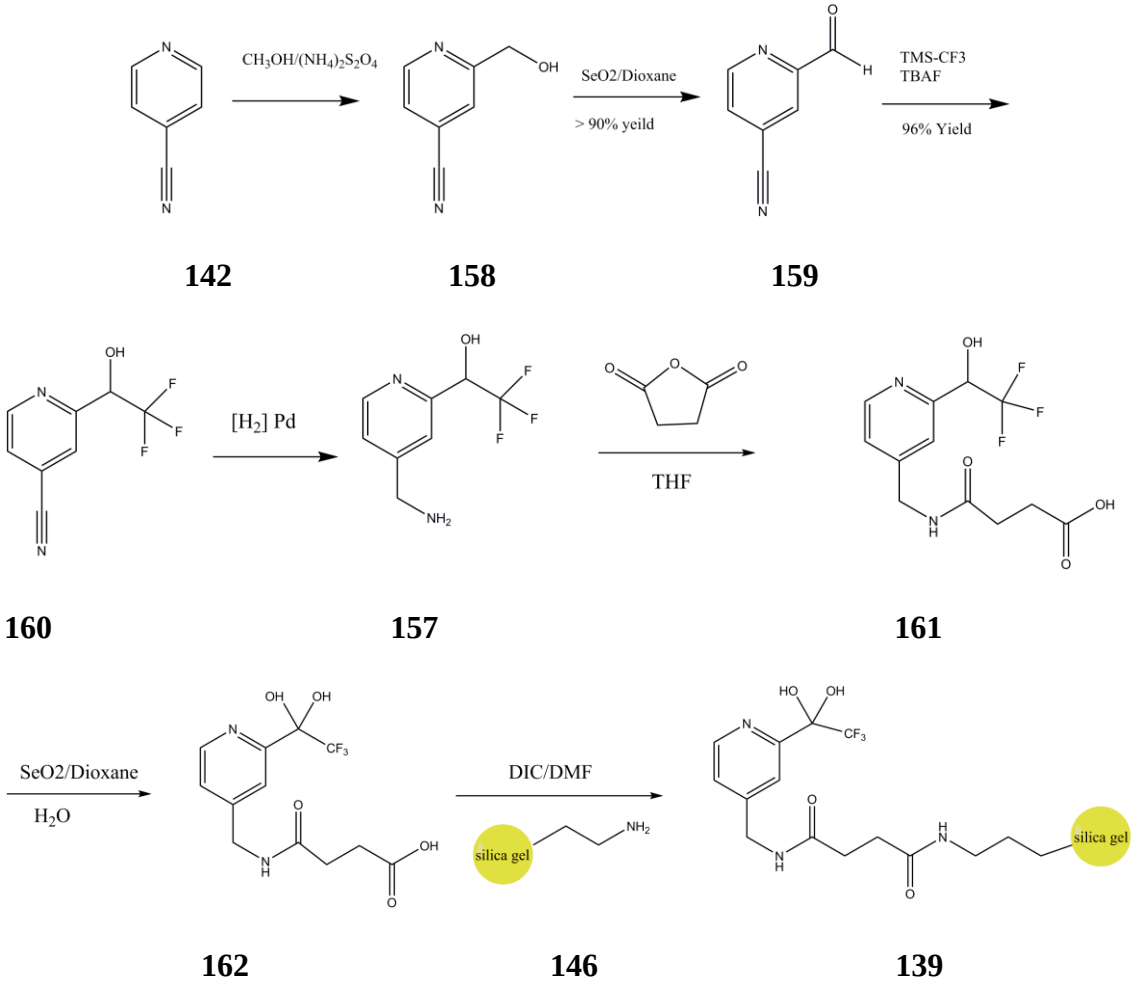


**Figure 93:** Synthesis of TSA (trifluoromethyl diol) silica gel **139**.

### 4.3.2 Affinity chromatography testing.

After the three functionalized silica gel columns were made, the next step was to determine the retention time of each building block and each amine-aldehyde-zinc combination when put on the different columns. Solvent is a very important parameter in HPLC. Of all the solvent mixtures that were tested, hexane/EtOH was found to be

the best option due to availability, solubility of the ligands and Zn-complexes, and non-reactivity with the affinity ligand.

Several ligands were tested by passing each of them individually though both the substrate analog and the reference column. Generally speaking, the peak retention times were between ~ 8 to 22 minutes, depending on the particular ligands and the ethanol/hexane ratio. However, the peaks had unacceptably poor resolution with the peak length (front to tail) of up to 20 minutes. Several reasons and solutions have been proposed to increase the resolution of the peaks including: baking the column or changing to a new solvent mixture. However, it was thought that the main reason for low resolution is the fast equilibrium in HPLC time scale between the reversible reaction of amine + aldehyde and imine + water. The imine ligand can be hydrolyzed into aldehyde and amine building blocks during the time inside the columns (**Figure 94 top**). Due to the difference in retention time of each ligand building block, the final result is a big hump that is equal to the average retention time of all the building blocks – a similar phenomenon to slow exchange in NMR experiment. To overcome this problem, excess $Zn^{2+}$ (in form of $Zn(OTf)_2$ salt) was added into the solvent mixture as buffer ($10^{-2}$ M) to drive the equilibrium into (imine)$Zn(OTf)_2$ (**Figure 94 bottom**). Interestingly, adding $Zn^{2+}$ into the solvent mixture significantly improved the peak resolution. The 60/40 volume hexane/ethanol mixture with $10^{-2}$ M $Zn(OTf)_2$ salt as buffer is the optimal solvent. Therefore, this mixture was used in all chromatography experiments.

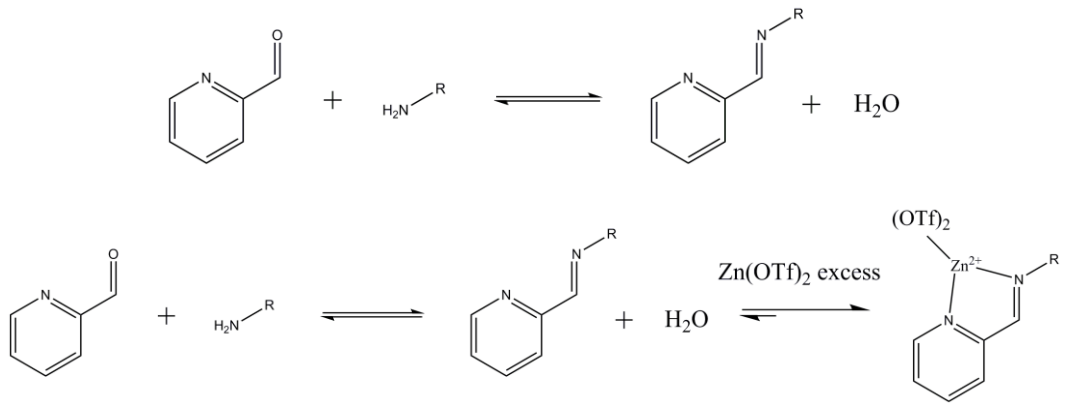


**Figure 94:** Imine equilibrium (top) and the solution (bottom)

For the purpose of peak identification, a total of 14 (imine)$Zn^{2+}$ complexes (from **125** to **138**) were injected into the HPLC separately and the retention time of each complex was compared with its building block's retention times. Also the HPLC UV detector was set at 375, 325 and 254 nm for maximum absorbance. At these wavelengths the molar absorptivity of the aldehyde and amine building blocks are negligible compared to those of the (imine)$Zn(OTf)_2$ complexes. For the purpose of further verification, each peak (a total of 14 (imine)$Zn(OTf)_2$ complexes) eluted from the TSA bound column was collected and analyzed by ESI-MS. Also (**137**)$Zn(OTf)_2$ eluents from the benzyl reference column and substrate column were also collected and analyzed by ESI-MS. In all of the cases, at least the M/z of each following complexes corresponding to (imine)$Zn(OTf)^+$, (imine)$Zn(OTf)(MeOH)^+$ or (imine)$Zn(OTfO)(OTfH)^+$ was detected. The retention time of each complex is presented in **Table 13**.

| (imine)Zn(OTf)$_2$ complexes | Reference column (min) | Substrate column (min) | TSA column (min) | Substrate – reference (min) | TSA – substrate (min) |
|---|---|---|---|---|---|
| **125** | 6.8 | 7.1 | 8.6 | 0.3 | 1.5 |
| **126** | 15.3 | 19.9 | 16.4 | 4.6 | -3.5 |
| **127** | 4.7 | 8.6 | 9.4 | 3.9 | 0.8 |
| **128** | 5.2 | 12.0 | 8.2 | 6.8 | -3.8 |
| **129** | 4.7 | 6.0 | 6.2 | 1.3 | 0.2 |
| **130** | 5.1 | 6.7 | 7.3 | 1.7 | 0.6 |
| **131** | 5.5 | 6.8 | 8.2 | 1.3 | 1.4 |
| **132** | 8.0 | 8.0 | 9.7 | 0.0 | 1.7 |
| **133** | 21.7 | 26.7 | 20.4 | 5.0 | -6.3 |
| **134** | 8.4 | 12.1 | 11.1 | 3.7 | -1.0 |
| **135** | N/A | N/A | N/A | N/A | N/A |
| **136** | 6.2 | 6.6 | 6.7 | 0.4 | 0.2 |
| **137** | 6.4 | 9.1 | 8.2 | 2.6 | -0.8 |
| **138** | 6.7 | 8.0 | 9.7 | 1.3 | 1.7 |

**Table 13:** Retention times of (imine)Zn(OTf)$_2$ complexes with benzyl, substrate and TSA bound columns.

Generally speaking, the retention time trend of the (imine)Zn(OTf)$_2$ complexes cannot be explained by simple polar/non-polar characteristics. The only reasonable explanation for the trend of retention time is the internal interaction between substrate, TSA and benzyl moieties on the respective columns with (imine)Zn(OTf)$_2$ complexes. The substrate – reference retention column in **Table 13** theoretically correlates with the

binding of the solid supported substrate analog with (imine)$Zn(OTf)_2$ complexes, while the TSA – substrate column binding affinity will roughly correlate with the activation energy or rate of the reaction. However, unlike the value in the substrate – reference column, some values in the TSA – substrate column are negative. This abnormal phenomenon and solutions will be discussed in more detail in the discussion section.

### 4.3.3 Kinetics assay.

In the previous study, the rates of only 7 (imine)$Zn^{2+}$ complexes were measured.[70] In this study, we expanded the ligand systems by adding aniline **94** and included 1-methyl benzimidazole 2-carboxaldehyde with all other amines. With this expansion, the library will have total of 14 imine ligands. In order to obtain a more complete understanding of the catalyst behavior, the catalysts were subjected to a Michaelis-Menten treatment, yielding data for substrate affinity as well as transition state activation energy via the rate constant for that step. In order to make the Michaelis-Menten treatment effective, rates were measured as initial rates with the substrate at 16 mM, 14 mM, 12 mM, and 10 mM in the final mixture and at low catalyst loading (0.08 mM after mixing) with samples taken every 7 seconds and the time from minute 1 to minute 3 used for data processing. Over the course of the observation window, the most substrate that was ever converted was $3x10^{-5}$M, or less than 1% conversion. The $K_M$, $V_{max}$, and $k_{cat}$ were calculated from the absorbance vs. time data and are shown in **Table 14**. These values were obtained by plotting the raw data on a Lineweaver-Burk plot to obtain an $R^2$ value for the data and on an Eadie-Hofstee plot to obtain the values of $K_M$ and $V_{max}$. For convenience, since $K_M$ is an inverse constant,

$1/K_M$ is also provided to compare binding affinities (association constants) more directly. Ligand **135** was unable to be effectively processed because it decomposed in solution to an unknown degree, making any data collected for it not comparable to the other ligands.

| **Ligand** | **$K_M$** | **$1/K_M$** | **$V_{max}$** (M/min) | **$k_{cat}$** ($M^2$/min) |
|---|---|---|---|---|
| **125** | 0.026 | 38.43 | $1.69x10^{-5}$ | 0.2113 |
| **126** | 0.022 | 45.74 | $3.99\ x10^{-5}$ | 0.4981 |
| **127** | 0.017 | 58.94 | $2.63X10^{-5}$ | 0.3291 |
| **128** | 0.005 | 195.4 | $2.05X10^{-5}$ | 0.2561 |
| **129** | 0.032 | 31.22 | $4.56X10^{-5}$ | 0.5703 |
| **130** | 0.051 | 19.79 | $6.17X10^{-5}$ | 0.7710 |
| **131** | 0.016 | 62.10 | $2.88X10^{-5}$ | 0.3605 |
| **132** | 0.034 | 29.24 | $3.055X10^{-5}$ | 0.3818 |
| **133** | 0.010 | 101.7 | $2.53X10^{-5}$ | 0.3163 |
| **134** | 0.015 | 65.77 | $3.09X10^{-5}$ | 0.3860 |
| **135** | N/A | N/A | N/A | N/A |
| **136** | 0.037 | 27.29 | $5.65X10^{-5}$ | 0.7058 |
| **137** | 0.016 | 63.93 | $2.98X10^{-5}$ | 0.3727 |
| **138** | 0.024 | 42.03 | $3.92X10^{-5}$ | 0.4901 |

**Table 14:** Kinetic data of 14 tested ligands.

Reek's group demonstrated that the stronger the substrate-catalyst binding constant, quantified by MS, the less active the catalyst.[174] The main reason for this

phenomenon is that if the substrate-catalyst binding constant is favorable, then the activation energy required for the reaction should be larger (assuming that the energy of the transition state is unchanged), thus the reaction is slower. Interestingly, the same phenomenon was also observed here.

**Figure 95** showed a decent negative logarithm correlation ($R^2$ = 0.5) between $1/K_M$ vs $k_{cat}$. In the original publication, Reek also suggested a negative logarithm relationship between binding constant versus rate of the reaction. While ligand **125** and **132** could be tridentate ligands with (imine)$Zn^{2+}$, the rest of the tested ligands can only be bidentate, thus might lead to an invalid comparison of binding constant. Because of the above reason, **Figure 96** was plotted with all of 2-coordinate ligands and **Figure 97** was plotted with all of the bidentate ligands with an –OH moiety. In both of the cases, better $R^2$ values (0.82 and 0.87 respectively) were observed. This result agreed very well with the theory and the precedent literature that if the substrate-catalyst complex is too stable it will inhibit the catalyst activity

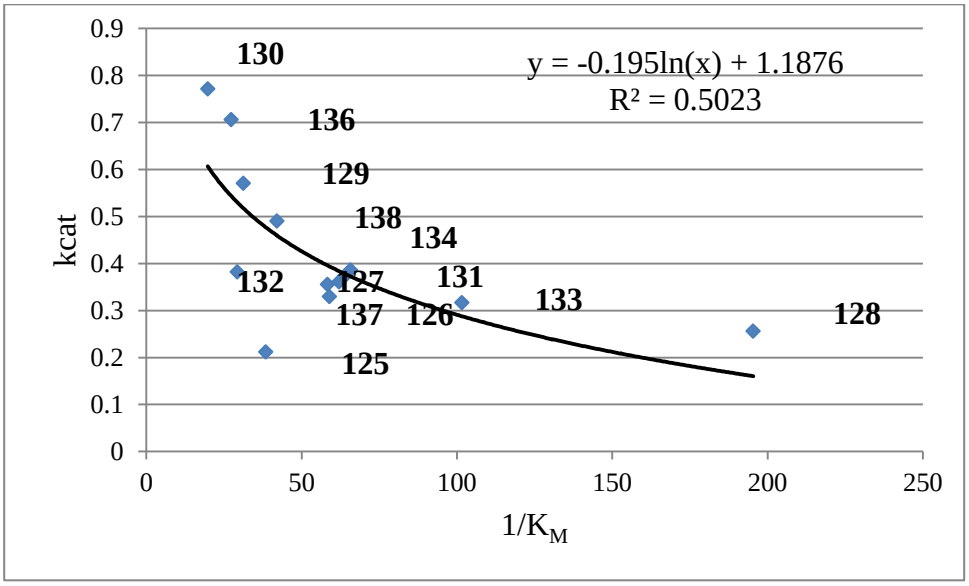


**Figure 95:** Plot of binding constant vs $k_{cat}$ with all of the tested ligands.

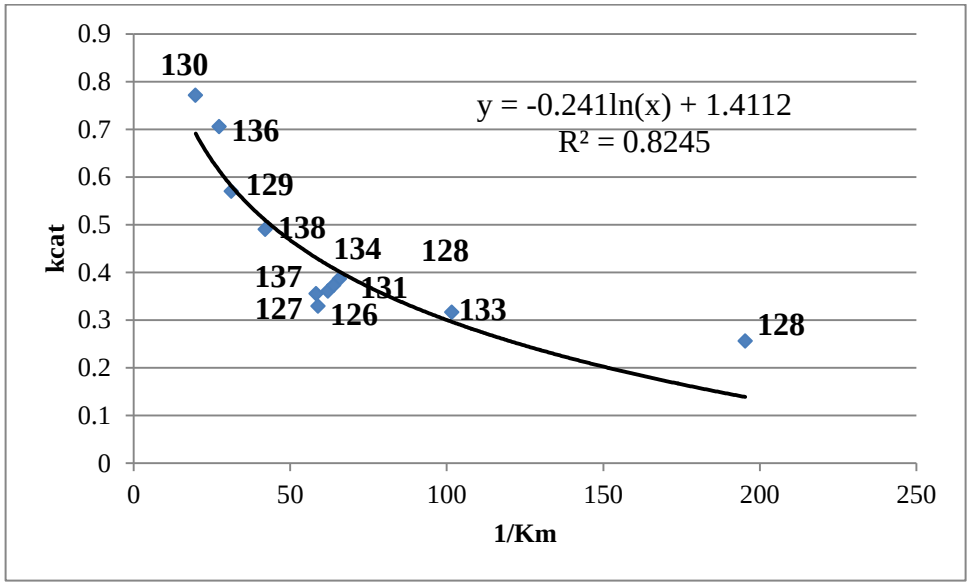


**Figure 96:** Plot of binding constant vs $k_{cat}$ with 2-coordinate ligands.

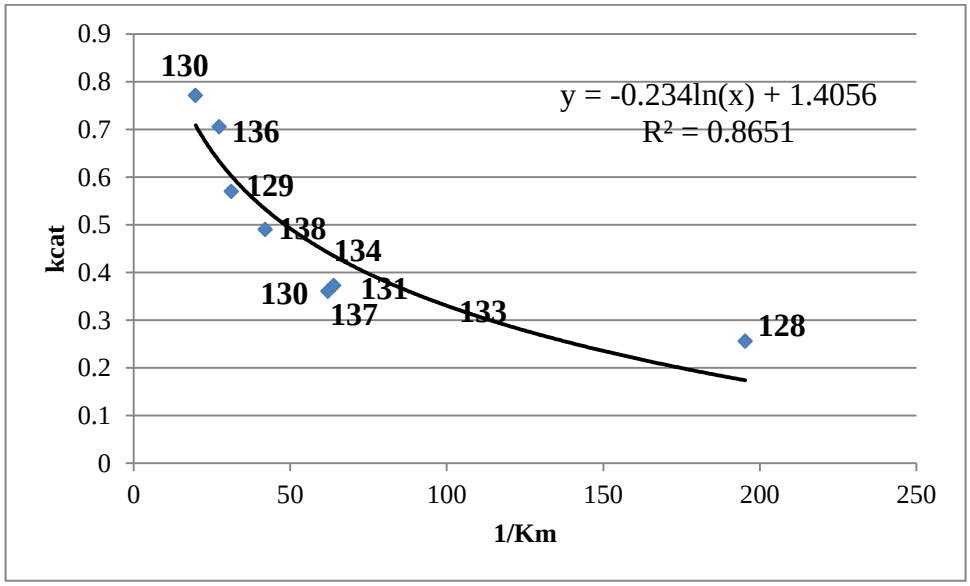


**Figure 97:** Plot of binding constant vs kcat with 2-coordinate –OH ligands.

### 4.3.4. Discussion.

There is a correlation between $1/K_M$ and the difference in retention time of the same complex in benzyl reference column and substrate analog column. The main reason is that if the substrate-catalyst binding constant is large (large $1/K_M$), then the same catalyst would require longer time to be eluted through the substrate column. However, there also might be non-specific binding between the complexes and the silica gel and as well as complex – linker interactions, thus the "corrected" retention time (substrate – benzyl retention) was used. The first plot was made between these parameters for all 13 ligand complexes with the data from **Table 13** and **Table 14** (**Figure 98**). **Figure 98** shows a reasonably good positive correlation between substrate-benz retention time vs $1/K_M$. The blue line is plotted with 0,0 intercept which theoretically, if a ligand has no specific binding with substrate column, should have no difference in retention time between substrate column and reference column (0,0 y-intercept). The red line is plotted with best fit for minimal $R^2$ value. In either case, the $R^2$ values are about the same 0.70 and 0.71 respectively, which indicates a good correlation between theoretical and experimental results.

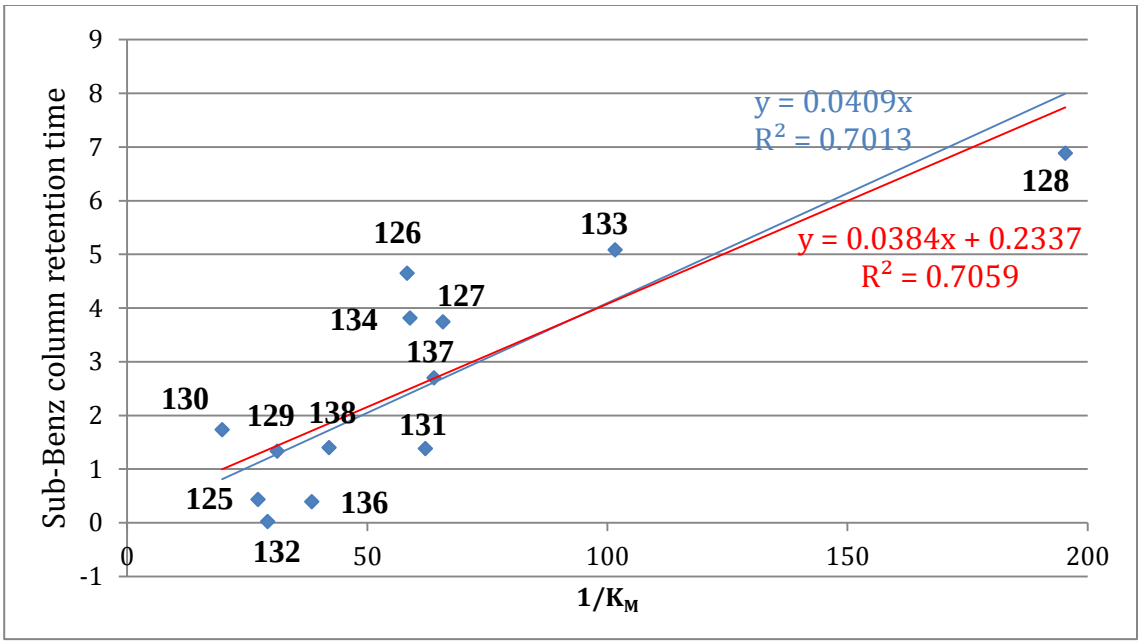


**Figure 98:** Plot of substrate column – benzyl column retention time vs $1/K_{M.}$

It was also thought that in such a wide structural range of complexes, there might be a difference in the mechanism of the catalysis. In particular, all catalysts that have an OH moiety could have additional hydrogen bonding with incoming OH moiety of either water (in hydrolysis) or methanol (in methanolysis). In the other hand, the OH moiety brings in the potential Zn-OH coordination which also increases the acidity and nucleophilicity of Zn-OR. Because of this extra bonding, the catalysts that have an OH moiety could have a slight difference when binding with the substrate as well as in the transition state. The substrate column – benzyl column retention time vs $1/K_M$ of all catalysts that have ligand-OH groups was also plotted. **Figure 99** was also plotted with the red line for the lowest $R^2$ possible and the the blue line with 0,0 intercept with 7 data points for two-coordination ligand with an OH. In both of the cases, two excellent positive correlations with $R^2 = 0.92$ were found. This indicates that the substrate analog

column near perfectly mimics the binding between substrate and complex as measured by 1/Km from the kinetics measurements.

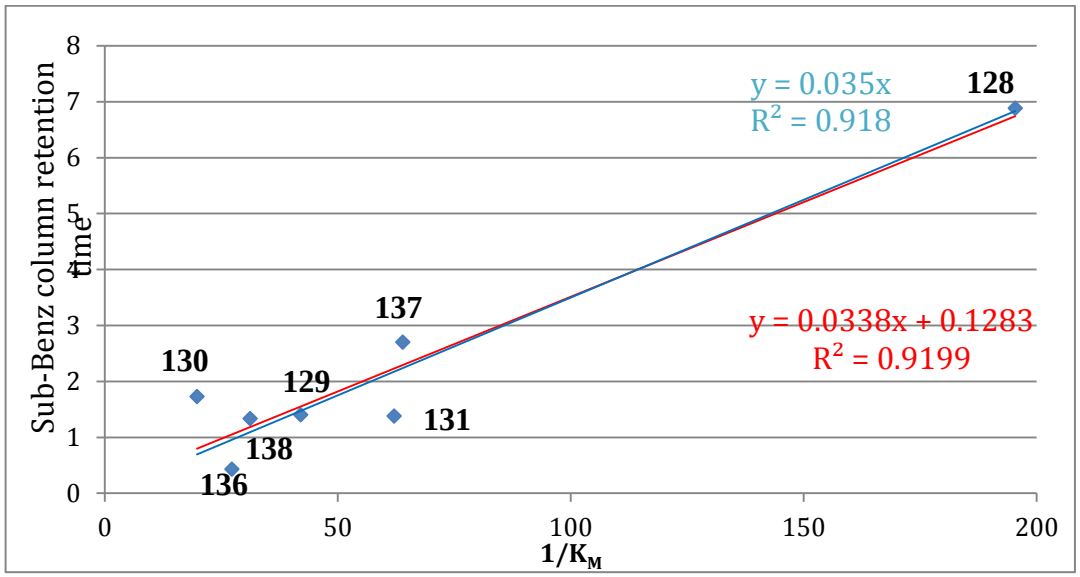


**Figure 99:** Plot of substrate column – benzyl column retention time vs $1/K_M$ for two-coordination hydroxyl catalysts.

The remaining non-hydroxyl pedant catalysts were divided into two different groups: the tridentate ligands (**125** and **132**) and the bidentate, non-hydroxyl ligands (**126**, **127**, **133** and **134**). The two-coordination non hydroxyl ligand group was also plotted with the same method as in **Figure 98**. The blue line, plotted with 0,0 intercept, showed a very bad correlation with 4 data points ($R^2$ = -0.89) while the red line, plotted with minimal $R^2$, also showed a poor correlation with $R^2$ = 0.49 (**Figure 100**). Both ways of plotting data show positive slopes which mean some positive correlation. However, due to the fact that the $R^2$ value is low, the correlation is less statistically significant. One possible explanation is that the number of data points is not enough (4

points) and accumulated in a small range of $1/K_M$ and retention time. Expanding the ligand system could bring a better correlation as well as statistical significance.

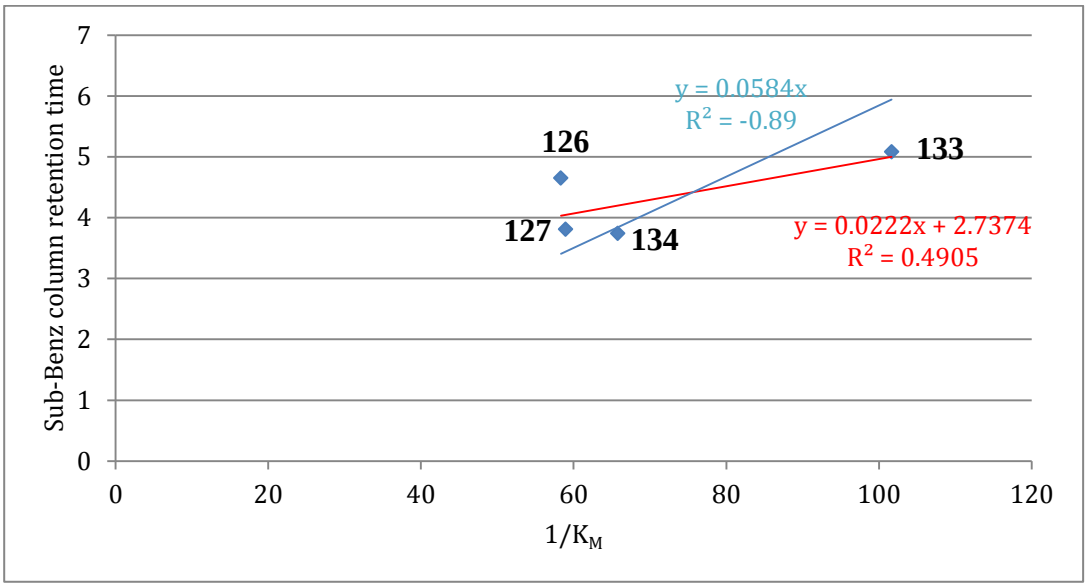


**Figure 100:** Plot of substrate column – benzyl column retention time vs $1/K_M$ for bidentate, non-hydroxyl ligand complexes.

From the previous experiments and literature precedent, it is clear that a linear relationship exists between binding constant and equilibrium constant (**Equation 1**).[193] In this equation, K is the equilibrium constant between mobile complex and the affinity ligand, k is retention factor ($k_{TSA} = \frac{RT_{TSA}}{RT_{Benz}} - 1$; $k_{Sub} = \frac{RT_{Sub}}{RT_{Benz}} - 1$: RT being the retention time of the complex on the subscripted column), V is column volume and m is the number of mol of active binding sites. For the purposes of this work, V and m are assumed to be constant.

$$\boldsymbol{K = \frac{kV}{m} \therefore K \, \alpha \, k \therefore \frac{K_1}{K_2} = \frac{k_1}{k_2}}$$

**Equation 1:** Relation between retention factor and equilibrium constant.

From the catalyzed energy diagram (**Figure 101**), the activation energy ($\Delta G^{\ddagger}$) equals $\Delta G_{TSA} - \Delta G_{sub}$ in which $\Delta G^{\ddagger}$ is the activation energy of the reaction, $\Delta G_{TSA}$ is the activation energy of catalyst binding to transition state directly and $\Delta G_{sub}$ is the activation energy of catalyst-substrate binding. From the Gibbs free energy equation $\Delta G = -RT\ln K$. Substituting the Gibbs free energy expression into the activation energy equation gives **Equation 2**. Rearranging the Arrhenius equation for the activation energy transition state with $\Delta G^{\ddagger}$ from **Equation 2** gives **Equation 3** in which $k_{cat}$ is the rate constant of the rate limiting step.

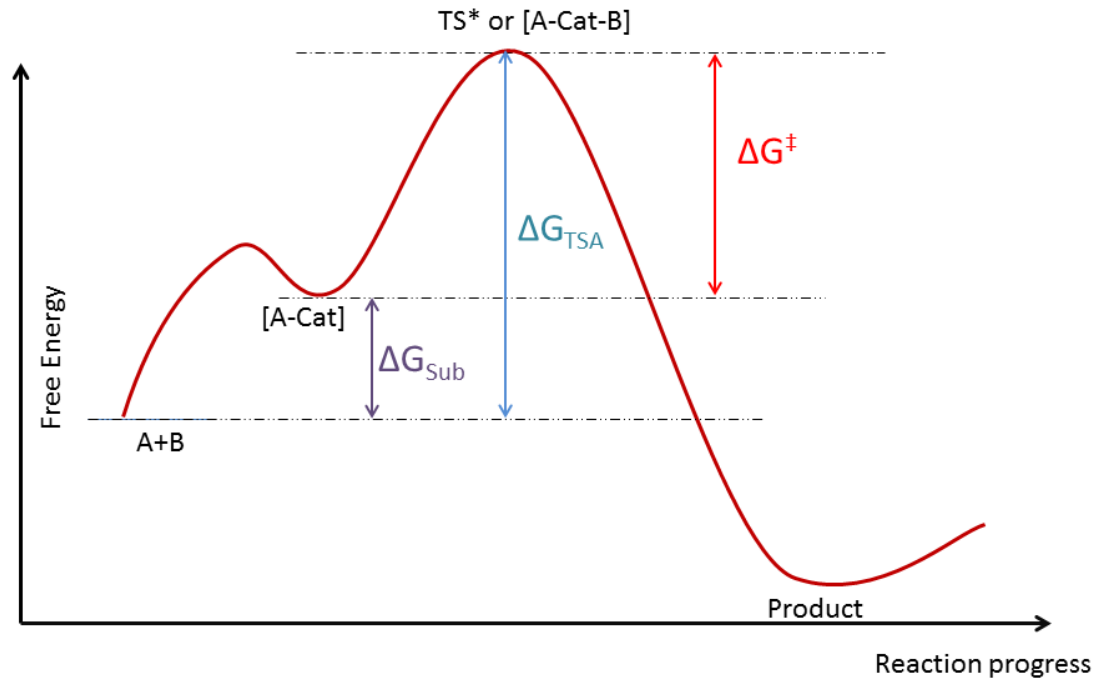


**Figure 101:** Catalyzed reaction energy diagram.

$$\Delta G^{\ddagger} = \Delta G_{TSA} - \Delta G_{Sub} = -RT\ln(K_{TSA}) + RT\ln(K_{Sub}) = -RT(\ln K_{TSA} - \ln K_{Sub})$$

$$= -RT\ln\left(\frac{K_{TSA}}{K_{Sub}}\right) = -RT\ln\left(\frac{k_{TSA}}{k_{Sub}}\right)$$

**Equation 2: Rearrangement of Gibbs free energy equation.**

$$k_{cat} = \frac{k_B T}{h} e^{-\frac{\Delta G^{\ddagger}}{RT}} = \frac{k_B T}{h} e^{\ln\left(\frac{k_{TSA}}{k_{Sub}}\right)} = \frac{k_B T}{h}\left(\frac{k_{TSA}}{k_{Sub}}\right)$$

**Equation 3:** Rearrangement of Arrhenius equation.

From **Equation 3** the $\frac{k_B T}{h}$ factor is considered constant at room temperature for all experiments thus it is concluded that there will be a linear correlation between $k_{TSA}/k_{sub}$ and $k_{cat}$. The plot of all 11 data points for the complexes of the bidentate ligands is shown in **Figure 102**. There is a positive slope which indicates positive correlation between $k_{TSA}/k_{sub}$ and $k_{cat}$. However the $R^2$ = 0.19 which means the correlation is less statistically significant. If the bindentate ligands with - OH moiety catalysts were plotted separately, a better correlation is found with $R^2$ = 0.86 (**Figure 103)**. From the kinetic experiments, the best catalyst is the one that has basic ligand (imidazole derivatives are better than benzimidazole) with an –OH moiety for additional hydrogen bonding.

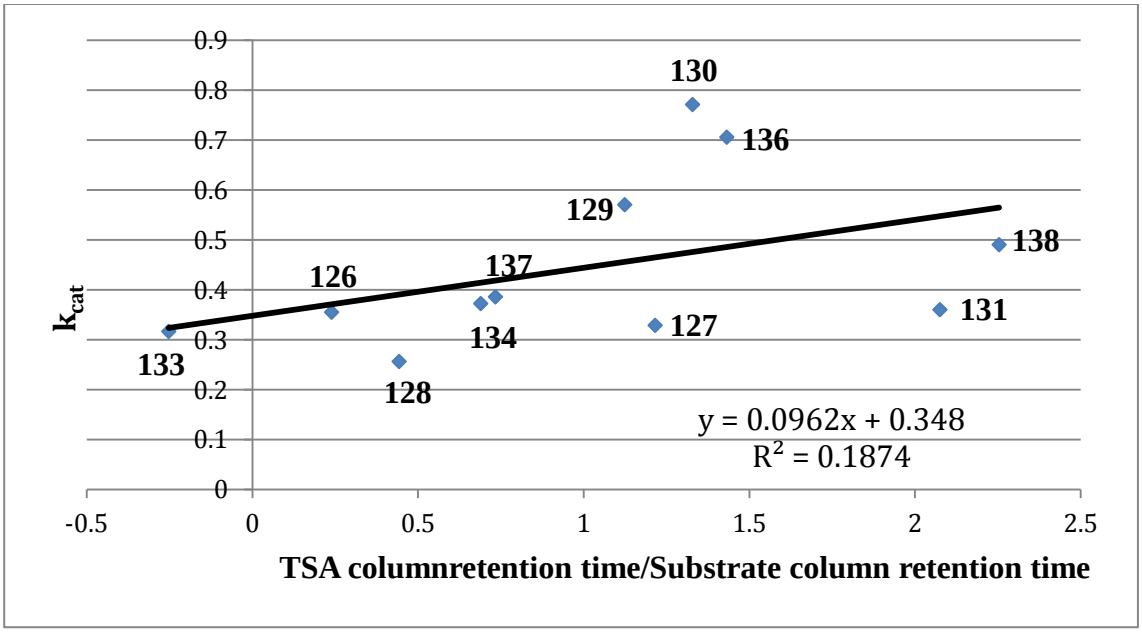


**Figure 102:** Plot of $k_{TSA}/k_{sub}$ and $k_{cat}$ for two-coordinate catalysts.

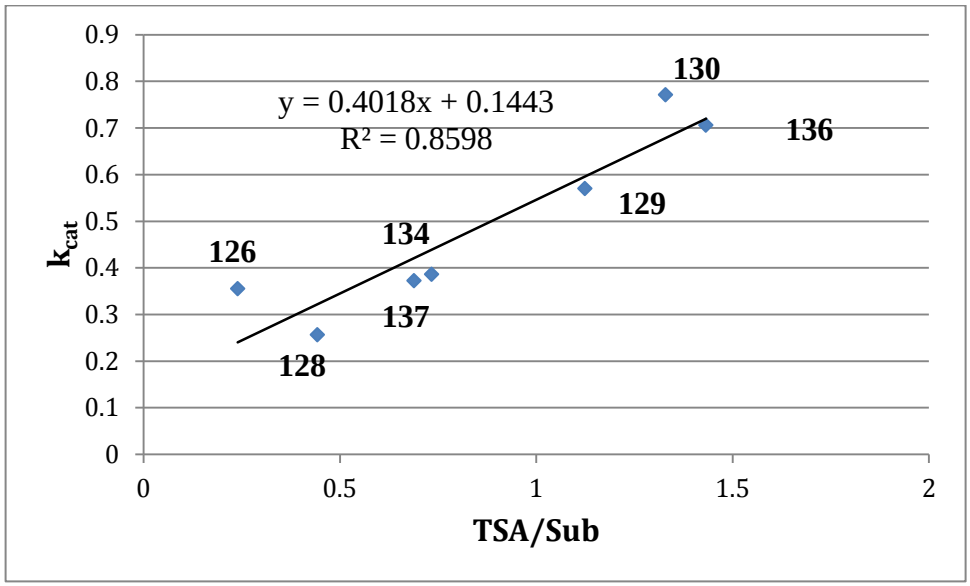


**Figure 103:** Plot of $k_{TSA}/k_{sub}$ and $k_{cat}$ for two-coordinate with - OH moiety catalysts.

There may be several reasons for the poor correlation between catalyst-TSA binding and rate of the reaction. One of the important assumptions for comparing retention time across different columns is that the m values, the number of mol of active binding site, are the same on all columns. The assumption might be correct on the benzyl reference column and the substrate column, but it might not be correct with the TSA column due to the fact that DIC can dehydrate the hydrated trifluoromethyl ketone to make trifluoromethyl ketone. At this point the trifluoromethyl ketone can be a strong electrophile and thus can be attacked by the amino moiety of the silica gel (**Figure 104**). The reaction would form a trifluoromethyl imine instead of amide coupling. The other explanation is that the ketone – hemiacetal – acetal equilibrium is significant at the high concentration of ethanol (40% solvent volume) forming the hemiacetal or acetal instead of hydrated ketone which are, of course, not correct TSAs (**Figure 105**).[193]

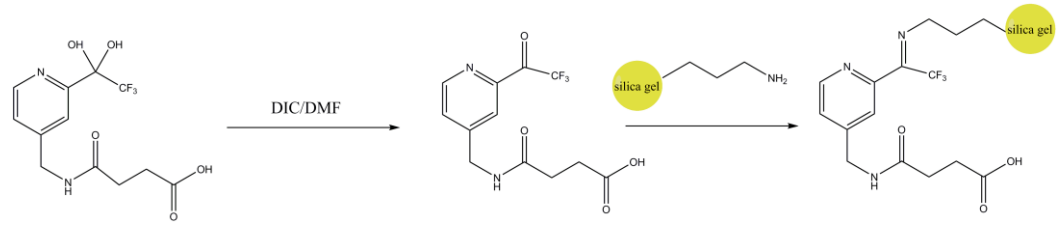


**Figure 104:** Possible side reaction chain when attaching **162** onto the silica gel.

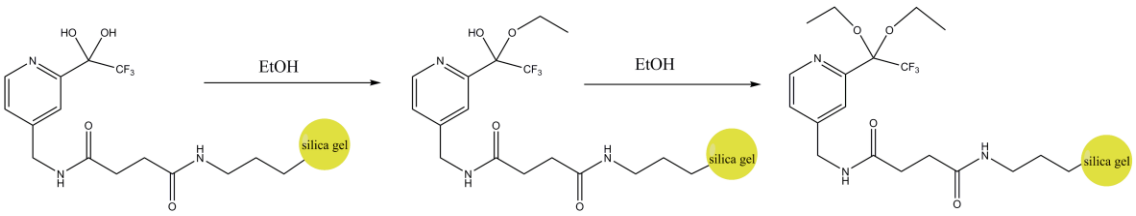


**Figure 105:** Possible hydrated ketone - hemiacetal – acetal problem.

### 4.4 Conclusion.

To investigate the relation of substrate analog and TSA as affinity ligand in affinity chromatography with substrate-catalyst binding constant ($1/K_M$) and the rate of the catalyzed reaction (kcat), three columns: substrate analog column, TSA column and benzyl reference column have been made. The functionalized columns have been successfully synthesized using 2 to 7 step linear syntheses.

In addition to the 7 ligands that were tested from previous study, the library of catalysts has been expanded to 14 ligands, which adds more catalyst structural and electronic variation. All 14 complexes were evaluated for catalytic activity with the Michaelis-Menten kinetics method, which yielded results for substrate-catalysts affinity ($1/K_M$) as well as information about the catalytic rate constants ($k_{cat}$). This new way of treatment also increased the data reliability and yielded more information about the

reaction than the previous study. A strong negative logarithm correlation with high statistical significant was found between substrate-catalyst binding constant ($1/K_M$) versus rate of the reaction ($k_{cat}$).

The substrate analog affinity column shows excellent linear positive correlation between catalyst retention time versus catalyst-substrate binding affinity. This strong correlation indicates that the substrate analog perfectly mimics the substrate in the substrate-catalyst binding step. The TSA column shows a positive correlation with less statistically significant between catalyst retention time versus $k_{cat}$. A better statistically significant value was found with $Zn^{2+}$ bidentate imine with an OH moiety catalysts, presumably are having the same mechanism. In both of the cases, positive correlations were found between catalyst retention time versus catalyst-substrate binding constant and catalyst activity ($k_{cat}$). These positive correlations prove the concept of using affinity chromatography as a promising tool for catalyst selection.

**4.5 Future directions.**

Because the trifluoromethyl ketone hydrate either seems to be a poor TSA for the hydrolysis reaction or the synthesis plan of coupling TSA with the solid support might not be efficient, the phosphonate esters are good alternatives. Compared to trifluoromethyl ketone hydrate, phosphonate esters have been used as TSA for the hydrolysis in catalyst antibodies much earlier and are easier to make.[6-8] Our group has also successfully employed the phosphonate esters as the TSA for ester hydrolysis reactions.[70-72] Two phosphonate esters could be used as the TSA affinity ligand for the experiments are proposed below (**Figure 106**). Compound **163** employed the same idea

as the trifluoromethyl ketone hydrate while compound **164** is slightly different where the linker is attracted to the alcohol moiety. Either compound **163** or **164** can be made with fewer steps from commercially available chemicals compared to the trifluoromethyl ketone hydrate. Moreover, the coupling reaction should be less sophisticated because of no anticipated side reactions.

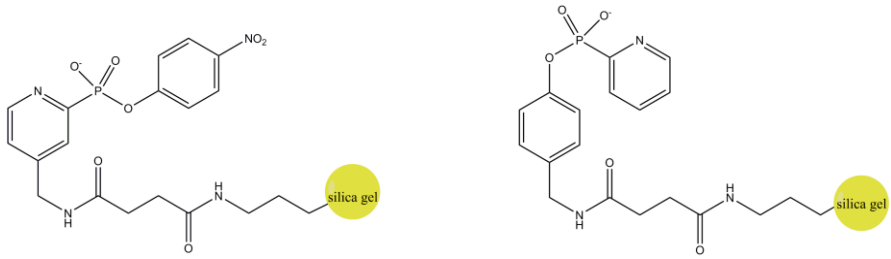


**163** **164**

**Figure 106:** Proposed phosphonate esters as the new TSA affinity ligands.

While the substrate analog perfectly mimics the substrate in the substrate-catalyst binding step and the new phosphate ester could be a better alternative for the trifluoromethyl ketone hydrated as the TSA, the non-specific binding problem is still unsolved. If the non-specific binding is minimized to negligible then the benzyl reference column can be eliminated. The suspects for the non-specific binding are two amide groups and the short chain linker which potentially coordinate with ligands and/or $Zn^{2+}$ thus increase catalyst retention time. If a long aliphatic linker, preferably 18 carbon chain like the revered phase column, was employed then the interaction between polar catalysts, (imine)$Zn^{2+}$, and the linker are negligible. On the other hand, ether linkages are, generally speaking, less susceptible to nucleophilic attack and less likely to form strong coordinate with $Zn^{2+}$ than the amide linkages thus ether linkages should be more stable and less non-specific binding compared with amide linkages. The

combination of long aliphatic chain and ether linkages in the linker should eliminate most of the non-specific binding with the column. The best linkage that chemically available is a long C-C bond directly from silica gel to the affinity ligand. However making such a long C-C chain bond with in column synthesis method, practically, would be a big challenging.

While it is not demonstrated in this study but with the observed good peak resolution (base to base less than 1 minute in most of the cases) and retention time range (from 4.7 to 26 min), it may be possible to conduct a high throughput catalyst selection with this method. In particular, a mixture of catalysts is passing the columns and the best catalyst is the one that has longest retention time in the solid supported TSA column and the catalyst with the best catalyst-substrate binding constant is the one that have longest retention time in the solid supported substrate analog column.

## 4.6 Experimental.

### 4.6.1. Materials preparation.

The following compounds were synthesized by literature methods:

*4-cyano ethyl picolinate* (**143**)[181]. $^1$H-NMR: (300 MHz, $CDCl_3$): δ 8.97 (d, 1H, J= 3.8 Hz), 8.35 (d, 1H, J = 2.0 Hz), 7.21 (dd, 1H, J = 5.4; 1.8 Hz), 4.52 (q, 2H, J = 7.2 Hz), 1.47 (t, 3H, J= 6.9 Hz).

*4-(benzylamino)-4-oxobutanoic acid* (**148**)[182] $^1$H-NMR: (300 MHz, DMSO-$D_6$): δ 12.19 (s, 1H); 8.44 (t, 1H, J = 5.1 Hz); 7.36 (m, 4H); 4.31 (t, 2H, J = 5.1 Hz); 2.49 (m, 4H). IR: Need IR here.

*2-(hydroxymethyl) isonicotinonitrile* (**158**)[188] $^1$H-NMR: (300 MHz, $CDCl_3$): δ 8.75 (d, 1H, J = 5.1 Hz), 7.59 (s, 1H), 7.45 (d, 1H, J = 4 Hz), 4.85 (d, 2H, J = 4.5Hz), 3.25 (t, 1H, J= 4.5 Hz)

*2-formylisonicotinonitrile* (**159**)[188] $^1$H-NMR: (300 MHz, $CDCl_3$): δ 10.11 (s, 1H), δ 9.00 (d, 1H, J = 6.0Hz), δ 8.18 (d, 1H, J = 1.5Hz), δ 7.77 (dd, 1H, J = 6.0; 1.5 Hz).

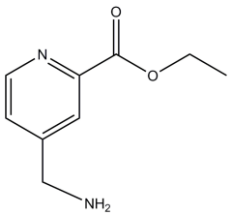


*4-(aminomethyl) ethyl picolinate* (**144**). Into a high pressure stainless steel reactor a solution of 4-cyano ethyl picolinate (**143**) (5.28 g; 30 mmol) in 50 ml MeOH was added together with Pd on C (0.636 g ~ 0.3 mmol; Aldrich Degussa type E101 NEW). The reactor was sealed and the $H_2$ pressure was maintained at 700 psi (~ 50 bar) during the reaction. After 1 hour, the reaction was stopped and the solvent was evaporated in vacuo. The black solid was added with 100ml of EtOAc and the Pd on C was filtered off through a silica gel column. The solvent was evaporated under vacuum to yield 4.95 g (25.5 mmol, 85%) of a yellow liquid. The compound was immediately used for the next step to prevent intermolecular reaction. No further purification was needed. $^1$H-NMR: (300 MHz, $CDCl_3$): δ 8.54 (d, 1H, J = 5.4Hz), δ 8.01 (s, 1H, J = 1.2Hz), 7.38 (dd, 1H, J = 5.4; 1.2Hz), 4.38 (q, 2H, J = 7.0Hz), 3.902 (s, 2H), 1.35 (t, 3H, J= 6.9 Hz) (**Figure 107**). $^{13}$C-NMR (75 MHz, $CDCl_3$): 165.3, 153.4, 149.9, 148.3, 125.1, 123.4, 61. 9, 45.0, 14.1 (**Figure 108**): HRMS (ESI) calculated for $C_9H_{13}N_2O_2$ ($M+H^+$) 181.0977, found 181.1178; calculated for $C_9H_{12}N_2O_2Na$ ($M + Na^+$) 203.0796, found 203.0809; calculated for $C_9H_{12}N_2O_2K$ ($M + K^+$) 219.0536, found 209.0787.

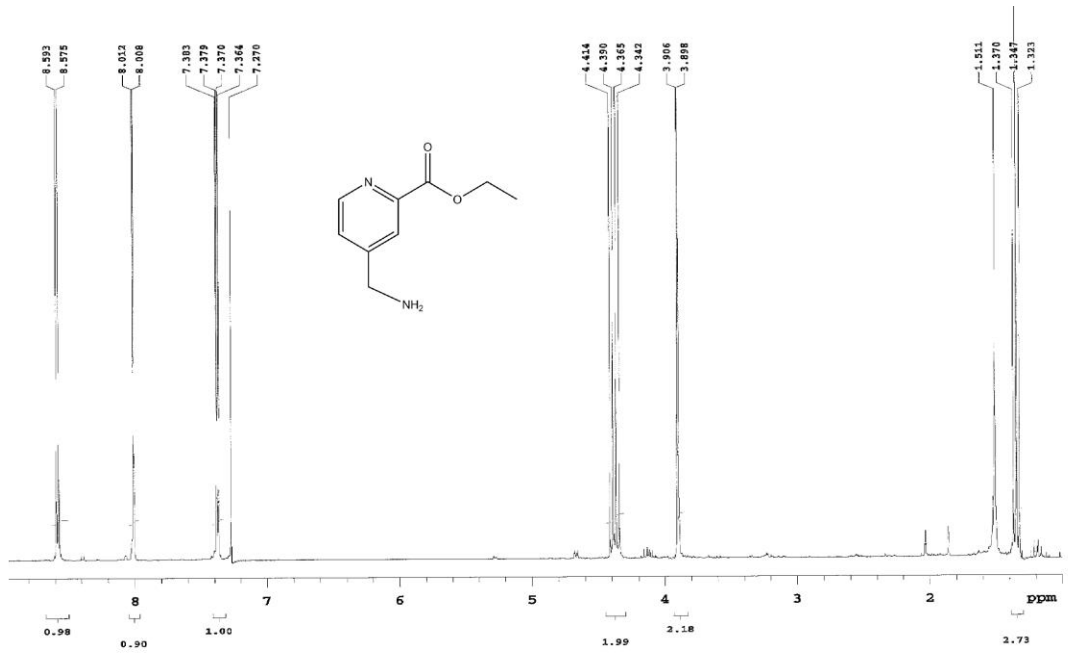


**Figure 107:** $^{1}$H-NMR spectrum of **144.**

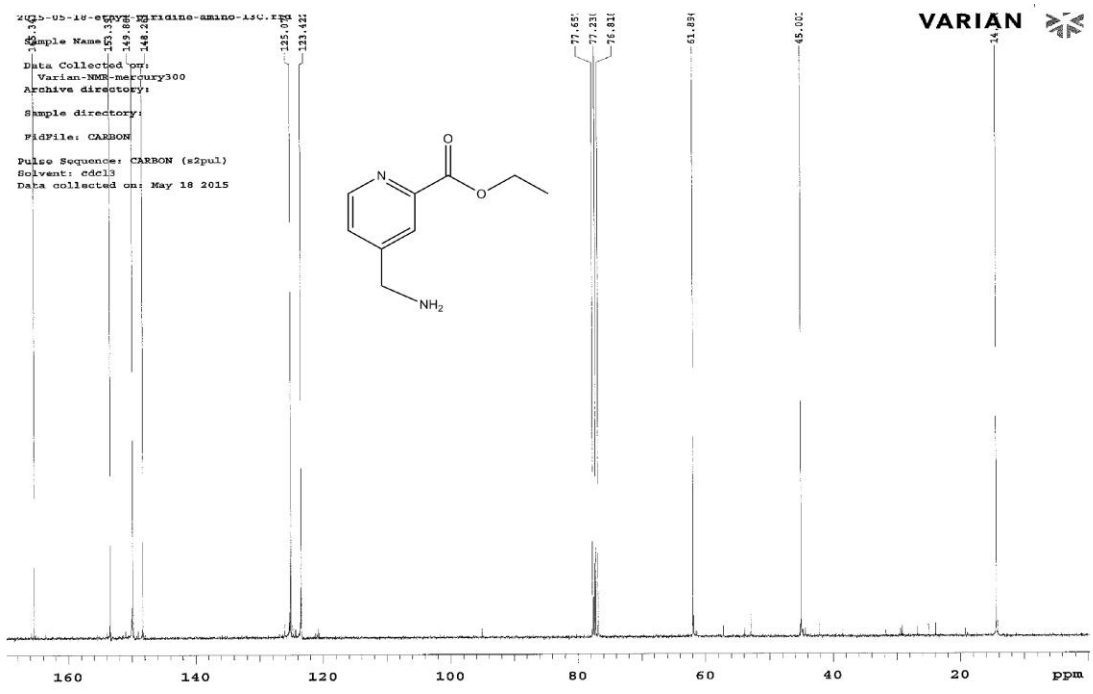


**Figure 108:** $^{13}$C-NMR spectrum of **144.**

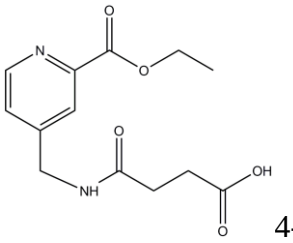


4-2-(ethoxycarbonyl)pyridin-4-yl)methylamino-4-oxobutanoic acid (**145**). To a solution of **144** (4.95 g, 25.5 mmol, in 50 ml THF), a saturated solution of succinic anhydride (2.55 g, 25.5 mmol) in THF was added at once. The solution was gently stirred overnight. The next morning the solid white precipitate was filtered with a Büchner funnel and then washed with 50 ml THF and 50 ml EtOAc. The solid white material was dried under high vacuum to yield 6.43 g (2.29 mmol, 90% yield). No further purification was needed. $^{1}$H-NMR: (300 MHz, DMSO-$D_6$): δ 8.64 (d, 1H, J= 5.4 Hz), 8.60 (t, 1H, J = 5.7Hz), 7.96 (s, 1H), 7.53 (d, 1H, J = 4.5 Hz), 4.41-4.34 (m, 4H), 2.53-2.46 (m, 4H), 1.35 (t, 2H, J= 6.9 Hz) (**Figure 109**). $^{13}$C-NMR (75 MHz, DMSO-$D_6$): 173.9, 171.7 164.9, 150.4, 149.7, 147.7, 125.4, 123.1, 61.3, 41.1, 30.0, 29.1, 14.2- (**Figure 110**). HRMS (ESI) calculated for $C_{13}H_{17}N_2O_5$ ($M+H^+$) 281.1137, found 281.1149; $C_{13}H_{16}N_2O_5Na$ ($M+Na^+$) 303.0957, found 303.1213; $C_{13}H_{16}N_2O_5K$ ($M+K^+$) 319.0696 found 319.1044. FTIR (KBr pellet) $cm^{-1}$ (s): 3306; 1721; 1661; 1608; 1549 (**Figure 111**)

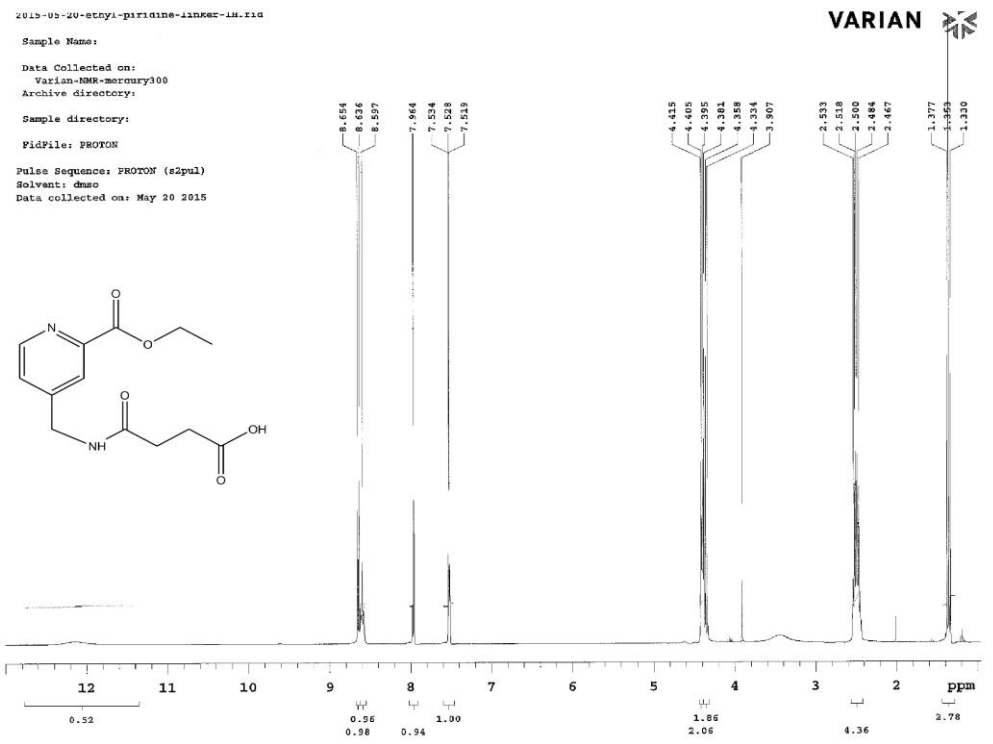


**Figure 109:** $^{1}$H-NMR spectrum of **145**

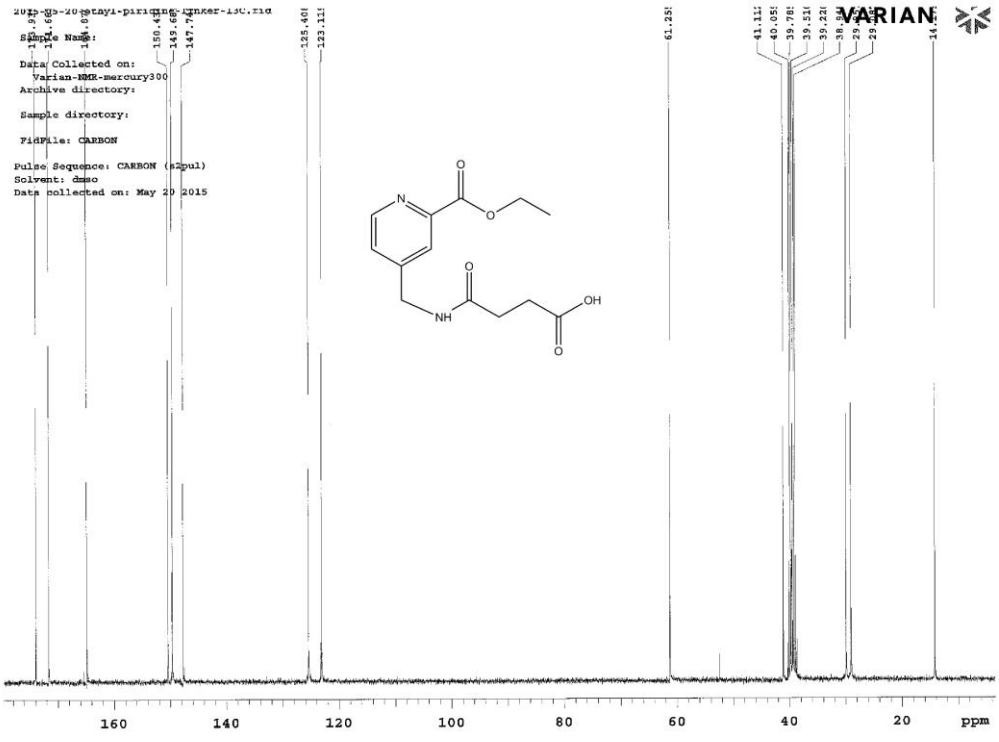


**Figure 110:** $^{13}$C-NMR spectrum of **145**

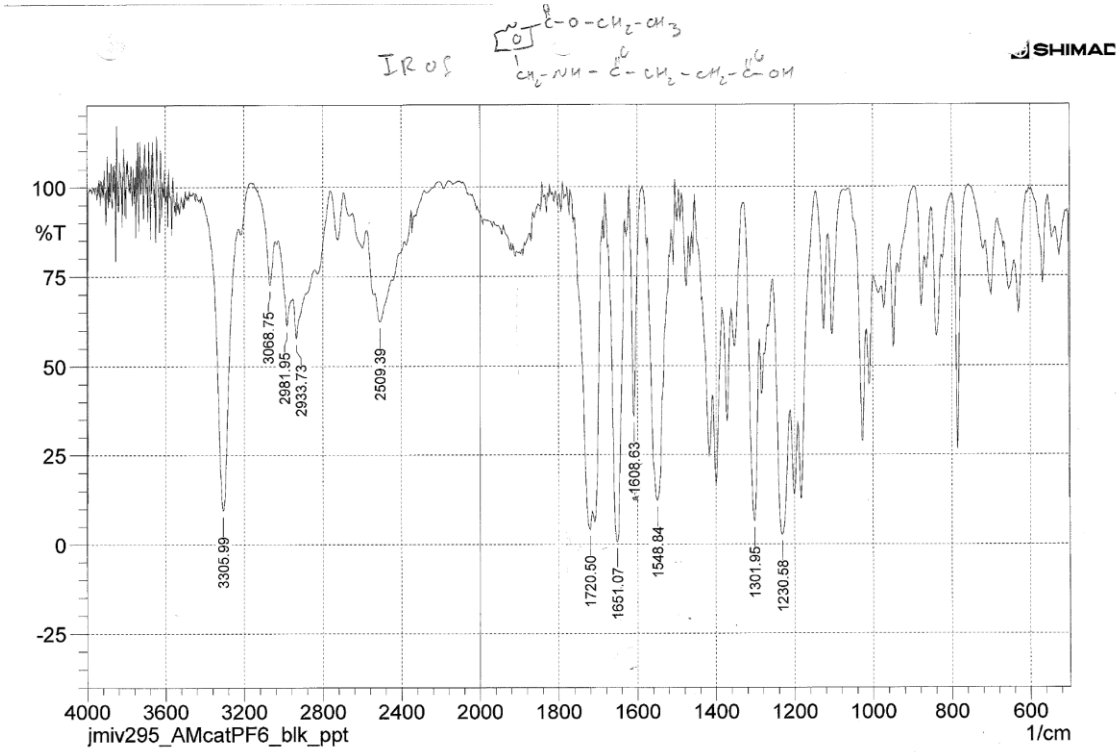


**Figure 111:** FTIR spectrum of **145**

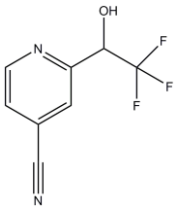


2-(2,2,2-trifluoro-1-hydroxyethyl)isonicotinonitrile (**160**). In a nitrogen atmosphere, to a solution of **159** (5.40 g, 41 mmol) in 50 ml of dry THF (distilled over Na benzophenone), Ruppert-Prakash reagent ($TMSCF_3$, 6.64 ml, 45 mmol) was added at once and followed by carefully adding tetrabutylammonium fluoride (1M in THF; 0.4 ml, 0.4 mmol). The solution changed into a dark brown color. After 3 hours, 4N HCl (100 ml) was added at once and the solution was kept stirring for an additional 1 hour. The organic layer was separated and the aqueous layer was washed with 3 x 50 ml of EtOAc. The organic portions were combined and washed with 100 ml DI water. The

organic layer was dried over $MgSO_4$ and the solvent was removed under reduced pressure to yield 7.96 g of a light brown solid (39.4 mmol, 96% yield). No further purification was needed. $^{1}$H-NMR: (300 MHz, $CDCl_3$): δ 8.85 (d, 2H, J = 5.1Hz); 7.71 (s, 1H); 7.65 (d, 1H, J = 5.1Hz); 5.13 (q, 1H, J = 6.3Hz); 4.96 (d, 1H, J = 7.2Hz) (**Figure 112**). $^{13}$C-NMR (75 MHz, $CDCl_3$): 153.4; 149.8; 126.4; 125.6; 124. 7; 123.5 (q, $J_{C\text{-}F\ short}$ = 284.0 Hz); 115. 9; 70.9 (q, $J_{C\text{-}F\ long}$ = 32.2 Hz) $^{19}$F-NMR (282 MHz, $CDCl_3$) -77. 8 (d, 3F, J= 7.1Hz) (**Figure 114**). HRMS (ESI) calculated for $C_8H_6F_3KN_2O$ ($M + K^+$) 242.0069, found 242.2859.

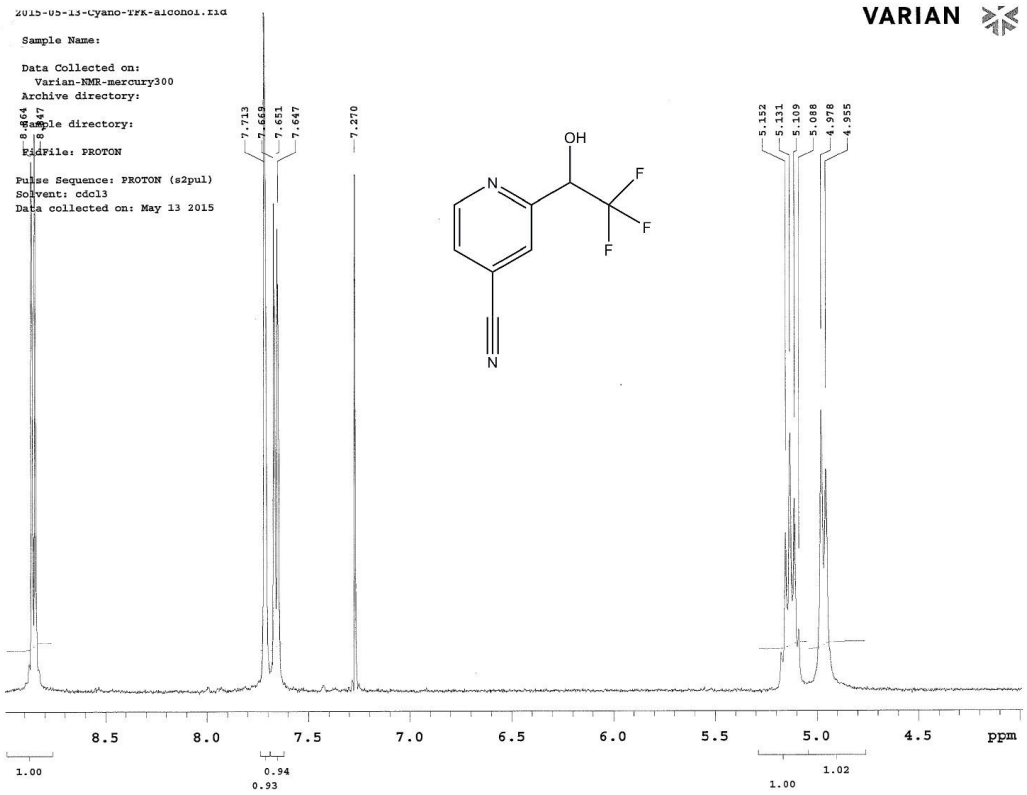


**Figure 112:** $^{1}$H-NMR spectrum of **160.**

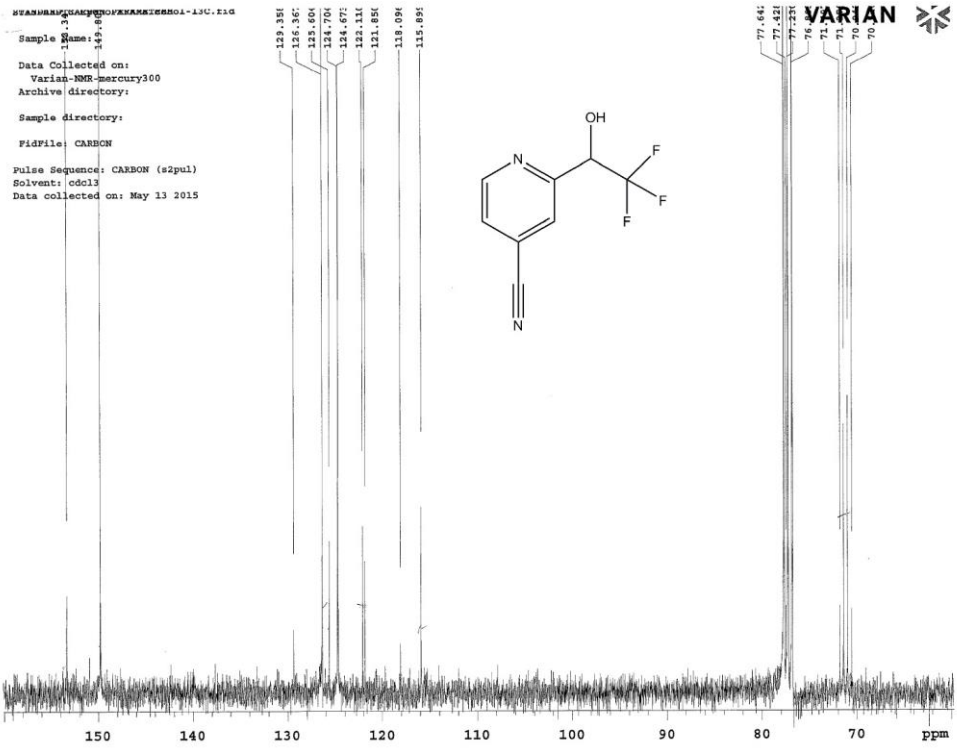


**Figure 113:** $^{13}$C-NMR spectrum of compound **160.**

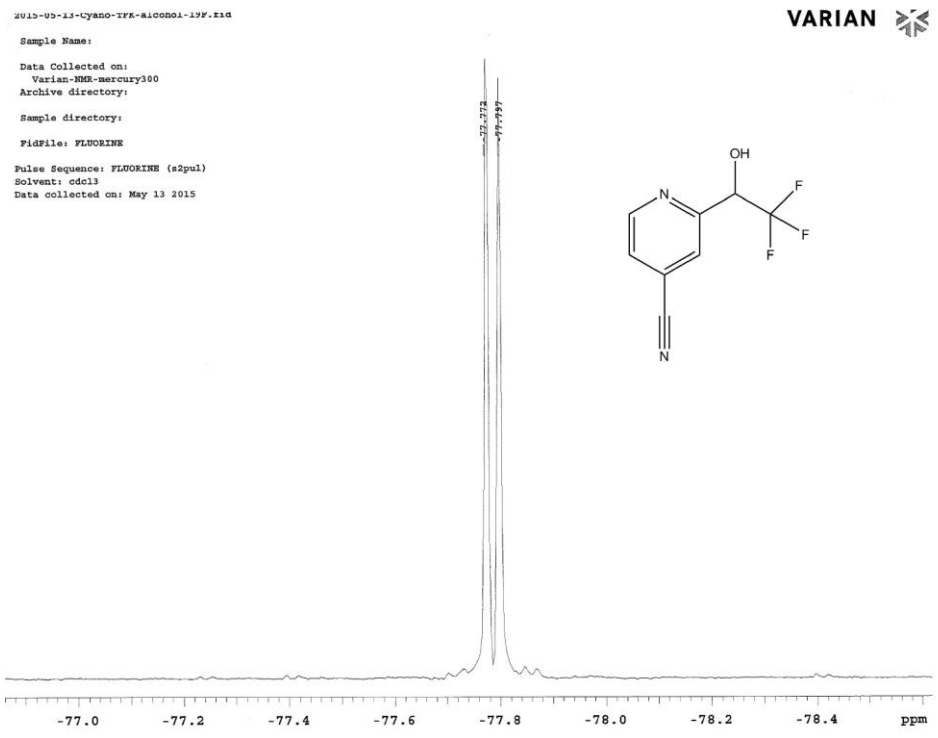


**Figure 114:** $^{19}$F-NMR spectrum of compound **160.**

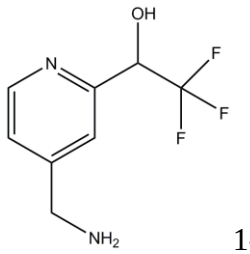


1-(4-(aminomethyl)pyridin-2-yl)-2,2,2-trifluoroethan-1-ol (**157**). In a high pressure reactor, to a solution of 2-(2,2,2-trifluoro-1-hydroxyethyl)isonicotinonitrile (**160**) (7.96g; 39.4 mmol ) in 50 ml MeOH was added Pd on C (0.848g ~ 0.4mmol; Aldrich Degussa type E101 NEW). The reactor was sealed and the $H_2$ pressure was maintained at 700psi (~ 50 bar) during the reaction. After 4 hour, the reaction was stopped and the solvent was evaporated in vacuo. The black mixture was added 200ml of EtOAc and the Pd on C was filtered off through a silica gel column. The solvent was evaporated under vacuum to yield a light yellow liquid 7.46 g (36.2 mmol, 92% isolated yield). No further purification was needed. $^{1}$H-NMR: (300 MHz, $CDCl_3$): δ 8.55 (d, 1H, J = 4.5 Hz); 7.42 (s, 1H); 7.36 (d, 1H, J = 4.5Hz); 5.02 (q, 1H, J = 6.6 Hz); 3.98 (s, 2H); ~3.5-2.8 (br, 2H) (**Figure 115**). $^{13}$C-NMR (75 MHz, $CDCl_3$): 155.2; 150.0; 148.6; 125.2 (q, $J_{C\text{-}F\ short}$ = 283 Hz); 122.2, 120.3; 72.1 (q, $J_{C\text{-}F\ long}$ = 30.2 Hz) (**Figure 116**). $^{19}$F-NMR (282.282 MHz, $CDCl_3$) -77.93 (d, 3F, J = 6.8 Hz) (**Figure 117**). HRMS (ESI) calculated for $C_8H_{10}F_3N_2O$ ($M + H^+$) 207.0745 found 207.0557; calculated for $C_8H_9F_3N_2ONa$ ($M + Na^+$) 229.0565 found 229.0598.

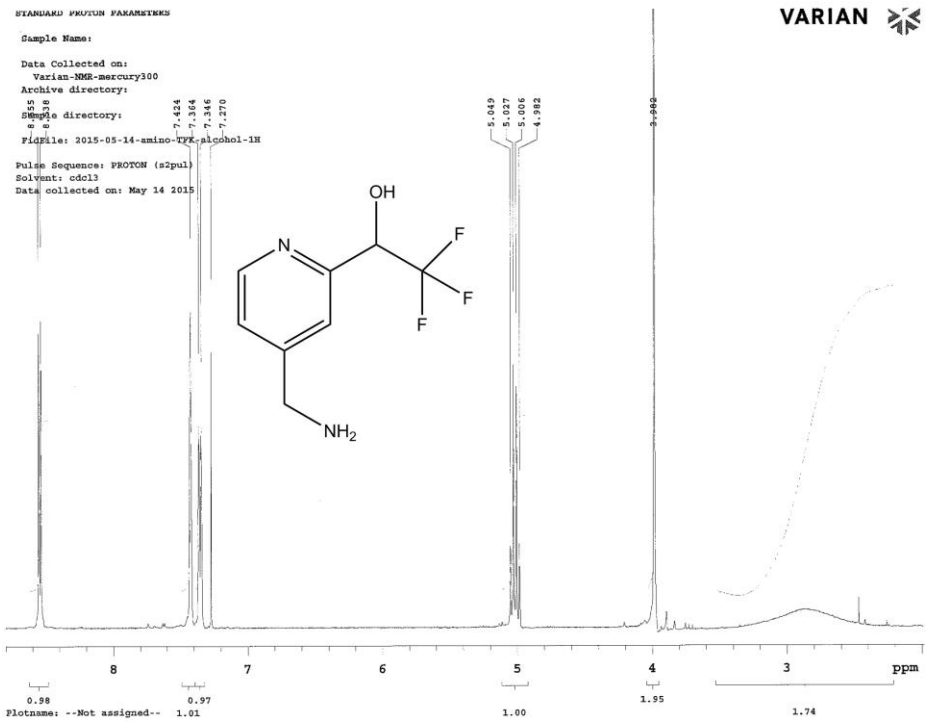


**Figure 115:** $^{1}$H-NMR spectrum of **157.**

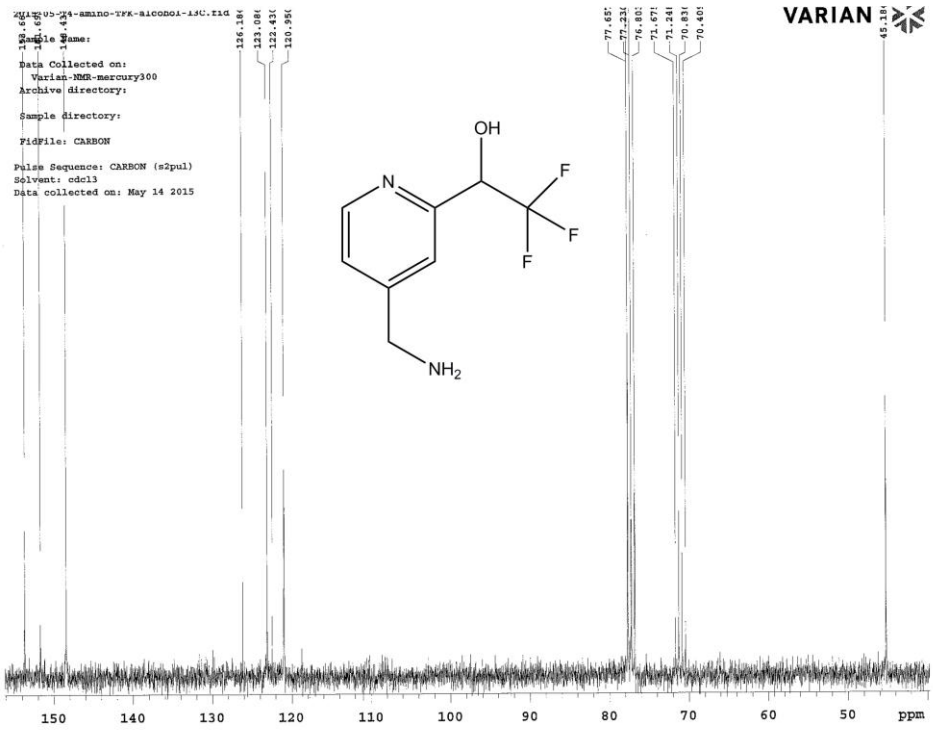


**Figure 116:** $^{13}$C-NMR spectrum of **157.**

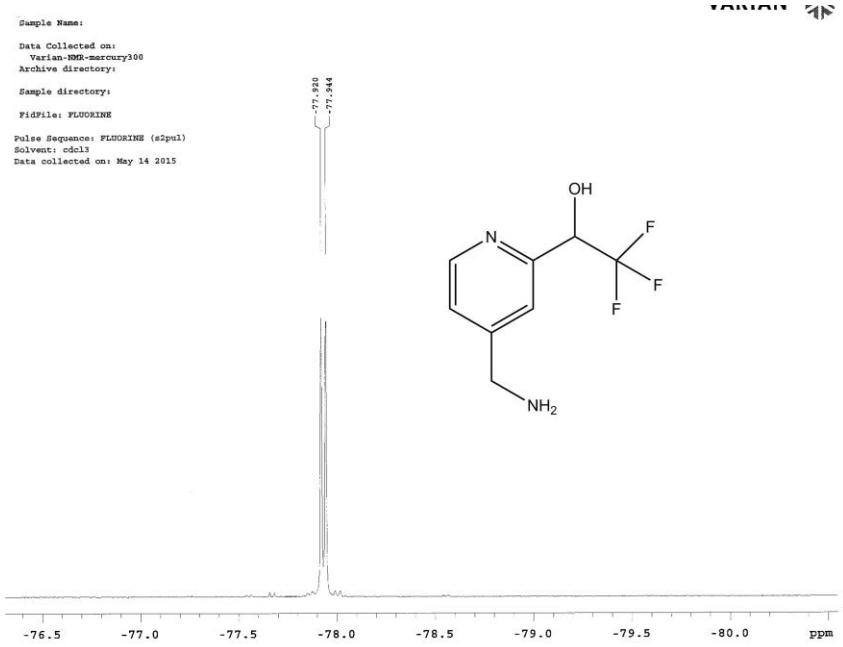


**Figure 117:** $^{19}$F-NMR spectrum of **157.**

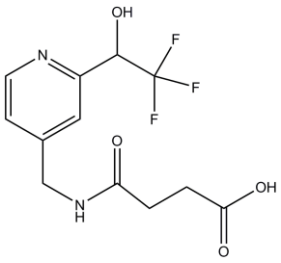


4-oxo-4-2-(2,2,2-trifluoro-1-hydroxyethyl)pyridin-4-yl methylamino-butanoicacid (**161**). To a solution containing 7.46 g of 1-(4-(aminomethyl)pyridin-2-yl)-2,2,2-trifluoroethan-1-ol (**157**) in 100 ml of THF, a saturated solution of succinic anhydride (3.62 g, 36.2 mmol) in THF was added at once. The solution was gently stirred and left overnight. The next morning the solvent was removed and 100 ml of EtOAc was added. The solid white precipitate was collected by filtration through a 0.45 µm Millipore® nylon 66 filter and then washed with 20 ml THF and 50 ml EtOAc. The solid white material was dried under high vacuum to yield 8.86 g (28.96 mmol, 80% yield). No further purification was needed. $^{1}$H-NMR: (300

MHz, DMSO-$D_6$): δ 8.62 (t, 1H, J = 6.0Hz), 8.55 (d, 1H, J = 4.5Hz), 7.65 (s, 1H), 7.39 (d, 1H, J = 4.5Hz), 4.39 (d, 2H, J = 6.0Hz), 2.48 (m, 4H) (**Figure 118**). $^{13}$C-NMR (100 MHz, DMSO-$D_6$): 173.8; 171.5; 155.13; 150.0; 148.6; 124.8 (q, $J_{C\text{-}F\ short}$ = 238 Hz); 122.20; 120.22; 72.07 (q, $J_{C\text{-}F\ long}$ = 29.3 Hz); 41.16; 29.95; 29.07 (**Figure 119**). $^{19}$F-NMR (282.282 MHz, DMSO-$D_6$) -75.70 (d, 3F, J = 7.1 Hz) (**Figure 120**). HRMS (ESI) calculated for $C_{12}H_{14}F_3N_2O_4$ ($M + H^+$) 307.0906 found 307.0714; calculated for $C_{12}H_{13}F_3N_2O_4Na$ ($M + Na^+$) 329.0725, found 329.0982.

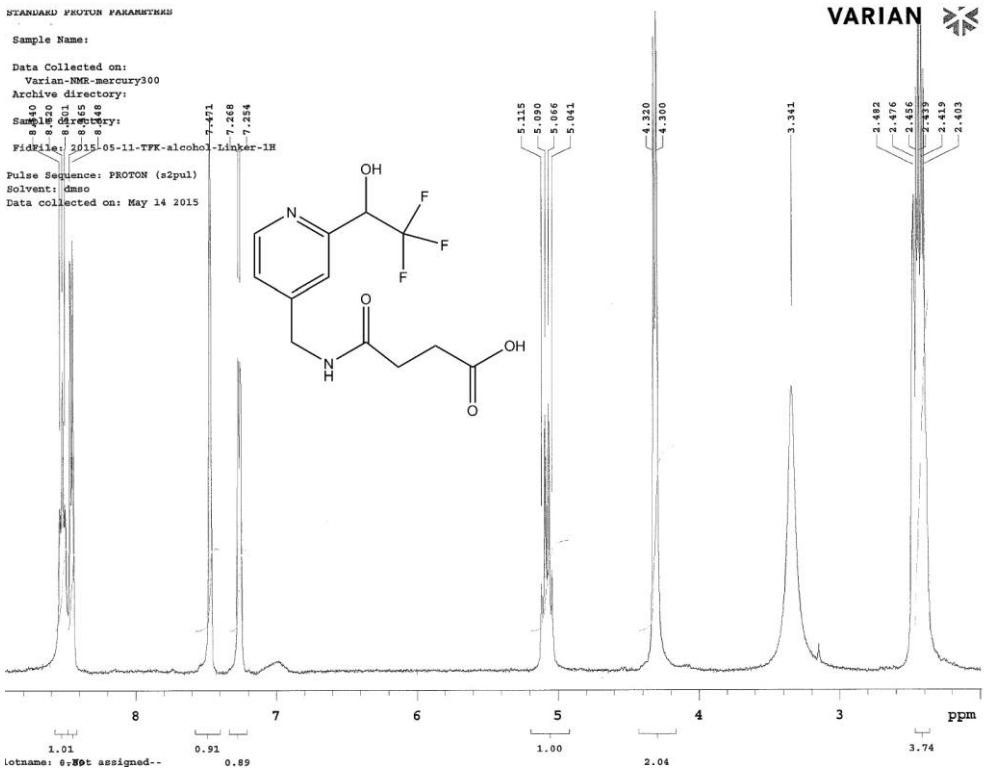


**Figure 118:** $^1$H-NMR spectrum of **161.**

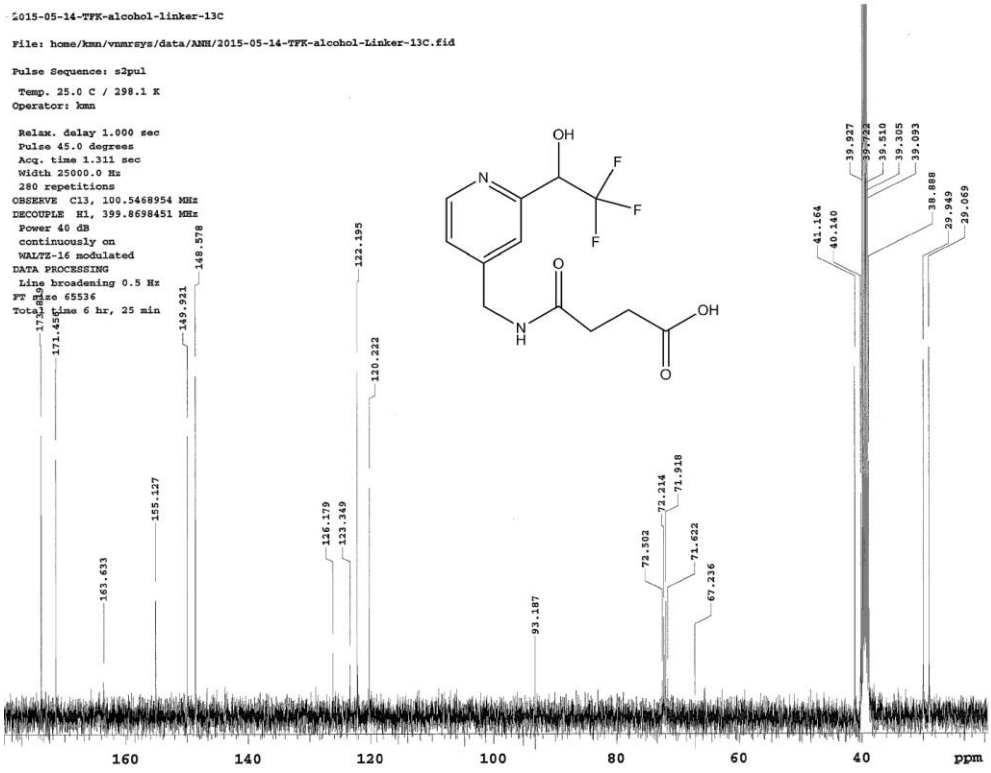


**Figure 119:** $^{13}$C-NMR spectrum of **161.**

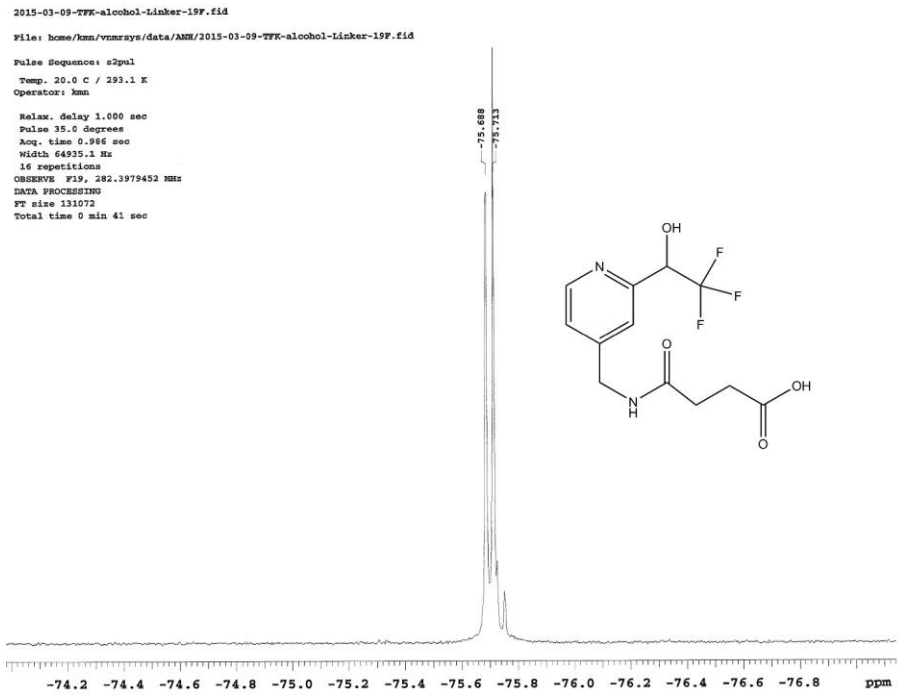


**Figure 120:** $^{19}$F-NMR spectrum of **161.**

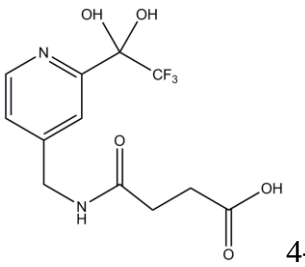


4-oxo-4-2-(2,2,2-trifluoro-1,1-dihydroxyethyl)pyridin-4-yl)methyl)amino)butanoic acid (**162**). To a round bottom flash, 8.86 g (28.96 mmol) of 4-oxo-4-(((2-(2,2,2-trifluoro-1-hydroxyethyl)pyridin-4-yl)methyl)amino)butanoic acid (**161**) was added in 100 ml of 1,4-dioxane. The mixture was heated at $80^0$C and stirred until clear. Selenium dioxide (1.92 g, 17.3 mmol) was added at once and the reaction was stopped after 1 hour. The temperature of the oil bath ($80^0$C) is critical for this reaction. The solid black selenium was filtered off (0.45 µm Millipore® nylon 66) to give a red solution. The 1,4-dioxane was evaporated under reduced pressure to give a thick red liquid. 2ml of DI water was added to the red liquid above and the mixture was washed with 2 x 50 ml of EtOAc then 2 x 50 ml of methylene chloride. Upon addition of methylene chloride the liquid spontaneously solidified. Actively pumping the red solid under high vacuum for 24 hours gave 8.21g (25.5 mmol, 88% yield) of **162**. The compound is pure (NMR) however it has red color from selenium as a contaminant. This contaminant will be removed in the next step. $^1$H-NMR: (300 MHz, DMSO-$D_6$): δ 8.62 (t, 1H, J = 6.0Hz), 8.55 (d, 1H, J = 4.5Hz), 7.65 (s, 1H), 7.39 (d, 1H, J = 4.5 Hz), 4.39 (d, 2H, J = 6.0Hz), 2.48 (m, 4H) (**Figure 121**). $^{13}$C-NMR (75 MHz, DMSO-$D_6$): 174.1, 171.8, 155.7; 150.5; 148.0; 123.6 (q, $J_{C\text{-}F\ short}$ = 288.4 Hz); 123.0; 120.4; 92.3 (q, $J_{C\text{-}F\ long}$ = 30.9 Hz); 41.39; 30.11; 29.225 (**Figure 122**). $^{19}$F-NMR (282.282 MHz, DMSO-$D_6$) -81.90 (s, 3F) **(Figure 123).** HRMS (ESI) calculated for $C_{12}H_{14}F_3N_2O_5$ (M + $H^+$) 323.0855 found 323.1277; calculated for methyl hemiketal $C_{13}H_{16}F_3N_2O_5$ (M

+MeO$^-$) 337.2752, found 329.1306. FTIR (KBr pellet) cm$^{-1}$: 3290, 1734, 1655, 1543, 1419 (**Figure 124**).

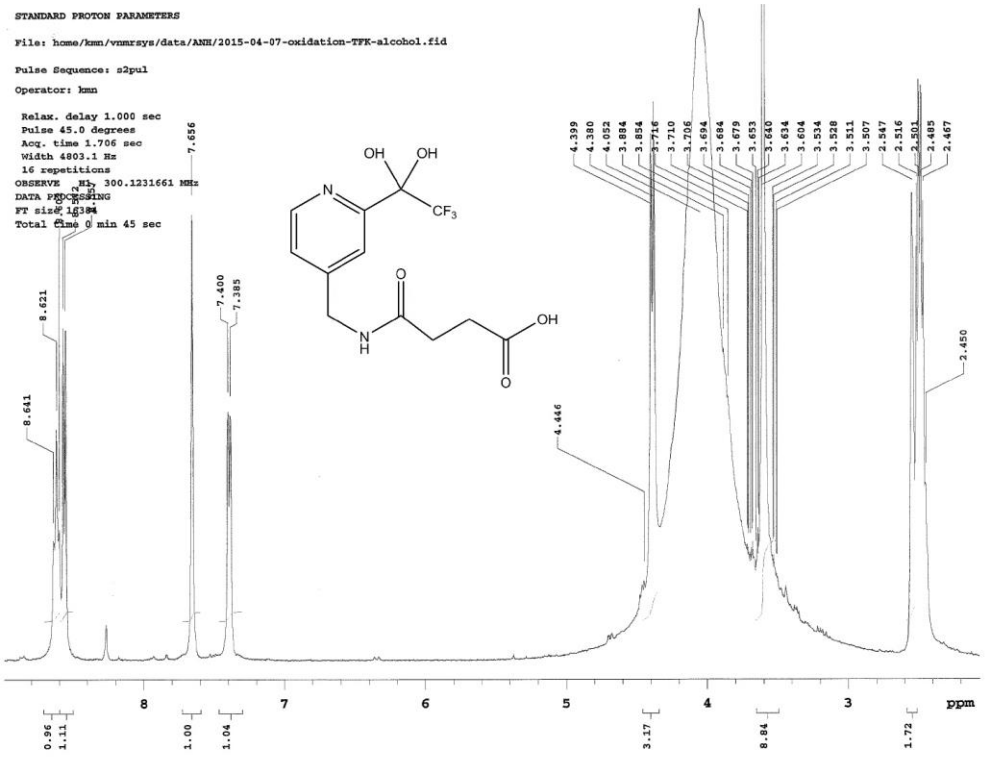


**Figure 121:** $^1$H-NMR spectrum of **162**

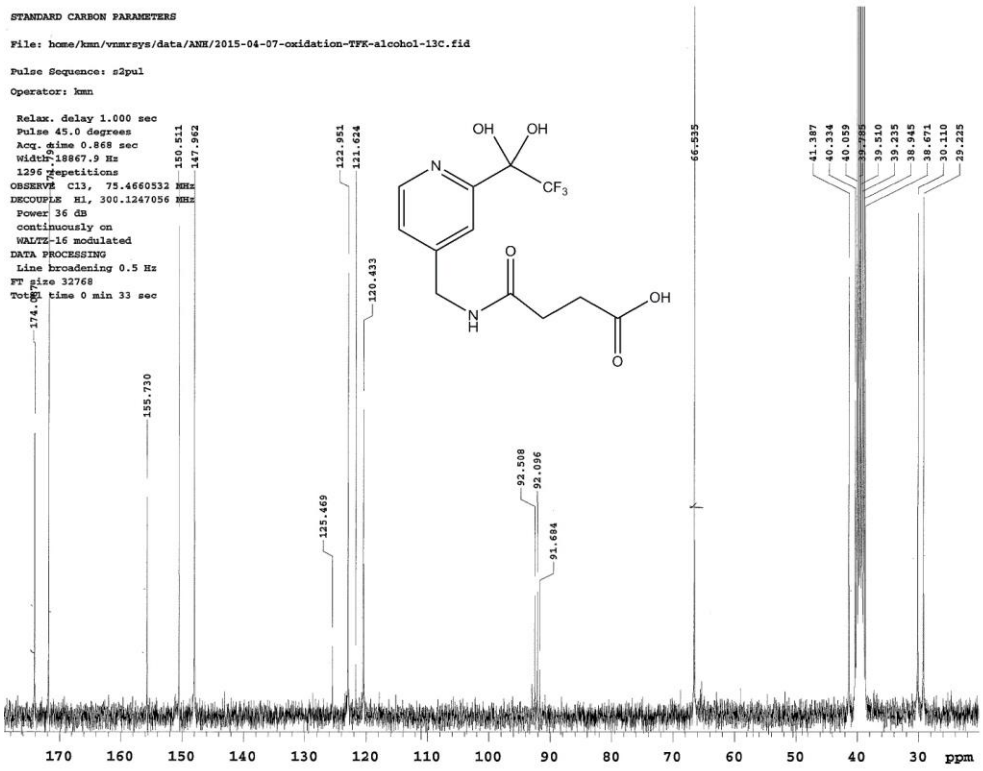


**Figure 122:** $^{13}$C-NMR spectrum of **162**

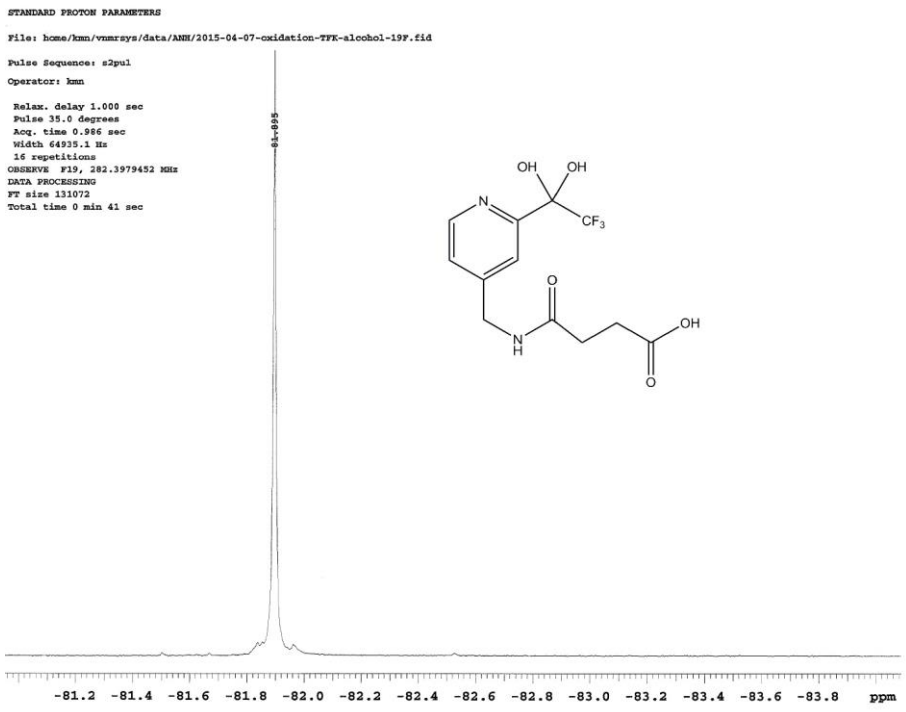


**Figure 123:** $^{19}$F-NMR spectrum of **162**

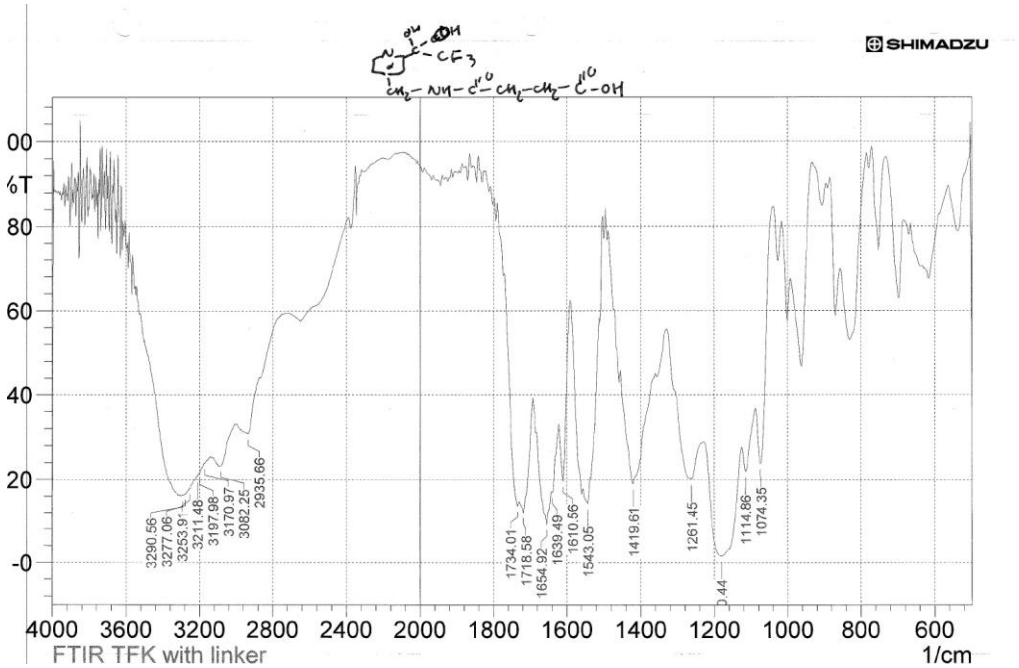


**Figure 124:** IR spectrum of compound **162**.

### 4.6.2 Silica Functionalization

For the purpose of method validation, three homemade 150x4.6 mm HPLC columns were packed with 3-aminopropyl-funcinalized silica gel (Sigma Aldrich product number 364258-10G). Each column was functionalized by the below procedure with the substrate analog with linker **140**, the benzyl reference with linker **141** or the TSA with linker **139**. After the test, a small portion of the silica gel at both the inlet and the outlet was removed for IR analysis. For the purpose of making columns for the chromatography studies, three identical brand new HPLC amino columns (Zobax $NH_2$ 4.5 x 150 mm 5 µm, product number 883952-708) were used.

Drying column: Pure nitrogen gas was run through the column at the rate ~ 1 ml/min for 4 hours then the oven was turned on to $80^0$C for 24 hour. The oven was turned off and let cool down to room temperature while the $N_2$ gas was still running. After the oven and column reached room temperature, the $N_2$ gas was shut off. The

HPLC line was flushed with THF (dried Na/benzophenone), then the column was connected and washed with an additional 50 ml of dry THF.

To 50 ml of dry DMF (Drisolv®), 10 mmol of either the substrate analog with linker **145** (2.80 g), the benzyl reference with linker **148** (2.07 g) or the TSA with linker **162** (3.22g) was added. The mixture was stirred until clear and DIC (12 mmol, 1.87 ml) was added and hydroxybenzotriazole (HOBt) (1.62 g, 12 mmol) was added after 20 min. The mixture was left at room temperature for 2 hours and the solid was collected by filtration (Millipore® nylon 66).

In column functionalization: The instrument was set up as in the **Figure 125**. The filtered mixture was pumped at the rate of 1.0 ml/min through the column during the reaction. The reaction was set at room temperature for 5 hours, then the temperature was slowly ramped up to $80^0$C over 2 hours and hold at $80^0$C overnight. The next day the oven was turned off and the column was cooled down to room temperature (HPLC pump still on). The column was subsequently washed with 50 ml of DMF, 50 ml of dry THF and 100 ml of MeOH. During the reaction, if the back pressure rises above 3500 psi then the pump was stopped for filter cleaning or changing (if needed).

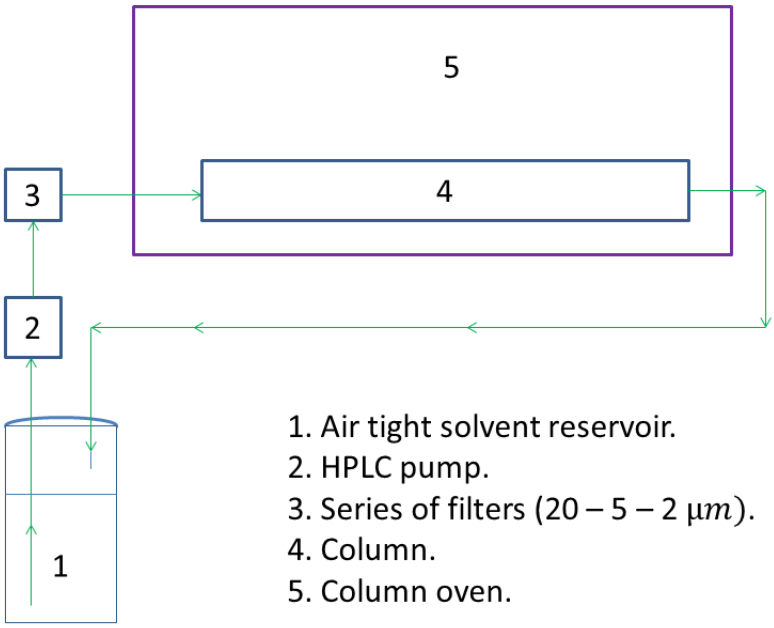


**Figure 125:** In column functionalization set up.

The IR analysis showed no difference in the spectra of the inlet and outlet ends. The spectrum of amino silica gel before and after the functionalization with compound **145**, **148** and **162** are in **Figure 126**, **Figure 127**, **Figure 128** and **Figure 129** respectively.

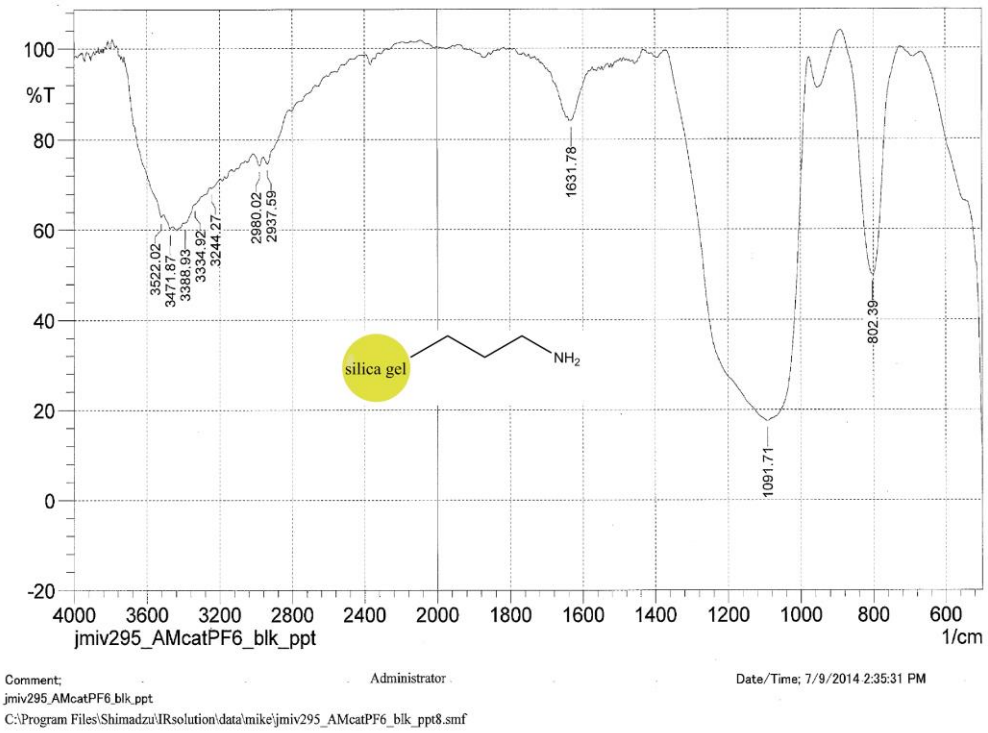


**Figure 126:** IR spectrum of amino silica gel **146**.

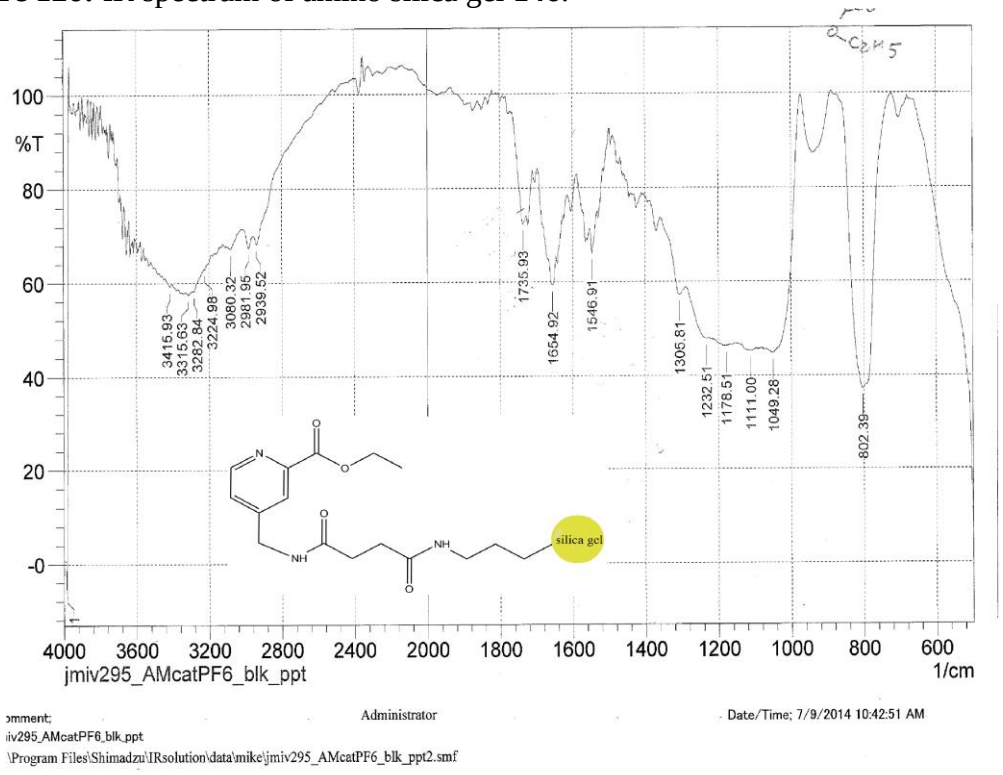


**Figure 127:** IR spectrum of substrate analog with linker on silica gel 140.

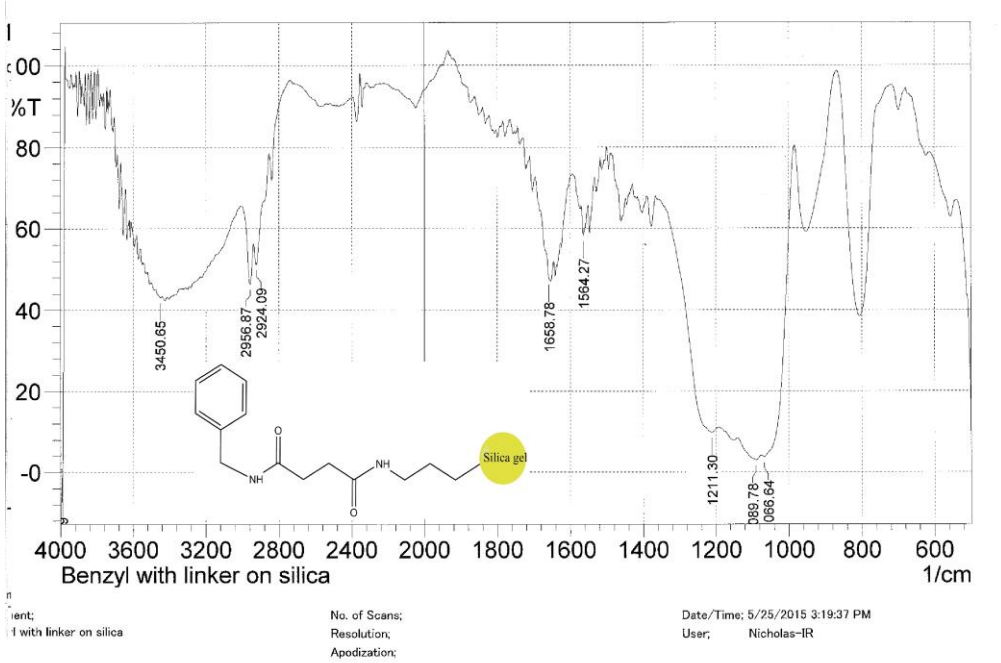


**Figure 128:** IR spectrum of benzyl reference with linker **141**.

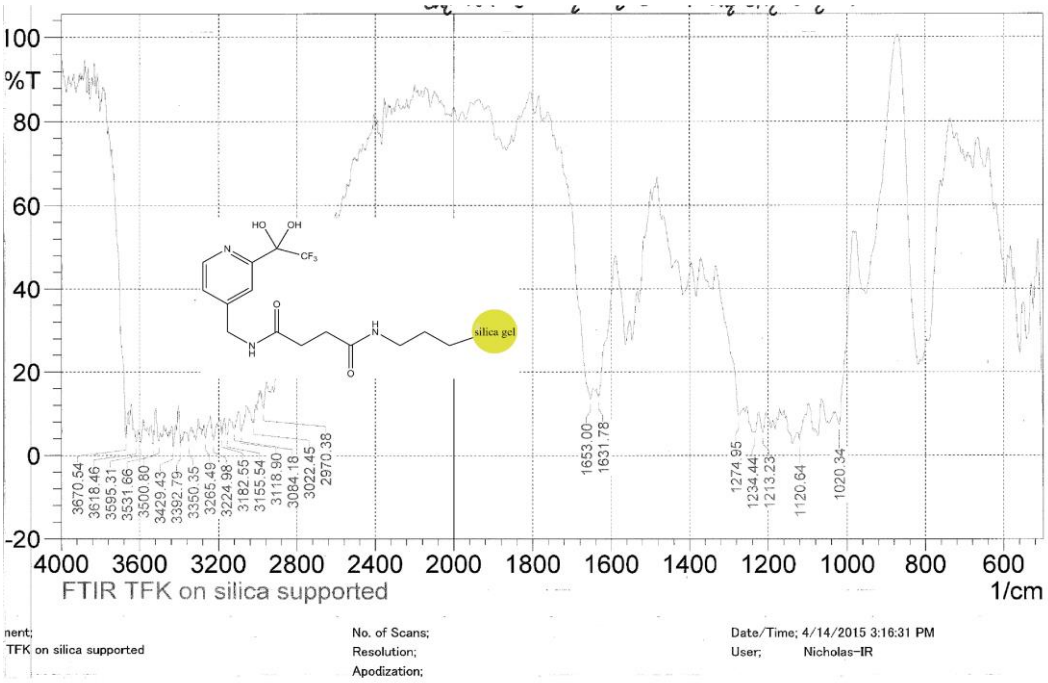


**Figure 129:** IR spectrum of TSA with linker 139.

### 4.6.3 Kinetics measurements.

Ligands **125** through **138** were prepared by mixing 0.1 mmol each of the constituent aldehyde, the constituent amine, and zinc trifluoromethanesulfonate in 25 mL methanol and allowing the mixtures to equilibrate for no less than 48 hours. Each of these was then diluted 1:10 to produce 0.4 mM solutions for use in the assay. The buffer solution used was 100 mM MOPS at pH 7.5. The substrate **122** was prepared by following the literature procedure.[194] The substrate solution at 40 mM was prepared in a 10 mL volumetric flask using dry acetonitrile (dried and distilled over $CaH_2$) and stored under nitrogen in the freezer when not in use. A new substrate solution was prepared each morning and discarded at the end of the day to minimize the effect of any water in the acetonitrile hydrolyzing the substrate over the course of the day. For the purpose of converting absorbance values to concentrations, a calibration curve was prepared using p-nitrophenol **124** in water with excess KOH to ensure the compound is in the colored (phenolate) form. The concentrations used for the calibration curve were $10^{-4}$ M, $7.5x10^{-5}$ M, $5x10^{-5}$ M, and $2.5x10^{-5}$ M. The extinction coefficient was found by this method to be 17851 $cm^{-1}M^{-1}$.

Measurements were performed in a 1 cm quartz cuvette in a diode array spectrophotometer (HP8452A) at ambient temperature (22 - 24C) The absorbance at 400 nm was monitored for nitrophenolate production and the absorbance at 520 nm was monitored for variations in the baseline to ensure the data was trustworthy. Samples were taken every 7 seconds for 7 minutes, with minutes 1-3 used for data processing. The solutions used in the cuvette were made from 800 µL MOPS solution, 400 µL catalyst solution, 500-800 µL substrate solution, and acetonitrile added to fill volume

for a total of 2 mL reaction mixture. The data was only kept if the $R^2$ value of the Lineweaver-Burk plot was >0.96 and the average $R^2$ for all 13 tested ligand is 0.989.

## References


(1) Eyring, H. *J. Chem. Phys.* **1935**, *3*, 107.
(2) Evans, M. G.; Polanyi, M. *J. Chem. Soc., Faraday Trans.* **1935**, *31*, 875.
(3) Jencks, W. P. *Catalysis in Chemistry and Enzymology*; McGraw-Hill: New York, 1987
(4) Pauling, L. *Chem. Eng. News* **1946**, *24*.
(5) Hilvert, D. *Annu. Rev. Biochem* **2000**, *69*, 751.
(6) Pollack, S.; Jacobs, J.; Schultz, P. *Science* **1986**, *234*, 1570.
(7) Tramontano, A.; Janda, K.; Lerner, R. *Science* **1986**, *234*, 1566.
(8) Jacobs, J.; Schultz, P. G.; Sugasawara, R.; Powell, M. *J. Am. Chem. Soc.* **1987**, *109*, 2174.
(9) Janda, K.; Schloeder, D.; Benkovic, S.; Lerner, R. *Science* **1988**, *241*, 1188.
(10) Benedetti, F.; Berti, F.; Colombatti, A.; Ebert, C.; Linda, P.; Tonizzo, F. *Chem. Commun.* **1996**, 1417.
(11) Gao, C.; Lavey, B. J.; Lo, C.-H. L.; Datta, A.; Wentworth, P.; Janda, K. D. *J. Am. Chem. Soc.* **1998**, *120*, 2211.
(12) Bender, M. L.; Homer, R. B. *J. Org. Chem.* **1965**, *30*, 3975.
(13) Bruice, T. C.; Holmquist, B. *J. Am. Chem. Soc.* **1968**, *90*, 7136.
(14) Holmquist, B.; Bruice, T. C. *J. Am. Chem. Soc.* **1969**, *91*, 2993.
(15) Pratt, R. F.; Bruice, T. C. *J. Am. Chem. Soc.* **1970**, *92*, 5956.
(16) Wentworth, P.; Datta, A.; Smith, S.; Marshall, A.; Partridge, L. J.; Blackburn, G. M. *J. Am. Chem. Soc.* **1997**, *119*, 2315.
(17) Tanaka, F. *Chem. Rev.* **2002**, *102*, 4885.
(18) Dinaut, A. N.; Chen, M.-J.; Marks, A.; Batey, R. A.; Taylor, S. D. *Chem. Commun.* **2000**, 385.
(19) Janda, K.; Benkovic, S.; Lerner, R. *Science* **1989**, *244*, 437.
(20) Hilvert, D.; Hill, K. W.; Nared, K. D.; Auditor, M. T. M. *J. Am. Chem. Soc.* **1989**, *111*, 9261.
(21) Brown, F. K.; Houk, K. N. *Tetrahedron Lett.* **1984**, *25*, 4609.
(22) Wagner, J.; Lerner, R. A.; Barbas, C. F. *Science* **1995**, *270*, 1797.
(23) Cook, C. E.; Allen, D. A.; Miller, D. B.; Whisnant, C. C. *J. Am. Chem. Soc.* **1995**, *117*, 7269.
(24) Hilvert, D.; Carpenter, S. H.; Nared, K. D.; Auditor, M. T. *Proc. Natl. Acad. Sci.* **1988**, *85*, 4953.
(25) Hilvert, D.; Nared, K. D. *J. Am. Chem. Soc.* **1988**, *110*, 5593.
(26) Braisted, A. C.; Schultz, P. G. *J. Am. Chem. Soc.* **1994**, *116*, 2211.
(27) Lewis, C.; Kramer, T.; Robinson, S.; Hilvert, D. *Science* **1991**, *253*, 1019.
(28) Reymond, J.-L. In *Catalytic Antibodies*; Wiley-VCH Verlag GmbH & Co. KGaA: 2005, p 217.
(29) Takeuchi, T.; Matsui, J. *Acta Polym.* **1996**, *47*, 471.
(30) Mayes, A. G.; Whitcombe, M. J. *Adv. Drug Deliv. Rev.* **2005**, *57*, 1742.
(31) Kriz, D.; Kriz, C. B.; Andersson, L. I.; Mosbach, K. H. *Anal. Chem.* **1994**, *66*, 2636.
(32) Puoci, F. I., F.; Picci, N. *Curr. Drug Delivery* **2008**, *5*.
(33) Lucci, P.; Núñez, O.; Galceran, M. T. *J. Chromatogr., A* **2011**, *1218*, 4828.

(34) Li, W.; Li, S. In *Oligomers - Polymer Composites - Molecular Imprinting*; Springer Berlin Heidelberg: 2007; Vol. 206, p 191.
(35) Ge, Y.; Turner, A. P. F. *Eur. J. Org. Chem.* **2009**, *15*, 8100.
(36) Bossi, A.; Bonini, F.; Turner, A. P. F.; Piletsky, S. A. *Biosens. Bioelectron.* **2007**, *22*, 1131.
(37) Robinson, D. K.; Mosbach, K. *J. Chem. Soc., Chem. Commun.* **1989**, 969.
(38) Ohkubo, K.; Funakoshi, Y.; Urata, Y.; Hirota, S.; Usui, S.; Sagawa, T. *J. Chem. Soc., Chem. Commun.* **1995**, 2143.
(39) Leonhardt, A.; Mosbach, K. *React. Funct. Polym.* **1987**, *6*, 285.
(40) Sellergren, B.; Shea, K. J. *Tetrahedron: Asymmetry* **1994**, *5*, 1403.
(41) Sellergren, B.; Karmalkar, R. N.; Shea, K. J. *J. Org. Chem.* **2000**, *65*, 4009.
(42) Liu, X.-C.; Mosbach, K. *Macromol. Rapid Commun.* **1997**, *18*, 609.
(43) Visnjevski, A.; Schomäcker, R.; Yilmaz, E.; Brüggemann, O. *Catal. Commun.* **2005**, *6*, 601.
(44) Müller, R.; Andersson, L. I.; Mosbach, K. *Macromol. Rapid Commun.* **1993**, *14*, 637.
(45) Liu, X.-C.; Mosbach, K. *Macromol. Rapid Commun.* **1998**, *19*, 671.
(46) Matsui, J.; Nicholls, I. A.; Karube, I.; Mosbach, K. *J. Org. Chem.* **1996**, *61*, 5414.
(47) Polborn, K.; Severin, K. *Eur. J. Org. Chem.* **2000**, *6*, 4604.
(48) Polborn, K.; Severin, K. *Chem. Commun.* **1999**, 2481.
(49) Mayes, A. G.; Mosbach, K. *TrAC, Trends Anal. Chem.* **1997**, *16*, 321.
(50) Matsui, J.; Kato, T.; Takeuchi, T.; Suzuki, M.; Yokoyama, K.; Tamiya, E.; Karube, I. *Anal. Chem.* **1993**, *65*, 2223.
(51) Mayes, A. G.; Mosbach, K. *Anal. Chem.* **1996**, *68*, 3769.
(52) Hosoya, K.; Yoshizako, K.; Shirasu, Y.; Kimata, K.; Araki, T.; Tanaka, N.; Haginaka, J. *J. Chromatogr., A* **1996**, *728*, 139.
(53) Zimmerman, S. C.; Lemcoff, N. G. *Chem. Commun.* **2004**, 5.
(54) Corbett, P. T.; Leclaire, J.; Vial, L.; West, K. R.; Wietor, J.-L.; Sanders, J. K. M.; Otto, S. *Chem. Rev.* **2006**, *106*, 3652.
(55) Ladame, S. *Org. Biomol. Chem.* **2008**, *6*, 219.
(56) Furlan, R. L. E.; Otto, S.; Sanders, J. K. M. *Proc. Natl. Acad. Sci.* **2002**, *99*, 4801.
(57) Rowan, S. J.; Cantrill, S. J.; Cousins, G. R. L.; Sanders, J. K. M.; Stoddart, J. F. *Angew. Chem. Int. Ed.* **2002**, *41*, 898.
(58) Sanders Jeremy, K. M. In *Pure Appl. Chem.* 2000; Vol. 72, p 2265.
(59) Sanders, J. K. M. *Eur. J. Org. Chem.* **1998**, *4*, 1378.
(60) R. L. Cousins, G.; Poulsen, S.-A.; K. M. Sanders, J. *Chem. Commun.* **1999**, 1575.
(61) Furlan, R. L. E.; Ng, Y.-F.; Otto, S.; Sanders, J. K. M. *J. Am. Chem. Soc.* **2001**, *123*, 8876.
(62) Furlan, R. L. E.; Ng, Y.-F.; Cousins, G. R. L.; Redman, J. E.; Sanders, J. K. M. *Tetrahedron* **2002**, *58*, 771.
(63) Corbett, P. T.; Tong, L. H.; Sanders, J. K. M.; Otto, S. *J. Am. Chem. Soc.* **2005**, *127*, 8902.

(64) Polyakov, V. A.; Nelen, M. I.; Nazarpack-Kandlousy, N.; Ryabov, A. D.; Eliseev, A. V. *J. Phys. Org. Chem.* **1999**, *12*, 357.
(65) Lüning, U. *J. Inclusion Phenom. Mol. Recognit. Chem.* **2004**, *49*, 81.
(66) Brisig, B.; Sanders, J. K. M.; Otto, S. *Angew. Chem. Int. Ed.* **2003**, *42*, 1270.
(67) Vial, L.; Sanders, J. K. M.; Otto, S. *New J. Chem.* **2005**, *29*, 1001.
(68) Loran, J. S.; Naylor, R. A.; Williams, A. *J. Chem. Soc., Perkin Trans. 2* **1976**, 1444.
(69) Salvador, R. L.; Saucier, M. *Tetrahedron* **1971**, *27*, 1221.
(70) Matsumoto, M.; Estes, D.; Nicholas, K. M. *Eur. J. Inorg. Chem.* **2010**, *2010*, 1847.
(71) Kannappan, R.; Nicholas, K. M. *ACS Combi. Sci.* **2012**, *15*, 90.
(72) Kannappan, R.; Matsumoto, M.; Hallren, J.; Nicholas, K. M. *J. Mol. Catal. A: Chem.* **2011**, *339*, 72.
(73) Hage, D. S.; Anguizola, J. A.; Li, R.; Matsuda, R.; Papastavros, E.; Pfaunmiller, E.; Sobansky, M.; Zheng, X. In *Liquid Chromatography*; Lloyd, S. F. R. H. F. P. S., Ed.; Elsevier: Amsterdam, 2013, p 1.
(74) Tuchman, M.; Plante, R. J. *Hum. Mutat.* **1995**, *5*, 293.
(75) Hoogenraad, N. J. *Arch. Biochem. Biophys.* **1978**, *188*, 137.
(76) Hoogenraad, N. J.; Sutherland, T. M.; Howlett, G. J. *Anal. Biochem.* **1980**, *101*, 97.
(77) Hammock, B. D.; Wing, K. D.; McLaughlin, J.; Lovell, V. M.; Sparks, T. C. *Pestic. Biochem. Physiol.* **1982**, *17*, 76.
(78) Hammock, B. D.; Abdel-Aal, Y. A. I.; Hanzlik, T.; Jones, D.; Jones, G.; Roe, R. M.; Rudnicka, M.; Sparks, T. C.; Wing, K. D. In *Biosynthesis, Metabolism and Mode of Action of Invertebrate Hormones*; Hoffmann, J., Porchet, M., Eds.; Springer Berlin Heidelberg: 1984, p 416.
(79) Abdel-Aal, Y.; Hammock, B. *Science* **1986**, *233*, 1073.
(80) West, K. R.; Ludlow, R. F.; Corbett, P. T.; Besenius, P.; Mansfeld, F. M.; Cormack, P. A. G.; Sherrington, D. C.; Goodman, J. M.; Stuart, M. C. A.; Otto, S. *J. Am. Chem. Soc.* **2008**, *130*, 10834.
(81) Diels, O.; Alder, K. *Justus Liebigs Annalen der Chemie* **1928**, *460*, 98.
(82) Nicolaou, K. C.; Snyder, S. A.; Montagnon, T.; Vassilikogiannakis, G. *Angew. Chem. Int. Ed.* **2002**, *41*, 1668.
(83) Kirby, G. W.; Nazeer, M. *J. Chem. Soc., Perkin Trans. 1* **1993**, 1397.
(84) Pellissier, H. *Tetrahedron* **2009**, *65*, 2839.
(85) Alder, K. In *Neuere Methoden der Praparativen Organischen Chemie* Verlag Chemie: 1943, p 251.
(86) Ishihara, K.; Sakakura, A. In *Comprehensive Organic Synthesis II (Second Edition)*; Knochel, P., Ed.; Elsevier: Amsterdam, 2014, p 409.
(87) Roush, W. R. In *Comprehensive Organic Synthesis*; Trost, B. M., Fleming, I., Eds.; Pergamon: Oxford, 1991, p 513.
(88) Gresham, T. L.; Steadman, T. R. *J. Am. Chem. Soc.* **1949**, *71*, 737.
(89) Larsen, S. D.; Grieco, P. A. *J. Am. Chem. Soc.* **1985**, *107*, 1768.
(90) Jørgensen, K. A. *Angew. Chem. Int. Ed.* **2000**, *39*, 3558.
(91) Wichterle, O. *Collec. Czech. Chem. Commun.* **1947**, 292.
(92) Arbuzov, Y. A. *Dokl. Akad. Nauk SSSR* **1948**, *60*, 993.

(93) Freer, A. A.; Islam, M. A.; Kirby, G. W.; Mahajan, M. P. *J. Chem. Soc., Perkin Trans. 1* **1991**, 1001.
(94) Corrie, J. E. T.; Kirby, G. W.; Mackinnon, J. W. M. *J. Chem. Soc., Perkin Trans. 1* **1985**, 883.
(95) Kirby, G. W.; Bentley, K. W.; Horsewood, P.; Singh, S. *J. Chem. Soc., Perkin Trans. 1* **1979**, 3064.
(96) Li, J.; Lang, F.; Ganem, B. *J. Org. Chem.* **1998**, *63*, 3403.
(97) Aoyagi, S.; Tanaka, R.; Naruse, M.; Kibayashi, C. *J. Org. Chem.* **1998**, *63*, 8397.
(98) Jana, C. K.; Studer, A. *Eur. J. Org. Chem.* **2008**, *14*, 6326.
(99) Li, F.; Brogan, J. B.; Gage, J. L.; Zhang, D.; Miller, M. J. *J. Org. Chem.* **2004**, *69*, 4538.
(100) Yamamoto, H.; Kawasaki, M. *Bull. Chem. Soc. Jpn.* **2007**, *80*, 595.
(101) Bodnar, B. S.; Miller, M. J. *Angew. Chem. Int. Ed.* **2011**, *50*, 5630.
(102) Krchňák, V.; Moellmann, U.; Dahse, H.-M.; Miller, M. J. *J. Comb. Chem.* **2007**, *10*, 104.
(103) Lin, W.; Gupta, A.; Kim, K. H.; Mendel, D.; Miller, M. J. *Org. Lett.* **2008**, *11*, 449.
(104) Li, F.; Yang, B.; Miller, M. J.; Zajicek, J.; Noll, B. C.; Möllmann, U.; Dahse, H.-M.; Miller, P. A. *Org. Lett.* **2007**, *9*, 2923.
(105) Labaziewicz, H. L., Karl R.; Kejonen, T. H. *Heterocycles* **1989**, *29*, 2327.
(106) Yang, B.; Miller, P. A.; Möllmann, U.; Miller, M. J. *Org. Lett.* **2009**, *11*, 2828.
(107) Flower, K. R.; Lightfoot, A. P.; Wan, H.; Whiting, A. *J. Chem. Soc., Perkin Trans. 1* **2002**, 2058.
(108) Yamamoto, Y.; Yamamoto, H. *J. Am. Chem. Soc.* **2004**, *126*, 4128.
(109) Yamamoto, Y.; Yamamoto, H. *Angew. Chem. Int. Ed.* **2005**, *44*, 7082.
(110) Chow, C. P.; Shea, K. J. *J. Am. Chem. Soc.* **2005**, *127*, 3678.
(111) Momiyama, N.; Yamamoto, H. *J. Am. Chem. Soc.* **2004**, *126*, 5360.
(112) Nitsch, H.; Kresze, G. *Angew. Chem.* **1976**, *88*, 801.
(113) Felber, H.; Kresze, G.; Prewo, R.; Vasella, A. *Helv. Chim. Acta.* **1986**, *69*, 1137.
(114) Kirby, G. W.; Nazeer, M. *Tetrahedron Lett.* **1988**, *29*, 6173.
(115) Ding, X.; Ukaji, Y.; Fujinami, S.; Inomata, K. *Chem. Lett.* **2003**, *32*, 582.
(116) Fukui, K.; Yonezawa, T.; Shingu, H. *J. Chem. Phys.* **1952**, *20*, 722.
(117) Longuet-Higgins, H. C.; Abrahamson, E. W. *J. Am. Chem. Soc.* **1965**, *87*, 2045.
(118) Woodward, R. B.; Hoffmann, R. *Angew. Chem. Int. Ed. in English* **1969**, *8*, 781.
(119) Hoffmann, R.; Woodward, R. B. *J. Am. Chem. Soc.* **1965**, *87*, 2046.
(120) Houk, K. N. *J. Am. Chem. Soc.* **1973**, *95*, 4092.
(121) Houk, K. N. *Acc. Chem. Res.* **1975**, *8*, 361.
(122) Houk, K. *Organic Chemistry*; Springer Berlin Heidelberg: 1979; Vol. 79, p 1.
(123) Sustmann, R.; Schubert, R. *Angew. Chem. Int. Ed.* **1972**, *11*, 840.
(124) Sauer, J.; Sustmann, R. *Angew. Chem. Int. Ed.* **1980**, *19*, 779.
(125) Leach, A. G.; Houk, K. N. *Chem. Commun.* **2002**, 1243.
(126) McCarrick, M. A.; Wu, Y. D.; Houk, K. N. *J. Org. Chem.* **1993**, *58*, 3330.
(127) Leach, A. G.; Houk, K. N. *J. Org. Chem.* **2001**, *66*, 5192.
(128) Jana, C. K.; Grimme, S.; Studer, A. *Eur. J. Org. Chem.* **2009**, *15*, 9078.
(129) Jana, C. K.; Studer, A. *Angew. Chem. Int. Ed.* **2007**, *46*, 6542.

(130) Bollans, L.; Bacsa, J.; O'Farrell, D. A.; Waterson, S.; Stachulski, A. V. *Tetrahedron Lett.* **2010**, *51*, 2160.
(131) Calvet, G.; Blanchard, N.; Kouklovsky, C. *Synthesis* **2005**, *2005*, 3346.
(132) Miller, C. A.; Batey, R. A. *Org. Lett.* **2004**, *6*, 699.
(133) Hiroki Sakai, X. D., Tetsusuke Yoshida, Shuhei Fujinami, Yutaka Ukaji, and Katsuhiko Inomata *Heterocycles* **2008**, *76*, 1285.
(134) Resmini, M. M., A. A. P.; Pandit, U. K *Pure Appl. Chem.* **1996**, *68*, 2025.
(135) Meekel, A. A. P.; Resmini, M.; Pandit, U. K. *J. Chem. Soc., Chem. Commun.* **1995**, 571.
(136) Siegert, U.; Hahn, H.; Lang, H. *Inorg. Chim. Acta* **2010**, *363*, 944.
(137) Nitschke, J. R. *Acc. Chem. Res.* **2006**, *40*, 103.
(138) Riesgo, E.; Hu, Y.-Z.; Bouvier, F.; Thummel, R. P. *Inorg. Chem.* **2001**, *40*, 2541.
(139) Tran, A. T.; Liu, P.; Houk, K. N.; Nicholas, K. M. *J. Org. Chem.* **2014**, *79*, 5617.
(140) Nitschke, J. R.; Hutin, M.; Bernardinelli, G. *Angew. Chem. Int. Ed.* **2004**, *43*, 6724.
(141) Schultz, D.; Nitschke, J. R. *Proc. Natl. Acad. Sci.* **2005**, *102*, 11191.
(142) Schultz, D.; Nitschke, J. R. *J. Am. Chem. Soc.* **2006**, *128*, 9887.
(143) Brodbelt, J. S. *Int. J. Mass spectrom.* **2000**, *200*, 57.
(144) Brodbelt, J. S. *Annu. Rev. Anal. Chem.* **2010**, *3*, 67.
(145) Chow, C.-F.; Fujii, S.; Lehn, J.-M. *Angew. Chem. Int. Ed.* **2007**, *46*, 5007.
(146) Schröder, D. *Acc. Chem. Res.* **2012**, *45*, 1521.
(147) Marquis-Rigault, A.; Dupont-Gervais, A.; Baxter, P. N. W.; Van Dorsselaer, A.; Lehn, J.-M. *Inorg. Chem.* **1996**, *35*, 2307.
(148) Zhao, Y.; Truhlar, D. G *Theor. Chem. Acc.* **2008**, *120*, 215.
(149) Zhao, Y.; Truhlar, D. G. *Acc. Chem. Res.* **2008**, *41*, 157.
(150) Tomasi, J.; Mennucci, B.; Cammi, R. *Chem. Rev.* **2005**, *105*, 2999.
(151) Scalmani, G.; Frisch, M. J. *J. Chem. Phys.* **2010**, *132*.
(152) Tedim, J.; Biernacki, K.; Fonseca, J.; Patrício, S.; Carneiro, A.; Magalhães, A. L.; Gurman, S. J.; Freire, C.; Hillman, A. R. *J. Electroanal. Chem.* **2013**, *688*, 308.
(153) Champouret, Y. D. M.; Marechal, J.-D.; Chaggar, R. K.; Fawcett, J.; Singh, K.; Maseras, F.; Solan, G. A. *New J. Chem.* **2007**, *31*, 75.
(154) Hollas, A. M.; Gu, W.; Bhuvanesh, N.; Ozerov, O. V. *Inorg. Chem.* **2011**, *50*, 3673.
(155) Kaya, Y.; Icsel, C.; Yilmaz, V. T.; Buyukgungor, O. *Spectrochim Acta A* **2013**, *108*, 133.
(156) Carfagna, C.; Gatti, G.; Paoli, P.; Binotti, B.; Fini, F.; Passeri, A.; Rossi, P.; Gabriele, B. *Organometallics* **2013**, *33*, 129.
(157) Taylor, E. C.; Tseng, C. P.; Rampal, J. B. *J. Org. Chem.* **1982**, *47*, 552.
(158) López-Rodríguez, R.; Ros, A.; Fernández, R.; Lassaletta, J. M. *J. Org. Chem.* **2012**, *77*, 9915.
(159) Lishchynskyi, A.; Muñiz, K. *Eur. J. Org. Chem.* **2012**, *18*, 2212.
(160) Prema, D.; Wiznycia, A. V.; Scott, B. M. T.; Hilborn, J.; Desper, J.; Levy, C. J. *J. Chem. Soc., Dalton Trans.* **2007**, 4788.

(161) Endeshaw, M. M.; Bayer, A.; Hansen, L. K.; Gautun, O. R. *Eur. J. Org. Chem.* **2006**, *2006*, 5249.
(162) Saito, T.; Takekawa, K.; Takahashi, T. *Chem. Commun.* **1999**, 1001.
(163) Zhou, Y.; Zhu, Y.; Lin, L.; Zhang, Y.; Zheng, J.; Liu, X.; Feng, X. *Eur. J. Org. Chem.* **2014**, *20*, 16753.
(164) Hu, Y.; Xu, K.; Zhang, S.; Guo, F.; Zha, Z.; Wang, Z. *Org. Lett.* **2014**, *16*, 3564.
(165) Samoshin, A. V.; Hawker, C. J.; Read de Alaniz, J. *ACS Macro Lett.* **2014**, *3*, 753.
(166) Umamaheswari, V.; Cias, P.; Poppl, A.; Kaupp, M.; Gescheidt, G. *J. Chem. Soc., Dalton Trans.* **2014**, *43*, 698.
(167) Rajarajeswari, C.; Loganathan, R.; Palaniandavar, M.; Suresh, E.; Riyasdeen, A.; Akbarsha, M. A. *J. Chem. Soc., Dalton Trans.* **2013**, *42*, 8347.
(168) Stafford, C.; Arndtsen, B. A. *Inorg. Chim. Acta* **2011**, *369*, 231.
(169) Bogojeski, J.; Jelic, R.; Petrovic, D.; Herdtweck, E.; Jones, P. G.; Tamm, M.; Bugarcic, Z. D. *J. Chem. Soc., Dalton Trans.* **2011**, *40*, 6515.
(170) Herrmann, A. *Org. Biomol. Chem.* **2009**, *7*, 3195.
(171) Taylor, E. C.; Harrison, K. A.; Rampal, J. B. *J. Org. Chem.* **1986**, *51*, 101.
(172) A. Fletcher, D.; G. Gowenlock, B.; G. Orrell, K. *J. Chem. Soc., Perkin Trans. 2* **1997**, 2201.
(173) Yang, B.; Lin, W.; Krchnak, V.; Miller, M. J. *Tetrahedron Lett.* **2009**, *50*, 5879.
(174) Wassenaar, J.; Jansen, E.; van, Z.-J.; Bickelhaupt, F. M.; Siegler, M. A.; Spek, A. L.; ReekJoost, N. H. *Nat. Chem.* **2010**, *2*, 417.
(175) Akerman, M. P.; Chatturgoon, T.; Munro, O. Q. *Inorg. Chim. Acta* **2014**, *421*, 292.
(176) Falk, A.; Fiebig, L.; Neudörfl, J.-M.; Adler, A.; Schmalz, H.-G. *Adv. Synth. Catal.* **2011**, *353*, 3357.
(177) Carmona, D.; Viguri, F.; Asenjo, A.; Lahoz, F. J.; García-Orduña, P.; Oro, L. A. *J. Mol. Catal. A: Chem.* **2014**, *385*, 119.
(178) Tan, E. H. P.; Lloyd-Jones, G. C.; Harvey, J. N.; Lennox, A. J. J.; Mills, B. M. *Angew. Chem. Int. Ed.* **2011**, *50*, 9602.
(179) Bowles, M. R.; King, G. J.; Berndt, M. C.; Zerner, B. *BBA-Protein Struct. M* **1996**, *1298*, 167.
(180) Brady, K.; Abeles, R. H. *Biochemistry* **1990**, *29*, 7608.
(181) Heinisch, G.; Lötsch, G. *Angew. Chem.* **1985**, *97*, 694.
(182) Sadovoy, A. V.; Kovrov, A. E.; Golubeva, G. A.; Sviridova, L. A. *Chem. Heterocycl. Comp.* **2011**, *46*, 1215.
(183) Aubert, C.; Begue, J.-P.; Charpentier-Morize, M.; Nee, G.; Langlois, B. *J. Fluorine Chem.* **1989**, *44*, 377.
(184) Shcherbakova, I.; Huang, G.; Geoffroy, O. J.; Nair, S. K.; Swierczek, K.; Balandrin, M. F.; Fox, J.; Heaton, W. L.; Conklin, R. L. *Bioorg. Med. Chem.* **2005**, *15*, 2537.
(185) Koldobskii, A. B.; Solodova, E. V.; Verteletskii, P. V.; Godovikov, I. A.; Kalinin, V. N. *Tetrahedron* **2010**, *66*, 9589.
(186) Singh, R. P.; Cao, G.; Kirchmeier, R. L.; Shreeve, J. n. M. *J. Org. Chem.* **1999**, *64*, 2873.

(187) Babadzhanova, L. A.; Kirij, N. V.; Yagupolskii, Y. L.; Tyrra, W.; Naumann, D. *Tetrahedron* **2005**, *61*, 1813.
(188) Aicher, T. D.; Cortez, G. S.; Groendyke, T. M.; Khilevich, A.; Knobelsdorf, J. A.; Magnus, N. A.; Marmsater, F. P.; Schkeryantz, J. M.; Tang, T. P.; Google Patents: 2006.
(189) Aicher, T. D.; Cortez, G. S.; Groendyke, T. M.; Khilevich, A.; Knobelsdorf, J. A.; Magnus, N. A.; Marmsater, F. P.; Schkeryantz, J. M.; Tang, T. P.; Google Patents: 2012.
(190) Kelly, C. B.; Mercadante, M. A.; Hamlin, T. A.; Fletcher, M. H.; Leadbeater, N. E. *J. Org. Chem.* **2012**, *77*, 8131.
(191) Cheng, H.; Pei, Y.; Leng, F.; Li, J.; Liang, A.; Zou, D.; Wu, Y.; Wu, Y. *Tetrahedron Lett.* **2013**, *54*, 4483.
(192) Scott, J. D.; Stamford, A. W.; Gilbert, E. J.; Cumming, J. N.; Iserloh, U.; Misiaszek, J. A.; Li, G.; Google Patents: 2011.
(193) Cheng, Y.; Ho, E.; Subramanyam, B.; Tseng, J.-L. *J. Chromatogr. B* **2004**, *809*, 67.
(194) Sigman, D. S.; Jorgensen, C. T. *J. Am. Chem. Soc.* **1972**, *94*, 1724.